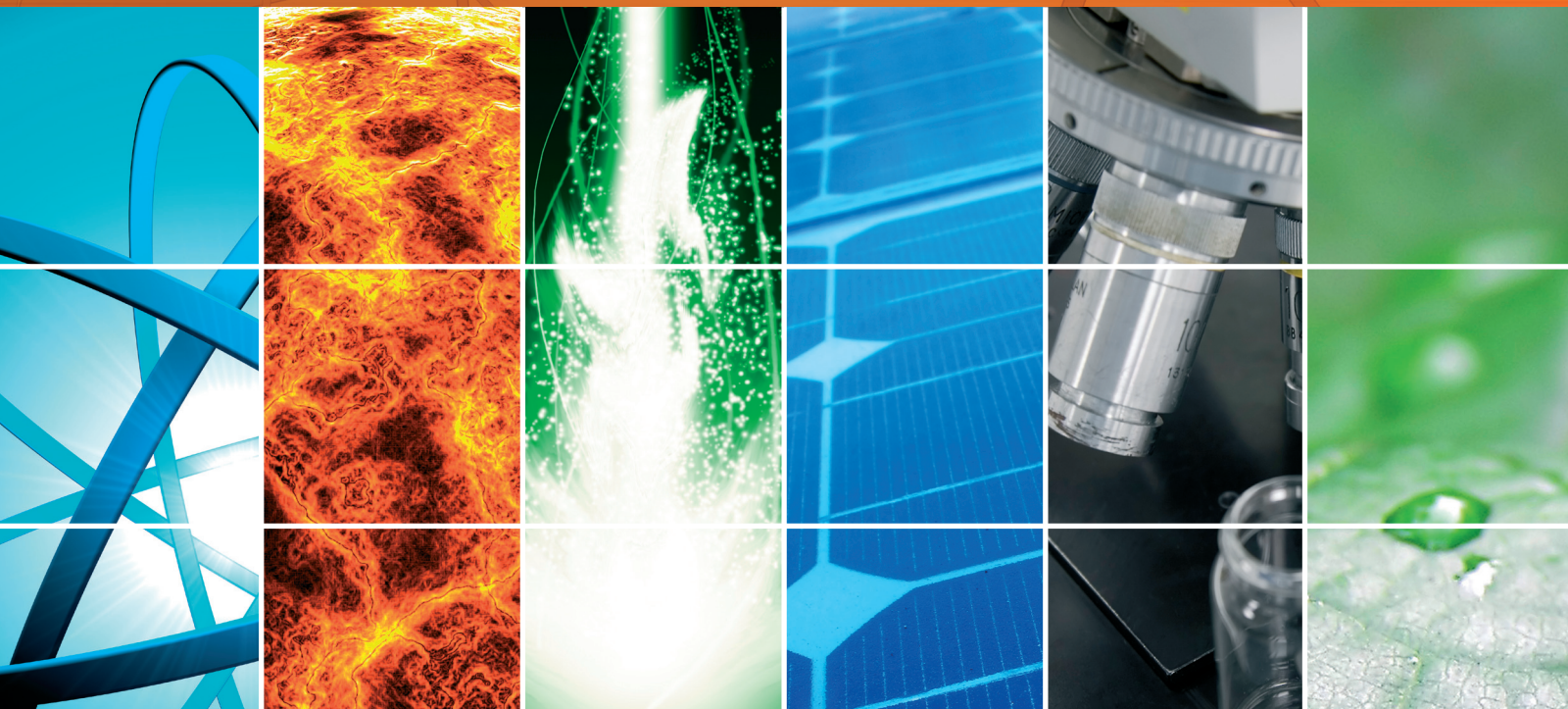


Thin-Film Photovoltaics

Guest Editors: Leonardo Palmisano, Aldo Di Carlo, Gaetano Di Marco,
Stephen M. Goodnick, Mario Pagliaro, and Stanislaw M. Pietruszko





Thin-Film Photovoltaics

International Journal of Photoenergy

Thin-Film Photovoltaics

Guest Editors: Leonardo Palmisano, Aldo Di Carlo,
Gaetano Di Marco, Stephen M. Goodnick, Mario Pagliaro,
and Stanislaw M. Pietruszko



Copyright © 2010 Hindawi Publishing Corporation. All rights reserved.

This is a special issue published in volume 2010 of “International Journal of Photoenergy.” All articles are open access articles distributed under the Creative Commons Attribution License, which permits unrestricted use, distribution, and reproduction in any medium, provided the original work is properly cited.

Editorial Board

M. Sabry Abdel-Mottaleb, Egypt
M. A., United Arab Emirates
Nihal Ahmad, USA
Nicolas Alonso-Vante, France
Wayne A. Anderson, USA
Vincenzo Augugliaro, Italy
Detlef W. Bahnemann, Germany
Ignazio Renato Bellobono, Italy
Raghu N. Bhattacharya, USA
Gion Calzaferri, Switzerland
Sebastiano Campagna, Italy
Vikram L. Dalal, USA
D. Demetriou Dionysiou, USA
Abderrazek Douhal, Spain
Samy El-Shall, USA
Beverly Glass, Australia

Shahed Khan, USA
Cooper H. Langford, Canada
Yuexiang Li, China
Gianluca Li Puma, UK
Panagiotis Lianos, Greece
Stefan Lis, Poland
Gilles Mailhot, France
Ugo Mazzucato, Italy
Jacek Miller, Poland
Franca Morazzoni, Italy
Leonardo Palmisano, Italy
David Lee Phillips, Hong Kong
Xie Quan, China
Tijana Rajh, USA
Saffa Riffat, UK
Peter Robertson, UK

Jean-Louis Scartezzini, Switzerland
Pathiyamattom Joseph Sebastian, Mexico
Panagiotis Smirniotis, USA
Sam-Shajing Sun, USA
Masanori Tachiya, Japan
Gopal Nath Tiwari, India
Veronica Vaida, USA
Roel van De Krol, The Netherlands
Mark van Der Auweraer, Belgium
Johannes Vos, Ireland
David Worrall, UK
Fahrettin Yakuphanoglu, Turkey
Jimmy C. Yu, Hong Kong
Klaas Zachariasse, Germany
Jincai H. Zhao, China

Contents

Thin-Film Photovoltaics, Gaetano DiMarco and Leonardo Palmisano
Volume 2010, Article ID 528512, 2 pages

Metal Nanoparticles and Carbon-Based Nanostructures as Advanced Materials for Cathode Application in Dye-Sensitized Solar Cells, Pietro Calandra, Giuseppe Calogero, Alessandro Sinopoli, and Pietro Giuseppe Gucciardi
Volume 2010, Article ID 109495, 15 pages

Organic Solar Cells: Problems and Perspectives, G. Chidichimo and L. Filippelli
Volume 2010, Article ID 123534, 11 pages

Bridged Phthalocyanine Systems for Sensitization of Nanocrystalline TiO₂ Films, Gloria Zanotti, Nicola Angelini, Sara Notarantonio, Anna Maria Paoletti, Giovanna Pennesi, Gentilina Rossi, Angelo Lembo, Daniele Colonna, Aldo Di Carlo, Andrea Reale, Thomas M. Brown, and Giuseppe Calogero
Volume 2010, Article ID 136807, 11 pages

Investigation of Low-Cost Surface Processing Techniques for Large-Size Multicrystalline Silicon Solar Cells, Yuang-Tung Cheng, Jyh-Jier Ho, William J. Lee, Song-Yeu Tsai, Yung-An Lu, Jia-Jhe Liou, Shun-Hsyung Chang, and Kang L. Wang
Volume 2010, Article ID 268035, 6 pages

New Components for Dye-Sensitized Solar Cells, Stefano Caramori, Vito Cristino, Rita Boaretto, Roberto Argazzi, Carlo Alberto Bignozzi, and Aldo Di Carlo
Volume 2010, Article ID 458614, 16 pages

Progress in Polycrystalline Thin-Film Cu(In,Ga)Se₂ Solar Cells, Udai P. Singh and Surya P. Patra
Volume 2010, Article ID 468147, 19 pages

Preparation and Characterization of Sb₂Te₃ Thin Films by Coevaporation, Bin Lv, Songbai Hu, Wei Li, Xia Di, Lianghuan Feng, Jingquan Zhang, Lili Wu, Yaping Cai, Bing Li, and Zhi Lei
Volume 2010, Article ID 476589, 4 pages

ZnO-Nanorod Dye-Sensitized Solar Cells: New Structure without a Transparent Conducting Oxide Layer, Ming-Hong Lai, Auttasit Tubtimtae, Ming-Way Lee, and Gou-Jen Wang
Volume 2010, Article ID 497095, 5 pages

Fabrication of Dye-Sensitized Solar Cells with a 3D Nanostructured Electrode, Guo-Yang Chen, Ming-Way Lee, and Gou-Jen Wang
Volume 2010, Article ID 585621, 7 pages

Efficiency Improved by H₂ Forming Gas Treatment for Si-Based Solar Cell Applications, Yuang-Tung Cheng, Jyh-Jier Ho, William Lee, Song-Yeu Tsai, Liang-Yi Chen, Jia-Jhe Liou, Shun-Hsyung Chang, Huajun Shen, and Kang L. Wang
Volume 2010, Article ID 634162, 6 pages

Debundling and Selective Enrichment of SWNTs for Applications in Dye-Sensitized Solar Cells, F. Bonaccorso
Volume 2010, Article ID 727134, 14 pages



Lateral Infrared Photovoltaic Effects in Ag-Doped ZnO Thin Films, Wenwei Liu, Songqing Zhao, Kun Zhao, and Wei Sun
Volume 2010, Article ID 793481, 4 pages

Characterizations of Chitosan-Based Polymer Electrolyte Photovoltaic Cells, M. H. Buraidah, L. P. Teo, S. R. Majid, R. Yahya, R. M. Taha, and A. K. Arof
Volume 2010, Article ID 805836, 7 pages

Preparation of a Counter Electrode with P-Type NiO and Its Applications in Dye-Sensitized Solar Cell, Chuen-Shii Chou, Chin-Min Hsiung, Chun-Po Wang, Ru-Yuan Yang, and Ming-Geng Guo
Volume 2010, Article ID 902385, 9 pages

Editorial

Thin-Film Photovoltaics

Gaetano Di Marco¹ and Leonardo Palmisano²

¹ CNR- Istituto per i Processi Chimico-Fisici, Viale Ferdinando Stagno d'Alcontres, 37 98158 Messina, Italy

² Dipartimento di Ingegneria Elettrica, Elettronica e delle Telecomunicazioni, Università di Palermo, Viale delle Scienze, 90128 Palermo, Italy

Correspondence should be addressed to Leonardo Palmisano, palmisano@dicpm.unipa.it

Received 2 November 2010; Accepted 2 November 2010

Copyright © 2010 G. Di Marco and L. Palmisano. This is an open access article distributed under the Creative Commons Attribution License, which permits unrestricted use, distribution, and reproduction in any medium, provided the original work is properly cited.

A solution to obtain energy in a sustainable manner for the environment and to benefit the people of the earth is the use of the sun as a primary source. The development of new technologies is strategic for the scientific community and is a challenge for the 21st century. In fact, the amount of energy that the sun radiates into the earth is about ten thousand times greater than what mankind uses.

Thin-film photovoltaic systems are quickly diffusing in these last years, and they now account for some 12% of solar installation around the world. Thin-film (TF) photovoltaic cells are less expensive to manufacture than the traditional crystalline silicon-based ones and have considerably lowered the barrier to the entry into the photovoltaic energy business. Significantly, the production cost of first solar CdSe modules is now lower than $1\$/W_p$. The sector is thus rapidly switching from the heavy fragile silicon panels to thin-film technologies which use a number of different inorganic and organic photovoltaic (PV) semiconductors, and the revenue market share of TFPVs is expected to rise very much next years.

This special issue collects some research papers mainly reporting preparation, characterization, and testing of thin-films, some of which could be of importance in the near future by an application point of view to assemble new photovoltaic cells.

The essentials of each papers are described below.

Progress in Polycrystalline Thin Film CGIS Solar Cells. A variety of methods are presented to prepare CIGS [Cu(InGa)Se₂ or Cu(InGa)(Se,S)₂] thin films, and important parameters

(optoelectronic properties, substrates, partner layers) are assessed to improve efficiency of solar cells.

Preparation and Characterization of Sb₂Te₃ Thin Films by Coevaporation. New materials such as Sb₂Te₃ have the peculiarity of forming a stable ohmic back contacts with CdTe; as a matter of fact, the cadmium telluride shows interesting performances for photovoltaic applications. Electrical properties, structure, morphology, and preparation of antimony telluride are described.

Investigation of Low-Cost Surface Processing Techniques for Large-Size Multicrystalline Silicon Solar Cells. A simple method is presented to enhance conversion performance in large-size solar cells using multicrystalline silicon (mc-Si) wafer. In particular, a single layer (SL) and dual layer (DL) of silicon nitride (Si₃N₄) are deposited in mc-Si by plasma-enhanced chemical vapor deposition. Quantum efficiency measurements show that DL coating can get the best results.

Efficiency Improved by H₂ Forming Gas Treatment for Si-Based Solar Cell Application. Forming gas treatments (FG) on single-crystalline (sc) and on multicrystalline (mc) silicon (Si) components useful for solar cells improve their photovoltaic effects. The increment is larger in mc-Si than in sc-Si. The internal quantum efficiency increases with FG, especially in the visible region.

Lateral Infrared Photovoltaic Effects in Ag-Doped ZnO Thin Films. Ag-doped ZnO thin films exhibit a lateral-induced

photovoltage under 1064 nm pulse laser radiation. High photovoltaic responsivity and position sensitivity values are observed. This circumstance proposes the ZnO thin film as a good candidate for IR position photo-detector.

Organic Solar Cells: Problems and Perspectives. The use of semiconducting conjugated polymers in organic-based photovoltaic (OPV) cells is discussed as a current research topic. In this brief review, some interesting aspects connected to efficiency, diffusion, dissociation, and transport charge of the aforesaid material are described.

ZnO-Nanorod Dye Sensitized Solar Cells: New Structure without a Transparent Conducting Oxide Layer. Dye-sensitized solar cells (DSSCs) based on ZnO nanorod/film structure without transparent conducting oxide (TCO, typically fluoride-doped tin oxide/FTO) and two preparation methods are proposed. The new DSSCs yield interesting photovoltaic features.

Bridged Phthalocyanine Systems for Sensitization of Nanocrystalline TiO₂ Films. The paper explains the construction of DSSCs by using metal phthalocyanines and their derivatives. The reason why these dyes are considered “appealing materials” is pointed out. Furthermore, the synthesis strategy for conjugated superchromophore is presented.

Preparation of a counter Electrode with p-Type NiO and its Applications in Dye Sensitized Solar Cell. The effect of counter electrode with a p-type semiconductor (NiO film) on power conversion efficiency of DSSC, is investigated. The study compares different cathodes, and a photoelectrochemical analysis is carried out. It seems that the NiO film increases the electrocatalytic activity of the counterelectrode.

Metal Nanoparticles and Carbon-Based Nanostructures as Advanced Materials for Cathode Application in Dye-Sensitized Solar Cells. Advanced methods for the fabrication of cathodes for DSSCs, employing nanostructured materials, are reviewed. The attention is focused on metal nanoparticles and nanostructured carbon, among which nanotubes and graphene, whose good catalytic properties make them ideal for the development of high performance catalyst materials.

Fabrication of Dye Sensitized Solar Cells with a 3D Nanostructured Electrode. An original photoanode for DSSCs is fabricated. The electrode is realized by a sputtered 3D nanostructured indium tin oxide (ITO), electrophoretic deposition of TiO₂ nanoparticles and dye sensitization. The final device reveals improved performances in respect to the conventional ones.

New Components for Dye-Sensitized Solar Cells. DSSCs are third-generation photovoltaic devices that can be used in various applications, due to their low cost and ease of fabrication. In this contribution, recent advances in molecular

sensitizers, electron mediators, conductive polymers, and catalytic materials are reviewed.

Characterizations of Chitosan-Based Polymer Electrode Photovoltaic Cells. Solid polymer electrolytes are employed in the fabrication of solid-state photoelectrochemical cells. Several electrolytic compositions, electrical conduction, and photoelectrical performance are reported. Dyes extracts from local vegetables are also used to reduce the environmental impact.

Debundling and Selective Enrichment of SWNTs for Applications in Dye-Sensitized Solar Cells. The state of the art is reviewed on the use of single-wall carbon nanotubes (SWNTs) in DSSCs, where they can serve multiple purposes. The paper, together with a wide and comprehensive critical analysis of the literature, highlights the possible strategies and indicates a few useful directions for future research to improve the performance of nanotube-based DSSCs.

Gaetano Di Marco
Leonardo Palmisano

Review Article

Metal Nanoparticles and Carbon-Based Nanostructures as Advanced Materials for Cathode Application in Dye-Sensitized Solar Cells

Pietro Calandra, Giuseppe Calogero, Alessandro Sinopoli, and Pietro Giuseppe Gucciardi

CNR, Istituto per i Processi Chimico-Fisici, Sede di Messina, Salita Sperone, C.da Papardo, 98158 Faro Superiore Messina, Italy

Correspondence should be addressed to Giuseppe Calogero, calogero@me.cnr.it

Received 31 December 2009; Revised 12 February 2010; Accepted 25 February 2010

Academic Editor: Gaetano Di Marco

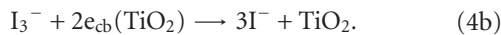
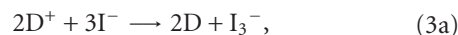
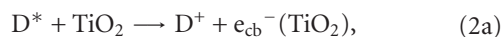
Copyright © 2010 Pietro Calandra et al. This is an open access article distributed under the Creative Commons Attribution License, which permits unrestricted use, distribution, and reproduction in any medium, provided the original work is properly cited.

We review the most advanced methods for the fabrication of cathodes for dye-sensitized solar cells employing nanostructured materials. The attention is focused on metal nanoparticles and nanostructured carbon, among which nanotubes and graphene, whose good catalytic properties make them ideal for the development of counter electrode substrates, transparent conducting oxide, and advanced catalyst materials.

1. Introduction

A photovoltaic cell (PC) is a device converting incident light to electrical energy. Dyes-sensitized solar cells (DSSCs) are devices devoted to the conversion of solar energy into electricity based on a large band gap nanocrystalline semiconductor sensitized by a dye which is chemically linked to the semiconductor surface and has substantial absorption in the visible range. The nanocrystalline DSSC technology was pioneered by Grätzel in the early nineties and its best conversion efficiency reported is more than 10% [1]. DSSCs have emerged as an important low in cost photovoltaic technology. A DSSC, as shown in Figure 1, consists of a transparent photoanode, an electrolyte solution containing a redox couple (I^-/I_3^-) and a counter electrode (CE) sandwich type assembled.

The photoanode consists of a film of titanium oxide nanoparticles deposited onto a conductive glass coated with a thin layer of doped Fluorine Tin oxide (FTO-Glass). The sensitizer is usually a ruthenium polypyridine complex. The principal photophysical and redox processes for a DSSC are listed below:



Under irradiation of light at frequency ν , the dye is excited to state D^* (1). The dye is chosen in such a way that its electronic excited state lies energetically above the conduction band (cb) edge of the semiconductor nanoparticles. In these conditions, the electron injection to the semiconductor (2a) can occur successfully, competing with the deactivation reaction (2b). In order to achieve a high current generation the oxidation of iodide (3a) and reduction of iodine (4a) must effectively compete with the charge-separated

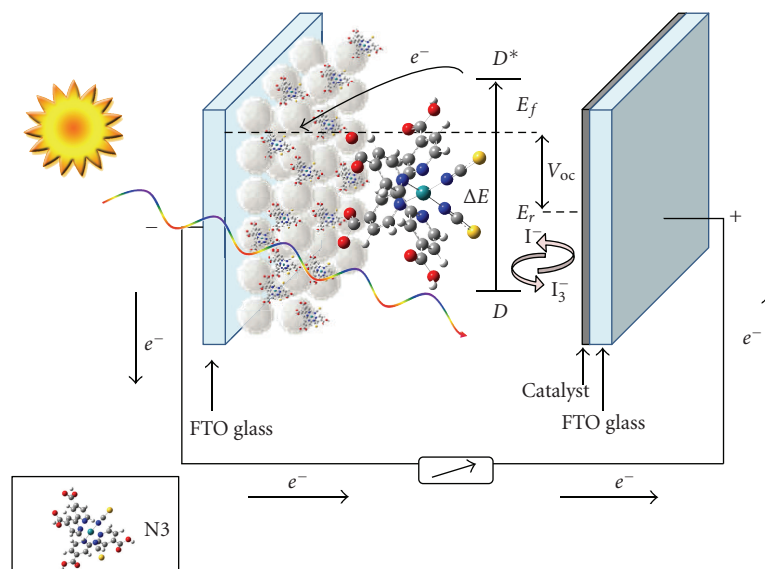


FIGURE 1: Schematic representation of the DSSC, based on a dye ruthenium-based (N3), to indicate the electron energy level and electron flux in different processes. The cell voltage (V_{oc}) observed under illumination corresponds to the difference ΔV between the quasi-Fermi level of titanium and the electrochemical potential of the electrolyte.

states recombination reactions (3b), (4b) which decrease the current production. Usually synthetic inorganic compounds such as Ruthenium (II) complexes with carboxylated polypyridyl ligands, especially [Ru(II)(2,2'-bipyridyl-4,4'-dicarboxylic-acid)₂(NCS)₂] (called N3), are employed as molecular sensitizers (D) in DSSCs [2]. A mixture of I_3^-/I^- ions in organic solvents commonly serves as charge carriers; Sapp et al. [3] have recently developed a new redox couple based on Cobalt organometallic complexes. The sealing procedures in assembling a DSSC are of key importance. An optimal sealing is necessary to prevent the electrolyte loss by leakage and/or the solvent evaporation, requiring the use of sealing materials resistant to the electrolyte corrosion.

Finally, another essential component for a long-time operation of the DSSC is the counter electrode, the place where the regeneration of the charge mediator (4a) takes place. The role of the counter electrode is twofold: first, it transfers electrons arriving from the external circuit back to the redox system, and second, it catalyzes the reduction of the oxidized charge mediator. Main requirements for a material to be used as counter electrode in a DSSC are a low charge-transfer resistance and high exchange current densities for the reduction of the oxidized form of the charge mediator [4]. Furthermore, such materials must possess chemical and electrochemical stability in the electrolyte system used in the cell. One of the best catalyst materials providing high exchange current for this reduction is platinum. But even graphite-based materials could be used as low cost cathode materials [5].

In a PC generation of electrical power under illumination is achieved by the photovoltaic device capability to produce a voltage over an external load and a current through the load at the same time. Several physical parameters are used to assess the PC performances. When the cell is short circuited

under illumination, the current (called short circuit current, I_{sc}) is at its maximum but the voltage is zero; on the other hand, under open circuit conditions, the voltage reaches its maximum value (called the open circuit voltage, V_{oc}) and the current is zero. So in a typical current versus voltage curve, the point maximising the current*voltage product defines the cell maximum power (Pmax). Another important parameter to assess the solar cell performance is the fill factor (FF), namely, the ratio of the cell maximum power (Pmax) over the product $V_{OC} * I_{sc}$.

In this minireview we report the state of the art of the two main catalyst materials type used in DSSC such as metal and carbon-based nanostructures (Figure 2) for cathodes preparation. One of the characteristics of the cathodes, also named counter electrodes (CEs), is the ability to keep the overvoltage low at photocurrent densities up to 20 mA/cm². So far, platinum has been the preferred material for the CE since it is a good catalyst for the triiodide reduction. A light reflecting CE is usually employed, consisting of a conducting TCO glass onto which a 2 μ m thick Pt mirror is deposited by sputtering, as shown in Figure 3. Our sputtering system consists of an RF-magnetron of 150 watts of power which generally works at low pressure (10^{-5} – 10^{-3} torr) under an N₂ gas flow. This kind of preparation is, however, too expensive for large-scale production. For such applications, and in order to obtain transparent devices, the procedure to prepare the CE consists (see Figure 4) in (1) spreading a small quantity of a hexachloroplatinic acid solution (5 mmol L⁻¹) in isopropanol on the conductive surface of a glass-FTO electrode and (2–4) heating the coated electrode at 500°C for 15 minutes (as shown in Figure 4). Otherwise, it is possible to use electrodeposition methods, were a platinum plate and a FTO-glass were used as anode and cathode, respectively. The electrodeposition is usually performed at

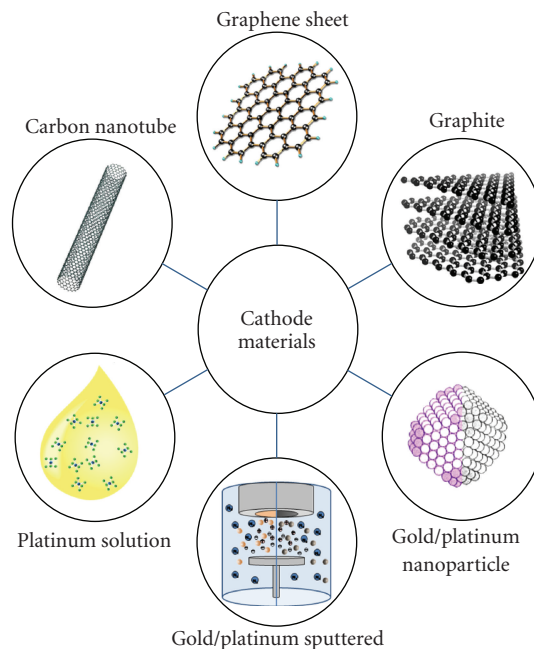


FIGURE 2: Schematic representation of the materials which can be used in DSSC as catalyst.

constant current (10 mA for 3 seconds in a 0.002 M H_2PtCl_6 aqueous solution).

In principle, even a fine Pt powder could be used, but for a thin platinum layer of 50 nm, is a large amount of metal (1 g/m^2) necessary. This amount could be reduced using a porous substrate of conducting material. However, the platinum might dissolve in the electrolyte solution by slow oxidation and complex formation as PtI_4 or H_2PtI_6 [6]; this could redeposit on the TiO_2 surface and short-circuit the cell by catalyzing the recombination process (4b). In metal nanoparticles, the porosity of the powder and the stability of the metal crystals could be combined. Another interesting material alternative to platinum in DSSC is carbon; it combines low cost, corrosion resistance, sufficient conductivity, catalytic activity, heat stability, and easy manipulation.

Porous carbon cathode is easily prepared from graphite powder dispersed in liquid solvent deposited on a conductive substrate and dried. To increase the catalytic activity and for a good adherence avoiding scratch of the carbon layer a binder (TiO_2 paste) is required. The resulting composite is fired at 450°C and a layer of $50 \mu\text{m}$ is necessary for an optimal conductivity [5].

For educational purposes a CE can be made by simply blackening a FTO glass with a pencil.

2. Advanced Counter Electrodes

2.1. Metal Nanoparticles. As mentioned above, in the optics of ever improving DSSC performance it turns out that the cathode material is required to provide high exchange current. This means that the available catalytic surface in the electrode plays a crucial role in determining the overall

device current. So we recently focused attention on the preparation of rough/porous electrodes which, being characterised by a higher surface, are expected to assure a higher number density of catalytic sites. The metal film preparation and its deposition onto the cathode will influence the final film structure/properties and ultimately the final device performance. In this framework, it is obvious that the use of nanoparticles, that is, particles whose size is in the nanometer range, results to be the answer to the need of advanced, high-surface materials.

Generally the strategies inspiring any synthetic method are roughly divided into two categories: the bottom-up and the top-down approaches. The distinction arises from the starting point in the synthetic route to prepare nanoparticles: being nanoparticles in between molecular species and macroscopic samples, their synthesis can be achieved:

- (i) from macroscopic precursors through subsequent subdivision in ever smaller particles by strong milling of solids or through lithographic processes, and this is the philosophy of the top-down approach (sputtering, laser ablation, vapour phase deposition, lithography, etc.)
- (ii) starting from their atomic and molecular precursors, through chemical reactions and modulating their self-assembling in order for nanoparticles to have desired structural and/or morphological characteristic, which is the philosophy of the bottom-up approach.

It is important to point out that, whatever the approach used, there is not any best synthetic method for all materials, but each one has its advantages and disadvantages and can reveal efficient for some classes of materials but not

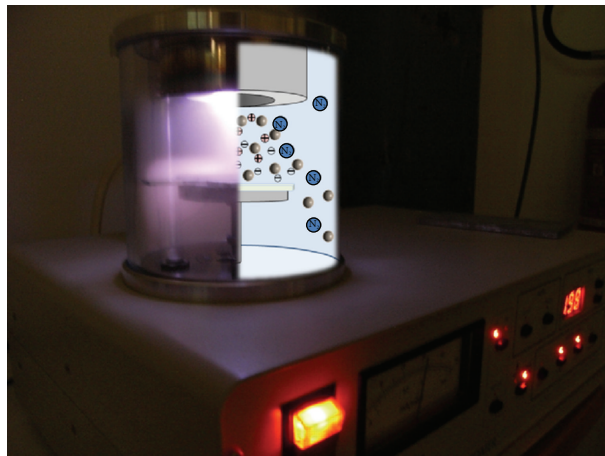


FIGURE 3: Sputtering system for metal deposition.

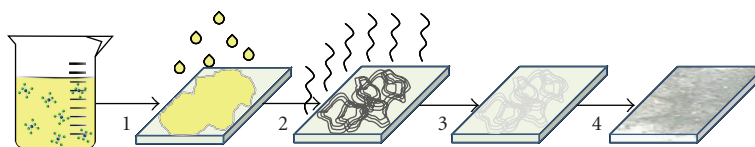


FIGURE 4: Schematic representation of the steps involved in preparation of Pt thin film in DSSC counter electrodes by means of hexachloroplatinic acid solution.

suitable for others. So, in the last few decades a wide range of protocols have been set up and now it is possible to synthesise nanoparticles of every kind of size and shape and of almost any kind of materials. However, the choice of the synthetic method must therefore take into account for it and be finalised to the subsequent use of the nanoparticles.

In this framework, top-down approaches (sputtering itself has been used to prepare also nanoparticles) [7–9] are generally quite expensive and resource-consuming; on the other hand chemical methods, which are typical bottom-up techniques, are generally cheaper and better fit for large scale applications. Moreover, since chemical methods allow in principle the control at a molecular level, we believe that they are to be preferred in view of advanced applications.

Other advantages of chemical methods are as follows:

- (i) they all are rapid;
- (ii) the synthesis can be carried out at room temperature;
- (iii) they allow a fine size and polydispersity control;
- (iv) in principle, they can be implemented to prepare 2D and/or 3D nanoparticle arrays.

Going deeper into details, the leading philosophy is to exploit the natural tendency toward specific self-aggregation exhibited by certain complex systems so chemical methods are generally based on the use of microheterogeneous systems (colloids, liquid crystals, gels, and micellar solutions). Moreover particles are suspended like colloids and, being the particle size usually less than 100 nm, these systems are optically clear and suitable for optical absorption investigations and this constitutes another specific advantage.

Incidentally, since this approach works at the atomic level, it is easy to prepare interesting nanocomposites by coating or doping, for example, nanoparticles with other materials in desired amount at mild conditions. Analogous procedures by top-down approaches involving bulk materials as starting materials would be more difficult: they would require extreme conditions as high temperatures to enhance thermal diffusion [10, 11].

The presence of the solvent or other molecules can represent a drawback since they can be actually regarded as “contaminants” that need to be removed making the synthesis “dirty”.

Generally, metal nanoparticles are produced in a liquid (“liquid chemical methods”) by reduction of chloroauric acid or hexachloroplatinate (HAuCl_4 or H_2PtCl_6). After dissolving the desired precursor, a reducing agent is added. This causes metal ions to be reduced to neutral metal atoms. As more and more of these atoms form, the solution becomes supersaturated, and the metal gradually starts to precipitate in the form of sub-nanometer particles. The rest of already formed metal atoms/clusters tend to stick to the existing particles, and so do the successively formed atoms/clusters.

This is the reason why, especially for the chemical synthesis of nanoparticles in liquid media, the achievement of stable nanoparticles is of crucial importance. This is not a trivial point since nanoparticles tend spontaneously to grow with no limits. The thermodynamic reason is obvious, that is, the trend to minimize the surface contribution to the total free energy.

In fact the free energy (G) of a phase depends, at constant pressure and temperature, on the surface A through the

surface tension γ :

$$dG_{\text{surface}} = \gamma dA. \quad (5)$$

Now, γ is usually positive, reflecting the fact that the surface atoms are in a high-energy state; so nanoparticles have the natural tendency to reduce this contribution by minimizing the surface-to-volume ratio. This results in a natural nanoparticle tendency to growth, which can take place through a wide number of mechanisms: agglomeration, coalescence, ripening, and so forth.

Detailed discussions on the possible mechanisms of nanoparticle growth can be found in the literature [12, 13].

From another point of view, the driving force of any growth process is the surface atoms attempt to form bonds in order to complete their coordination structure. Incidentally, it can be expected that and the more efficient is the saturation of surface dangling bonds by growing, the more powerful is the driving force to grow. Hence, an efficient synthetic protocol should inhibit nanoparticle growth allowing the size control in the nanosize regime.

This can be achieved basically by the following:

- (1) adsorption of suitable molecules at the nanoparticle surface, the role of such molecules is twofold: first, they act as surface-active molecules reducing the nanoparticle interfacial energy, and, secondly, they coat the nanoparticle with a protective shell preventing them from ripening/coalescence;
- (2) charging of particles; so charged nanoparticles cannot aggregate owing to the repulsive interparticle forces;
- (3) compartmentalization in distinct domains; so nanoparticles cannot come into contact to aggregate.

Of course the microscopic processes enabling growth inhibition are of utmost importance in determining the microscopic structure of the nanoparticles and, consequently, their properties.

Effective stability against the thermodynamically spontaneous unlimited growth can be conferred to nanoparticles by the use of a particular molecules which are able to bind nanoparticle surface.

In this case, nanoparticle stabilization can be obtained through the aid of the so-called "steric" stabilizer, generally constituted by polymers that are able to form complex with the metal precursor. After metal reduction with the formation of nanoparticles, further nanoparticles growth is inhibited by steric effects due to the presence of the polymer. The production of (catalytically active) metal sols by aqueous methanol reduction of metal salts in the presence of a steric stabilizer was first reported by Hirai and coworkers [14–16].

They studied the mechanism of particle formation in the Rh-poly(vinyl alcohol)-methanol-water systems but they also demonstrated similar syntheses of platinum sols, including the reduction of H_2PtCl_6 by aqueous methanol solution in presence of poly (vinyl pyrrolidone).

Another method for nanoparticle stabilization, based on the same approach, relies on the use of "chemical" stabilizer

exploiting the capability exhibited by some chemical species (as thiols, thioethers, sulphides, phosphines, amines, etc.) to form stable bonds with metal surface. The molecule-metal link allows nanoparticle coating and formation of a monolayer of opportunely oriented molecules. It is worth noting that if on the one hand this inhibits all the aforementioned mechanism of agglomeration/coalescence preserving nanoparticles from their growth, on the other hand this opens new directories in the controlled synthesis of macrostructures combining nanoparticles characteristics and molecular properties which can be exploited in sensors design, in the controlled drug delivery, and so forth.

Obviously different molecules possess different affinity towards metal surface so different degrees of stabilisation can be obtained. It is worth to highlight here that the strongest nanoparticle stabilisation can be obtained by the use of alkylic thiols and in particular those with alkylic chains with a number of C atom between 6 and 18 ($\text{C}_6\text{--C}_{18}$).

However, when such nanoparticles are exploited as enhanced catalysts as in DSSC, an easy accessibility of their surface to reacting species is needed. This requirement can be fulfilled by choosing easily displaceable coating agents, that is loosely adsorbed on the nanoparticle surface or by a stabilisation mechanism based on the surface charge adsorption.

Following this strategy, an important method was proposed by Turkevich in 1951 and refined by Frens in 1970s, which allows the synthesis of 20 nm golden, water-soluble, nanoparticles stabilised by citrate [17–19].

In this method, the sodium citrate first acts as a reducing agent. At the first step an extensive networks of gold nanowires is formed as a transient intermediate [20], after which gold nanoparticle formation takes place. The negatively-charged citrate ions are adsorbed onto the gold nanoparticles, introducing the surface charge that repels the particles and prevents them from aggregating. The reduction in the amount of sodium citrate as a consequence of the redox reaction will reduce the amount of the citrate ions available for stabilizing the particles, and this will cause the small particles to aggregate into bigger ones until the total surface area of all particles becomes small enough to be covered by the existing citrate ions.

Generally, this method is used to produce modestly monodisperse spherical gold nanoparticles suspended in water of about 10–20 nm in diameter. Larger particles can be produced by reducing the amount of sodium citrate but this comes at the cost of monodispersity and shape.

The most popular procedure to prepare Platinum nanoparticles by citrate reduction of PtCl_6^{2-} is described by Aika et al. (1976) [21]. Since citrate does not have a strong capability of linking gold nanoparticles, the stability is quite poor and an aggregation/coalescence usually occurs in short time.

Facing this problem Devi and rao [22] set up a method for the preparation of platinum nanoparticles from platinumous chloride (K_2PtCl_4) by reduction with H_2 and simultaneous addition of capping polymer material (sodium polyacrylic acid). The size of platinum nanoparticles was controlled by changing the ratio of concentration of a capping polymer

material, but, as it can be seen, the problem of an easily displaceable capping agent to prepare a surface-accessible nanosized catalyst again emerges. Better results can be obtained by a method based on the reaction path proposed by Brust et al. in 1994 for golden nanoparticle synthesis through chemical reduction of an Au(III) complex [23] with the only difference that the capping agent is not used.

The method is schematically depicted in scheme 1: briefly a Au(III) complex, usually HAuCl_4 , is transferred to an organic phase (usually toluene) through tetraoctyl ammonium bromide (TOAB). The Au(III) to Au(0) reduction is performed by adding an aqueous solution of NaBH_4 to the same reaction mixture. This simple procedure allows the preparation of 5–6 nm golden nanoparticles [24] although the size can be tuned by changing the experimental conditions; moreover the method has been used by us also for the synthesis of platinum nanoparticles simply by replacing the HAuCl_4 precursor salt with H_2PtCl_6 . In this reaction, TOAB is both the phase transfer catalyst and the stabilizing agent. Nanoparticle stabilisation occurs via the charge adsorption at the nanoparticle surface (the surfactant is responsible for this) without the use of any capping agent, so that the system is stable for a significant time. We would like to point out here an aspect that could be of utmost importance: a nanoparticle stabilisation without surface functionalisation with organic molecules implies a “nude” nanoparticle surface. This means that such nanoparticles can be chemically adsorbed onto a desired substrate establishing with it electrical junction, which is of utmost importance in the fabrication of photoelectrochemical devices.

The need for nanoparticle surface accessibility, the need of stabilising the particles in the nanometer regime, as well as the need to fulfil specific application specimens have inspired a wide variety of synthetic strategies have been exploited for this purpose such as photochemical [25] or controlled chemical reductions [26, 27], combined action of deposition/precipitation processes [28], ultrasound-induced reduction [29], and chemical reduction in microheterogeneous systems [30].

In this ambit, in the optics of avoiding the use of capping agents, which are chemically bonded to the metal nanoparticle surface, of particularly interest are surfactants because they are generally physically and reversibly adsorbed. A particularly successful method exploits solutions of water-containing reversed micelles as reaction and stabilizing media leading to quite monodisperse gold nanoparticles and allowing to control their size and shape simply by changing surfactant nature and/or system composition [31]. Using these systems, Chiang considered the possibility to obtain gold nanoparticles simply by chemical reduction of Au(III) salt with hydrazine, both dissolved in the aqueous core of reversed micelles according to the reaction



showing that nanoparticle size control can be achieved by changing the HAuCl_4 to hydrazine molar ratio. However, the resulting nanoparticle radius was never less than 50 Å. This is a considerable drawback because enhanced catalytic activity is expected for smaller nanoparticles.

In order to reach this goal, the confinement in dry reversed micelles using a simple and successful method [32] has been set up in the last few years. The proposed method scheme is depicted in Scheme 2.

The overall procedure consists in the following steps (i) entrapment of appropriate amount of the HAuCl_4 in the hydrophilic core of water-containing reversed micelles dispersed in apolar solvent, (ii) complete evaporation of volatile components (water and apolar solvent) of the salt-containing micellar solution, and (iii) resuspension of the salt/surfactant composite in apolar solvent leading to the formation of dry dispersions of salt nanoparticles coated by opportunely oriented surfactant molecules. The successive addition of a reductant solution (N_2H_4 /tetrahydrofuran) leads to the formation of ~ 14 Å gold nanoparticles [33].

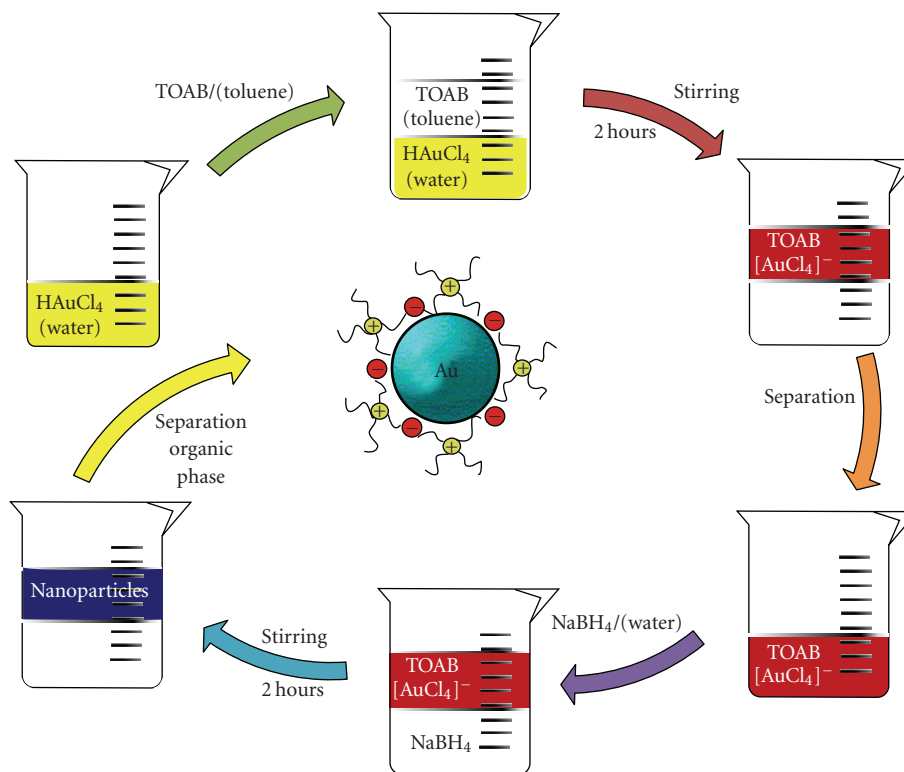
The advantages of this method are

- (i) the presence of very small nanoparticles,
- (ii) water absence, which reduces drawbacks such as inherent instability and secondary reactions.

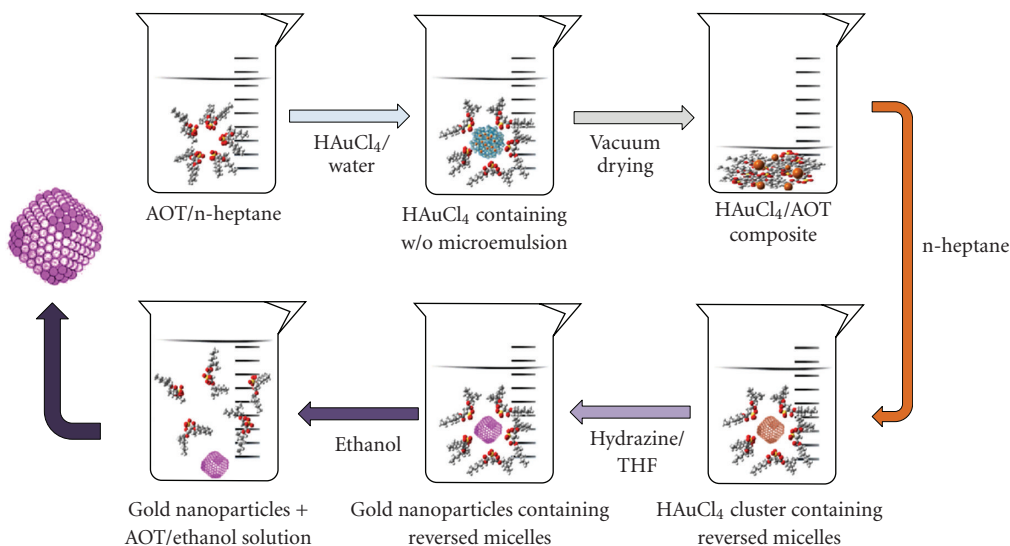
However, the most recent trend is directed towards the setting up of protocols avoiding the side products coming from chemical reduction leading to the metal nanoparticle formation. As already said, in fact, the chemical synthesis major drawback is the presence of side-products that could negatively affect not only nanoparticle physicochemical properties but also their catalytic activity, since they can most probably cause catalyst poisoning. So, the use of low-cost physical methods to produce high-purity metal nanoparticles, followed by their entrapment in surfactant solutions, could be an effective solution of the aforementioned problem.

An interesting example is given by the method we proposed in 2006, based on the combined action of the Solvated Metal Atom Dispersion (SMAD) technique and the confinement in anhydrous reversed micellar solution. In that work, we have exploited the SMAD technique to produce solvated gold atoms which were entrapped in n-heptane solutions of dry sodium bis(2-ethylhexyl)sulfosuccinate reversed micelles.

Scheme 3 shows schematically the procedure. Briefly, a metal filament was heated by Joule effect through a tuneable current: under certain conditions the heating causes the evaporation of metal atoms which are then collected by a controlled flow of cooled sodium bis(2-ethylhexyl)sulfosuccinate (AOT) micellar solution. In such conditions, competition between gold nanoparticle growth within the micellar core and surfactant adsorption on the nanoparticle surface leads to fast and complete inhibition of gold nanoparticle growth. By the combined action of SMAD technique and surfactant adsorption, two populations of gold nanoparticles confined in AOT liquid crystals were obtained. Owing to the soft coating of bigger Au nanoparticle by AOT molecules, these populations can be easily separated by resuspension of the solid nanocomposite in n-heptane. This leads to the formation of a precipitate of big (20–50 Å) Au nanoparticles, and a supernatant retaining the smaller size ones stabilising those with an optimal size. The high



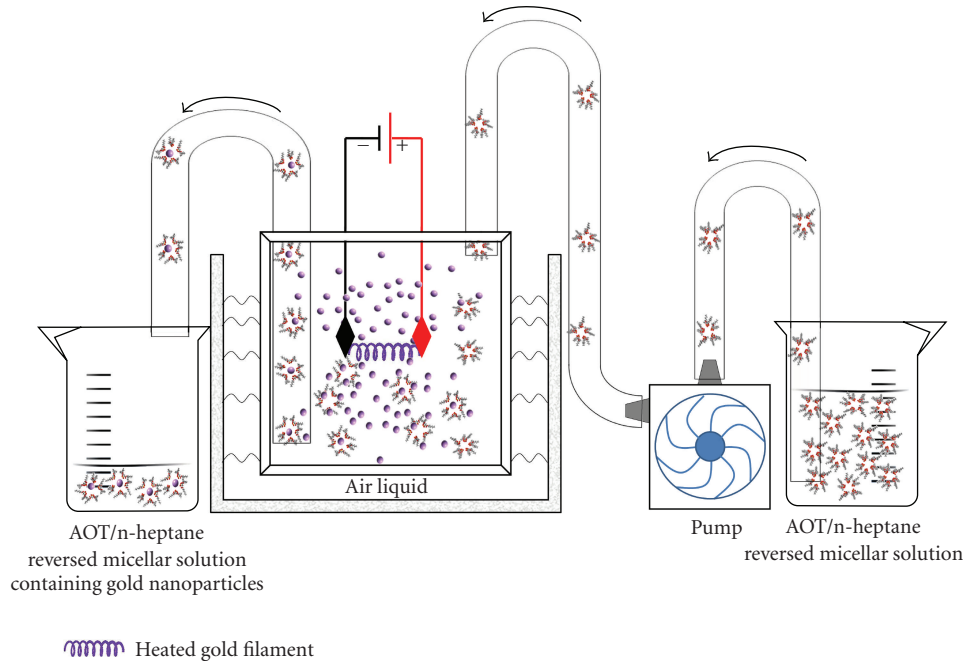
SCHEME 1: Scheme showing the synthetic steps involved in the Brust synthesis of gold nanoparticles. The method can be used to synthesize platinum nanoparticles by replacing the precursor salt to H_2PtCl_6 .



SCHEME 2: The protocol for gold nanoparticle synthesis based on the confinement of HAuCl_4 salt precursor in dry reversed micelles and its subsequent reduction to form $\sim 14 \text{ \AA}$ gold nanoparticles proposed by Calandra et al. [33].

AOT affinity for n-heptane, AOT polar headgroup specific interactions with gold nanoparticles and the presence of dispersion interactions were individuated to be the microscopic factors responsible for the observed behaviour. The relative proportions of these two populations should be varied by appropriate selection of the experimental procedure.

To conclude this brief survey on advanced techniques for metal nanoparticle preparation, it is worth to mention the recent experimental generation of gold particles by sonolysis, because of their low environmental impact. In such process, an aqueous solution of HAuCl_4 with glucose is used [34] and the reducing agents are hydroxyl and sugar pyrolysis radicals



SCHEME 3: Schematic mechanism of the method proposed by Calandra et al. [33], based on the combined action of the Solvated Metal Atom Dispersion (SMAD) technique and the confinement in anhydrous reversed micellar solution.

(formed at the interfacial region between the collapsing cavities and the bulk water). The obtained morphology is that of nanoribbons with width 30–50 nm and length of several micrometers. These ribbons are very flexible and can bend with angles larger than 90° so that they can form high interfacial surface skins. Spherical particles can also be obtained by replacing glucose with cyclodextrin.

2.2. Carbon Nanostructured Materials. Nanotechnology seems to help a lot in solar cells improvement. During the last decade, nanomaterials have emerged as new building blocks for constructing light-energy-harvesting assemblies, for the improvement of the cell efficiency and temporal stability [35]. Recent research in solar cell technology shows that a film of carbon nanotubes could replace two of the layers normally used in a solar cell, with improved performance and reduced costs. Carbonaceous materials feature good catalytic properties, electronic conductivity, corrosion resistance towards iodine, high reactivity, abundance, and low cost [36, 37]. In 1996 Kay and Grätzel demonstrated the importance of the high surface area introducing carbon black powder in graphite counter electrodes to enhance its catalytic activity [5]. Since then, other research groups have employed different carbon-based nanostructures such as graphite, carbon black, activated carbon, fullerene, hard carbon sphere, carbon nanotubes (CNTs) and graphene [38–47].

Single Wall Carbon Nanotubes (SWNTs) are made by rolling up a single graphene sheet [48, 49] with fullerene like end-cap [50] (see Figure 5). Because the structure of carbon nanotubes is closely related to that of graphene, nanotubes are generally labelled in terms of the graphene lattice unit

vectors \mathbf{a}_1 and \mathbf{a}_2 . The structure can be specified or indexed by its circumferential vector (\mathbf{C}_h), defined as the chiral vector which connects two crystallographically equivalent sites on a graphene sheet. In this way, the geometry of an SWNT is completely specified by the chiral vector, defined as

$$\mathbf{C}_h = n\mathbf{a}_1 + m\mathbf{a}_2, \quad (7)$$

where the pair of integers (n, m) are the so-called chiral indexes. The diameter d of the nanotube can be estimated from the following equation:

$$d = \left| \frac{\mathbf{C}_h}{\pi} \right| = \frac{\sqrt{3}a_{C-C}}{\pi} \sqrt{n^2 + n \cdot m + m^2}, \quad (8)$$

where a_{C-C} is the length of the C–C bond. The chiral vector \mathbf{C}_h uniquely defines a particular (n, m) tube, as well as its chiral angle θ , being the angle between \mathbf{C}_h and \mathbf{a}_1 . The chiral angle θ is given by

$$\theta = \tan^{-1} \left[\frac{\sqrt{3}m}{m + 2n} \right]. \quad (9)$$

The value of θ is in the $0^\circ \leq \theta \leq 30^\circ$ range, due to the hexagonal symmetry of the graphene lattice. The chiral angle also determines the tilt angle of the hexagon with respect to the nanotubes axis direction. This diameter and chirality dependence generates an interesting structural aspect, that is, the importance of structurally defined categories and families of nanotubes of different physical properties. For instance, nanotubes with $\text{mod}[(2n + m), 3] = 1$ or 2 are of

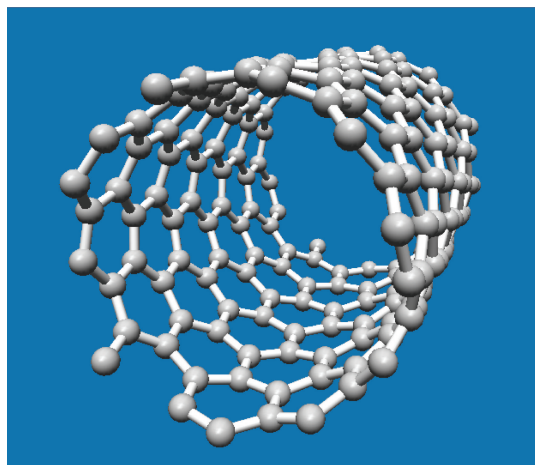


FIGURE 5: Schematic representation of a Single wall carbon nanotube (SWNT).

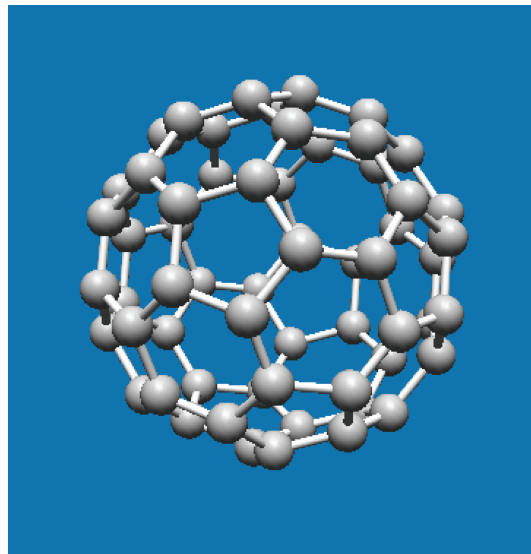


FIGURE 7: Schematic representation of a fullerene.

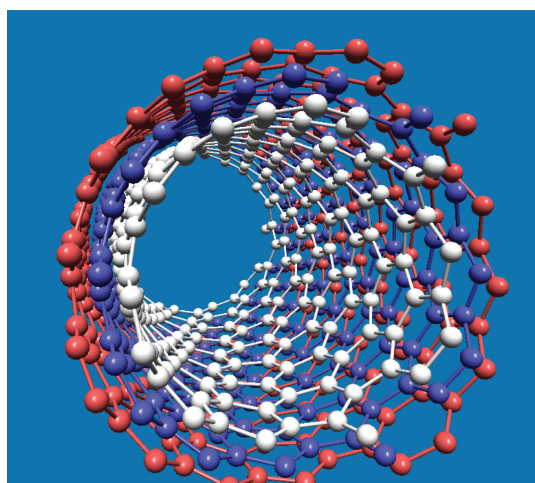


FIGURE 6: Schematic representation of a Multi wall carbon nanotube (MWNT).

semiconducting nature (type 1 or type 2), while tubes having $\text{mod}[(2n + m), 3] = 0$ are metallic [51].

Multiwall nanotubes (MWNTs) consist of multiple concentric SWNTs with random chirality making them metallic on average (see Figure 6) [52].

The unique electrical and electronic properties, wide electrochemical stability window, and high surface area have prompted many researchers to employ SWNTs assemblies for energy conversion and storage devices [53–60]. Fullerenes, for example (see Figure 7), exhibit rich photochemistry and act as an electron shuttle in photochemical solar cells [61, 62]. They also play an important role in improving the performance of organic photovoltaic cells [63].

In a typical photochemical solar cell, a semiconducting film serves as a photoactive electrode that upon excitation with visible light generates electron-hole pairs. As one of the charge carriers (e.g., the electron) is driven to the counter electrode, the other charge carrier (e.g., the hole) is scavenged by a redox couple present in the electrolyte, thus

generating a photocurrent. Commercially available SWNTs contain both metallic and semiconducting nanotubes with different chirality. The work function of SWNT bundles is known to be about -4.8 eV versus absolute vacuum scale (AVS). Carbon nanotubes are characterized by a bandgap usually occurring in the 0 – 1.1 eV range, depending upon their chirality and diameter [53, 63]. As-purchased SWNTs powders consist of bundles and ropes of nanotubes with random chiralities [64–66], losing their specific mechanical, thermal, and optical properties [67–70]. For optical characterization (determination of transition energies, chiralities, diameter distribution, etc.) of the SWNTs samples, a procedure for debundling and individualization is needed [71–74]. Ultrasonication in water-surfactant solutions is used to disaggregate the nanotubes bundles. The presence of the surfactant molecules guarantees the encapsulation of individual tubes, preventing reaggregation phenomena due to the strong surface forces [65]. Large impurities can be removed by filtration. A final ultracentrifugation step allows for separating the supernatant, rich of individual and small nanotubes bundles, from large residual bundles and insoluble materials [75–77]. In Figure 8 some samples prepared at IPCF-CNR (Istituto per i Processi Chimico-Fisici—Consiglio Nazionale delle Ricerche) in Messina are shown. SWNT films also show a high electrochemical activity in the iodide/tri-iodide redox reaction because of the one-dimensional nanofeature of SWNTs which can provide better electron transport. In detail, the redox reaction involved in a DSSC is catalyzed by the counter electrode.

In DSSCs with a liquid electrolyte, the conversion efficiency becomes higher by using nanocarbon electrodes because of their high surface areas, which enhances the electrochemical activity of the electrode. The recent development of depositing ultra-thin and homogeneous CNT films on transparent glass electrodes can be conveniently realized with the benefit of lowering the process cost and improving

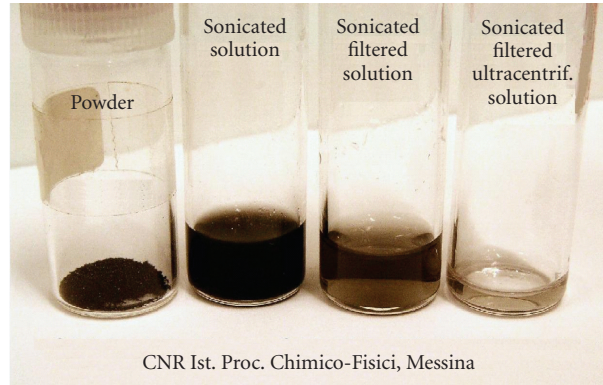


FIGURE 8: Pictures of the result of the debundling and dispersion process: from powders (left) to solutions of individual SWNT after ultracentrifugation (right).

the mechanical flexibility. Carbon nanotubes, in particular, combine advantages such as high electrical conductivity, chemical stability, and high surface area with good electrochemistry and catalytic properties making them suitable for applications in many energy conversion technologies such as catalytic counter electrode materials in DSSCs [78]. In particular, CNTs are efficient to catalyze the tri-iodide reduction and, thus, are good candidates to replace Platinum in DSSCs. The diameters of MWNTs are in the order of 3–10 nm, while SWNTs have the smallest diameters (<2 nm). These materials exhibit very large aspect ratios (> 10^3) and establish percolation pathways that can provide the means for high carrier mobility and an efficient charge transfer. Despite high catalytic activity towards I_3^- reduction, nanocarbon counter electrodes pose additional risks to the stability of DSSC, since the electrolyte made upon nanocarbon powders prolong exposure in corrosive iodine/iodide redox electrolyte may lead to the detachment of loosely bound particles from the rest of the electrode promoting dark current and degrade the device performance. Lee et al. [78]. investigate the effect of dark and room temperature aging on the performance of carbon powder counter electrode based DSSC. The cathode was prepared by mixing Carbon powders (20 nm) with an organic binder dissolved in aqueous solutions. The resulting homogenous paste was coated on FTO by doctor blading and sintered at 250°C for 1 hour; after DSSC TiO_2 electrode and carbon counter electrode were sandwiched with 80 micron thick polymer foil as a spacer, sealing was done by keeping the structure in a hot-press at 100°C for few seconds. The liquid electrolyte consisting of 0.5 M LiI, 0.05 M I_2 , and 0.5 M TBP in acetonitrile was introduced into the cell gap through predrilled hole on the counter electrode. Finally, the electrolyte injection hole was firmly sealed with surllyn and microscope cover glass. Under these conditions the carbon counter electrode shows a mesoporous structure facilitating the diffusion of the I_3^- ions, making the entire carbon film accessible to iodide ions. This yields DSSC performances similar to those employing Pt-counter electrodes, with $V_{oc} = 0.79$ V,

$J_{sc} = 16$ mA/cm², FF = 0.645, and efficiency = 7.56%. Studies carried out on the aging of this devices showed a decrease of only 16% of the performances over 60 days. Huang et al. [79] reported on the use of hard carbon spherules (HCS), a disordered carbon material, as counter electrode for DSSCs. HCS was prepared following the method reported in the literature [80]. Carbon counter electrode was prepared by screen-printing a slurry of carbon powder, conductive carbon black (30 nm average size) and polyvinylidene fluoride (PVDF) in N-methyl-2-pyrrolidone (NMP) onto the FTO glass substrate. Then the counter electrode was dried in vacuum oven at 100°C overnight. The cathode was integrated in a standard DSSC using a TiO_2 (average particle size 21 nm) film deposited on FTO, immersed in the dye (N3) and organic solvent-based liquid electrolyte (0.6 M dimethylpropylimidazolium iodide, 0.1 M of iodine, 0.5 M tert-butylpyridine, and 0.12 M of lithium iodide in 3-methoxyacetonitrile). When comparing the photocurrent-voltage characteristics of DSSCs using the HCS and sputtered Pt as the counter electrode it is found that the efficiency of HCS is slightly lower than Pt (5.7% against 6.5%), but notably higher than graphite (3.8%), indicating that the electrochemical activity of HCS is higher than graphite (containing 20% of carbon black). Koo et al. [81] investigated the possibility of using multi wall CNTs (MWCNT) as a new long stability counter electrode materials. DSSCs were made according to standard procedures, employing nanoporous TiO_2 films on FTO glass, N3 dyes [Ru(II)(2,2'-bipyridyl-4,4'-dicarboxylic-acid)₂(NCS)₂] and the I^-/I_3^- couple as redox electrolyte. Sealing was accomplished with Amosil 4 (Solaronix, SA). Counter electrodes were prepared by mixing multi wall carbon nanotubes powders (10–20 nm average diameter, 5 μ m in length) with deionized water and Carboxyl Methyl Cellulose, mechanically ball-milled for 24 hours. The obtained paste was deposited on FTO glass using doctor blade method and then dried at 70°C for 10 hours in air, thus obtaining a CNT film ~20–25 μ m thick. The authors reported a higher efficiency (8%) with respect to Pt-sputtered and electrodeposited

electrodes (5–6%), as well as a longer stability (>5 days compared with 3 days of Pt-electrodes). The better efficiency was attributed to a larger active area and good conductivity of the counter electrode. On the other hand, a higher stability against the electrolyte was found with respect to sputtered Pt counter electrodes and no detachment of CNT from the FTO glass was observed through electrochemical impedance spectroscopy measurements. Carbon nanotubes, thanks to their electrochemical activity, are efficient in catalyzing the reduction of triiodide so they are able to replace platinum in the DSSC [82]. Platinum was found to degrade over time while in contact with an iodide/triiodide liquid electrolyte, reducing the efficiency of a DSSC, whereas carbon nanotubes did not. The combination of high conductivity and transparency of carbon nanotubes films means that carbon nanotubes may be able to replace the TCO layer used in the DSSC as well as the platinum catalyst. (The transparency and conductivity also gives carbon nanotube films an advantage over other alternative catalysts, such as carbon black films, which have also been shown to be catalytic in the DSSC but are opaque and less conductive.) Carbon nanotube films are much more flexible and less prone to cracking than TCOs, making them ideal candidates for inexpensive roll-to-roll processing and varied installation configurations. Measuring the catalytic performance of nanotube films is crucial to explore methods for increasing their electrochemical activity through film processing. The catalytic activity of single walled carbon nanotube films in DSSCs has been studied by Trancik et al. [83]. Films were made from single-walled carbon nanotubes produced using arc discharge, suspended in a variety of solvents, sonicated and airbrushed onto a substrate placed on a hot plate at 100–150°C. Such tubes contain metal impurities consisting of nickel and yttrium catalyst particles as well as carbonaceous impurities in the form of amorphous carbon and graphitic nanoparticles. Chemical vapor deposition (CVD) was also used to grow both mats and forests of tubes consisting of long, nanotubes oriented along the plane of the substrate. This allowed to make ultrapure films, due to the extremely low metal (iron) to carbon ratio (metal content <0.01 wt%). By transferring a film of the forest tubes to a conducting glass substrate (using either direct contact or airbrushing tubes in an ethanol solution) and characterizing these samples using electrochemical impedance spectroscopy, it was possible to investigate the impact of metal impurities on the catalytic activity of the films. The reported measurements of the charge-transfer resistance associated with the reduction of triiodide as a function of film transparency and loading demonstrated that exposing the films to UV-generated ozone dramatically increases their catalytic activity, presumably by introducing defects. Ozone-treated tubes show high enough performance to replace platinum in the DSSC. These films could be used to replace both platinum and a TCO in the DSSC. Self assembled nanotube networks in thin films form are expected to facilitate the device fabrication process and provide opportunities for creating high performance solar cell devices with nanoscale building blocks. In this regard Zhu et al. [84] implemented a robust SWNT thin film into in anthocyanin-sensitized solar cells to improve

the transport of charge carriers from the light harvesting photoelectrode. Taking advantages of their intrinsic large surface areas and high electron conductivity of carbon nanotubes the authors have fabricated macrofilms of CNTs as counter electrodes, comparing the results with counter electrodes made of multi-walled, double-walled, activated carbon fabrics, and different high surface area carbon blacks were also investigated. Photo electrodes were prepared from a commercial TiO₂ powder (Degussa P25, average size 25 nm) using a screen printing techniques. The natural dye anthocyanin was extracted from frozen blackberries using methanol/acetic acid/water (25 : 4 : 21) [85]. The photo electrodes were immersed in the dye solution for at least 3 hours to ensure that the dye molecules were fully absorbed. The raw SWNT macrofilm (about 1 μm thick) was deposited on an FTO glass using a floating chemical vapor deposition technique [86], followed by an ethanol wetting in order to enhance the film-substrate adhesion. MWNTs were first treated to remove the catalysts and then stirred to introduce some functional groups and improve the conductivity. A thin film of entangled MWNTs (about 10 μm thick) was coated on an FTO glass after completely drying the sample. Vertically aligned DWNT films were prepared on an Al-coated silicon wafer by a water assisted CVD process [87] and then transferred to an FTO glass to make a 10 μm thick film after the ethanol wetting. different carbon blacks were tested. Counter electrodes of these carbon blacks were fabricated by mixing 80 wt% of the carbon black and 20 wt% of PVDF-HFP binder. A slurry of the above mixture was made using N-methyl-2-pyrrolidone (NMP) as a solvent and this was subsequently brush-coated onto an FTO glass. Compared with the cells using other carbon counter electrodes, the cells with CNT counter electrodes in general show better performance in conversion efficiency ($\eta = 1.46\%$, between 2 and 3 times the value observed with other nanostructures), which can be attributed to the increase in short circuit current density (J_{sc}). These values are comparable with the highest value ever reported for a cell using a natural dye and Pt counter electrode [88]. Besides the high surface area, the authors argue that the 1D nature of SWNTs significantly contributes to the charge transfer process owing to its improved electric conductivity. The utilization of CNT electrodes affects the kinetics of charge transfer at the electrolyte-carbon interface, as carbon blacks and nanocarbon materials have dissimilar surfaces onto which iodide/iodine absorbed. The contact interface between the counter electrode and surrounding electrolyte is better in CNT materials, which have nanoscale conducting channels and therefore are expected to enhance the electrochemical activity of the electrodes, as demonstrated from the experimental results [86–89]. More recently we have introduced a novel stainless steel cathode coated with commercial non purified SWNTs as an original, stable, low-cost, and high efficient counter electrode for DSSCs [89]. The counter electrodes were prepared by drop casting bundles of Carboxyl SWNTs dispersed in water onto an FTO conducting glass or a thin (2 mm) stainless steel sheet as substrates. SWNTs produced by arc discharge with nominal diameters and lengths range between $d_t = 1.2\text{--}1.5$ nm and $L = 2\text{--}5$ μm,

respectively, were used. SWNTs were dispersed in water by ultrasonication without any further pretreatment, and then cast onto the substrate at a temperature of 150°C. The photoanodes were prepared by depositing TiO₂ films on FTO conducting glass. After drying the TiO₂, the covered glass plates were sintered in air for 30 minutes at 450°C, cooled to about 80°C and soaked in N3 dye solution overnight. Measurements on 0.52 cm² test cells showed a maximum solar energy conversion efficiency of 3.92% for counter electrodes employing nanotubes on stainless steel, higher than the one obtained with Pt-transparent/FTO counter electrodes, and comparable to the one obtained with Pt mirrors. The stability test showed no significant change in fill factor, open circuit voltage, short circuit current density, and conversion energy efficiency within 1000 hours (corresponding to 41 days).

3. Conclusion

In a typical dye-sensitized solar cell (DSSC), usually platinum has been the preferred material for the counter electrode because of its high electrochemical activity. However, the costs of the platinum prevent the materials from having any large-scale applications in solar cells, thereby forcing the research community to find alternatives. A further problem actually delaying the commercialization of DSSC is the stability of the cell. The efficiency of a DSSC often rapidly drops with time in the initial several days after manufacturing due to the degradation of dye molecules and the reaction of electrolyte with sealing materials or counter electrode. Degradation of the sensitizer, evaporation or leakage of electrolyte solvent and dissolution of Pt/counter electrode in corrosive iodide/iodine redox electrolyte are some of the facts that deteriorate the long-term DSSC operation. Concerning the counter electrode corrosion, employing the emerging nanotechnologies researcher focused study on advanced nanostructured materials as new cathode materials. In this regard it has been suggested that expensive Pt counter electrode in DSSC could be replaced by nanosized carbon structures without affecting energy conversion. SWNT and MWNT are found to be competitive with the Pt even when electrode transparency is required. Another new original way to replace conventional cathode materials is to use Pt nanoparticles which combine their porosity and catalytic activity with their crystalline nanostructure. This solution pioneered by our group (work in preparation) could be extended to gold counter electrodes and employed with cobalt-based mediator. We hope this minireview give the opportunity to address new idea and new experiment to realize more stable and low-cost materials for cathode application in DSSCs.

Acknowledgments

The authors acknowledge Dott. Francesco Bonaccorso for fruitful discussion and Giuseppe Gismondo for technical assistance.

References

- [1] M. Graetzel, "Dye-sensitized solar cells," *Journal of Photochemistry and Photobiology C*, vol. 4, no. 2, pp. 145–153, 2003.
- [2] M. K. Nazeeruddin, A. Kay, I. Rodicio, et al., "Conversion of light to electricity by cis-X2bis(2,2'-bipyridyl-4,4'-dicarboxylate)ruthenium(II) charge-transfer sensitizers (X = Cl-, Br-, I-, CN-, and SCN-) on nanocrystalline TiO₂ electrodes," *Journal of the American Chemical Society*, vol. 115, no. 14, pp. 6382–6390, 1993.
- [3] S. A. Sapp, C. M. Elliott, C. Contado, S. Caramori, and C. A. Bignozzi, "Substituted polypyridine complexes of cobalt(II/III) as efficient electron-transfer mediators in dye-sensitized solar cells," *Journal of the American Chemical Society*, vol. 124, no. 37, pp. 11215–11222, 2002.
- [4] S. Anandan, "Recent improvements and arising challenges in dye-sensitized solar cells," *Solar Energy Materials and Solar Cells*, vol. 91, no. 9, pp. 843–846, 2007.
- [5] A. Kay and M. Grätzel, "Low cost photovoltaic modules based on dye sensitized nanocrystalline titanium dioxide and carbon powder," *Solar Energy Materials and Solar Cells*, vol. 44, no. 1, pp. 99–117, 1996.
- [6] Gmelin, *Handbuch der Anorganischen*, vol. 68C, Chemie, Weinheim, Germany, 1939.
- [7] S. Terauchi, N. Koshizaki, and H. Umehara, "Fabrication of Au nanoparticles by radio-frequency magnetron sputtering," *Nanostructured Materials*, vol. 5, no. 1, pp. 71–78, 1995.
- [8] B. Xu and S.-I. Tanaka, "Formation and bonding of platinum nanoparticles controlled by high energy beam irradiation," *Scripta Materialia*, vol. 44, no. 8–9, pp. 2051–2054, 2001.
- [9] A. Roy, M. Komatsu, K. Matsuiishi, and S. Onari, "Raman spectroscopic studies on Sb nanoparticles in SiO₂ matrix prepared by rf-cosputtering technique," *Journal of Physics and Chemistry of Solids*, vol. 58, no. 5, pp. 741–747, 1997.
- [10] K. Eguchi, N. Akasaka, H. Mitsuyasu, and Y. Nonaka, "Process of solid state reaction between doped ceria and zirconia," *Solid State Ionics*, vol. 135, no. 1–4, pp. 589–594, 2000.
- [11] L. Lei and X. Xin, "Solid state synthesis of a new compound Cu(HQ)Cl₂ and its formation reaction," *Thermochimica Acta*, vol. 273, no. 1–2, pp. 61–67, 1996.
- [12] O. Söhnel and J. Garside, *Precipitation*, Butterworth-Heinemann, 1992.
- [13] F. P. Ludwig and J. Schmelzer, *Zeitschrift für Physikalische Chemie*, vol. 192, p. 155, 1995.
- [14] H. Hirai, Y. Nakao, and N. Toshima, "Preparation of colloidal rhodium in poly(vinyl alcohol) by reduction with methanol," *Journal of Macromolecular Science. Chemistry*, vol. 12, no. 8, pp. 1117–1141, 1978.
- [15] H. Hirai, "Formation and catalytic functionality of synthetic polymer-noble metal colloid," *Journal of Macromolecular Science. Chemistry*, vol. 13, no. 5, pp. 633–649, 1979.
- [16] H. Hirai, Y. Nakao, and N. Toshima, "Preparation of colloidal transition metals in polymers by reduction with alcohols or ethers," *Journal of Macromolecular Science. Chemistry*, vol. 13, no. 6, pp. 727–750, 1979.
- [17] J. Turkevich, P. C. Stevenson, and J. Hillier, "A study of the nucleation and growth processes in the synthesis of colloidal gold," *Discussions of the Faraday Society*, vol. 11, pp. 55–75, 1951.
- [18] J. Kimling, M. Maier, B. Okenve, V. Kotaidis, H. Ballot, and A. Plech, "Turkevich method for gold nanoparticle synthesis revisited," *Journal of Physical Chemistry B*, vol. 110, no. 32, pp. 15700–15707, 2006.

- [19] G. Frens, "Particle size and sol stability in metal colloids," *Kolloid-Zeitschrift & Zeitschrift für Polymere*, vol. 250, no. 7, pp. 736–741, 1972.
- [20] B.-K. Pong, H. I. Elim, J.-X. Chong, W. Ji, B. L. Trout, and J.-Y. Lee, "New insights on the nanoparticle growth mechanism in the citrate reduction of gold(III) salt: formation of the Au nanowire intermediate and its nonlinear optical properties," *Journal of Physical Chemistry C*, vol. 111, no. 17, pp. 6281–6287, 2007.
- [21] K. Aika, L. T. Ban, I. Okura, S. Namba, and J. Turkevich, *Journal of the Research Institute for Catalysis, Hokkaido University*, vol. 24, p. 54, 1976.
- [22] G. Devi and V. J. Rao, "Room temperature synthesis of colloidal platinum nanoparticles," *Bulletin of Materials Science*, vol. 23, no. 6, pp. 467–470, 2000.
- [23] M. Brust, M. Walker, D. Bethell, D. J. Schiffrin, and R. Whyman, "Synthesis of thiol-derivatised gold nanoparticles in a two-phase liquid-liquid system," *Journal of the Chemical Society, Chemical Communications*, no. 7, pp. 801–802, 1994.
- [24] A. Manna, P.-L. Chen, H. Akiyama, T.-X. Wei, K. Tamada, and W. Knoll, "Optimized photoisomerization on gold nanoparticles capped by unsymmetrical azobenzene disulfides," *Chemistry of Materials*, vol. 15, no. 1, pp. 20–28, 2003.
- [25] K. Kurihara, J. Kizling, P. Stenius, and J. H. Fendler, "Laser and pulse radiolytically induced colloidal gold formation in water and in water-in-oil microemulsions," *Journal of the American Chemical Society*, vol. 105, no. 9, pp. 2574–2579, 1983.
- [26] L. Bronstein, E. Kramer, B. Berton, C. Burger, S. Forster, and M. Antonietti, "Successive use of amphiphilic block copolymers as nanoreactors and templates: preparation of porous silica with metal nanoparticles," *Chemistry of Materials*, vol. 11, no. 6, pp. 1402–1405, 1999.
- [27] S. Sato, K. Toda, and S. Oniki, "Kinetic study on the formation of colloidal gold in the presence of acetylenic glycol nonionic surfactant," *Journal of Colloid and Interface Science*, vol. 218, no. 2, pp. 504–510, 1999.
- [28] R. Zanella, S. Giorgio, C.-H. Shin, C. R. Henry, and C. Louis, "Characterization and reactivity in CO oxidation of gold nanoparticles supported on TiO₂ prepared by deposition-precipitation with NaOH and urea," *Journal of Catalysis*, vol. 222, no. 2, pp. 357–367, 2004.
- [29] W. Chen, W. Cai, L. Zhang, G. Wang, and L. Zhang, "Sonochemical processes and formation of gold nanoparticles within pores of mesoporous silica," *Journal of Colloid and Interface Science*, vol. 238, no. 2, pp. 291–295, 2001.
- [30] C.-L. Chiang, "Controlled growth of gold nanoparticles in AOT/C₁₂E₄/isooctane mixed reverse micelles," *Journal of Colloid and Interface Science*, vol. 239, no. 2, pp. 334–341, 2001.
- [31] M. P. Pileni, "Nanosized particles made in colloidal assemblies," *Langmuir*, vol. 13, no. 13, pp. 3266–3276, 1997.
- [32] P. Calandra, A. Longo, and V. Turco Liveri, "Preparation and characterisation of Na₂S and ZnSO₄ nanoparticles in water/sodium bis(2-ethylhexyl)sulphosuccinate/n-heptane microemulsions," *Colloid and Polymer Science*, vol. 279, no. 11, pp. 1112–1117, 2001.
- [33] P. Calandra, C. Giordano, A. Longo, and V. T. Liveri, "Physicochemical investigation of surfactant-coated gold nanoparticles synthesized in the confined space of dry reversed micelles," *Materials Chemistry and Physics*, vol. 98, no. 2-3, pp. 494–499, 2006.
- [34] J. Zhang, J. Du, B. Han, Z. Liu, T. Jiang, and Z. Zhang, "Sonochemical formation of single-crystalline gold nanobelts," *Angewandte Chemie: International Edition*, vol. 45, no. 7, pp. 1116–1119, 2006.
- [35] N. Robertson, "Optimizing dyes for dye-sensitized solar cells," *Angewandte Chemie: International Edition*, vol. 45, no. 15, pp. 2338–2345, 2006.
- [36] H. S. Wroblowa and A. Saunders, "Flow-through electrodes. II: the I₃⁻/I⁻ redox couple," *Journal of Electroanalytical Chemistry*, vol. 42, no. 3, pp. 329–346, 1973.
- [37] M. R. Tarasevich and E. I. Khrushcheva, "Electrocatalytic properties of carbon materials," in *Modern Aspects of Electrochemistry*, B. E. Conway, J. O'M. Bockris, and R. E. White, Eds., vol. 19, p. 295, Plenum Press, New York, NY, USA, 1989.
- [38] T. N. Murakami, S. Ito, Q. Wang, et al., "Highly efficient dye-sensitized solar cells based on carbon black counter electrodes," *Journal of the Electrochemical Society*, vol. 153, no. 12, pp. A2255–A2261, 2006.
- [39] K. Imoto, K. Takahashi, T. Yamaguchi, T. Komura, J.-I. Nakamura, and K. Murata, "High-performance carbon counter electrode for dye-sensitized solar cells," *Solar Energy Materials and Solar Cells*, vol. 79, no. 4, pp. 459–469, 2003.
- [40] Z. Huang, X. Liu, K. Li, et al., "Application of carbon materials as counter electrodes of dye-sensitized solar cells," *Electrochemistry Communications*, vol. 9, no. 4, pp. 596–598, 2007.
- [41] K. Li, Z. Yu, Y. Luo, D. Li, and Q. Meng, "Recent progress of counter electrodes in nanocrystalline dye-sensitized solar cells," *Journal of Materials Science and Technology*, vol. 23, no. 5, pp. 577–582, 2007.
- [42] K. Suzuki, M. Yamaguchi, M. Kumagai, and S. Yanagida, "Application of carbon nanotubes to counter electrodes of dye-sensitized solar cells," *Chemistry Letters*, vol. 32, no. 1, pp. 28–29, 2003.
- [43] J. E. Trancik, S. C. Barton, and J. Hone, "Transparent and catalytic carbon nanotube films," *Nano Letters*, vol. 8, no. 4, pp. 982–987, 2008.
- [44] T. Hino, Y. Ogawa, and N. Kuramoto, "Preparation of functionalized and non-functionalized fullerene thin films on ITO glasses and the application to a counter electrode in a dye-sensitized solar cell," *Carbon*, vol. 44, no. 5, pp. 880–887, 2006.
- [45] W. Hong, Y. Xu, G. Lu, C. Li, and G. Shi, "Transparent graphene/PEDOT-PSS composite films as counter electrodes of dye-sensitized solar cells," *Electrochemistry Communications*, vol. 10, no. 10, pp. 1555–1558, 2008.
- [46] J. Chen, K. Li, Y. Luo, et al., "A flexible carbon counter electrode for dye-sensitized solar cells," *Carbon*, vol. 47, no. 11, pp. 2704–2708, 2009.
- [47] X. Wang, L. Zhi, and K. Müllen, "Transparent, conductive graphene electrodes for dye-sensitized solar cells," *Nano Letters*, vol. 8, no. 1, pp. 323–327, 2008.
- [48] S. Iijima and T. Ichihashi, "Single-shell carbon nanotubes of 1-nm diameter," *Nature*, vol. 363, no. 6430, pp. 603–605, 1993.
- [49] D. S. Bethune, C. H. Kiang, M. S. De Vries, et al., "Cobalt-catalysed growth of carbon nanotubes with single-atomic-layer walls," *Nature*, vol. 363, no. 6430, pp. 605–607, 1993.
- [50] J.-C. Charlier, A. De Vita, X. Blasé, and R. Car, "Microscopic growth mechanisms for carbon nanotubes," *Science*, vol. 275, no. 5300, pp. 646–649, 1997.
- [51] S. Reich, C. Thomsen, and J. Maultzsch, "Carbon nanotubes, basic concepts and physical properties," *Journal of Colloid & Polymer Science*, vol. 282, p. 1299, 2004.
- [52] S. Iijima, "Helical microtubules of graphitic carbon," *Nature*, vol. 354, no. 6348, pp. 56–58, 1991.

- [53] L. Hu, D. S. Hecht, and G. Gruner, "Percolation in transparent and conducting carbon nanotube networks," *Nano Letters*, vol. 4, no. 12, pp. 2513–2517, 2004.
- [54] G. Che, B. B. Lakshmi, E. R. Fisher, and C. R. Martin, "Carbon nanotubule membranes for electrochemical energy storage and production," *Nature*, vol. 393, no. 6683, pp. 346–349, 1998.
- [55] A. Kongkanand, R. M. Dominguez, and P. V. Kamat, "Single wall carbon nanotube scaffolds for photoelectrochemical solar cells. Capture and transport of photogenerated electrons," *Nano Letters*, vol. 7, no. 3, pp. 676–680, 2007.
- [56] P. V. Kamat, "Harvesting photons with carbon nanotubes," *Nano Today*, vol. 1, no. 4, pp. 20–27, 2006.
- [57] D. M. Guldi, "Nanometer scale carbon structures for charge-transfer systems and photovoltaic applications," *Physical Chemistry Chemical Physics*, vol. 9, no. 12, pp. 1400–1420, 2007.
- [58] Z. Wu, Z. Chen, X. Du, et al., "Transparent, conductive carbon nanotube films," *Science*, vol. 305, no. 5688, pp. 1273–1276, 2004.
- [59] J. M. Planeix, N. Coustel, B. Coq, et al., "Application of carbon nanotubes as supports in heterogeneous catalysis," *Journal of the American Chemical Society*, vol. 116, p. 7935, 1994.
- [60] M. Ambrosio, A. Ambrosio, G. Ambrosone, et al., "Nanotechnology: a new era for photodetection?" *Nuclear Instruments and Methods in Physics Research A*, vol. 610, no. 1, pp. 1–10, 2009.
- [61] P. V. Kamat, M. Haria, and S. Hotchandani, " C^{60} cluster as an electron shuttle in a Ru (II)-polypyridyl sensitizer-based photochemical solar cell," *Journal of Physical Chemistry B*, vol. 108, no. 17, pp. 5166–5170, 2004.
- [62] D. M. Guldi and M. Prato, "Excited-state properties of C^{60} fullerene derivatives," *Accounts of Chemical Research*, vol. 33, no. 10, pp. 695–703, 2000.
- [63] H. Hoppe and N. S. Sariciftci, "Organic solar cells: an overview," *Journal of Materials Research*, vol. 19, no. 7, pp. 1924–1945, 2004.
- [64] J. Tersoff and R. S. Ruoff, "Structural properties of a carbon-nanotube crystal," *Physical Review Letters*, vol. 73, no. 5, pp. 676–679, 1994.
- [65] A. Thess, R. Lee, P. Nikolaev, et al., "Crystalline ropes of metallic carbon nanotubes," *Science*, vol. 273, no. 5274, pp. 483–487, 1996.
- [66] C. Journet, W. K. Maser, P. Bernier, et al., "Large-scale production of single-walled carbon nanotubes by the electric-arc technique," *Nature*, vol. 388, no. 6644, pp. 756–758, 1997.
- [67] A. B. Dalton, S. Collins, E. Muñoz, et al., "Super-tough carbon-nanotube fibres," *Nature*, vol. 423, no. 6941, p. 703, 2003.
- [68] J. N. Coleman, U. Khan, and Y. K. Gun'ko, "Mechanical reinforcement of polymers using carbon nanotubes," *Advanced Materials*, vol. 18, no. 6, pp. 689–706, 2006.
- [69] S. Berber, Y.-K. Kwon, and D. Tománek, "Unusually high thermal conductivity of carbon nanotubes," *Physical Review Letters*, vol. 84, no. 20, pp. 4613–4616, 2000.
- [70] Y.-L. Li, I. A. Kinloch, and A. H. Windle, "Direct spinning of carbon nanotube fibers from chemical vapor deposition synthesis," *Science*, vol. 304, no. 5668, pp. 276–278, 2004.
- [71] K. D. Ausman, R. Piner, O. Lourie, R. S. Ruoff, and M. Korobov, "Organic solvent dispersions of single-walled carbon nanotubes: toward solutions of pristine nanotubes," *Journal of Physical Chemistry B*, vol. 104, no. 38, pp. 8911–8915, 2000.
- [72] S. Giordani, S. D. Bergin, V. Nicolosi, et al., "Debundling of single-walled nanotubes by dilution: observation of large populations of individual nanotubes in amide solvent dispersions," *Journal of Physical Chemistry B*, vol. 110, no. 32, pp. 15708–15718, 2006.
- [73] T. Hasan, P. H. Tan, F. Bonaccorso, et al., "Polymer-assisted isolation of single wall carbon nanotubes in organic solvents for optical-quality nanotube—polymer composites," *Journal of Physical Chemistry C*, vol. 112, no. 51, pp. 20227–20232, 2008.
- [74] T. Hasan, Z. Sun, F. Wang, et al., "Nanotube: polymer composites for ultrafast photonics," *Advanced Materials*, vol. 21, no. 38–39, pp. 3874–3899, 2009.
- [75] M. F. Islam, E. Rojas, D. M. Bergey, A. T. Johnson, and A. G. Yodh, "High weight fraction surfactant solubilization of single-wall carbon nanotubes in water," *Nano Letters*, vol. 3, no. 2, pp. 269–273, 2003.
- [76] W. Wenseleers, I. L. Vlasov, E. Goovaerts, E. D. Obraztsova, A. S. Lobach, and A. Bouwen, "Efficient isolation and solubilization of pristine single-walled nanotubes in bile salt micelles," *Advanced Functional Materials*, vol. 14, no. 11, pp. 1105–1112, 2004.
- [77] Z. Sun, V. Nicolosi, D. Rickard, S. D. Bergin, D. Aherne, and J. N. Coleman, "Quantitative evaluation of surfactant-stabilized single-walled carbon nanotubes: dispersion quality and its correlation with zeta potential," *Journal of Physical Chemistry C*, vol. 112, no. 29, pp. 10692–10699, 2008.
- [78] W. J. Lee, E. Ramasamy, D. Y. Lee, and J. S. Song, "Efficient dye-sensitized solar cells with catalytic multiwall carbon nanotube counter electrodes," *Applied Materials & Interfaces*, vol. 6, pp. 1145–1149, 2009.
- [79] Z. Huang, X. Liu, K. Li, et al., "Application of carbon materials as counter electrodes of dye-sensitized solar cells," *Electrochemistry Communications*, vol. 9, no. 4, pp. 596–598, 2007.
- [80] Q. Wang, H. Li, L. Chen, and X. Huang, "Monodispersed hard carbon spherules with uniform nanopores," *Carbon*, vol. 39, no. 14, pp. 2211–2214, 2001.
- [81] B.-K. Koo, D.-Y. Lee, H.-J. Kim, W.-J. Lee, J.-S. Song, and H.-J. Kim, "Seasoning effect of dye-sensitized solar cells with different counter electrodes," *Journal of Electroceramics*, vol. 17, no. 1, pp. 79–82, 2006.
- [82] K. Suzuki, M. Yamaguchi, M. Kumagai, and S. Yanagida, "Application of carbon nanotubes to counter electrodes of dye-sensitized solar cells," *Chemistry Letters*, vol. 32, no. 1, pp. 28–29, 2003.
- [83] J. E. Trancik, S. C. Barton, and J. Hone, "Transparent and catalytic carbon nanotube films," *Nano Letters*, vol. 8, no. 4, pp. 982–987, 2008.
- [84] H. Zhu, H. Zeng, V. Subramanian, C. Masarapu, K.-H. Hung, and B. Wei, "Anthocyanin-sensitized solar cells using carbon nanotube films as counter electrodes," *Nanotechnology*, vol. 19, no. 46, Article ID 465204, 2008.
- [85] N. J. Cherepy, G. P. Smestad, M. Graetzel, and J. Z. Zhang, "Ultrafast electron injection: implications for a photoelectrochemical cell utilizing an anthocyanin dye-sensitized TiO_2 nanocrystalline electrode," *Journal of Physical Chemistry B*, vol. 101, no. 45, pp. 9342–9351, 1997.
- [86] H. W. Zhu and B. Q. Wei, "Direct fabrication of single-walled carbon nanotube macro-films," *Chemical Communications*, vol. 29, pp. 3042–3044, 2007.
- [87] L. Ci, R. Vajtai, and P. M. Ajayan, "Vertically aligned large-diameter double-walled carbon nanotube arrays having ultralow density," *Journal of Physical Chemistry C*, vol. 111, no. 26, pp. 9077–9080, 2007.

- [88] H. L. Wei, H. S. Yen, G. T. Lay, and H. H. Min, "Commercial and natural dyes as photosensitizers for a water-based dye-sensitized solar cell loaded with gold nanoparticles," *Journal of Photochemistry and Photobiology*, vol. 195, pp. 307–313, 2008.
- [89] G. Calogero, F. Bonaccorso, O. M. Maragò, P. G. Gucciardi, and G. Di Marco, "Single wall carbon nanotubes deposited on stainless steel sheet substrates as novel counter electrodes for ruthenium polypyridine based dye sensitized solar cells," *Dalton Transactions*, vol. 39, no. 11, pp. 2903–2909, 2010.

Review Article

Organic Solar Cells: Problems and Perspectives

G. Chidichimo and L. Filippelli

Dipartimento di Chimica, Università degli Studi della Calabria, 87036 Arcavacata di Rende, Italy

Correspondence should be addressed to G. Chidichimo, chidichi@unical.it and L. Filippelli, l.filippelli@unical.it

Received 18 March 2010; Accepted 12 May 2010

Academic Editor: Leonardo Palmisano

Copyright © 2010 G. Chidichimo and L. Filippelli. This is an open access article distributed under the Creative Commons Attribution License, which permits unrestricted use, distribution, and reproduction in any medium, provided the original work is properly cited.

For photovoltaic cells to convert solar into electric energy is probably the most interesting research challenge nowadays. A good efficiency of these devices has been obtained by using inorganic semiconductor materials. On the other hand, manufacture processes are very expensive in terms of both materials and techniques. For this reason organic-based photovoltaic (OPV) cells are attracting the general attention because of the possible realization of more economical devices. Organic materials are abundant and easily handling. Unfortunately OPV cells efficiency is significantly lower than that of inorganic-based devices, representing a big point of weakness at the present. This is mainly due to the fact that organic semiconductors have a much higher band gap with respect to inorganic semiconductors. In addition, OPV cells are very susceptible to oxygen and water. In this paper we will describe some of the different approaches to the understanding and improving of organic photovoltaic devices.

1. Introduction

Semiconducting conjugated polymers are the organic materials used in OPV cells, since they possess the base property required to activate the fundamental mechanisms to transform the radiative energy of light into an electric current. When a donor (D) and an acceptor (A) material are being in contact, the result is the so-called heterojunction and this is the basis for the operation of organic solar cells [1–9]. As a solar photon is absorbed, an exciton occurs which is a coulombically bound electron-hole pair, and it distributes to the D/A interface. At this stage the excitons are separated into free holes and electrons by the electric field. Two types of architectures are currently used to create a D/A heterojunction, that is, bilayer heterojunction and bulk heterojunction (BHJ) solar cells. The latter system is to date the most investigated way to produce solar devices. This is mainly due to the favorable combination of an easy manipulation in the production process and a higher conversion efficiency because of a markedly larger D/A interface. From a schematic point of view, organic solar cells operate the conversion of the incident solar irradiation to electrical current, through essentially four-steps process. Figure 1 depicts this process. In this view, the donor is termed

the holes transporting material and it makes contact with the anode, while the electrons transporting material is the acceptor, which is in contact with the cathode.

The creation of an exciton after the absorption of a photon is the first step. The exciton diffuses inside the material to reach the donor-acceptor interface where it will be separated. All of these four steps are potential targets for researchers to improve performances of the OPV. Absorption efficiency, that is how much light is harvested, mainly depends upon the absorption spectra of the organic materials. However the design of the devices, including their thickness, has not a minor role in capturing as much as incident wavelengths. The exciton diffusion length is the parameter that accounts for the efficiency of the second step. It comes out that longer diffusion length corresponds to a greater probability that the exciton reaches the D/A interface raising the holes-electrons production. Clearly the morphology of the D/A boundary also is of great importance. In fact the acceptor has possibly to be very close to the donor so that the D/A interface is always next to the point where the exciton is created. Indeed the third step is the exciton split-up into free charges and this step depends mainly on the properties of the donor and acceptor but also the overall device architecture plays an important role. The last step,

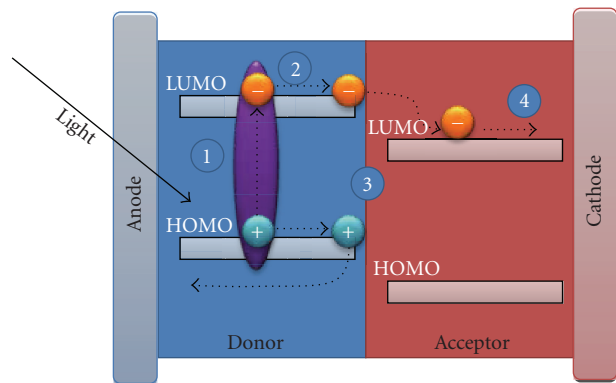


FIGURE 1: Scheme of operative sequence of an OPV.

that is the transport of the free charges through the sample and their collection at the electrodes, is the final step and it can be considered as central in a organic photovoltaic device. This crucial function derives from the fact that organic film structures are generally amorphous and disordered and, consequently, charge recombination is strongly favored. In addition, film resistance is large and reduces, thus, the current efficiency. The molecular structures of some of the materials are shown in Figures 2(a) and 2(b).

2. Absorption Efficiency

Conjugated π -systems are extensively used as both donor and acceptor materials (Figures 2(a) and 2(b)) and they are often referred as organic semiconductors. However they are intrinsically different from classic crystalline inorganic semiconductors which, for instance, can absorb a continuous spectrum of light and the three-dimensional rigid lattice provides large carrier mobility and broad conduction and valence bands. Typically conjugated materials exhibit intense and broad absorption, but since the thickness of organic semiconductors has to be tiny, because of short exciton diffusion lengths, the incident light is not captured efficiently. In addition organic semiconductors have well-defined electronic transitions that are typically quite narrow and have a propensity to be very susceptible to the background. Nevertheless when organic semiconductors can reach an ordered solid crystalline structure, their absorption band becomes broadened with evident benefits with respect to the solar cell efficiency. Hence the molecular structures and the eventual propensity to aggregate have a considerable influence on the absorption spectrum. For instance, many papers reported CuPc and SubPc (Figure 3) as materials used in organic solar cells. Phthalocyanines in general have been used as the only donor material within the system or as dye molecule in combination with a different donor [10–14]. The absorption spectra of the above mentioned CuPc and SubPc have similar profiles when recorded in very dilute solutions, but they are very different in the solid state [15]. Furthermore the absorption spectrum of a thin film of SubPc is comparable to that of SubPc in solution while the CuPc spectrum recorded in solid state is quite different

from the spectrum of CuPc in solution. This is mainly due to the fact that films made of CuPc show the presence of the cofacial aggregates of planar phthalocyanine molecules [16–19] whereas SubPc forms a very smooth and amorphous film [20].

Sometimes although a good combination of donor and acceptor is found, the efficiency of the cell is low unless a dye is introduced into the system to improve its performances. For example, one of the most investigated organic solar cell is based on the bulk heterojunction poly (3-hexylthiophene) (P3HT) : [6,6]-phenyl-C(61)butyric acid methyl ester (PCBM) (Figures 2(a) and 2(b)) blend film, where relatively high values of efficiencies (4%–5%, see Table 1) have been reported [21–25]. However, the major inconvenience of P3HT is the scarce matching of its absorption spectrum with the solar emission spectrum. The absorption of P3HT is limited to wavelengths below 650 nm, and as a consequence it is only able to collect little more than 20% of the solar photons [19, 26]. Introducing a dye in this system can improve performances. For example, 9,10-diphenylanthracene (DPA) has been used as a conjugated dye with different concentrations into a solar cell P3HT:PCBM system [27] and the photocurrent was improved by a factor 3.7. In addition all of the solar cell performance parameters and power conversion efficiency improved as a result of improvement in the light harvesting and charge carrier transfer taking place between P3HT and PCBM through the conjugated DPA molecules. The efficiency of the photogeneration can be also improved rising the exciton generation rate. We have already mentioned that the low charge mobility (high resistance) of organic semiconductors obliges the device thickness to stay thin. Hence the wavelength of the incident light is longer than film thickness causing optical interference. A standing wave occurs at each interface within the device and the complex refraction indices and the thickness of the different layers govern this wave pattern. The latter interference pattern can be precisely calculated and it corresponds to the exciton generation rate within the whole structure [28–30]. Therefore the enhancement of photocurrent might be possible, at least for planar heterojunction cells, through the modulation of the thicknesses of the layers [31, 32]. In the next paragraphs we will resume the critical points of the other three steps of the working sequence of an OPV. Although each step can be viewed and treated separately from the others, the four different phases are strictly interrelated. Improving a single step might not lead to the overall improvement of the device or the enhancement might be less than expected. It is the case, for example, of the bulk heterojunction that greatly enlarged the interface area between donor and acceptor leading to a great production of separated charges, but the random nature of the phase separation did not help the charges to reach the electrodes and be collected.

3. Exciton Diffusion

Once the exciton is generated, the electron and hole remain localized on a few polymer repetition units or a molecule

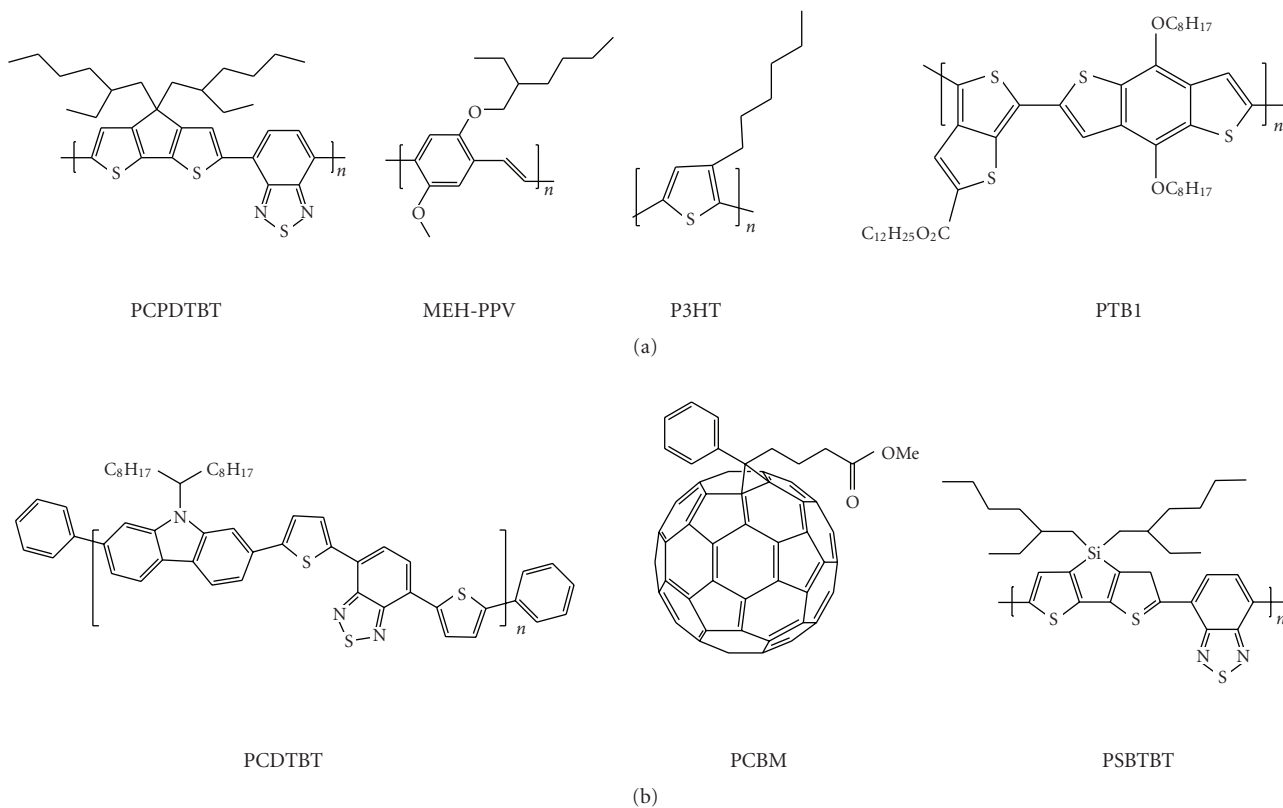


FIGURE 2: Examples of materials used as donors (a) and acceptors (b).

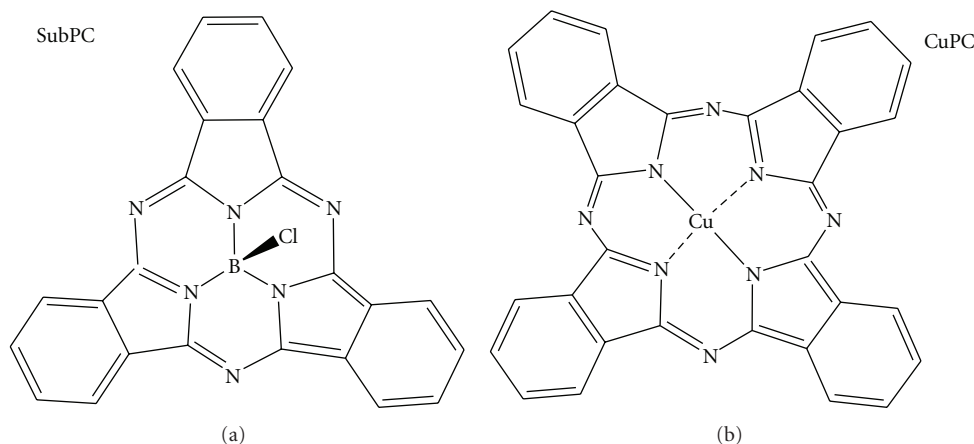


FIGURE 3: Molecular Structure of SubPC and CuPC.

and they are bound to each other by the electrostatic attraction. This is also called intrachain exciton to indicate that the constituent charges are situated on the same polymer chain. It is believed that intra-chain excitons represent the main species that are formed after photoexcitation in conjugated polymers [33, 34]. Upon adding a charge to a polymer chain, the chain will deform in order to reduce the energy of the carrier. This charge and deformation together constitute a polaron. The energy levels of a polaron are within the HOMO-LUMO gap. Polarons can drift along the

conjugated chain. Once they reach the end of a conjugated segment, a hopping process to another conjugated chain can occur. It is known that in molecular crystals, excitons can diffuse efficiently by energy transfer and that the same mechanism takes place in thin layers of molecular semiconductors [35]. However the research efforts are currently not so much devoted to increase diffusion lengths by modeling new molecules, but most of the researchers focus their action to decreasing the distance between donor and acceptor [36–39].

4. Charge Dissociation

BHJ structures were designed for this purpose and they accomplished the requirement of reducing distances between D and A. In fact only when the exciton reaches the D/A boundary they will separate effectively. The energetic driving force for separating the positive and negative charges relies in the difference between the LUMO levels of the donor and acceptor. If this energy is larger than the binding energy of the exciton in the donor, then the dissociative process became more favorable. In this view donor and acceptor should stay very close each other as they do in the BHJ devices.

5. Charge Transport and Materials

However once separated, charges need to travel through the materials towards electrodes and the random oriented domains of donor can greatly reduce the cell efficiency not providing the necessary conductivity that charges require in order to be collected in the last step of the operating sequence. In this view, ordered structures are supposed to improve conductivity of the system thus cell efficiency. Unfortunately a real control on the morphology of these systems is not achieved yet.

Trying to accomplish the necessity of an ordered array of D/A, nanorods and nanotubes of donor and acceptor materials have been investigated. In particular organic solar cells were made of Single Walls carbon Nano Tubes (SWNTs) employed as acceptor, and the poly(3-octylthiophene) (P3OT) as donor [40]. The open circuit voltage V_{oc} of the device was found to be 0.75 V, quite larger than expected. It was proposed that the improvement in the photovoltaic properties is caused by the internal polymer/nanotube links within the polymer matrix. Once dissociating the exciton, there is a uninterrupted way for electron and hole transport towards electrodes. On the other hand, the photocurrent of such devices is relatively low due to the partial phase separation and scarce quantity of absorbed light. The difference between the optical absorption of the polymer and the solar spectrum causes the low photocurrent. In addition the nanotubes do not supply the photogeneration process. Thus the same authors incorporated a high absorbing organic dye at the polymer/nanotube junctions and the photogeneration process was improved, especially for the UV portion of the solar spectrum [41]. The short circuit current was found 5 times larger than the nondye system. However the open circuit voltage was lowered by 0,1 V and under solar illumination the overall performances did not improve significantly (current $1 \mu\text{Acm}^{-2}$). A blend of two conjugated polymers as the photoactive film was reported in 1995 [42, 43], and since then, polymer-polymer solar cells have not attracted so much attention. However, regardless their modest performances (less than 2% efficiency) [44], these kinds of devices might be exploited for a series of advantages they can provide. As for solar absorption, for instance, two conjugated polymers could be tuned as harvesting a wider spectral wavelength. Moreover, the manipulation of polymers in terms of adjusting the donor-acceptor energy levels, is fairly easy. The main obstacle for the technology

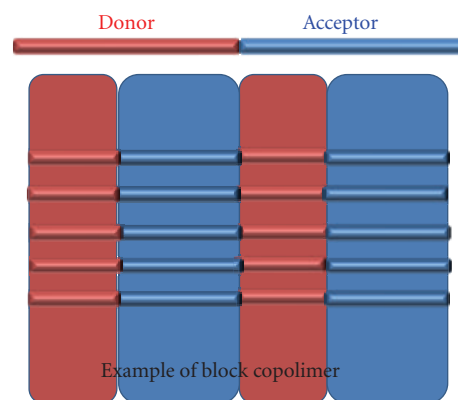


FIGURE 4: Schematic representation of block copolymer as an OPV device.

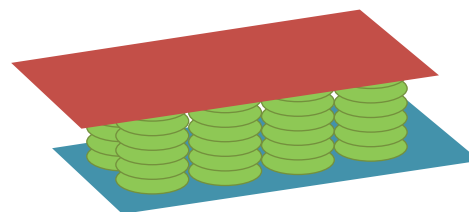


FIGURE 5: Ideal architecture of discotic LC-based solar devices.

based on polymer-polymer solar cells resides in designing conducting acceptors polymers which should have properties similar to those showed by fullerenes. In this view the use of block copolymers for solar cells is an early stage research area. Block copolymers (BCPs) synthesis would be one potential approach because periodic, adjustable nanostructures can be obtained [45]. An ideal BCP can be described as a block containing a p-type donor and block containing an n-type acceptor (Figure 4).

Nevertheless as the use of block copolymer for solar cell devices was theoretically predicted [46], efficiencies beyond the 0.5% were not achieved [47, 48]. In the field of materials, when order and mobility are required, it is natural to think about liquid crystals. They are currently considered as the new generation of organic semiconductors. By using conjugated LCs one can, in principle, control order in the bulk and at interfaces, from molecular to macroscopic distances. Because of their liquid-like character they can self-repair structural defects. Large single domains can be obtained by simply thermal annealing [49, 50]. By easily tuning parameters such as concentration or temperature [51, 52] and irradiation with polarized light [53] or surface alignment layers [54, 55], one can orient molecules inside these large domains. In addition defect-free chemical structures and a high purity level can be obtained due mainly to the low molecular weight of conjugated LCs. In this frame discotic liquid crystals have been reported as semiconductors [56–59, 48]. Disk-like LCs molecules can self-assembly in a columnar array (Figure 5) [58].

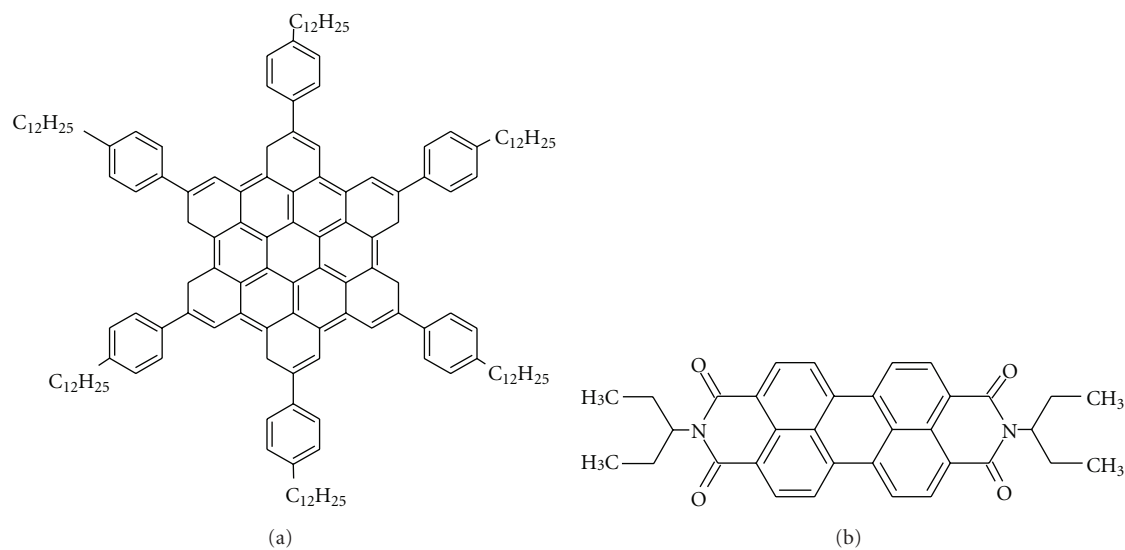


FIGURE 6: (a) Hexa-peri-hexabenzocoronene. (b) perylene dye.

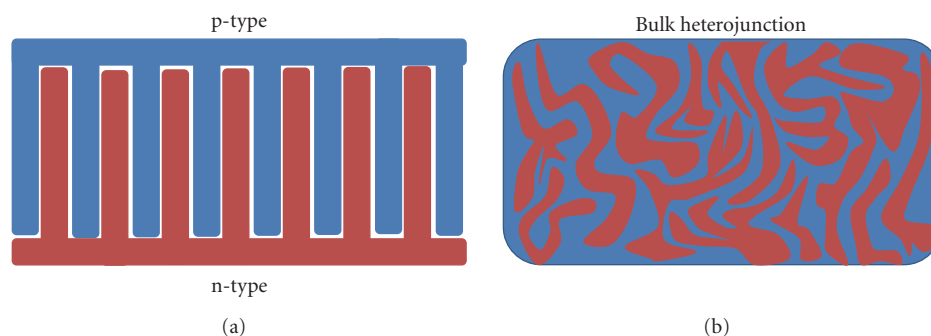


FIGURE 7: (a) The ideal device architecture. (b) BHJ architecture.

Columns of discotic mesogens display one-dimensional charge transport and within the columns adjacent disc-like molecules experience a large orbital overlap. The band width has been measured as 1.1 eV [60], and high values of the charge carrier mobility (μ), that is, 0.2–1.3 cm² V⁻¹ s⁻¹, in their liquid crystalline (LC) mesophases were reported [61–64]. Furthermore the measurement of the exciton diffusion length in the same columnar mesophases was about 70 nm [65]. Probably the best discotic-based photovoltaic devices would be made by the columnar array of the donor, perpendicularly oriented to the substrate, which is embedded in an acceptor environment. Such a device has been proposed and an external efficiency of 5% with an external quantum efficiency (EQE, photon to current) of 34% at a monochromatic wavelength of 490 nm has been claimed [66]. The discotic liquid crystal hexa-peri-hexabenzocoronene (Figure 6(a)) as hole conductor was blended with a perylene dye (Figure 6(b)) to create thin films with separated perylene and hexabenzocoronene perpendicularly oriented.

However the ideal morphology showed in Figure 5 that it is quite difficult to be obtained and the overall efficiency of about 0.5% reported is an evidence that the perfect

blend discotic-perylene was not achieved. Very likely the high performance for the EQE is quenched by a scarce phase separation and high percentage of recombination phenomena due to the fact that perylene molecules infiltrate within columnar stacks of the discotic liquid crystal. Thus the optimal device would be composed of ordered structures of separate donor and acceptor lamellae as Figure 7(a) shows.

To get this goal the homeotropic alignment of liquid crystals can be a promising way to pursue. In fact uniformly oriented textures of oligomers and polymers each other connected can be obtained by polymerization processes (photo induced, as an example) performed in liquid crystalline systems that have been prepared, in a homeotropic alignment by application of electric fields or by standing surface interaction (Figure 8) [67]. In the sketch reported below is represented a possible way to overcome the problems caused by the bulk heterojunction architectures.

The red drawn molecules are polymerizable liquid crystals while the blue ones are not polymerizable liquid crystals. The result of the polymerization of “red molecules” allows getting the textures as presented in Figure 9 [67].

Electro-optical data, performed in our laboratory, confirm the noticeable evidence: the polymer forms structures

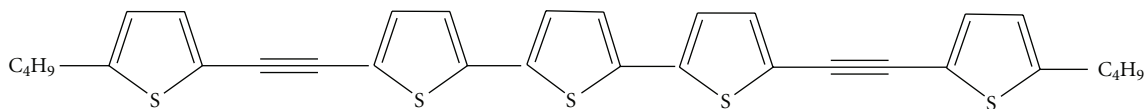


FIGURE 11: A L. C. polythiophene.

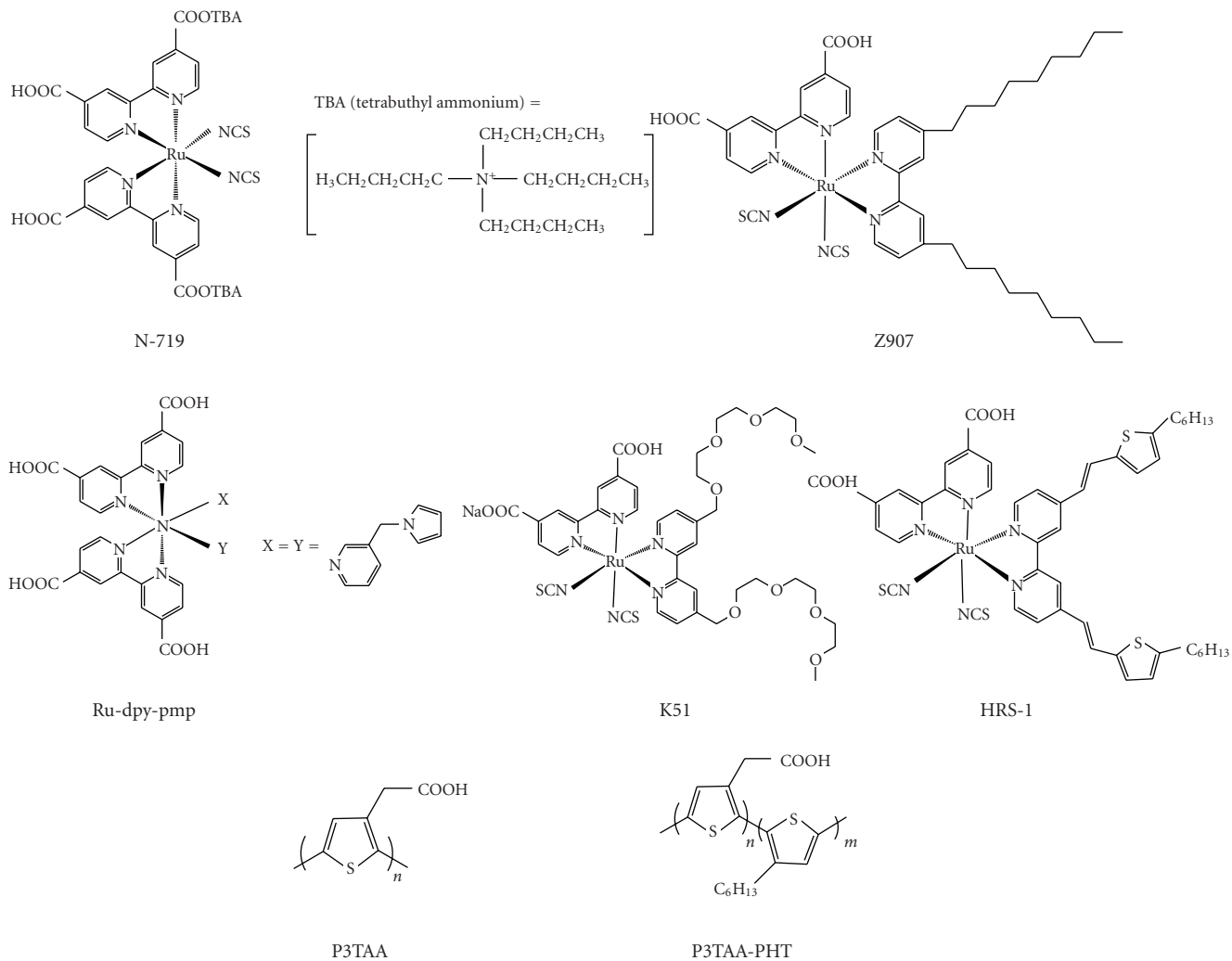


FIGURE 12: Examples of hole transporting materials (P3TAA, P3TAA-PHT) and dyes.

TABLE 1: Best performances of different systems.

System D/A	Conversion efficiency η (%)	System D/A	Conversion efficiency η (%)
P3HT-PCBM	4	DSSC	13
P3HT-PCBM-DPA	6	Iodine free DSSC	<2
P3OT-SWNT	<0.5	Gelled DSSC	4
P3OT-SWNT-DYE	<0.5	TiO ₂ /polythiophene	0.16
Polymer-Polymer	2	TiO ₂ /polypyrrole	0.8
BCP	<0.5	HBCC/perylene	<0.5
ZnO/P3HT/PCBM	3		

that can be assumed as small cylinders filled with the not polymerized liquid crystal. The cylinder diameter is less than $1\ \mu\text{m}$, but it can be controlled through parameters such as temperature and relative concentrations of the components. The not polymerized component can experience a phase transition to crystalline solid without any effect for the preformed structures. This kind of ordered microscopic structure would represent a great promise for application in organic photovoltaic. Although they cannot be strictly classified as OPVs, DSSC (Dye Sensitizer Solar Cells) photovoltaic cells [68], because of their very good performances (11% conversion efficiency), are worthy to be mentioned. They are made with a dye which is absorbed into nanocrystalline TiO_2 , ruthenium complex sensitizers, electrolytes containing fluid I^-/I_3^- redox couple, and Pt-coated counter electrode. The redox couple donates its own electron in order to regenerate the dye and it avoids the reduced form of the dye to take back the injected electron. However, I^-/I_3^- redox system can substantially decrease long-term stability and can be incompatible with some metallic components. Furthermore iodine is an oxidizing agent and it can rust metals, particularly if water and oxygen are present. Additionally, photocurrent loss can be induced because of the electrolytes I^-/I_3^- absorb visible light ($\lambda \sim 430\text{nm}$). In the view of the mentioned working principles, the titania layer can be considered as the electron-transporting and the I^-/I_3^- redox couple as the hole-transporting layer. Thus I^-/I_3^- redox couple can be substituted by a p-type semiconducting material as a hole-transporting material (HTM). A first reported alternative to I^-/I_3^- was a new couple, cobalt(II)-bis[2,6-bis(1'-butylbenzimidazol-2'-yl)pyridine] (Figure 10), and it was found to act as a redox couple in DSSC systems [69].

Other copper complexes were examined as substitutes of the I^-/I_3^- redox couple [70] and the operative working of the cells was demonstrated. However, low efficiencies (under 2%) were obtained. In addition, the time decay of the original DSSC performances has been attributed to a solvent loss of the electrolyte mixture. Therefore gelled-electrolyte-based DSSC systems were prepared and studied [71], but none of the proposed nonvolatile solvent-based cells has reached the original performance of the liquid electrolyte system. Iodide/iodine-free DSSCs using conductive polymers (Polymeric Hole-Transport Materials pHTM) such as polythiophene derivatives (Figures 11 and 12) were attempted to construct using a spin-coating technique and related dip-coating methods.

Poly(3-butylthiophene) [72] and poly(octylthiophene) [73] were investigated using N3 dye as sensitizer, giving very poor results (efficiency 0.16%). Recent attempts using regioregular poly(3-hexylthiophene) (P3HT) for hole-transporting layer of N-719-sensitized DSSC gave a little improved performance.

The nanoporous structures of the titania layer represent a barrier for polymeric hole transporting material to infiltrate into the nanospace. A more complex way is to synthesize HTM polymers *in situ*; that is, the HTM is introduced as monomer in the system and then it is polymerized within the nanopore of the dyed nc-TiO_2 electrode. The first reported

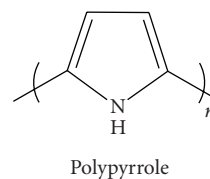


FIGURE 13: Chemical structure of polypyrrole.

system is a polypyrrole-based DSSC as a iodide/iodine-free DSSC. In order to plug polypyrrole into the pores of the dye-adsorbed titania layer, *in situ* photoelectrochemical polymerization (PEP) of pyrrole (Figure 13) [74] was used but a scarce conversion efficiency has been achieved (0.8%).

Among the attempts to reach the perfect structure, it is worth to mention the devices based onto ZnO nanorods [75]. Vertically aligned ZnO nanostructures coupled to a polythiophene (P3HT) through a fullerene mediator gave an efficiency of about 3%. In the end we cite another interesting experimental approach which has been carried out by Sicot et al. [76] that verified the improving of the performance of a polythiophene-based photovoltaic cell when a molecular orientation has been induced. The authors reported the so-called molecular rectification through dipole orientation. Layers of polythiophene, dye and small amount of a polar molecule (4-(dibutylamino)-4'-nitroazobenzene-DRPR) embedded in a polymer matrix, were used to make up the photovoltaic cell. By applying a DC-field under resonant illumination of DRPR, a photoinduced reorientation is achieved. Although the measured efficiencies were very low, the authors observed an increase of one order of magnitude of the power efficiency of the oriented as compared to the nonoriented cells.

6. Conclusion

As a concluding remark of this brief review concerning organic solar cell, we like to stress the fact that this field of research is just at the beginning. Efforts need to be done in order to get bulk-ordered separated structures of p and n organic semiconductors in order to improve contemporaneously both the charge separation processes and the transport of the free charge to the electrodes. In our opinion one of the most promising work directions is to investigate the possibility to use liquid crystal semiconductor molecules and to study phase separation strategies between these base components, in order to obtain fine cell bulk architectures.

References

- [1] R. N. Marks, J. J. M. Halls, D. D. C. Bradley, R. H. Friend, and A. B. Holmes, "The photovoltaic response in poly(p-phenylene vinylene) thin-film devices," *Journal of Physics: Condensed Matter*, vol. 6, no. 7, pp. 1379–1394, 1994.

- [2] G. Yu, J. Gao, J. C. Hummelen, F. Wudl, and A. J. Heeger, "Polymer photovoltaic cells: enhanced efficiencies via a network of internal donor-acceptor heterojunctions," *Science*, vol. 270, no. 5243, pp. 1789–1791, 1995.
- [3] C. J. Brabec, N. S. Sariciftci, and J. C. Hummelen, "Plastic solar cells," *Advanced Functional Materials*, vol. 11, no. 1, pp. 15–26, 2001.
- [4] W. Brutting, Ed., *Physics of Organic Semiconductors*, Wiley-VCH, Weinheim, Germany, 2005.
- [5] C. Brabec, V. Dyakonov, J. Parisi, and N. S. Sariciftci, Eds., *Organic Photovoltaics: Concepts and Realization*, Springer, New York, NY, USA, 2003.
- [6] S. S. Sun and N. S. Sariciftci, Eds., *Organic Photovoltaics: Mechanisms, Materials, and Devices*, Taylor & Francis, New York, NY, USA, 2005.
- [7] S. Günes, H. Neugebauer, and N. S. Sariciftci, "Conjugated polymer-based organic solar cells," *Chemical Reviews*, vol. 107, no. 4, pp. 1324–1338, 2007.
- [8] J. Xue, B. P. Rand, S. Uchida, and S. R. Forrest, "A hybrid planar-mixed molecular heterojunction photovoltaic cell," *Advanced Materials*, vol. 17, no. 1, pp. 66–71, 2005.
- [9] B. Kippelen and J.-L. Brédas, "Organic photovoltaics," *Energy and Environmental Science*, vol. 2, no. 3, pp. 251–261, 2009.
- [10] C. W. Tang, "Two-layer organic photovoltaic cell," *Applied Physics Letters*, vol. 48, no. 2, pp. 183–185, 1986.
- [11] B. P. Rand, J. Genoe, P. Heremans, and J. Poortmans, "Solar cells utilizing small molecular weight organic semiconductors," *Progress in Photovoltaics: Research and Applications*, vol. 15, no. 8, pp. 659–676, 2007.
- [12] K. L. Mutolo, E. I. Mayo, B. P. Rand, S. R. Forrest, and M. E. Thompson, "Enhanced open-circuit voltage in subphthalocyanine/C60 organic photovoltaic cells," *Journal of the American Chemical Society*, vol. 128, no. 25, pp. 8108–8109, 2006.
- [13] H. Gommans, D. Cheyns, T. Aernouts, C. Girotto, J. Poortmans, and P. Heremans, "Electro-optical study of subphthalocyanine in a bilayer organic solar cell," *Advanced Functional Materials*, vol. 17, no. 15, pp. 2653–2658, 2007.
- [14] P. Peumans, A. Yakimov, and S. R. Forrest, "Small molecular weight organic thin-film photodetectors and solar cells," *Journal of Applied Physics*, vol. 93, no. 7, pp. 3693–3723, 2003.
- [15] H. Paul, C. David, and B. P. Rand, "Strategies for increasing the efficiency of heterojunction organic solar cells: material selection and device architecture," *Accounts of Chemical Research*, vol. 42, no. 11, pp. 1740–1747, 2009.
- [16] H. Ogata, R. Higashi, and N. Kobayashi, "Electronic absorption spectra of substituted phthalocyanines in solution and as films," *Journal of Porphyrins and Phthalocyanines*, vol. 7, no. 8, pp. 551–557, 2003.
- [17] R. D. George, A. W. Snow, J. S. Shirk, and W. R. Barger, "The alpha substitution effect on phthalocyanine aggregation," *Journal of Porphyrins and Phthalocyanines*, vol. 2, no. 1, pp. 1–7, 1998.
- [18] E. Bundgaard and F. C. Krebs, "Low band gap polymers for organic photovoltaics," *Solar Energy Materials and Solar Cells*, vol. 91, no. 11, pp. 954–985, 2007.
- [19] G. P. Smestad, F. C. Krebs, C. M. Lampert et al., "Reporting solar cell efficiencies in Solar Energy Materials and Solar Cells," *Solar Energy Materials and Solar Cells*, vol. 92, no. 4, pp. 371–373, 2008.
- [20] R. F. Bailey-Salzman, B. P. Rand, and S. R. Forrest, "Near-infrared sensitive small molecule organic photovoltaic cells based on chloroaluminum phthalocyanine," *Applied Physics Letters*, vol. 91, no. 1, Article ID 013508, 3 pages, 2007.
- [21] C.-J. Ko, Y.-K. Lin, F.-C. Chen, and C.-W. Chu, "Modified buffer layers for polymer photovoltaic devices," *Applied Physics Letters*, vol. 90, no. 6, Article ID 063509, 3 pages, 2007.
- [22] G. Li, V. Shrotriya, J. Huang et al., "High-efficiency solution processable polymer photovoltaic cells by self-organization of polymer blends," *Nature Materials*, vol. 4, no. 11, pp. 864–868, 2005.
- [23] W. Ma, C. Yang, X. Gong, K. Lee, and A. J. Heeger, "Thermally stable, efficient polymer solar cells with nanoscale control of the interpenetrating network morphology," *Advanced Functional Materials*, vol. 15, no. 10, pp. 1617–1622, 2005.
- [24] M. Reyes-Reyes, K. Kim, and D. L. Carroll, "High-efficiency photovoltaic devices based on annealed poly(3-hexylthiophene) and 1-(3-methoxycarbonyl)-propyl-1-phenyl-(6,6) C61 blends," *Applied Physics Letters*, vol. 87, no. 8, Article ID 083506, 3 pages, 2005.
- [25] M. Reyes-Reyes, K. Kim, J. Dewald et al., "Meso-structure formation for enhanced organic photovoltaic cells," *Organic Letters*, vol. 7, no. 26, pp. 5749–5752, 2005.
- [26] R. Kroon, M. Lenes, J. C. Hummelen, P. W. M. Blom, and B. De Boer, "Small bandgap polymers for organic solar cells (polymer material development in the last 5 years)," *Polymer Reviews*, vol. 48, no. 3, pp. 531–582, 2008.
- [27] Y. A.M. Ismail, T. Soga, and T. Jimbo, "Improvement in light harvesting and performance of P3HT:PCBM solar cell by using 9,10-diphenylanthracene," *Solar Energy Materials and Solar Cells*, vol. 93, no. 9, pp. 1582–1586, 2009.
- [28] P. Peumans, A. Yakimov, and S. R. Forrest, "Small molecular weight organic thin-film photodetectors and solar cells," *Journal of Applied Physics*, vol. 93, no. 7, pp. 3693–3723, 2003.
- [29] L. A. A. Pettersson, L. S. Roman, and O. Inganäs, "Modeling photocurrent action spectra of photovoltaic devices based on organic thin films," *Journal of Applied Physics*, vol. 86, no. 1, pp. 487–496, 1999.
- [30] D. Cheyns, B. P. Rand, B. Verreet, J. Genoe, J. Poortmans, and P. Heremans, "The angular response of ultrathin film organic solar cells," *Applied Physics Letters*, vol. 92, no. 24, Article ID 243310, 2008.
- [31] H. Gommans, D. Cheyns, T. Aernouts, C. Girotto, J. Poortmans, and P. Heremans, "Electro-optical study of subphthalocyanine in a bilayer organic solar cell," *Advanced Functional Materials*, vol. 17, no. 15, pp. 2653–2658, 2007.
- [32] B. Verreet, S. Schols, D. Cheyns et al., "The characterization of chloroboron (iii) subnaphthalocyanine thin films and their application as a donor material for organic solar cells," *Journal of Materials Chemistry*, vol. 19, no. 30, pp. 5295–5297, 2009.
- [33] R. H. Friend, G. J. Denton, J. J. M. Halls et al., "Electronic excitations in luminescent conjugated polymers," *Solid State Communications*, vol. 102, no. 2–3, pp. 249–258, 1997.
- [34] R. H. Friend, G. J. Denton, J. J. M. Halls et al., "Electronic processes of conjugated polymers in semiconductor device structures," *Synthetic Metals*, vol. 84, no. 1–3, pp. 463–470, 1997.
- [35] J. Simon and J.J. André, *Molecular Semiconductors*, Springer, Berlin, Germany, 1985.
- [36] M. Riede, T. Mueller, W. Tress, R. Schueppel, and K. Leo, "Small-molecule solar cells—status and perspectives," *Nanotechnology*, vol. 19, no. 42, Article ID 424001, 2008.

- [37] B. P. Rand, J. Genoe, P. Heremans, and J. Poortmans, "Solar cells utilizing small molecular weight organic semiconductors," *Progress in Photovoltaics: Research and Applications*, vol. 15, no. 8, pp. 659–676, 2007.
- [38] B. C. Thompson and J. M. J. Fréchet, "Polymer-fullerene composite solar cells," *Angewandte Chemie - International Edition*, vol. 47, no. 1, pp. 58–77, 2008.
- [39] G. Dennler, M. C. Scharber, and C. J. Brabec, "Polymer-fullerene bulk-heterojunction solar cells," *Advanced Materials*, vol. 21, no. 13, pp. 1323–1338, 2009.
- [40] E. Kymakis, I. Alexandrou, and G. A. J. Amaratunga, "High open-circuit voltage photovoltaic devices from carbon-nanotube-polymer composites," *Journal of Applied Physics*, vol. 93, no. 3, pp. 1764–1768, 2003.
- [41] E. Kymakis and G. A. J. Amaratunga, "Photovoltaic cells based on dye-sensitisation of single-wall carbon nanotubes in a polymer matrix," *Solar Energy Materials and Solar Cells*, vol. 80, no. 4, pp. 465–472, 2003.
- [42] J. J. M. Halls, C. A. Walsh, N. C. Greenham et al., "Efficient photodiodes from interpenetrating polymer networks," *Nature*, vol. 376, no. 6540, pp. 498–500, 1995.
- [43] G. Yu and A. J. Heeger, "Charge separation and photovoltaic conversion in polymer composites with internal donor/acceptor heterojunctions," *Journal of Applied Physics*, vol. 78, no. 7, pp. 4510–4515, 1995.
- [44] C. R. McNeill, A. Abrusci, J. Zaumseil et al., "Dual electron donor/electron acceptor character of a conjugated polymer in efficient photovoltaic diodes," *Applied Physics Letters*, vol. 90, no. 19, Article ID 193506, 2007.
- [45] F. S. Bates and G. H. Fredrickson, "Block copolymers—designer soft materials," *Physics Today*, vol. 52, no. 2, pp. 32–38, 1999.
- [46] F. Meyers, A. J. Heeger, and J. L. Brédas, "Fine tuning of the band gap in conjugated polymers via control of block copolymer sequences," *The Journal of Chemical Physics*, vol. 97, no. 4, pp. 2750–2758, 1992.
- [47] M. Sommer, A. S. Lang, and M. Thelakkat, "Crystalline-crystalline donor-acceptor block copolymers," *Angewandte Chemie. International Edition*, vol. 47, no. 41, pp. 7901–7904, 2008.
- [48] Q. Zhang, A. Cirpan, T. P. Russell, and T. Emrick, "Donor-acceptor poly(thiophene-block-terylene diimide) copolymers: Synthesis and solar cell fabrication," *Macromolecules*, vol. 42, no. 4, pp. 1079–1082, 2009.
- [49] V. de Cupere, J. Tant, P. Viville et al., "Effect of interfaces on the alignment of a discotic liquid-crystalline phthalocyanine," *Langmuir*, vol. 22, no. 18, pp. 7798–7806, 2006.
- [50] A. J. J. M. van Breemen, P. T. Herwig, C. H. T. Chlon et al., "Large area liquid crystal monodomain field-effect transistors," *Journal of the American Chemical Society*, vol. 128, no. 7, pp. 2336–2345, 2006.
- [51] A. Tracz, J. K. Jeszka, M. D. Watson, W. Pisula, K. Müllen, and T. Pakula, "Uniaxial alignment of the columnar superstructure of a hexa (alkyl) hexa-*peri*-hexabenzocoronene on untreated glass by simple solution processing," *Journal of the American Chemical Society*, vol. 125, no. 7, pp. 1682–1683, 2003.
- [52] W. Pisula, A. Menon, M. Stepputat et al., "A zone-casting technique for device fabrication of field-effect transistors based on discotic hexa-*peri*-hexabenzocoronene," *Advanced Materials*, vol. 17, no. 6, pp. 684–689, 2005.
- [53] H. Monobe, K. Awazu, and Y. Shimizu, "Change of liquid-crystal domains by vibrational excitation for a columnar mesophase," *Advanced Materials*, vol. 12, no. 20, pp. 1495–1499, 2000.
- [54] S. Zimmermann, J. H. Wendorff, and C. Weder, "Uniaxial orientation of columnar discotic liquid crystals," *Chemistry of Materials*, vol. 14, no. 5, pp. 2218–2223, 2002.
- [55] O. Bunk, M. M. Nielsen, T. I. Sølling, A. M. Van de Craats, and N. Stutzmann, "Induced alignment of a solution-cast discotic hexabenzocoronene derivative for electronic devices investigated by surface X-ray diffraction," *Journal of the American Chemical Society*, vol. 125, no. 8, pp. 2252–2258, 2003.
- [56] F. J. M. Hoeben, P. Jonkheijm, E. W. Meijer, and A. P. H. J. Schenning, "About supramolecular assemblies of π -conjugated systems," *Chemical Reviews*, vol. 105, no. 4, pp. 1491–1546, 2005.
- [57] J. A. A. W. Elemans, A. E. Rowan, and R. J. M. Nolte, "Mastering molecular matter. Supramolecular architectures by hierarchical self-assembly," *Journal of Materials Chemistry*, vol. 13, no. 11, pp. 2661–2670, 2003.
- [58] C. D. Simpson, J. Wu, M. D. Watson, and K. Müllen, "From graphite molecules to columnar superstructures—an exercise in nanoscience," *Journal of Materials Chemistry*, vol. 14, no. 4, pp. 494–504, 2004.
- [59] D. Adam, P. Schuhmacher, J. Simmerer et al., "Fast photoconduction in the highly ordered columnar phase of a discotic liquid crystal," *Nature*, vol. 371, no. 6493, pp. 141–143, 1994.
- [60] X. Crispin, J. Cornil, R. Friedlein et al., "Electronic delocalization in discotic liquid crystals: a joint experimental and theoretical study," *Journal of the American Chemical Society*, vol. 126, no. 38, pp. 11889–11899, 2004.
- [61] J. M. Warman, M. P. De Haas, G. Dicker, F. C. Grozema, J. P. P. M. B. de Jong, and M. G. Debije, "Charge mobilities in organic semiconducting materials determined by pulse-radiolysis time-resolved microwave conductivity: π -Bond-conjugated polymers versus π - π -stacked discotics," *Chemistry of Materials*, vol. 16, no. 23, pp. 4600–4609, 2004.
- [62] Z. An, J. Yu, S. C. Jones et al., "High electron mobility in room-temperature discotic liquid-crystalline perylene diimides," *Advanced Materials*, vol. 17, no. 21, pp. 2580–2583, 2005.
- [63] B. A. Jones, M. J. Ahrens, M.-H. Yoon, A. Facchetti, T. J. Marks, and M. R. Wasielewski, "High-mobility air-stable n-type semiconductors with processing versatility: dicyanoperylene-3,4:9,10-bis(dicarboximides)," *Angewandte Chemie - International Edition*, vol. 43, no. 46, pp. 6363–6366, 2004.
- [64] H. Iino, Y. Takayashiki, J.-I. Hanna, R. J. Bushby, and D. Haarer, "High electron mobility of 0.1 cm²V⁻¹s⁻¹ in the highly ordered columnar phase of hexahexylthiotriphenylene," *Applied Physics Letters*, vol. 87, no. 19, Article ID 192105, 3 pages, 2005.
- [65] D. Markovitsi, S. Marguet, J. Bondkowski, and S. Kumar, "Triplet excitation transfer in triphenylene columnar phases," *Journal of Physical Chemistry B*, vol. 105, no. 7, pp. 1299–1306, 2001.
- [66] L. Schmidt-Mende, A. Fechtenkötter, K. Müllen, E. Moons, R. H. Friend, and J. D. MacKenzie, "Self-organized discotic liquid crystals for high-efficiency organic photovoltaics," *Science*, vol. 293, no. 5532, pp. 1119–1122, 2001.
- [67] G. Chidichimo, G. De Filipo, S. Manfredi et al., "High contrast reverse mode PDLC films: A morphologic and electro-Optical analysis," *Molecular Crystals and Liquid Crystals*, vol. 500, pp. 10–22, 2009.
- [68] M. Grätzel, "Photoelectrochemical cells," *Nature*, vol. 414, no. 6861, pp. 338–344, 2001.

- [69] H. Nusbaumer, J.-E. Moser, S. M. Zakeeruddin, M. K. Nazeeruddin, and M. Grätzel, "Co^{II}(dbbip)₂²⁺ complex rivals tri-iodide/iodide redox mediator in dye-sensitized photovoltaic cells," *Journal of Physical Chemistry B*, vol. 105, no. 43, pp. 10461–10464, 2001.
- [70] S. Hattori, Y. Wada, S. Yanagida, and S. Fukuzumi, "Blue copper model complexes with distorted tetragonal geometry acting as effective electron-transfer mediators in dye-sensitized solar cells," *Journal of the American Chemical Society*, vol. 127, no. 26, pp. 9648–9654, 2005.
- [71] W. Kubo, K. Murakoshi, T. Kitamura et al., "Quasi-solid-state dye-sensitized TiO₂ solar cells: effective charge transport in mesoporous space filled with gel electrolytes containing iodide and iodine," *Journal of Physical Chemistry B*, vol. 105, no. 51, pp. 12809–12815, 2001.
- [72] L. Sicot, C. Fiorini, A. Lorin, J.-M. Nunzi, P. Raimond, and C. Sentein, "Dye sensitized polythiophene solar cells," *Synthetic Metals*, vol. 102, no. 1–3, pp. 991–992, 1999.
- [73] D. Gebeyehu, C. J. Brabec, N. S. Sariciftci et al., "Hybrid solar cells based on dye-sensitized nanoporous TiO₂ electrodes and conjugated polymers as hole transport materials," *Synthetic Metals*, vol. 125, no. 3, pp. 279–287, 2002.
- [74] K. Murakoshi, R. Kogure, Y. Wada, and S. Yanagida, "Fabrication of solid-state dye-sensitized TiO₂ solar cells combined with polypyrrole," *Solar Energy Materials and Solar Cells*, vol. 55, no. 1–2, pp. 113–125, 1998.
- [75] I. Gonzalez-Valls and M. Lira-Cantu, "Vertically-aligned nanostructures of ZnO for excitonic solar cells: a review," *Energy and Environmental Science*, vol. 2, no. 1, pp. 19–34, 2009.
- [76] L. Sicot, C. Fiorini, A. Lorin, P. Raimond, C. Sentein, and J.-M. Nunzi, "Improvement of the photovoltaic properties of polythiophene-based cells," *Solar Energy Materials and Solar Cells*, vol. 63, no. 1, pp. 49–60, 2000.

Research Article

Bridged Phthalocyanine Systems for Sensitization of Nanocrystalline TiO₂ Films

Gloria Zanotti,¹ Nicola Angelini,² Sara Notarantonio,² Anna Maria Paoletti,² Giovanna Pennesi,² Gentilina Rossi,² Angelo Lembo,¹ Daniele Colonna,¹ Aldo Di Carlo,¹ Andrea Reale,¹ Thomas M. Brown,¹ and Giuseppe Calogero³

¹ Center for Hybrid and Organic Solar Energy (CHOSE), University of Rome "Tor Vergata", Via Giacomo Peroni 400/402, 00131 Rome, Italy

² CNR-Istituto Struttura della Materia, Via Salaria Km. 29.5, Monterotondo Stazione, 00016 Rome, Italy

³ CNR, Istituto per i Processi Chimico-Fisici, Salita Sperone Contrada Papardo, Faro Superiore, 98158 Messina, Italy

Correspondence should be addressed to Gentilina Rossi, gentilina.rossi@ism.cnr.it

Received 1 June 2010; Accepted 28 June 2010

Academic Editor: Leonardo Palmisano

Copyright © 2010 Gloria Zanotti et al. This is an open access article distributed under the Creative Commons Attribution License, which permits unrestricted use, distribution, and reproduction in any medium, provided the original work is properly cited.

Phthalocyanines based-dyes represent attractive alternatives to the expensive and polluting pyridyl based Ru complexes because of their photochemical and thermal stability, they do show in fact intense absorption in the UV/blue (Soret band) and the red/near IR (Q band) spectral regions and appear very promising as sensitizer dyes for DSSC. In this contribution we review the state of the art and the recent progress in the application of these materials as dyes for DSSC and present three new dyes which are bridged derivatives of Iron phthalocyanine. Synthesis, optical properties, electrochemical characterization and device performances are discussed with regard to the different substitution degree of the macrocycle.

1. Introduction

The achievement of an efficient conversion of sun light into electricity is a compelling scientific target considering the worldwide increasing demand for energy and the fact that the sunlight is certainly the largest and available single source of clean energy. Although several new technologies have been developed for this purpose they are not yet an economically viable alternative to fossil fuels [1]. Among organic photovoltaic (OPV) family, Dye Sensitized Solar Cells (DSSC) exhibit a conversion efficiency value lower than the corresponding photovoltaic devices based on silicon [2]. Nevertheless they represent, nowadays, a solid alternative for less-expensive photovoltaic energy production attracting the commercial interest of many industrial companies such as Aisin Seiki, Konarka, Dyesol, and G24 innovations, Limited.

In a schematic way the assembly of a typical DSSC is realised by a mesoporous TiO₂ film (photoanode), with a charge transfer dye anchored on the surface, placed in contact with a solid state hole-conductor film (shuttle

and a photoinert counter electrode (cathode) [3]. In the most studied and efficient devices to date, light is adsorbed by a polypyridyl ruthenium-based complex (dye) that is linked to titanium oxide surface via carboxylate moieties; the photoanode is a thick (~12 μm) film of TiO₂ nanoparticles (10–20 nm), yielding a conversion efficiency (η) up to 10%–11% and stable operation for millions of turnovers. The photoexcitation of the Ru-complex results in an intramolecular metal-to-ligand charge-transfer (MLCT) transition and the photoexcited electrons located on the bipyridyl ligands can be efficiently injected into the conduction band of the TiO₂ on an ultrafast time scale via carboxyl group anchored to the TiO₂ surface [4]. A large electronic coupling between the photosensitizer and the conduction band is exhibited by this combination. Conversely, the recombination between the injected electrons and the dye cation is a slow process [5] and it is considered to be a result of the large separation between the TiO₂ and the Ru³⁺ due to the bipyridyl ligands. Developing new effective organic dye sensitizers with good light-harvesting features is a current challenge

for many research groups as the polypyridyl-type complexes of ruthenium, successfully employed, show some significant restrictions as the low optical absorbance in the red/near infrared spectral regions as well as a low molar extinction coefficient and a nonenvironmental friendly production of the ruthenium. As it is believed that the simultaneous development of new dyes, shuttles, and photoanodes will lead to DSSCs with efficiencies exceeding 16% [6], the extensive research efforts targeting new sensitising molecules as alternative candidates suitable to overcome at least some of these limits appear to be more than justified. A large number of new organic dyes have been developed during these last few years, several research groups have developed metal-free organic sensitizers and obtained efficiencies in the range of 4%–8% [7]. The major advantages of these metal-free dyes are their tunable absorption and electrochemical properties through suitable molecular design [8]. Remarkable results was reported by Tian et al. [9] and Hagberg et al. [10] with novel metal-free dyes that showed a broader incident photon-to-current conversion efficiency spectrum over the whole visible range extending into the near-IR region up to 920 nm; in one case they reached the conversion efficiency of 7.20% under standard AM 1.5 sun light. Among dyes that address both spectral coverage and absorptive issue are included indolines [11]; a significant improvement in the cell performances was also made by the group of Hara et al. [12, 13], using coumarin or polyene type sensitizers, achieving solar to electric power conversion efficiencies reaching up to 7.7% in full sunlight. Natural pigments containing anthocyanins and carotenoids, although have shown overall solar energy conversion efficiencies around 1%, are also currently investigated [14]. Both porphyrins (Ph) and phthalocyanines (Pc) represent a class of dyes considered attractive alternatives to the expensive and polluting pyridyl-based Ru complexes, the former because of the analogy with natural photosynthetic molecules the latter because of their photochemical and thermal stability [15]. However porphyrins cannot compete with Ru-complexes due to their lack of red light and near IR absorption while phthalocyanines seem more promising because of their intense absorption in the UV/blue and the red/near IR spectral regions and because of the flexibility in modulating the spectroscopic features and tuning the electrochemical properties.

In this contribution we extensively review the state of art on these specific dyes, pointing out the most relevant achieved results in terms of efficiency of the related DSSCs and key points still to be improved. Furthermore, the synthesis strategy and preliminary data on new dyes based on phthalocyanine bridged systems as building blocks for highly conjugated superchromophores will be presented.

2. Phthalocyanine-Based Dyes for DSSCs: State of Art

Phthalocyanines and their metalloderivatives are a very well-known class of materials for their industrial applications as green and blue dyestuffs, but more recently renewed and growing interest, due to their outstanding chemical

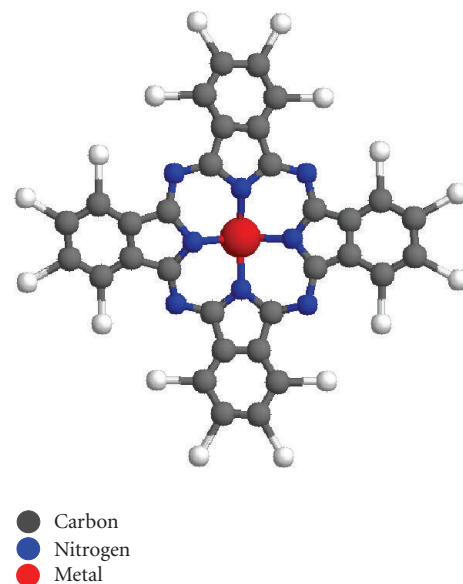


FIGURE 1: General structure of a metal phthalocyanine.

and physical properties, has been involving many research groups, and different fields of science and technology are currently investigated. They include, among others, chemical sensors, electrochromic display devices, molecular metals and conducting polymers, photodynamic cancer therapy, liquid crystal, catalysts, and photovoltaic cell elements, with both fundamental and applied aspects continuously explored [16]. In Figure 1 the metal phthalocyanine molecule is sketched and some fundamental features can be pointed up; it is a strictly planar molecule with high charge delocalisation (18π electrons), high thermal stability, easy processability, low solubility in the most conventional organic solvents, and intense colour (blue, green, purple). It also exhibits linear and nonlinear optical properties, magnetic properties (depending on the central metal), electrochemical (electrochromic displays), and electrical (semiconductor, photoconductor) features. Next to their unusual chemical and physical characteristics a further advantage is offered by the tailoring of these properties; for instance, the introduction of bulky groups or alkylic chains in the peripheral ring enhances the solubility as well as influences their electronic configurations. Furthermore, metal phthalocyanines can be also combined as building blocks with other organic molecules to assemble new molecular aggregates of interest in electronics and optoelectronics [17].

In this contribution we want to limit our update to the exploit of metal phthalocyanines and its derivatives in the construction of solar cells (DSSC), and to underline that in spite of the fact that phthalocyanine-based cells still do not reach efficiencies as good as Ru-based cells, they are as well considered “appealing materials” for photoconversion process because of their already described features [18]. Indeed a DSSC device is a sophisticated multicomponents system not yet understood in detail; certainly the optimisation of all the constituents of the device would participate in determining

the final performance even if the dye, together with other elements, is a key factor because of its light harvesting function [19]. A single dye normally does not absorb all the photons from the visible and near-infrared region, so the research for innovative approaches that increase the number of active sites on the semiconductor surface and the charge collection efficiencies is a significant issue that has been originally faced from the study by Hardin et al. in [20] exploiting the Forster resonant energy process obtained adding a highly luminescent chromophores inside the liquid electrolyte, and from the study by Lee et al. in [21], developing an original method to get a selective positioning of organic dyes on the surface of the TiO₂ semiconductor. Basically, the theoretical requirements for a good dye are numerous [22]: (1) it should be strongly attached to the semiconductor surface, (2) it should exhibit absorption in the whole solar spectrum, (3) its LUMO (Lowest Unoccupied Molecular Orbital) should present a higher energy than the conduction band (CB) edge of the semiconductor and good orbital overlap to facilitate electron injection, (4) charge recombination between the injected electron and the oxidized dye should be slow enough for the electron transport to the external circuit, (5) its redox potential should be more positive than the one of the redox couple in the electrolyte so that it can be quickly regenerated, (6) it should be stable for long-time exposure to natural sunlight, and (7) it should be soluble in a solvent compatible with the semiconductor and favourable for adsorption of nonaggregated monolayer on the surface. It is obviously difficult to design a dye fulfilling all the requisites and, with regard to those owned by phthalocyanine derivatives, it can be highlighted that they do show intense absorption in the Uv/blue (Soret band) and in the red/near IR (Q band) spectral region, and they are also transparent over a large region of the visible spectrum, offering the possibility of using them as “photovoltaic windows”. Phthalocyanines can be anchored to the TiO₂ semiconductor surface in two different ways allowing to dispose the molecules in a parallel arrangement (anchoring group in the axial position) [23–25] or in a more or less perpendicular orientation (anchoring group inserted in the peripheral macrocycle) [26]. Their applications in DSSCs have been limited up to date for two essential reasons: the first one is associated with the aggregation phenomena of the macrocycles on the semiconductor surface, resulting in a rapid deactivation of the dye’s excited state; the second one is due to the LUMO level position considered too low and lacking of the appropriate directionality for the electron transfer into the TiO₂ conduction band; this latter, being a key point for efficient overlapping between the molecular orbitals and the semiconductor CB, is an aspect to be considered in designing new phthalocyanine-based dyes.

In order to exceed the first limitation, sterically hindered phthalocyanines bearing peripheral phenyl groups have been synthesized by Eu et al. [27] and, in the presence of a high degree of substitutions, suppressed aggregation phenomena have been shown. The incorporation of tyrosine groups into zinc phthalocyanine molecule reduces, as well, the surface aggregation which can always be assigned to steric

hindrance [22]. However the introduction of bulky groups produces a low improvement in device performance; better results have been achieved when small organic acids have been contextually added [28]. In a recent paper [29] the influence of coadsorbents upon interfacial electron transfer has been deeply investigated. The authors prove, in a detailed study, that the addition of two additives as Li⁺ and chenodeoxycholic acid (CHENO) in a series of novel ruthenium phthalocyanines produces a considerable effect on the electron transfer dynamics; the influence of the two coadsorbents on the electron injection into the semiconductor CB, on the recombination of the oxidized dye with the electrons in TiO₂, and on the regeneration of the oxidized dye by the redox electrolyte are thoroughly discussed. The results show that the justification for the enhanced photocurrent is not the suppression of dye aggregates but the slower recombination of dye cations with the TiO₂ electrons and the faster regeneration of the dye cations by the electrolyte.

The use of an axial ligation besides lowering the aggregation phenomena also allows to control the distance between the HOMO orbital of the dye and the TiO₂ surface and thereby the electron injection and recombination dynamics. The control over the formation of molecular aggregates onto the semiconductor nanoparticles still remains a key point to achieve better efficiencies but it is not sufficient to explain the low-incident photon to current conversion efficiency (IPCE) observed for phthalocyanine-based dyes, being the factor concerning energy and geometry of LUMO orbitals the second important limit to be overcome.

To this purpose, it has been recently reported [30] that the use of a substituted zinc phthalocyanine with three pushing *tert*-butyl groups and two pulling carboxylic acid groups, results in a sensitizer that exhibits an IPCE of 75%. The cell sensitised with this compound gives a short-circuit photocurrent density of $(6.50 \pm 0.20) \text{ mA cm}^{-2}$, an open-circuit voltage of $(635 \pm 30) \text{ mV}$, and a fill factor of 0.74 ± 0.03 , which corresponds to an overall conversion efficiency of 3.05%. The presence of such substituents minimizes the aggregation process, increases the solubility in organic solvents, and, owing to their push-pull character, induces directionality in the excited state of the zinc phthalocyanine. Nazeruddin, Cid et al. [31] further extended this “push-pull” idea, presenting a novel zinc phthalocyanine derivative with the same *tert*-butyl substitution and with the carboxylic group directly linked to the Pc ring inducing directionality in the excited state of the molecule. The efficiency of the corresponding solar cell was $\eta = 3.5\%$ under standard illumination condition. In the same paper the authors stress the possibility to introduce a secondary dye with a complementary visible spectrum (i.e., J.K.2) to obtain the panchromatic sensitisation of the photoelectrode and enhance the efficiency of the device, as a matter of fact they reached the highest value ($\eta = 7.08\%$) among those measured with each single dye. This result suggests that Pcs can be also considered as good candidates for multiple dye cosensitized solar cells.

For the same aim of reaching a large coverage of the visible spectrum, a supramolecular phthalocyanine-squaraine ensemble has been synthesised and characterised.

It exhibits an optical spectrum corresponding to the sum of the absorption of the single components [32], but the low IPCE measured forces the authors to investigate the relationship of processing—microstructure and photovoltaic response.

The strategy in designing new dyes for DSSCs by combining two or more molecules complementing each other in their spectral features to achieve the desired “full-spectrum solar cells” includes dyads systems: new dyes containing ruthenium phthalocyanine and bipyridyl chromophores have been synthesised [33]. DSSCs fabricated using the phthalocyanine dyads were less efficient, however, on the basis of the number of molecules linked to TiO₂ they appear more efficient in the photocurrent generation. These results indicate that the ability of these molecules to cover TiO₂ surface, related to the molecular size, is another significant feature in their success as sensitizing dyes. Nevertheless, the presence of push-pull groups inserted into macrocycle ring shows its effectiveness in the case of a novel zinc phthalocyanine with an extended π -conjugation [34] resulting in an overall conversion efficiency of 2.35%. More recently O'Regan et al. [35] reported the evidence, for a ruthenium phthalocyanine dye, of voltage reduction occurring at both the TiO₂ and SnO₂ surface, caused by the electron/electrolyte recombination reaction catalyzed by the dye. They warn that this problem could be present in other organic dyes and so they consider necessary to determine the molecular basis of this catalytic process in order to develop design rules to avoid it. Another aspect emphasized by Torres group [36, 37] is the role played by the anchoring group (spacer group): the way in which it affects the electron injection from the photoexcited dye into the nanocrystalline TiO₂ has been shown, the recombination rates have been investigated, and the efficiency of the cells has been measured for different anchoring groups. The outcome presented indicates that the IPCE for phthalocyanine bearing an insulating spacer is as low as 9% whereas for those with a conducting spacer an outstanding 80% IPCE was obtained.

It appears entirely evident, from the above listed results, that phthalocyanine-based dyes give performances distant from those obtained with the ruthenium complexes; nevertheless, thanks to the helpful chemical tailoring achievable through organic synthesis, this class of compounds still appear encouraging as sensitizer dyes.

3. Bridged Phthalocyanine-Based Dyes for DSSC: Preliminary Results

The results presented here originate from a project aimed to set up different strategies, mainly through synthetic work, for the achievement of new dyes based on metal macrocycles like phthalocyanine or porphyrins as building-blocks for highly conjugated super chromophores. These oligomers should provide the possibility to link themselves to the TiO₂ surface through a suitable anchoring group axially coordinated to the central metal of the macrocycles. In this way some parameters as light-harvesting property, coupling with the semiconductor CB and recombination processes, would be

affected and a strong influence on the surface aggregation is expected as well. The approach is focused on testing the performances of bridged phthalocyanine systems containing two macrocycles per molecule and in comparing the results with those obtained with the correspondent monomeric forms which are the subject of most of scientific work carried on up to now. Here we report the synthesis, the electrochemical measurements, and the optical investigation of three bridged systems (Figure 2), namely, μ -carbide bridged iron phthalocyanine (I), hemisubstituted μ -carbide bridged iron phthalocyanine (II), and amphi-substituted μ -carbide iron phthalocyanine (III) as sensitizers for nanocrystalline TiO₂. The testing of compound (I) in a DSSC cell was also performed and preliminary results in terms of efficiency are reported.

3.1. Experimental. Iron phthalocyanine was purchased by Aldrich and purified by vacuum sublimation at 400°C. Tetra-*tert*-butyl iron phthalocyanine was synthesized according to an existent procedure [38]. All the solvents were anhydrous and distilled before use. Reactions were monitored by TLC employing a polyester layer coated with 250 mm F₂₅₄ silica gel. Purification of compounds was performed by column chromatography using silica gel Carlo Erba Reactifs SDS 60A C.C. 35–70 mm. Infrared spectra were recorded on a Shimadzu IR prestige-21 spectrometer in KBr pellets or in nujol mull. UV-vis spectra were recorded on a Perkin-Elmer Lambda 950 UV-vis. NIR spectrophotometer. Thermal analysis was performed with TA Instrument SDT Q600 simultaneous TGA-DTA-DSSC apparatus.

3.1.1. Synthesis

Synthesis of μ -Carbide Bridged Iron Phthalocyanine: $FePc=C=FePc$ (I). The μ -carbide compound has been prepared and characterised according to the procedure already reported in literature [39]. A mixture of iron phthalocyanine and sodium dithionite was heated 140–145°C in 1-chloronaphthalene then carbon tetraiodide was added, and the solution was stirred for 40 minutes. After cooling, the reaction mixture was filtered, and the solid residue washed with acetone, distilled water, and acetone again and then dried to constant weight under vacuum. The crude product was dissolved in N-methylimidazole (1-Meim) and the resulting [(1-Meim)(FePc)]₂C was recrystallized from 1:1 hexane/acetone. The crystalline compound was then treated at 250° for 30 minutes to remove N-methylimidazole and obtain the desired molecule. Elemental analysis, visible, infrared, and NMR spectra were performed to check the purity of the product.

Synthesis of Hemisubstituted μ -Carbide Bridged Iron: $(t-bu)_4PcFe=C=FePc$ (II). The procedure followed is similar to the previous one: 86 mg (0.15 mmol) of iron phthalocyanine and 120 mg (0.15 mmol) of tetra-*tert*-butyl iron phthalocyanine were dissolved in xylene (7 ml) with 303 mg (1.7 mmol) of sodium dithionite. The mixture was then heated to reflux and then 312 mg (0.60 mmol) of

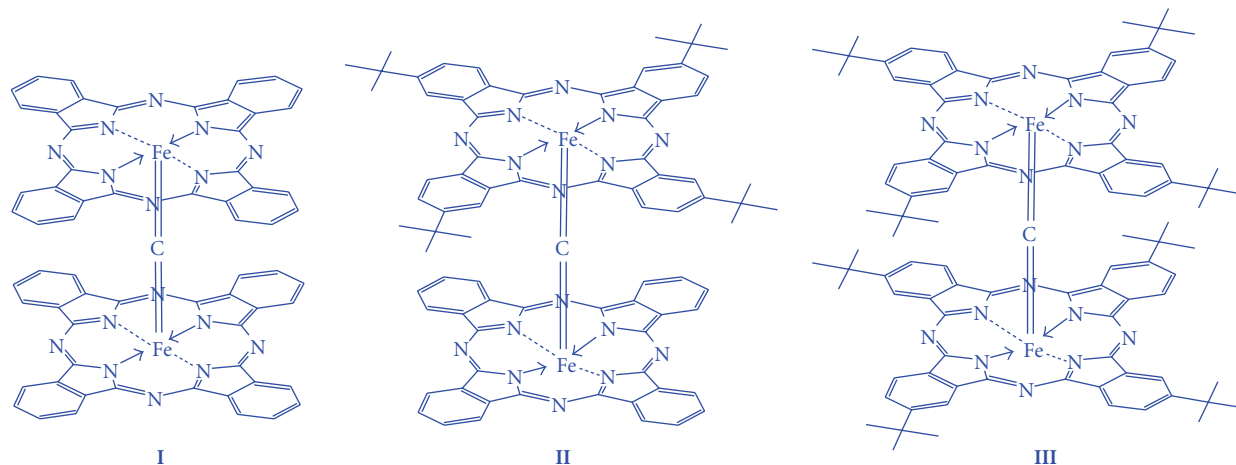


FIGURE 2: μ -carbide bridged iron phthalocyanine (I), hemisubstituted μ -carbide bridged iron phthalocyanine (II), and amphi-substituted μ -carbide iron phthalocyanine (III).

Cl_4 were added. After 45 minutes it was cooled to room temperature, diluted with diethyl ether, washed with water and $\text{Na}_2\text{S}_2\text{O}_3$ (saturated solution), dried over sodium sulphate, and concentrated under reduced pressure. The crude product, consisting of three species, was then purified with column chromatography on silica gel using 10 : 1 and 9 : 1 petroleum ether/dioxane as mobile phase.

Synthesis of Amphi-Substituted μ -Carbide Bridged Iron Phthalocyanine: $(t\text{-bu})_4\text{PcFe}=\text{C}=\text{FePc}(t\text{-bu})_4$ (III). 150 mg (0.19 mmol) of tetra-tert-butyl iron phthalocyanine were dissolved in 5 ml of xylene with 190 mg (1.1 mmol) of sodium dithionite. The mixture was heated to reflux in an oil bath and then 195 mg (0.37 mmol) of Cl_4 were added. After 45 minutes the solution was cooled, diluted with diethyl ether, washed with water and with a saturated solution of $\text{Na}_2\text{S}_2\text{O}_3$, dried over sodium sulphate, and concentrated under reduced pressure. The crude product was then purified by column chromatography on silica gel using a mixture of petroleum ether and dioxane (9 : 1) as mobile phase. The compound is soluble in the most common organic solvents, such as dichloromethane, chloroform, ethanol, and THF.

General Procedure for the Adducts Formation with Isonicotinic Acid (IsA). 1 equivalent of (I), (II) or (III) was dissolved in a few ml. of THF and stirred at room temperature, then 2 equivalent of isonicotinic acid were added and the mixture was stirred for one, two, or three days, depending on the chosen bridged system. Then, for the unsubstituted $(\text{FePc})_2\text{C}$ the solution was centrifuged, the solid residue was washed several times with $\text{H}_2\text{O}/\text{MeOH}$ 1 : 1 to remove the excess of isonicotinic acid, and then dried under vacuum. In the other cases the mixture was first concentrated under reduced pressure and then washed as previously described. Thermogravimetric analysis showed that two molecules of IsA were lost in one step with a loss of weight of 14.0%, ($T = 180 - 210^\circ\text{C}$) being the theoretical value of 13.3%.

3.1.2. Spectroscopic Study. Time resolved fluorescence measurements were carried out by a time-correlated-single-photon-counting (TCSPC) [40] homemade apparatus ($\lambda_{\text{ex}} = 575\text{ nm}$), which has been already described in [41]. The fluorescence decay profiles were analysed through a nonlinear least-squares iterative deconvolution procedures based on the Marquardt algorithm [42] achieving an instrumental resolution of about few tens of picoseconds. The total fluorescence decay curves were fitted to a multiexponential decay equation [43]: $I(t) = I_0 \sum \alpha_i \exp(-t/\tau_i)$, where $I(t)$ is the total fluorescence decay curve, I_0 is the intensity at $t = 0$, and α_i and τ_i are relative amplitude and lifetime of i th component (the normalization condition being $\sum_i \alpha'_i = 1$), respectively.

3.1.3. Electrochemical Measurements. Cyclic voltammograms were recorded at 25°C with a computer-aided system (AMEL INSTRUMENTS 2059 potentiostat/galvanostat, 568 function generator) in a conventional three-electrode cell; a platinum disk was used as working electrode together with a platinum wire as auxiliary electrode. The reference electrode was Ag/AgNO_3 (0.01 M) in distilled acetonitrile (E_0 versus SCE = 0.298 V). The samples solutions were 10^{-4} M in distilled anhydrous dichloromethane, and tetra(*n*-butyl)ammonium tetrafluoroborate (TBATFB, 0.1 M) was used as supporting electrolyte. The solutions were previously purged for 10 minutes with nitrogen and all measurements were performed in inert atmosphere. Because the solubility of some of these compounds in CH_2Cl_2 was poor, we added 1-Meim as coordinating base when needed.

3.1.4. DSSC Fabrication. 0.25 cm^2 TiO_2 (P25-Degussa) active area was deposited onto FTO conducting glass through "doctor-blade" technique, TiO_2 layer was sintered at 450°C for 45 minutes, then kept at 80°C within 3 hours and immediately used for the dipping process (averaged thickness 16–18 μm). A 0.5 mM solution of $(\text{IsAFcPc})_2\text{C}$ in THF was freshly prepared and used to sensitize the TiO_2 layer and

no coadsorbents or antiaggregation agents such as CHENO (deoxycholic acids) were used. Dipping time was 14 hours (during night) at room temperature; after that the photoanode was rinsed with THF. A sandwich cell was prepared using the dye anchored TiO₂ film as working electrode and a second conducting glass, coated with chemically deposited platinum (PT-1 platinum paste purchased from Dyesol) as photocathode. The two electrodes were superimposed with a thin transparent film of Surlyn polymer gasket (25 μm) and the device was sealed by heating. The internal space was filled with HSE electrolyte (purchased by Dyesol) by using a vacuum backfilling system. The electrolyte-injecting hole on the counter electrode glass substrate was sealed with a Surlyn sheet and a thin glass cover by heating.

4. Results and Discussion

4.1. Spectroscopic Properties. The UV/Vis spectra of the compounds (I–III) in solution exhibit the feature typical of phthalocyanine complexes (Figure 3) with an intense band in the range of 550–750 nm (Q band). As expected the *ter*-butyl substitution moves the maximum of the absorption peak from 620 nm (unsubstituted bridge) to 637 nm (substitution on both macrocycles) for the increasing number of pushing groups on the peripheral rings. A similar trend was observed in the fluorescence spectra as well as shown in Table 1. As far as concern of the IR spectra, it is worthy to point out that in all the cases a strong band between 997 and 1007 cm⁻¹, already attributed to the Fe=C=Fe stretching was observed [38]. In the hemisubstituted compound [(*t*-bu)₄PcFe=C=FePc] this band is split likely owing to the different strength constants of the two parts of the bridged system. In addition, the presence of four or eight *ter*-butyl groups is well shown in the aliphatic C–H stretching region (2950 cm⁻¹) while a gradual decreasing of intensity of phenyl C–H stretching in the range 1600–700 cm⁻¹ is observed going from compound (I) to (III).

4.2. Emission Measurements. The photo properties of the unsubstituted bridged system (I) have been investigated in dichloromethane, and the steady-state fluorescence emission spectrum ($\lambda_{\text{ex}} = 620$ nm) is shown in Figure 4. A rather broad absorption with maximum centred around 650 nm can be observed, while in the inset its excitation spectrum ($\lambda_{\text{em}} = 680$ nm) presents an intense band at 620–625 nm attributable to the π - π^* transition of the compound (Q band).

Fluorescence emission decays of the adduct (IsAFePc)₂C in THF ($\lambda_{\text{em}} = 650$ nm) exhibits a biexponential behaviour with two contributions (Figure 5); the first corresponding to 82% of amplitude has a life time of 0.9 ns and the second one (18%) has a life time of 8.2 ns. We suggest that the more accelerated decay, which is prevalent, is attributable to the μ -carbide bridge while the slower can be assigned to a monomeric species often present as impurity. Time resolved emission measurements of (IsAFePc)₂C sensitised TiO₂ show a very efficient quenching with a life time of 0.3 ns ($a = 98\%$). This appreciable reduction of the

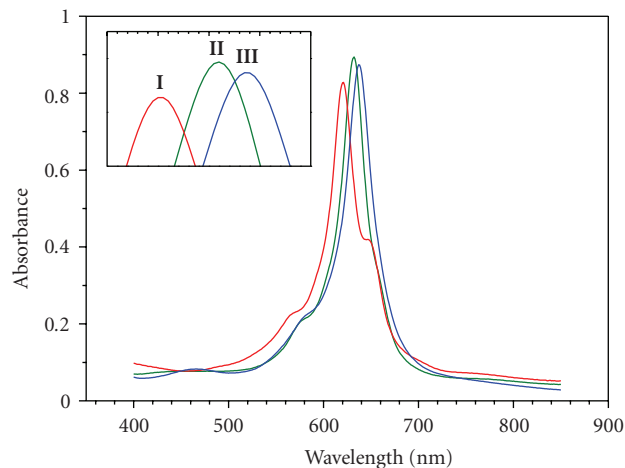


FIGURE 3: Visible spectra of compounds I, II, and III.

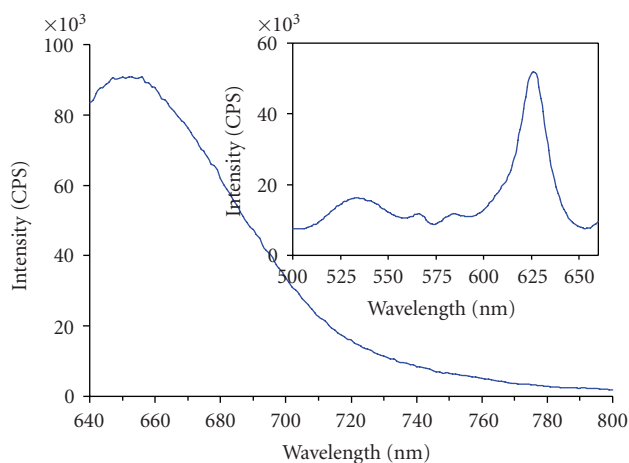


FIGURE 4: Steady-state fluorescence emission spectrum ($\lambda_{\text{ex}} = 620$ nm) and (inset) corresponding excitation spectrum ($\lambda_{\text{em}} = 680$ nm) of compound (I).

fluorescence life time (from 0.9 to 0.3 ns) is, in principle, indicative of an efficient electron injection occurring at the interface, likely due to electron injection from the singlet excited state of the molecule into the conduction band of the TiO₂. Semiquantitative estimation of time scale of this latter phenomenon can be performed taking into account that $\tau \propto 1/\Sigma k_i$ ($k =$ kinetic constant of i th process of excited state deactivation): in our case the measured fluorescence lifetime of the dye goes from 0.9 ns to 0.3 ns in solution and TiO₂, respectively, and the kinetic of electron injection process would be estimated to occur at ≈ 0.45 ns⁻¹. This value can be considered fast enough in relation to the lifetime of the compound in solution and it is in the same order of magnitude of that one measured for several monomeric phthalocyanines [35].

4.3. Electrochemical Measurements. To assign the electric potential of the HOMO orbitals of these bridged systems, we investigated their electrochemical properties in the anodic

TABLE 1: Experimental Spectral and Electrochemical data of **I–III** dyes.

dye	Abs _{max} ^a [nm]	Em _{max} ^a [nm]	E _(S^{+/S}) ^b [V] versus SCE	E ₍₀₋₀₎ ^c [V] (Abs/Em)	E _(S^{+/S*}) ^d [V] versus SCE
(I) + 1-Methylimidazole	621	696	0.434	1.88	-1.45
(II)	632	702	0.419	1.86	-1.44
(II) + 1-Methylimidazole	620	702	0.328	1.87	-1.54
(III)	637	702	0.387	1.86	-1.47
(III) + 1-Methylimidazole	627	702	0.383	1.86	-1.48

^aAbsorption and emission spectra in CH₂Cl₂ solution. ^bGround state oxidation potential versus SCE. ^c0-0 transition energy estimated from the intercept of the normalized absorption and emission spectra. ^dEstimated LUMO energies from the estimated HOMO energies (ground state oxidation potential) and the 0-0 transition energies.

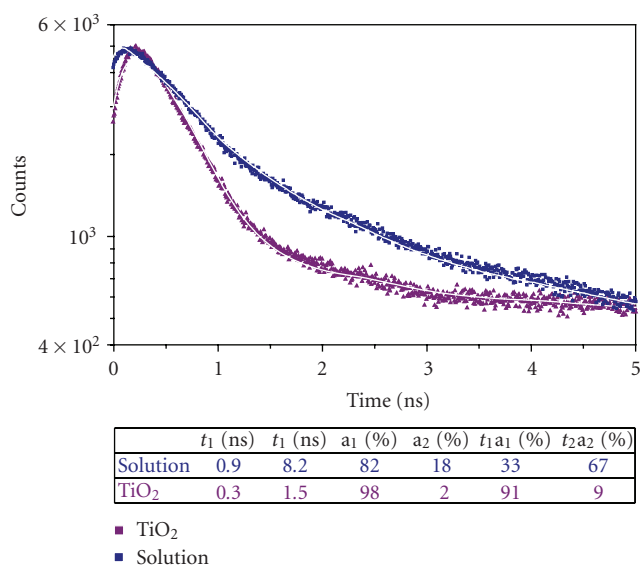


FIGURE 5: Experimental (dot) and calculated (line) fluorescence emission decays of (IsAFcPc)₂C ($\lambda_{em} = 650$ nm), in solution and on TiO₂ substrate; at the bottom table of fitting results; τ : life-time, a : amplitude.

range with cyclic voltammetry, allowing the electrochemical characterization to assess the energetic position of frontier orbital HOMO by the ground-state excitation potential $E_{(S^+/S)}$ of the first oxidation process. In Table 1 are summarised the first oxidation potentials of the **I**, **II**, and **III** compounds together with their correspondent spectral data and LUMO calculated energy levels.

Because the solubility of unsubstituted compound **I** was very low it has been possible to carry on the electrochemical measurements only on the corresponding more soluble 1-methylimidazole bis-adduct, while substituted compounds **II** and **III**, considerably more soluble, have been tested both in adducted form and not. The electrochemical behaviour of the μ -carbido iron complex (**I**) has been already investigated in the past both for phthalocyanine and porphyrin systems [44, 45]. In general, two oxidations and two reductions are expected for these systems being all processes centred on the macrocycles: the central metal iron is in a high-oxidation state (IV) and it does not undertake further oxidative processes. The oxidation potentials are specific to

the ligand-directed singly and doubly oxidized complex and there is a distinct separation of the half-wave potential in the successive ring oxidations. Due to the strong excitonic interactions of the closely adjacent Pc ligands in such diphthalocyanine compounds, the first macrocycle is oxidized more easily while the second one requests higher potentials. Furthermore, it is well known [45] that the first oxidation potential of nonmonomeric phthalocyanine derivatives is ~ 0.3 V (versus SCE), lower than the analogous potential of monomeric species which show ring-centred redox process, because of the delocalization of the positive charge over the whole system. Also, axial ligation with azo-bases and peripheral substitution with electron-releasing groups are known to affect the first oxidation potential because of the above mentioned effect, even if it is not predictable which of the two effects is more meaningful. In presence of 1-N-methylimidazole our experimental results on (**I**) are in total accord with what is published by Lancon and Kadish. [45] and the general trend is consistent being the first oxidation potential of the compound (**I**) > (**III**), due to the presence of *ter*-butyl groups that have a further stabilizing effect on the monooxidized complex. An apparent anomalous value, always in the presence of N-base, has been found for the system (**II**) that shows the lowest oxidation potential value; in this system we have only one ring replaced with *ter*-butyl groups and we think that in this specific case the addition of the N-base coordinated to the metal central and the presence of pushing groups lead to the observed lowest value. In fact, if we compare the first oxidation potential values of (**II**) and (**III**) measured in absence of N-base, being the stabilizing effect exclusively determined by the presence of the pushing groups, the situation is reversed and as expected the first oxidation potential is lower when in both rings are inserted pushing groups.

The electrochemical data have allowed the assessment of the ground state potentials (S^+/S) of the species (**I**)–(**III**) and this data together with the correspondent 0-0 transition energies, estimated from the intercept of absorption and emission spectra, give the energy levels of the singlet excited state (LUMO) of the compounds according to the equation: $E_{(S^+/S^*)} = E_{(S^+/S)} - E_{(0-0)}$. In Table 1 are summarised all the relevant absorption/emission values and the calculated HOMO/LUMO energy levels for all the sensitizers.

The main observation is that the inserted pushing groups do not affect strongly the energy level position of LUMO

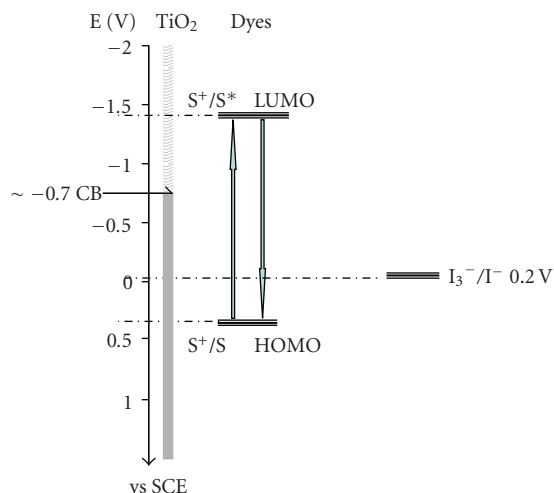


FIGURE 6: Energy level diagram from spectral and electrochemical data.

orbital and if we sketch the energy level diagram of the three compounds in comparison to the TiO_2 conduction band and the redox couple I^-/I_3^- (Figure 6) some significant remarks can be done. In principle we can say that one of the fundamental requisites have been satisfied: the LUMO position of the compounds (-1.44 ; -1.54) is widely more negative than the TiO_2 conduction band (-0.74 V versus SCE); therefore all compounds should have sufficient driving force for electron injection to the semiconductor. Nevertheless it is well known that this is a necessary but not sufficient condition. In fact to have a good overlap between the LUMO orbital and the TiO_2 conduction band, the excited states must possess directionality and also the kinetic of the process must be favourable. Furthermore, the HOMO levels of the dyes are lower than the energy level of the redox couple I^-/I_3^- (0.2 V versus SCE) enabling the dye regeneration reactions. The difference between the two levels appears more favourable for the compound (I) (circa 200 mV) while for compounds (II) and (III) this difference has so low values that the process of the dye regeneration from the couple I^-/I_3^- can seriously be called into question. Being well known that the efficiency of a cell depends on the balance between the electron injection into the conduction band and the back transfer of injected electrons from conduction band of TiO_2 towards the dye cation radical, we should ensure that there is enough driving force for the regeneration reaction in order to avoid the recapture by the dye cation or at least to make this process as slow as possible.

4.4. DSSC Device Performance. Dye sensitized solar cells with TiO_2 layer covered by $(\text{IsAFcPc})_2\text{C}$ present average V_{oc} and J_{sc} values in the range of hundred millivolt and microampere, respectively; to be more precise the best cell values (Figure 7) are $V_{oc} = 359$ mV, $J_{sc} = 305 \mu\text{A}/\text{cm}^2$, and $\text{FF} = 62.9\%$ and an efficiency of 0.07% . It is important to note that the cells reach these values after a quite long stabilizing period (see Table 2) during which it is possible to note a slow colour change of the electrolyte solution, from yellow to green,

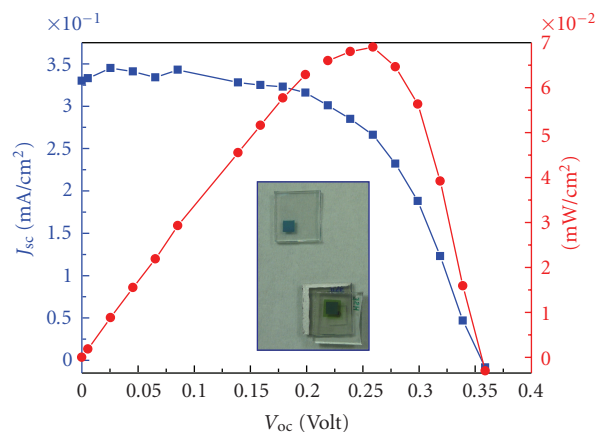


FIGURE 7: J/V plot of DSSC cell with compound (I) after 3 weeks; in the inset: picture of the cell as done (blue) and after 3 weeks.

TABLE 2: Performances of the same DSSC cell during time.

Measurements	Delay Time	J_{sc} ($\mu\text{A}/\text{cm}^2$)	V_{oc} (mV)	FF (%)	η (%)
(a)	24 hours	181	275	36.1	0.018
(b)	1 week	227	276	41.1	0.026
(c)	2 week	252	326	48.9	0.040
(d)	3 week	305	359	62.9	0.069

and similar effect is also visible for the sensitized TiO_2 , changing from deep blue to green (Figure 7 inset). This effect can be ascribable to the electrolyte system: it is known that different benzimidazole derivatives [46] are used as additives in the electrolyte solution and these compounds can coordinate the iron atom displacing the isonicotinic acid. Similar behaviour is expected if *ter*-butyl pyridine would be used [47].

Taking into account the molecular symmetry, this phenomenon can have a double effect: (1) benzimidazole derivative (that only for convenience is represented as *N*-methyl-benzimidazole) can remove the dye from the titanium layer displacing the isonicotinic acid directly bound to the TiO_2 surface; as direct consequence of that it is possible to note the electrolyte solution becomes green; (2) benzimidazole compound can alternatively substitute the TiO_2 -nonbound isonicotinic acid, inducing a general asymmetry in the molecule and, acting as pushing electron donating group, it can increase or create an axially aligned dipole moment which can improve the molecular performances (Figure 8). Considering the overall result observed during time (increased J_{sc} and V_{oc}) it is possible to confirm that the displacement of TiO_2 -nonbound isonicotinic acid is the main effect on the cell performance. These measurements underline how the design of new dyes has to be planned taking into account the whole system and how the electrolyte solution has to be tailored as a function of the physical-chemical properties of the dye.

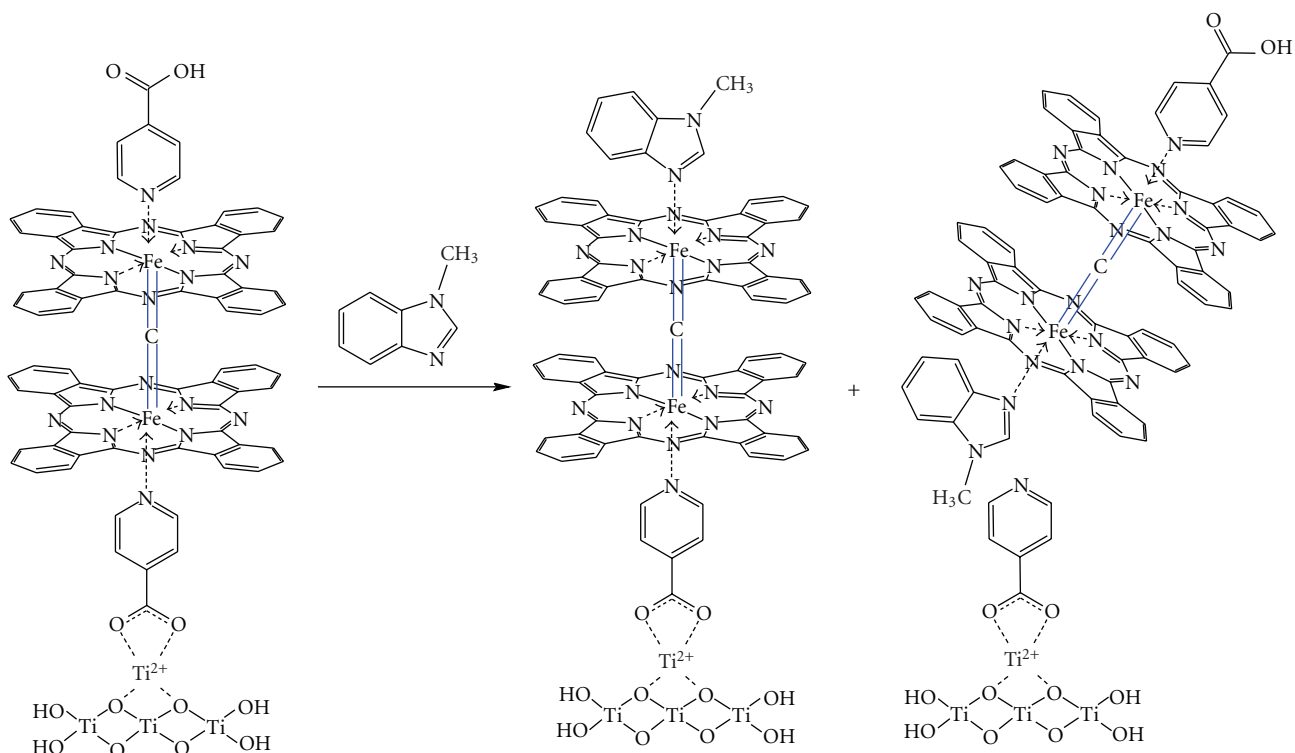


FIGURE 8: Hypothesis on interaction of benzoimidazole derivatives on the bonding of the dye over the TiO_2 substrate.

5. Conclusion

5.1. Conclusions. In this work we have presented the synthesis and characterization of new dyes for DSSC cells in the attempt of exploiting the behaviour of dimeric phthalocyanine systems in comparison with their monomeric forms widely investigated during the last years. Although only compound (**I**) has been tested in a DSSC cell and, in terms of efficiency, the obtained results are not so satisfactory, we want to point out some remarks: all compounds can be anchored to TiO_2 semiconductor without the presence of any anti-aggregation molecules, confirming that for such phthalocyanine systems the anchoring procedure to the semiconductor through the axial position prevents aggregation phenomena. As shown by time-resolved fluorescence measurements we observed a significant emission quenching attributable to an electron transfer from the dye to the semiconductor substrate with a sub-nanosecond kinetic process. In spite of that, we measured a poor efficiency very likely ascribed to different factors: (a) the probable replacement of isonicotinic acid by benzoimidazole derivative, and (b) the too low ionisation potential of the dye that makes difficult its regeneration by the I^-/I_3^- couple and the formation of a complex between the cation species and the I_3^- anion would be favoured. Taking into account all these considerations, it is not wrong to think that the performances of the cell could be considerably improved changing some elements in the cell construction up to redox shuttle and additives; it is well accepted that changing one of the greatest elements in a cell requires at least a simultaneous change/optimisation of

all other elements. Further experimental works to reach this purpose are under current investigation.

Acknowledgments

The authors and in particular G. Zanotti thank the project CHOSE (Centre for Hybrid and Organic Solar Energy) of Regione "Lazio" for supporting this paper. Many thanks also go to Francesco Ghetti (IBF-CNR, Pisa) for preliminary time-resolved measurements and Norberto Micali (IPCF-CNR, Messina) for making available the apparatus for definitive time-resolved fluorescence measurements. The authors are very grateful to Paolo Plescia (ISMN-CNR, Roma) for thermogravimetric analysis.

References

- [1] N. S. Lewis, "Powering the planet," *MRS Bulletin*, vol. 32, no. 10, pp. 808–820, 2007.
- [2] M. Grätzel, "Photoelectrochemical cells," *Nature*, vol. 414, no. 6861, pp. 338–344, 2001.
- [3] M. Grätzel, "Dye-sensitized solar cells," *Journal of Photochemistry and Photobiology C*, vol. 4, no. 2, pp. 145–153, 2003.
- [4] M. K. Nazeeruddin, A. Kay, I. Rodicio et al., "Conversion of light to electricity by cis- X_2 Bis(2,2'-bipyridyl-4,4'-dicarboxylate)ruthenium(II). Charge-transfer sensitizers ($\text{X} = \text{Cl}^-$, Br^- , I^- , CN^- , and SCN^-) on nanocrystalline TiO_2 electrodes," *Journal of the American Chemical Society*, vol. 115, no. 14, pp. 6382–6390, 1993.

- [5] Y. Tachibana, J. E. Moser, M. Grätzel, D. R. Klug, and J. R. Durrant, "Subpicosecond interfacial charge separation in dye-sensitized nanocrystalline titanium dioxide films," *Journal of Physical Chemistry*, vol. 100, no. 51, pp. 20056–20062, 1996.
- [6] T. W. Hamann, R. A. Jensen, A. B. F. Martinson, H. V. Ryswyk, and J. T. Hupp, "Advancing beyond current generation dye-sensitized solar cells," *Energy & Environmental Science*, vol. 1, no. 1, pp. 66–78, 2008.
- [7] A. Mishra, M. K. R. Fischer, and P. Bäuerle, "Metal-free organic dyes for dye-sensitized solar cells: from structure: property relationships to design rules," *Angewandte Chemie*, vol. 48, no. 14, pp. 2474–2499, 2009.
- [8] H. Tian and F. Meng, "Solar cells based on nanoporous titania films filled with conjugated polymers," in *Organic Photovoltaics: Mechanisms, Materials, and Devices*, S. S. Sun and N. S. Sariciftci, Eds., p. 313, CRC, London, UK, 2005.
- [9] H. Tian, X. Yang, R. Chen, A. Hagfeldt, and L. Sun, "A metal-free "black dye" for panchromatic dye-sensitized solar cells," *Energy & Environmental Science*, vol. 2, no. 6, pp. 674–677, 2009.
- [10] D. P. Hagberg, J.-H. Yum, H. Lee et al., "Molecular engineering of organic sensitizers for dye-sensitized solar cell applications," *Journal of the American Chemical Society*, vol. 130, no. 19, pp. 6259–6266, 2008.
- [11] S. Ito, S. M. Zakeeruddin, R. Humphry-Baker et al., "High-efficiency organic-dye-sensitized solar cells controlled by nanocrystalline-TiO₂ electrode thickness," *Advanced Materials*, vol. 18, no. 9, pp. 1202–1205, 2006.
- [12] K. Hara, K. Sayama, Y. Ohga, A. Shinpo, S. Suga, and H. Arakawa, "A coumarin-derivative dye sensitized nanocrystalline TiO₂ solar cell having a high solar-energy conversion efficiency up to 5.6%," *Chemical Communications*, no. 6, pp. 569–570, 2001.
- [13] K. Hara, M. Kurashige, Y. Dan-oh et al., "Design of new coumarin dyes having thiophene moieties for highly efficient organic-dye-sensitized solar cells," *New Journal of Chemistry*, vol. 27, no. 5, pp. 783–785, 2003.
- [14] G. Calogero, G. Di Marco, S. Cazzanti, et al., "Efficient dye-sensitized solar cells using red turnip and purple wild Sicilian prickly pear fruits," *International Journal of Molecular Sciences*, vol. 11, no. 1, pp. 254–267, 2010.
- [15] C. G. Claessens, U. Hahn, and T. Torres, "Phthalocyanines: from outstanding electronic properties to emerging applications," *The Chemical Record*, vol. 8, no. 2, pp. 75–97, 2008.
- [16] C. Leznoff and A. B. P. Lever, Eds., *Phthalocyanines: Properties and Applications*, vol. 1–4, Wiley-VCH, Cambridge, UK, 1989.
- [17] G. De La Torre, C. G. Claessens, and T. Torres, "Phthalocyanines: old dyes, new materials. Putting color in nanotechnology," *Chemical Communications*, no. 20, pp. 2000–2015, 2007.
- [18] H. Imahori, T. Umeyama, and S. Ito, "Large π -aromatic molecules as potential sensitizers for highly efficient dye-sensitized solar cells," *Accounts of Chemical Research*, vol. 42, no. 11, pp. 1809–1818, 2009.
- [19] Y. Ooyama and Y. Harima, "Molecular designs and syntheses of organic dyes for dye-sensitized solar cells," *European Journal of Organic Chemistry*, no. 18, pp. 2903–2934, 2009.
- [20] B. E. Hardin, E. T. Hoke, P. B. Armstrong et al., "Increased light harvesting in dye-sensitized solar cells with energy relay dyes," *Nature Photonics*, vol. 3, no. 7, pp. 406–411, 2009.
- [21] K. Lee, S. W. Park, M. J. Ko, K. Kim, and N.-G. Park, "Selective positioning of organic dyes in a mesoporous inorganic oxide film," *Nature Materials*, vol. 8, no. 8, pp. 665–671, 2009.
- [22] J. He, G. Benko, F. Korodi et al., "Modified phthalocyanines for efficient near-IR sensitization of nanostructured TiO₂ electrode," *Journal of the American Chemical Society*, vol. 124, no. 17, pp. 4922–4932, 2002.
- [23] M. D. K. Nazeeruddin, R. Humphry-Baker, M. Grätzel, and B. A. Murrer, "Efficient near IR sensitization of nanocrystalline TiO₂ films by ruthenium phthalocyanines," *Chemical Communications*, no. 6, pp. 719–720, 1998.
- [24] E. Palomares, M. V. Martínez-Díaz, S. A. Haque, T. Torres, and J. R. Durrant, "State selective electron injection in non-aggregated titanium phthalocyanine sensitized nanocrystalline TiO₂ films," *Chemical Communications*, vol. 10, no. 18, pp. 2112–2113, 2004.
- [25] A. Morandeira, I. Lopez-Duarte, M. V. Martínez-Díaz et al., "Slow electron injection on Ru-phthalocyanine sensitized TiO₂," *Journal of the American Chemical Society*, vol. 129, no. 30, pp. 9250–9251, 2007.
- [26] J. He, A. Hagfeldt, S.-E. Lindquist et al., "Phthalocyanine-sensitized nanostructured TiO₂ electrodes prepared by a novel anchoring method," *Langmuir*, vol. 17, no. 9, pp. 2743–2747, 2001.
- [27] S. Eu, T. Katoh, T. Umeyama, Y. Matano, and H. Imahori, "Synthesis of sterically hindered phthalocyanines and their applications to dye-sensitized solar cells," *Dalton Transactions*, no. 40, pp. 5476–5483, 2008.
- [28] J.-H. Yum, S.-R. Jang, R. Humphry-Baker et al., "Effect of coadsorbent on the photovoltaic performance of zinc phthalocyanine-sensitized solar cells," *Langmuir*, vol. 24, no. 10, pp. 5636–5640, 2008.
- [29] A. Morandeira, I. López-Duarte, B. O'Regan, et al., "Ru(II)-phthalocyanine sensitized solar cells: the influence of co-adsorbents upon interfacial electron transfer kinetics," *Journal of Materials Chemistry*, vol. 19, no. 28, pp. 5016–5026, 2009.
- [30] P. Y. Reddy, L. Giribabu, C. Lyness et al., "Efficient sensitization of nanocrystalline TiO₂ films by a near-IR-absorbing unsymmetrical zinc phthalocyanine," *Angewandte Chemie*, vol. 46, no. 3, pp. 373–376, 2007.
- [31] J.-J. Cid, J.-H. Yum, S.-R. Jang et al., "Molecular cosensitization for efficient panchromatic dye-sensitized solar cells," *Angewandte Chemie*, vol. 46, no. 44, pp. 8358–8362, 2007.
- [32] F. Silvestri, I. Lopez-Duarte, W. Seitz et al., "A squaraine-phthalocyanine ensemble: towards molecular panchromatic sensitizers in solar cells," *Chemical Communications*, no. 30, pp. 4500–4502, 2009.
- [33] T. Rawling, C. Austin, F. Buchholz, S. B. Colbran, and A. M. McDonagh, "Ruthenium phthalocyanine-bipyridyl dyads as sensitizers for dye-sensitized solar cells: dye coverage versus molecular efficiency," *Inorganic Chemistry*, vol. 48, no. 7, pp. 3215–3227, 2009.
- [34] L. Giribabu, C. V. Kumar, P. Y. Reddy, J.-H. Yum, M. Grätzel, and M. K. Nazeeruddin, "Unsymmetrical extended π -conjugated zinc phthalocyanine for sensitization of nanocrystalline TiO₂ films," *Journal of Chemical Sciences*, vol. 121, no. 1, pp. 75–82, 2009.
- [35] B. C. O'Regan, I. López-Duarte, M. V. Martínez-Díaz et al., "Catalysis of recombination and its limitation on open circuit voltage for dye sensitized photovoltaic cells using phthalocyanine dyes," *Journal of the American Chemical Society*, vol. 130, no. 10, pp. 2906–2907, 2008.
- [36] J.-J. Cid, M. García-Iglesias, J.-H. Yum, et al., "Structure-function relationships in unsymmetrical zinc phthalocyanines for dye-sensitized solar cells," *Chemistry - A European Journal*, vol. 15, no. 20, pp. 5130–5137, 2009.

- [37] F. Silvestri, M. García-Iglesias, J. Yumb, et al., "Carboxy-1,4-phenylenevinylene- and carboxy-2,6-naphthylene-vinylene unsymmetrical substituted zinc phthalocyanines for dye-sensitized solar cells," *Journal of Porphyrins and Phthalocyanines*, vol. 13, no. 3, pp. 369–375, 2009.
- [38] J. Metz, O. Schneider, and M. Hanack, "Synthesis and properties of substituted (phthalocyaninato)iron and -cobalt compounds and their pyridine adducts," *Inorganic Chemistry*, vol. 23, no. 8, pp. 1065–1071, 1984.
- [39] G. Rossi, V. L. Goedken, and C. Ercolani, " μ -carbido-bridged iron phthalocyanine dimers: synthesis and characterization," *Journal of the Chemical Society, Chemical Communications*, no. 1, pp. 46–47, 1988.
- [40] D.V. O'Connor and D. Phillips, *Time-Correlated Single Photon Counting*, Academic Press, New York, NY, USA, 1981.
- [41] N. Angelini, N. Micali, V. Villari, P. Mineo, D. Vitalini, and E. Scamporrino, "Interactions between water soluble porphyrin-based star polymer and amino acids: spectroscopic evidence of molecular binding," *Physical Review E*, vol. 71, no. 2, Article ID 021915, 7 pages, 2005.
- [42] D.W. Marquadt, "An algorithm for least-squares estimation of nonlinear parameters," *Journal of the Society for Industrial and Applied Mathematics*, vol. 11, no. 2, pp. 431–441, 1963.
- [43] J. R. Lakowicz, *Principles of Fluorescence Spectroscopy*, Kluwer Academic/Plenum Publishers, New York, NY, USA, 1999.
- [44] A. Kienast, L. Galich, K. S. Murray et al., " μ -carbido diporphyrinates and diphthalocyaninates of iron and ruthenium," *Journal of Porphyrins and Phthalocyanines*, vol. 1, no. 2, pp. 141–157, 1997.
- [45] D. Lancon and K. M. Kadish, "Electrochemistry of the μ -carbido iron tetraphenylporphyrin dimer, ((TPP)Fe)₂C, in nonaqueous media. Evidence for axial ligation by pyridine," *Inorganic Chemistry*, vol. 23, no. 24, pp. 3942–3947, 1984.
- [46] H. Choi, I. Raabe, D. Kim, et al., "High molar extinction coefficient organic sensitizers for efficient dye-sensitized solar cells," *Chemistry - A European Journal*, vol. 16, no. 4, pp. 1193–1201, 2010.
- [47] M. K. Nazeeruddin, F. De Angelis, S. Fantacci et al., "Combined experimental and DFT-TDDFT computational study of photoelectrochemical cell ruthenium sensitizers," *Journal of the American Chemical Society*, vol. 127, no. 48, pp. 16835–16847, 2005.

Research Article

Investigation of Low-Cost Surface Processing Techniques for Large-Size Multicrystalline Silicon Solar Cells

Yuang-Tung Cheng,¹ Jyh-Jier Ho,¹ William J. Lee,² Song-Yeu Tsai,² Yung-An Lu,¹
Jia-Jhe Liou,¹ Shun-Hsyung Chang,³ and Kang L. Wang⁴

¹Department of Electrical Engineering, National Taiwan Ocean University, No. 2 Pei-ning Rd., Keelung 20224, Taiwan

²Photovoltaics Technology Center, Industrial Technology Research Institute, No. 195 Chung Hsing Rd., 4 Sec. Chu Tung, Hsin Chu 31061, Taiwan

³Department of Microelectronic Engineering, National Kaohsiung Marine University, No. 142 Haijhuang Rd., Kaohsiung 81143, Taiwan

⁴Device Research Laboratory, Department of Electrical Engineering, University of California, Los Angeles, CA 90095, USA

Correspondence should be addressed to Jyh-Jier Ho, jackho@mail.ntou.edu.tw

Received 2 January 2010; Revised 8 March 2010; Accepted 13 March 2010

Academic Editor: Mario Pagliaro

Copyright © 2010 Yuang-Tung Cheng et al. This is an open access article distributed under the Creative Commons Attribution License, which permits unrestricted use, distribution, and reproduction in any medium, provided the original work is properly cited.

The subject of the present work is to develop a simple and effective method of enhancing conversion efficiency in large-size solar cells using multicrystalline silicon (mc-Si) wafer. In this work, industrial-type mc-Si solar cells with area of $125 \times 125 \text{ mm}^2$ were acid etched to produce simultaneously POCl_3 emitters and silicon nitride deposition by plasma-enhanced chemical vapor deposited (PECVD). The study of surface morphology and reflectivity of different mc-Si etched surfaces has also been discussed in this research. Using our optimal acid etching solution ratio, we are able to fabricate mc-Si solar cells of 16.34% conversion efficiency with double layers silicon nitride (Si_3N_4) coating. From our experiment, we find that depositing double layers silicon nitride coating on mc-Si solar cells can get the optimal performance parameters. Open circuit (V_{oc}) is 616 mV, short circuit current (J_{sc}) is 34.1 mA/cm^2 , and minority carrier diffusion length is $474.16 \mu\text{m}$. The isotropic texturing and silicon nitride layers coating approach contribute to lowering cost and achieving high efficiency in mass production.

1. Introduction

The multicrystalline silicon (mc-Si) solar cell is not only still heavily dependent on the material base in the semiconductor industry, but also features an excellent stability, mature technology, and easy acquisition [1, 2]. It also satisfies these requirements for the rapidly expanding solar energy markets [3–6]. The main reason why mc-Si solar cells are widely used is that mc-Si solar cells own the highest growth rate and the lowest fabrication cost in the mass-production level [5, 6]. Even though some commercial Si solar cell panels from company such as Samsung have above 18% conversion efficiency on float zone (FZ) Si wafers [7, 8], the structure of passivated emitter and rear cell is more complicated by using several expensive photolithography processes. However, the production of crystalline silicon (c-Si) solar cell with such

a high efficiency is very small compared to that of conventional Si solar cell because of complicated fabrication process with cost-intensive process steps and because of their small areas. In order to commercialize high-efficiency solar cell for optional consumer electronics, it is essential to produce cells with low cost on Czochralski (CZ) mc-Si wafers and simple fabrication processes proposed in our research.

The efficiency of mc-Si solar cells is mainly limited by minority carrier recombination. Major mc-Si disadvantages are wide varieties of defects inhomogeneously distributed, such as dislocations, grain boundaries, oxygen clusters, metal impurities, and dangling bond. In any *pn*-junction of the solar-cell process, meanwhile, the emitting electrons inside the c-Si are highly active and easily combine with other elements [9–12]. Besides, the mc-Si defects can lower the efficiency and decrease diffusion length [13–15].

The essential factors of achieving high efficiencies of Si-based wafer are the large minority carrier recombination lifetime and long diffusion length in mc-Si solar cells [16, 17]. Therefore, removing grain boundary on mc-Si surface by texturing is the present key issue of mc-Si research. We use large size CZ mc-Si wafer in order to investigate the influence of the grain boundary on the minority charge carrier diffusion length. Texturing the front surface of a solar cell generally results in performance improvement, because it removes surface damage or roughness and increases in the short-circuit current [18–20]. While the result of the bare wafers indicates a good effectiveness in acid etching experiment, a silicon nitride (Si_3N_4) coated on the surface of a real cell by plasma-enhanced chemical vapor deposited (PECVD) further changes the overall reflection properties. The hydrogen-rich PECVD Si_3N_4 layer can achieve good passivation [21–24]. In this research, a single layer (SL) Si_3N_4 and dual layers (DL) Si_3N_4 are deposited on large size ($125 \times 125 \text{ mm}^2$) mc-Si wafers by PECVD. From the experiment, we find that the effect on DL is better than that on SL. Therefore, our experiment mainly focuses on the concept of utilizing the DL refractive index of Si_3N_4 to minimize the reflection losses and passivation of the solar-cell surface.

2. Experiments

A series of experiments on mc-Si texturization were carried out with different approaches. For mc-Si solar cells fabrication, CZ (100)-oriented, p-type, 4-inch diameter, resistivity $1 \Omega\text{-cm}$, size $125 \times 125 \text{ mm}^2$, $300\text{-}\mu\text{m}$ thick wafers were used as a base material. The wafers were textured using acidic mixtures containing hydrofluoric acid (HF) and nitric acid (HNO_3) diluted with H_2O . The mixture of HF and HNO_3 was applied in a dipping bath for the removal of contaminations and lattice defects generated by the lapping of Si wafers. The removal of saw damage and the surface texturing are obtained in one step. High etching rate ($\sim 5 \mu\text{m}/\text{min}$) is preferable for large-scale production in which many wafers should be texturized in a short time. We have observed from scanning electron microscopy (SEM) micrographs that the Si surface that was etched with acidic solution of HF, HNO_3 and deionized (DI) water in the volume ratio 15 : 1 : 2.5 for 60 seconds showed uniform hemispherical etch pits. This was followed by a clean in 1 : 1 : 5 HCl : H_2O_2 : H_2O for 20 minutes and rinse in DI water. Next the n-type emitter was diffused by phosphorus (P) in open-tube furnace using conventional POCl_3 diffusion source at 835°C for 10 minutes predeposition followed by 20 minutes drive-in process.

After phosphorus glass removal and another clean, Si_3N_4 films were deposited by the PECVD in a conventional direct plasma reactor operating at 13.56 MHz using a mixture of the silane (SiH_4) and ammonia (NH_3) and the deposition temperature was set at 450°C . The refractive index (n) of solar cells depends on SiH_4 and NH_3 gas ratio. Common anti-reflection (AR) layer materials are SiO_2 ($n = 1.5$), Si_3N_4 ($n = 2.0$), and TiO_2 ($n = 2.5$) [25, 26]. Figure 1 shows refractive indices of the Si_3N_4 films deposited

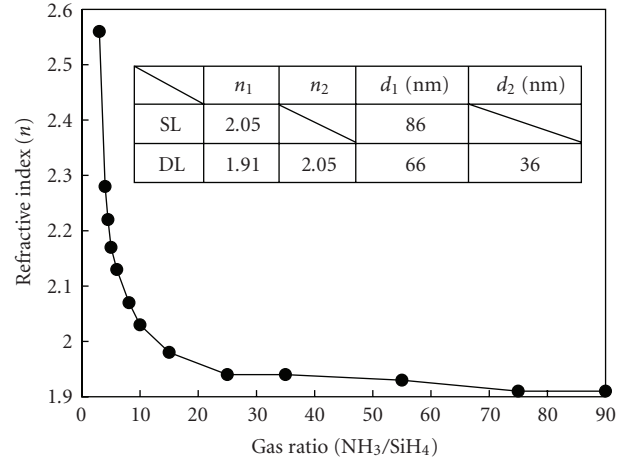


FIGURE 1: Refractive indices (n) of Si_3N_4 films deposited with different ratios of gas-flow rate. The inset table is the measured n with corresponding thickness (d) values for SL and DL AR films.

on the mc-Si wafers at different ratios of gas flow rate and refractive indices during PECVD process. When the ratios of gas flow increase from 3 to 90, the values of n are decreased dramatically initially, then moderately, and n saturated at 1.91 as gas-flow ratio is larger than 75. The optimal n value with thickness (d) allows us to measure the properties of different AR coatings by using elliptical polarizer. Corresponding expressions for the transmission and reflection coefficients are determined. The inset table also shows the measured n with corresponding d values for SL and DL AR films. Therefore, for the SL coating, the measured values for n_1 and d_1 are 2.05 and 86 nm, respectively. For DL coating, the measured upper layer parameters of n_1 and d_1 are 1.91 and 66 nm and the measured bottom layer parameters of n_2 and d_2 are 2.05 and 36 nm, respectively.

The front and back metallizations of the diffused mc-Si wafers were carried out using standard Ag-paste and Al paste for screen-printed metallization technique followed by baking and cofiring at a temperature of 750°C in a conveyer belt furnace. Finally, the solar cells were edge isolated using a dicing saw. For simplification of terrestrial solar-cell characterization, the induced current density-voltage (J - V) curves of the developed devices were measured under the air mass (AM1.5G) of the solar simulator (Wacom, Model: WXS-220S-L2) illumination at $1000 \text{ W}/\text{m}^2$ on a Keithley 4200 instrument. The quality of the surface passivation was revealed by lifetime measurements, which were obtained by Semilab WT-2000. We also measured the sample's quantum efficiency (QE) by PV Measurement (Model: QEX7).

3. Treatment Result and Discussion

A series of experiments on mc-Si texturization were carried out with different approaches. Our first results regarding the variation of the morphological studies of different hemispherical structure are formed in large area $125 \times 125 \text{ mm}^2$ mc-Si wafer. For the theoretical approach to get

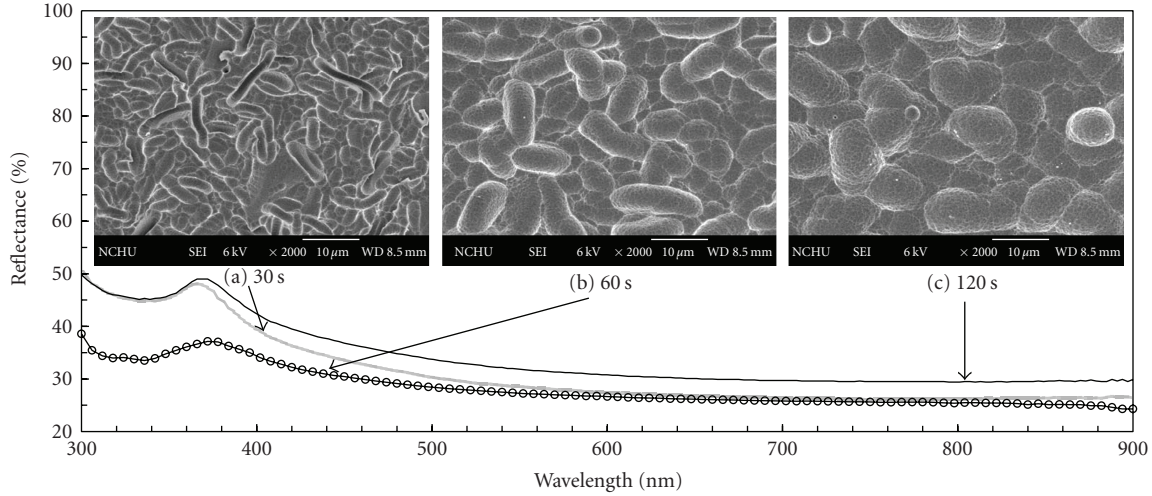


FIGURE 2: Reflectivity of the textured mc-Si surfaces after 30 seconds, 60 seconds, and 120 seconds of etching in HF : HNO₃ : H₂O = 15 : 2.5 : 1 solution. SEM micrographs of the textured mc-Si surfaces after 30 seconds, 60 seconds, and 120 seconds of etching are shown in inset figure (a), (b), and (c).

lower reflectance, we assumed it to be a part of a sphere for simplicity. The calculation was based on a ray-tracing method. As the texture is a part of a sphere, the relationship between width (D), depth (H), radius (r), and the surface reflectance (R) corresponding with function of incident angle ($f(\theta)$) can be calculated as follows [27]:

$$D^2 = 8rH - 4H^2, \quad (1)$$

$$R \propto \frac{\sum_{i=1}^n \{ [f(\theta)]^i \times \pi r^2 \}}{\pi(2rH - H^2)}.$$

In other words, the ratio (H/D) of depth and width of these etch pits determines the reflectance of the textured mc-Si [28]. Figures 2(a), 2(b), and 2(c) show the surface morphology after 30, 60, and 120 seconds of acid etching. Acid etching forms spherical etch pits on the surface of mc-Si which are generated by saw damage as template. The resulting surface structure after 30 seconds etching features the known homogeneous arranged oval etch warm shape pits with a mean width of 5–8 μm (shown as Figure 2(a)) and a depth of 2.5 μm . After 60 seconds, the shape changes from oval pits to mainly round structure with an average diameter of 10–15 μm as shown in Figure 2(b). These rounded features have good antireflection properties. After 120 seconds of etching, the shape changes from oval pits to become plainer due to longer etch times or higher etch rates. According to article [27], these structures increase the reflectance of silicon. After thorough observation with an optical microscope, it was found that the surface structures were not yet satisfactory in the case of texturing with three different ratios of HF : HNO₃ : H₂O for etching times over 60 seconds. If the time of etching is too long, the texturization disappears and the dislocations and grains boundary figures appear. The surface of mc-Si is not quite satisfactory for solar cell application even up to 60 seconds of etching as shown in Figure 2(c). Therefore, in the case of mc-Si after 60 etching for the rounds geometry, the lowest reflectance

corresponding to a geometry having the highest ratio of H/D was observed. And so it can be concluded that the most reduction of the reflectance is obtained at the optimized etching time of 60 seconds.

The reflectance is minimal for high ratios of H/D . Since the surface structure and precisely the ratio H/D are highly sensitive to the slightest changes in the reaction of the etchant, all influencing parameters arising during the electrochemical process like etching time and rate should be examined. Figure 2 shows the reflectance of the textured surface for wavelengths between 300 and 900 nm. These curves reveal the increasing importance of the geometry comparing to the etch time. Compared with that of the textured surface, the average reflectance of the mc-Si surface decreased to 25.3% after the acid texturing process while after texturing for 60 seconds, the decrease of the reflectance was rather weak, especially at long wavelengths. A significant reduction of the reflectance which is the optimized etching time for 60 seconds has to be noted.

The samples being acid texturized during 60 seconds were used in the next processes for phosphorus diffusion. The n-type emitter was formed by heavily doping with phosphorus using a POCl₃ source at high temperature. Figure 3 illustrates the (1) sheet resistance (in Ω/\square) and (2) conversion efficiency (in %) as a function of different temperatures (from 770°C to 900°C of the solar-cell with drive-in diffusion processes). Among the diffusion process included in the study, the maximum conversion efficiency value of 14.26% is obtained at 835°C diffusion temperature. Further increases in the diffusion temperature beyond 835°C cause decreased conversion efficiency. The sheet resistance decreases initially with increasing the diffusion temperatures, and reaches a minimum value at 835°C-diffusion temperature. With this optimal diffusion parameters at 835°C for a solar-cell prototype, the sheet resistance is measured to be 44.7 Ω/\square , and its corresponding conversion efficiency is 14.26%.

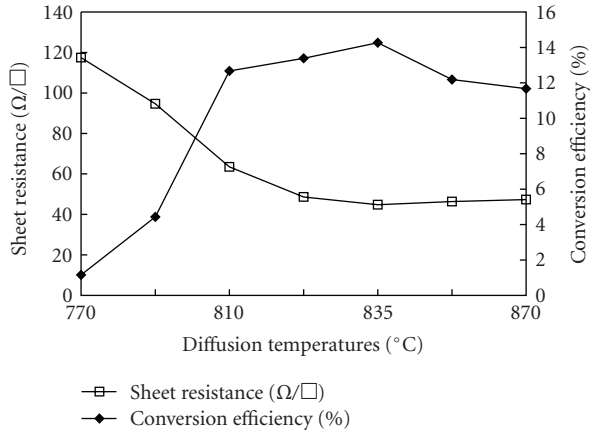


FIGURE 3: The sheet resistance (in Ω/\square) and conversion efficiency (in %) with respect to different temperatures (from 770°C to 900°C) of the solar-cell prototypes with and without drive-in diffusion processes.

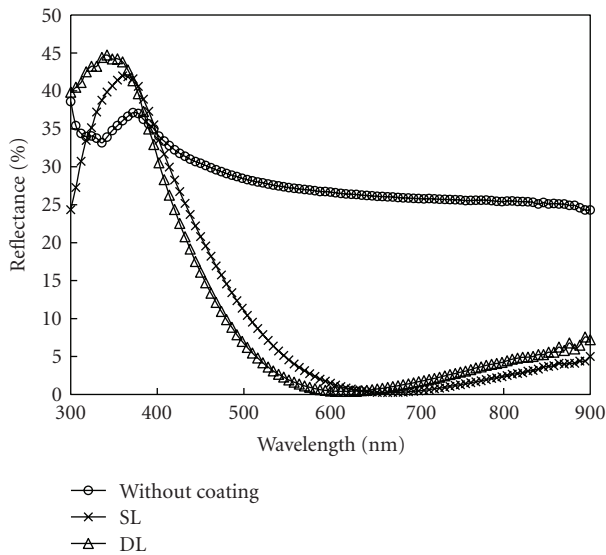


FIGURE 4: Comparison of reflectance of acid solution textured mc-Si surfaces with (SL, DL) and without Si_3N_4 coating. One can clearly show that the reflectance for the DL coating is a very low value of 1% between 572 nm and 672 nm wavelength.

The surface reflectance was further lowered after depositing Si_3N_4 layer on the large-area surface of the mc-Si solar cell, and the results are shown in Figure 4. The reflectance for the SL coating remains at a low value below 2.8% for an extended spectral range from 612 nm to 738 nm wavelength. In contrast, the reflectance for the DL coating is a very low value of 1% between 572 nm and 672 nm wavelength. We focus our attention on the 450–600 nm spectral range which corresponds to the maximum intensity of solar irradiation. Compared with the SL, the DL coating is characterized by a smaller reflectance precisely in this useful range. The character could significantly contribute to further improvements on solar cells' performance.

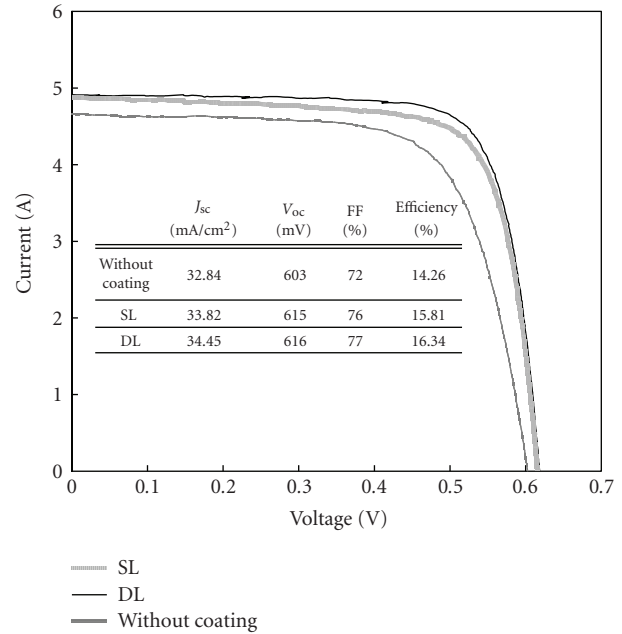


FIGURE 5: Comparison of IV-curves of a $125 \times 125 \text{ mm}^2$ of the different results from DL, SL, and without coating. DL's conversion efficiency is the highest.

As a matter of course, an increase in the light absorbed in the cell properly enhances the generation of electrical parameters of the cell if there is no loss from the deposition scheme. This could be confirmed by measuring of the I-V curve of the developed cell as in Figure 5. The solar cell surface with DL coating and the short-circuit current density (J_{sc}) of 34.45 mA/cm^2 cell are comparable to a solar cell without coating. The observed conversion efficiency (η) was 16.34%, which is a major advantage of Si_3N_4 films. The high conversion efficiency also electronically passivates the surface, leading to reduced recombination losses. To increase DL coating in the lightest absorbed in the cell properly enhances the generation of electron-hole pairs and the current density of the cell if there is no loss from the passivation process. The solar cell with the SL coating had the high efficiency. J_{sc} is 33.82 mA/cm^2 , open-circuit voltage (V_{oc}) is 615 mV, fill factor (FF) is 76%, and η is 15.81%. The difference in conversion efficiencies of cells with different surfaces basically comes from the variation of J_{sc} . They are mainly depositing condition-dependent parameter of the large-size solar cells. It seems that the V_{oc} and the FF are clearly not related to the AR coating. With these results, it can be concluded that our deposition scheme with DL coating creating AR surface is successful in achieving better J_{sc} and hence better conversion efficiency in large-area mc-Si solar cell.

The percentage refers to the fraction of light-generated carrier and the variations between one region and another are due to variations in the diffusion length in the solar cell caused by the light absorb in the mc-Si solar cells. Figure 6 shows average diffusion length of the SL and DL anti-reflection deposition in a large size mc-Si solar

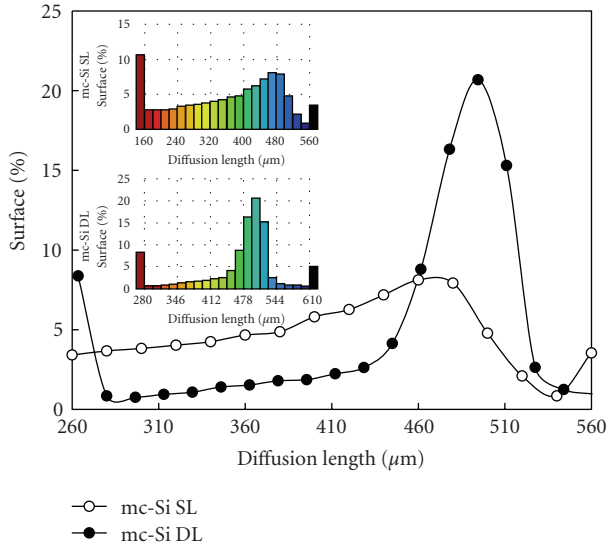


FIGURE 6: Comparison average diffusion length of the SL and DL antireflection deposition in large size mc-Si solar cell. Histograms of diffusion length against percentage wafer area for SL and DL coating solar cells are shown in the up-left inset.

cell. Histograms of diffusion length against percentage of large area for SL and DL coating solar cells are shown in the up-left inset. The measured average minority carrier diffusion lengths of SL and DL are $364.97 \mu\text{m}$, $474.16 \mu\text{m}$, respectively. By comparing the insert histograms for the solar cells deposited with larger size and SL, it can be found that if the cell does not have enough of the additional hydrogenation through Si_3N_4 passivation, grain boundaries result in recombination activity. Thus diffusion length is lower. The result obtained using the suggested that graded DL coating is therefore very satisfied, especially if we know that ideal coating layer that we could obtain by complete surface passivation can reduce recombination. Minority carrier lifetimes strongly depend on the passivation process and we found a conversion efficiency of 15.81% and 16.34% for SL and DL, respectively.

Figure 7 shows that the QE curve of the DL coated solar cell is higher than that of the SL coated solar cell in a wide-wavelength range (300–1200 nm). The DL coating having higher QE in a wavelength range of 450–1000 nm contributed to the lower reflection and the increase in effective minority carrier diffusion length. It is also seen that the SL QE decreases in the long wavelength region due to decrease in effective minority carrier diffusion length. This indicates a clear coat quality improvement and since the area under the curve is a measure for the cell current, one can see that the cell with the passivating Si_3N_4 has a higher short circuit current density and thus higher conversion efficiency.

4. Conclusion

For the large size solar cell process described above, an efficiency of 16.34% is achieved. We have shown that the

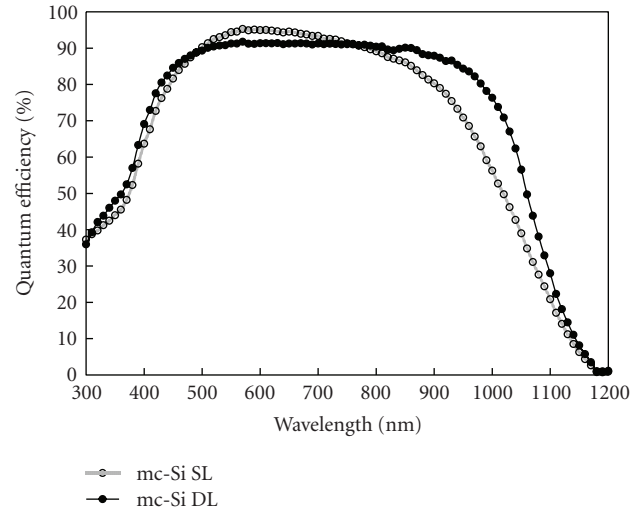


FIGURE 7: Results of quantum efficiency (QE) measurements SL and DL coated on large size mc-Si solar cells. It clearly shows the DL coating with higher QE in a wavelength range of 450–1000 nm contributed to the lower reflection and the increase in effective minority carrier diffusion length.

major advantages of the process are texture of a large size mc-Si with suitable acid solution ratio, no grain-boundary delineation, and significant reproducibility. These advantages improve the throughput in industrial production of solar cells. The n-type emitter was formed in the solar cell process by phosphorus diffusion at temperatures of 835°C for 10 minutes predeposition followed by 20 minutes drive-in. By the PECVD, Si_3N_4 layers provide both surface passivation and antireflection coating in silicon solar cells. In this work, the Si_3N_4 films with different refractive indices were prepared by varying the gas flow rate ratio of SiH_4 to NH_3 . The DL coated refractive index Si_3N_4 concept demonstrated that this could be used to decrease the reflection losses and surface hydrogen passivation. The increase in J_{sc} is an improvement in the number of layer coating and material thickness, especially for the minority carrier lifetime. The quantum efficiency measurements showed that the DL improvement in average diffusion length has been achieved compared to SL. Because the chemical etching for acid texturization and AR coating formation is very simple, cheap, and suitable for mass production, present technology is very promising for large-area mc-Si solar cells manufacturing. In the future, we will focus both on improving the mc-Si texturing quality and on implementing novel process features like different materials coating to obtain relatively high efficiency solar cells.

Acknowledgment

The authors acknowledge the financial support from *The National Science Council of R.O.C.* under contracts No. NSC 98-2622-E-019-006-CC3 and NSC 98-2221-E-019-003.

References

- [1] A. Jäger-Waldau, *PV Status Report 2008*, European Commission, DG Joint Research Centre, Ispra, Italy, 2008.
- [2] G. P. Willeke, "Thin crystalline silicon solar cells," *Solar Energy Materials & Solar Cells*, vol. 72, no. 1–4, pp. 191–200, 2002.
- [3] L. Sherwood, "U.S. solar market trends 2008," Annual Report, pp. 1–16, Interstate Renewable Energy Council, 2009.
- [4] Photovoltaic Technology Research Advisory Council (PV-TRAC) of European Commission, "A vision for photovoltaic technology," Tech. Rep., European Communities, Luxembourg, Belgium, 2005.
- [5] A. Goetzberger, C. Hebling, and H.-W. Schock, "Photovoltaic materials, history, status and outlook," *Materials Science and Engineering R*, vol. 40, no. 1, pp. 1–46, 2003.
- [6] A. Goetzberger, J. Luther, and G. Willeke, "Solar cells: past, present, future," *Solar Energy Materials and Solar Cells*, vol. 74, no. 1–4, pp. 1–11, 2002.
- [7] I. S. Moon, D. S. Kim, and S. H. Lee, "New method for patterning the rear passivation layers of high-efficiency solar cells," *Journal of Materials Science*, vol. 12, no. 10, pp. 605–607, 2001.
- [8] J. Kim, J. Hong, and S. H. Lee, "Application of PECVD SiNx films to screen-printed multicrystalline silicon solar cell," *Journal of the Korean Physical Society*, vol. 44, no. 2, pp. 479–482, 2004.
- [9] P. Kittidachachan, T. Markvart, D. M. Bagnall, R. Greef, and G. J. Ensell, "A detailed study of p-n junction solar cells by means of collection efficiency," *Solar Energy Materials & Solar Cells*, vol. 91, no. 2-3, pp. 160–166, 2007.
- [10] A. G. Aberle, B. Kuhlmann, R. Meyer, A. Hübner, C. Hampe, and R. Hezel, "Comparison of p-n junction and inversion-layer silicon solar cells by means of experiment and simulation," *Progress in Photovoltaics: Research and Applications*, vol. 4, no. 3, pp. 193–204, 1996.
- [11] N. M. Johnson and C. Herring, "Hydrogen immobilization in silicon p-n junctions," *Physical Review B*, vol. 38, no. 2, pp. 1581–1584, 1988.
- [12] A. G. Aberle, "Surface passivation of crystalline silicon solar cells: a review," *Progress in Photovoltaics: Research and Applications*, vol. 8, no. 5, pp. 473–487, 2000.
- [13] B. Sopori, M. I. Symko, R. Reedy, K. Jones, and R. Matson, "Mechanism(s) of hydrogen diffusion in silicon solar cells during forming gas anneal," in *Proceedings of the 26th IEEE Photovoltaic Specialists Conference (PVSC '97)*, pp. 25–30, Anaheim, Calif, USA, September-October 1997.
- [14] B. L. Sopori, X. Deng, J. P. Benner, et al., "Hydrogen in silicon: a discussion of diffusion and passivation mechanisms," *Solar Energy Materials and Solar Cells*, vol. 41-42, pp. 159–169, 1996.
- [15] P. Sana, A. Rohatgi, J. P. Kalejs, and R. O. Bell, "Gettering and hydrogen passivation of edge-defined film-fed grown multicrystalline silicon solar cells by Al diffusion and forming gas anneal," *Applied Physics Letters*, vol. 64, no. 1, pp. 97–99, 1994.
- [16] P. Würfel, T. Trupke, T. Puzzer, E. Schäffer, W. Warta, and S. W. Glunz, "Diffusion lengths of silicon solar cells from luminescence images," *Journal of Applied Physics*, vol. 101, no. 12, Article ID 123110, 10 pages, 2007.
- [17] P. S. Plekhanov, R. Gafiteanu, U. M. Gösele, and T. Y. Tan, "Modeling of gettering of precipitated impurities from Si for carrier lifetime improvement in solar cell applications," *Journal of Applied Physics*, vol. 86, no. 5, pp. 2453–2458, 1999.
- [18] M. Steinert, J. Acker, A. Henßge, and K. Wetzig, "Experimental studies on the mechanism of wet chemical etching of silicon in HF/HNO₃ mixtures," *Journal of the Electrochemical Society*, vol. 152, no. 12, pp. C843–C850, 2005.
- [19] M. Lipiński, P. Panek, and R. Ciach, "The industrial technology of crystalline silicon solar cells," *Journal of Optoelectronics and Advanced Materials*, vol. 5, no. 5, pp. 1365–1371, 2003.
- [20] M. S. Kulkarni and H. F. Erk, "Acid-based etching of silicon wafers: mass-transfer and kinetic effects," *Journal of the Electrochemical Society*, vol. 147, no. 1, pp. 176–188, 2000.
- [21] L. Carnel, H. Dekkers, I. Gordon, et al., "Study of the hydrogenation mechanism by rapid thermal anneal of siN:H in thin-film polycrystalline-silicon solar cells," *IEEE Electron Device Letters*, vol. 27, no. 3, pp. 163–165, 2006.
- [22] J.-J. Ho, C.-Y. Chen, R. Y. Hsiao, and O. L. Ho, "The work function improvement on indium-tin-oxide epitaxial layers by doping treatment for organic light-emitting device applications," *Journal of Physical Chemistry C*, vol. 111, no. 23, pp. 8372–8376, 2007.
- [23] J.-J. Ho, C.-Y. Chen, C.-M. Huang, W. J. Lee, W.-R. Liou, and C.-C. Chang, "Ion-assisted sputtering deposition of antireflection film coating for flexible liquid-crystal display applications," *Applied Optics*, vol. 44, no. 29, pp. 6176–6180, 2005.
- [24] J.-J. Ho and C.-Y. Chen, "Power effects in indium-zinc oxide thin films for OLEDs on flexible applications," *Journal of the Electrochemical Society*, vol. 152, no. 1, pp. G57–G61, 2005.
- [25] F. J. Beck, A. Polman, and K. R. Catchpole, "Tunable light trapping for solar cells using localized surface plasmons," *Journal of Applied Physics*, vol. 105, no. 11, Article ID 114310, 7 pages, 2009.
- [26] A. Lennie, H. Abdullah, S. M. Mustaza, and K. Sopian, "Photovoltaic properties of Si₃N₄ layer on silicon solar cell using Silvaco software," *European Journal of Scientific Research*, vol. 29, no. 4, pp. 447–453, 2009.
- [27] Y. Nishimoto, T. Ishihara, and K. Namba, "Investigation of acidic texturization for multicrystalline silicon solar cells," *Journal of the Electrochemical Society*, vol. 146, no. 2, pp. 457–461, 1999.
- [28] Z. Xi, D. Yang, W. Dan, C. Jun, X. Li, and D. Que, "Texturization of cast multicrystalline silicon for solar cells," *Semiconductor Science and Technology*, vol. 19, no. 3, pp. 485–489, 2004.

Review Article

New Components for Dye-Sensitized Solar Cells

**Stefano Caramori,¹ Vito Cristino,¹ Rita Boaretto,¹
Roberto Argazzi,² Carlo Alberto Bignozzi,¹ and Aldo Di Carlo³**

¹Dipartimento di Chimica, Università degli Studi di Ferrara, Via L. Borsari 46, 44100 Ferrara, Italy

²Dipartimento di Chimica, Istituto per la Sintesi Organica e la Fotoreattività (ISOF-CNR) c/o, Università degli Studi di Ferrara, Via L. Borsari 46, 44100 Ferrara, Italy

³Dipartimento di Ingegneria Elettronica, Università di Roma "Tor Vergata", Via del Politecnico 1, 00133 Roma, Italy

Correspondence should be addressed to Carlo Alberto Bignozzi, g4s@unife.it

Received 1 December 2009; Accepted 29 March 2010

Academic Editor: Gaetano Di Marco

Copyright © 2010 Stefano Caramori et al. This is an open access article distributed under the Creative Commons Attribution License, which permits unrestricted use, distribution, and reproduction in any medium, provided the original work is properly cited.

Dye-Sensitized Solar Cells (DSSCs) are among the most promising solar energy conversion devices of new generation, since coupling ease of fabrication and low cost offer the possibility of building integration in photovoltaic windows and facades. Although in their earliest configuration these systems are close to commercialization, fundamental studies are still required for developing new molecules and materials with more desirable properties as well as improving our understanding of the fundamental processes at the basis of the functioning of photoactive heterogeneous interfaces. In this contribution, some recent advances, made in the effort of improving DSSC devices by finding alternative materials and configurations, are reviewed.

1. Introduction

Dye-sensitized solar cells (DSSCs) are photoelectrochemical solar devices, currently subject of intense research in the framework of renewable energies being low-cost photovoltaic devices. DSSCs are based on the sensitization to visible light of mesoporous, nanocrystalline metal oxide films achieved by means of the adsorption of molecular dyes [1–3]. Photoinduced electron injection from the sensitizer dye (D) into the metal oxide conduction band initiates charge separation. Subsequently, the injected electrons are transported through the metal oxide film to a transparent electrode, while a redox-active electrolyte, such as I_3^-/I^- , is employed to reduce the dye cation and transport the resulting positive charge to a counter electrode (Figure 1).

DSSCs efficiencies up to 10.4% [4] have been reported for devices employing nanocrystalline TiO_2 films. Several studies have addressed the use of alternative metal oxides including SnO_2 [5, 6], ZnO [7, 8], and Nb_2O_5 [9]. The performance of dye-sensitized solar cells can be understood in view of the kinetic competition among the various redox processes involved in the conversion of light into electricity. Ultrafast electron injection (k_2) has been

observed in the femtosecond-picosecond (10^{-15} – 10^{-12} s) time domain. Regeneration of the oxidized dye (k_4) is typically characterized by rate constants of 10^7 – 10^9 s^{-1} . This is more than 100 times faster than recombination of injected electrons with the oxidized redox species (k_6) and orders of magnitude faster than back transfer to the dye cation in the absence of a redox mediator (k_3). As electron transport in the semiconductor electrode is generally one order of magnitude faster than recombination, the charge collection efficiency is near unit for optimized cells. Because of the prevailing role of electron transfer dynamics in DSSCs, the various processes have been widely studied in the last decade. While photo-electrochemical techniques proved to be most adequate for the study of electron transport, time-resolved optical spectroscopy remains the leading tool for the study of interfacial electron transfer. Dye regeneration and back transfer reactions have been intensely studied by nanosecond laser spectroscopy. On the other hand, due to its astonishing rate, the forward electron transfer reaction remained unresolved for several years: the advent of femtosecond laser spectroscopy opened the door to the domain of ultrafast chemical processes.

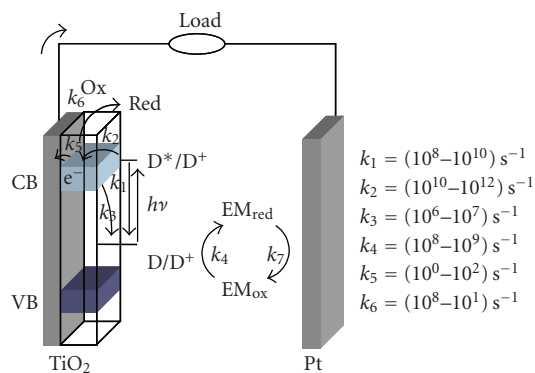


FIGURE 1: Electron transfer processes involved in a DSSC and their time scale.

The functioning of DSSCs is the interlacing of several subsystems which should work in tandem: the dye sensitizer, that is, the dye adsorbed on the semiconductor surface able to absorb the visible and near-IR photons and to pump electrons into the conducting band of semiconductor, the electron mediator for “hole” conduction and the counter electrode catalytic materials. We report here on the recent advances in the design of these DSSC components.

2. Molecular Sensitizers

One of the most important DSSC component, is the dye sensitizer, which represents the photodriven electron pump of the device. It allows an independent electron injection into the semiconductor conduction band and conversion of visible and near infrared photons to electricity.

Several organic and inorganic compounds have been investigated for semiconductor sensitization, such as chlorophyll derivatives [10], porphyrins [11], phtalocyanines [12, 13], platinum complexes [14, 15], fluorescent dyes [16], carboxylated derivatives of anthracene [17], polymeric films [18], and coupled semiconductors with lower-energy band-gaps [19], among others.

The best solar to electric power conversion efficiency has been achieved with polypyridyl complexes of ruthenium(II) [20] and osmium(II) [21] bearing carboxylated ligands, which are often employed as TiO_2 sensitizers in such cells. These species give rise to intense visible metal-to-ligand charge transfer (MLCT) bands with a favourable energetics for activationless charge injection. Among this family of compounds, excellent results have been achieved with thiocyanate derivatives. In particular, the performances of the Ru(II)-NCS complexes (Figure 2). In photoelectrochemical solar cells were found to be outstanding [20, 22]. The complexes show photoaction spectra dominating almost the entire visible region, short-circuit photocurrents exceeding 16 mA/cm^2 under simulated A.M. 1.5, sunlight and open-circuit photovoltages of the order of 0.7 V in the presence of I_3^-/I^- as redox electrolyte. Their high efficiency is related to hole delocalization across the NCS ligands [23, 24] which is responsible for an increased electronic coupling of the

electron transfer reaction involving $\text{TiO}_2/\text{Ru}^{\text{III}}\text{NCS}$ and I^- . This leads to an increase of the rate constant of the reductive process (k_4 , in Figure 1) and, as a consequence, of the IPCE (Incident Photon to Carrier Efficiency).

The photoelectrochemical performances obtained with the mononuclear complex $[\text{Ru}(\text{dcbH}_2)_2(\text{NCS})_2]$ have been surpassed by an analogous species based on the terpyridine ligand [4]. Indeed, TiO_2 electrodes covered with the complex $\text{Ru}(\text{L})(\text{NCS})_3$ ($\text{L} = 4,4',4''\text{-tricarboxy-2,2':6',2''-terpyridine}$) in its monoprotonated form displayed very efficient panchromatic sensitization covering the whole visible spectrum and extending the spectral response to the near IR region, up to 920 nm , with maximum IPCE values comparable to that obtained with the dithiocyanate complex. The panchromatic efficiency has been further extended in a series of cationic dyes, corresponding to the general formulae $[\text{M}(\text{H}_3\text{tcterpy})\text{LY}]^+$ [25]: $\text{M} = \text{Os}(\text{II})$ or $\text{Ru}(\text{II})$; ($\text{H}_3\text{tcterpy}$) is the tridentate ligand, $4,4',4''\text{-tricarboxy-2,2':6',2''-terpyridine}$, and L is a bidentate ligand of the type (bpy, $2,2'\text{-bipyridine}$) or (pyq, $2\text{-2'}\text{-pyridylquinoline}$) (Figure 3), which can be substituted both in the 4 and $4'$ positions by $\text{X} = \text{H}, \text{CH}_3, \text{COOH}$, or $\text{C}(\text{CH}_3)_3$, and $\text{Y} = \text{Cl}^-, \text{I}^-,$ or NCS^- . These dyes show reversible metal oxidations and, in the Os case, unprecedented photoconversion efficiency in the near infrared (NIR), approaching in the best case the value of 50% at 900 nm .

Many attempts to replace the thiocyanate donor ligands have been made, because the monodentate NCS^- is believed to be the weakest part of the complexes from the chemical stability point of view. Recently a novel thiocyanate-free cyclometalated ruthenium complex containing the $2\text{-(2,4-Difluorophenyl)pyridine}$ has been observed to produce a remarkable incident monochromatic photon-to-current conversion efficiency of 83% [26]. The solar cell employing a liquid-based electrolyte exhibits a short circuit photocurrent density of 17 mA/cm^2 , an open circuit voltage of 800 mV , and a fill factor of 0.74, corresponding to an overall conversion efficiency of 10.1% at standard AM 1.5 sunlight.

Besides metal organic dyes, relevant efforts are currently being directed towards the synthesis of novel types of ruthenium-free organic dye sensitizers which display intense visible bands and favourable ground and excited state energetics. Usually the organic dye efficiency is lower than that displayed by MLCT complexes, but considerable success has been recently met with a careful synthetic design of chlorophylls [27] push-pull porphyrins [26, 28], phtalocyanines [29], and some squaraine dyes [30], particularly suited to harvest the NIR portion of the solar spectrum.

Fruit and vegetable extracts have also been used as natural sensitizers in photoelectrochemical solar cells [31, 32]. The interest in natural dyes arises from the possibility of achieving an efficient sensitization without expensive and time consuming synthetic and purification procedures. Among raw natural dyes, cyanines and betalains have achieved maximum monochromatic photon to electron conversions exceeding 60% and short circuit photocurrents approaching 10 mA/cm^2 , under 0.1 W/cm^2 simulated solar irradiation. Red turnip, wild prickly pear, and eggplant were identified, up to now, as, respectively, the best natural sources

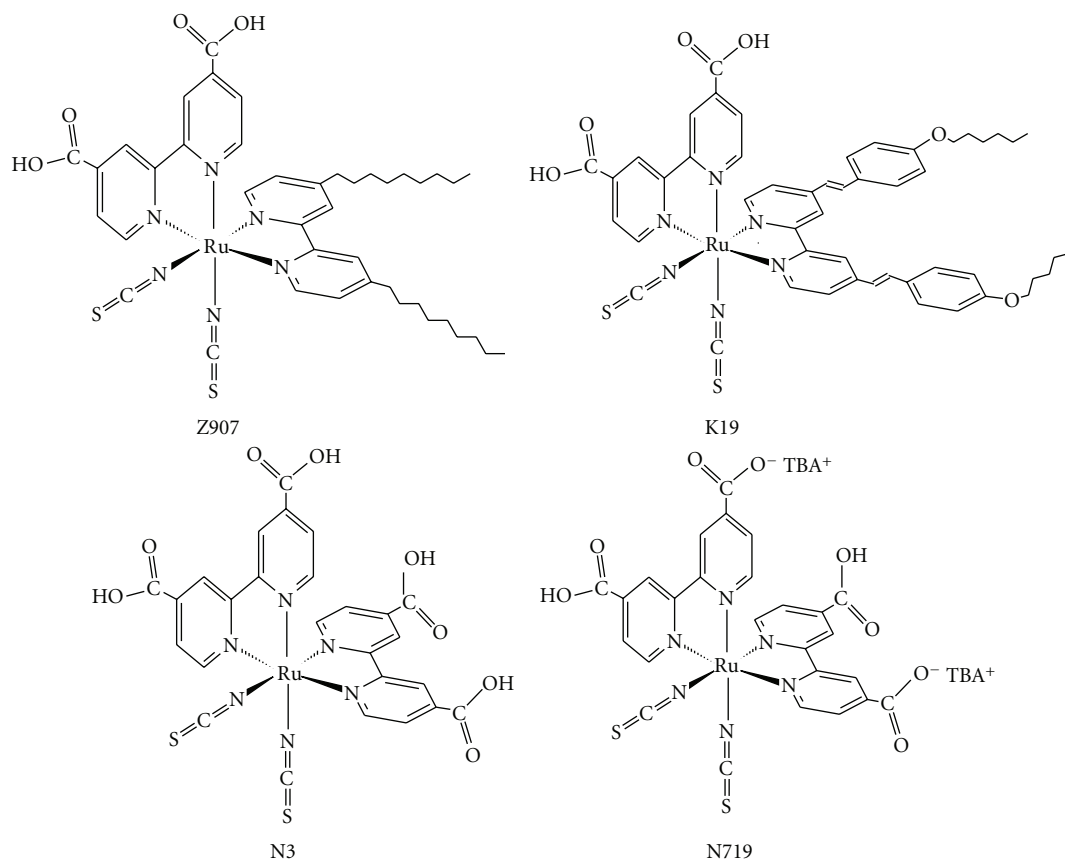


FIGURE 2: Structure of some of the most successful polypyridine Ru(II) dye based on the NCS ancillary ligand.

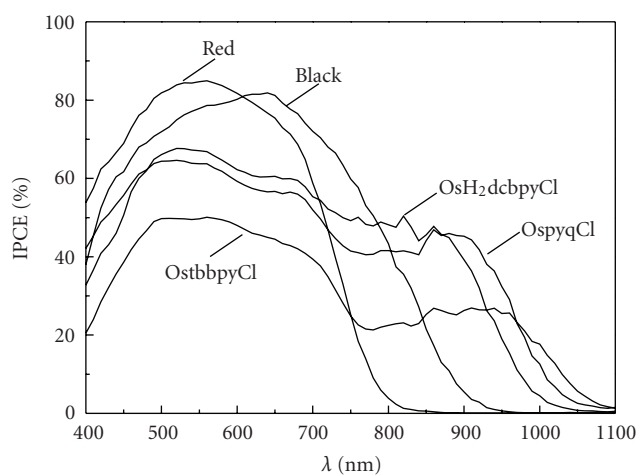


FIGURE 3: Photoaction spectra of Os dyes measured in sandwich type solar cells (nanocrystalline TiO_2 films, electrolyte made of 2 M LiI + 0.1 M I_2 in γ -butyrolactone). $\text{OsH}_2\text{dcbpyCl} = [\text{Os}(\text{H}_3\text{tcterpy})(\text{H}_2\text{dcbpy})(\text{Cl})]^+$; $\text{OstbbpyCl} = [\text{Os}(\text{H}_3\text{tcterpy})(\text{tbbpy})(\text{Cl})]^+$; $\text{OsipyqCl} = [\text{Os}(\text{H}_3\text{tcterpy})(\text{ipyq})(\text{Cl})]^+$. Red and black dye are N3 and $\text{Ru}(\text{H}_3\text{Tcterpy})(\text{NCS})_3$, respectively.

of betalain and antocyanines pigments for TiO_2 sensitization (Figure 4).

In general, the natural dyes tested so far suffer from low Voc (440–480 mV) which is at best 100 mV lower than an equivalent N 719 sensitized cell. This can be due to possible efficient electron/dye cation recombination pathways and to

the acidic dye adsorption environment. In fact, it is necessary an acidic environment to obtain a satisfactory dye coverage of the semiconductor surface and it is well known that H^+ are potential determining ions for TiO_2 causing a positive shift of the Fermi level of the TiO_2 and limiting the maximum photovoltage that can be delivered by the cells. Electron/dye

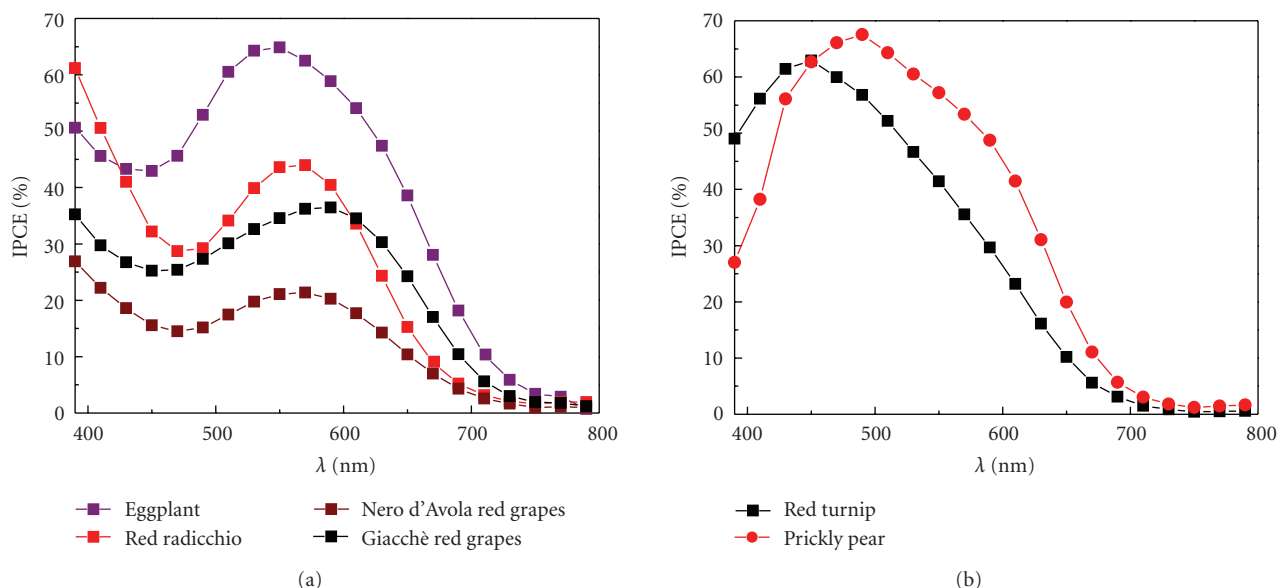


FIGURE 4: Photoaction spectra on transparent TiO_2 of (a) anthocyanine raw extracts from eggplant (purple), red radicchio (red), Giacchè red grapes (black), and Nero d'Avola red grapes (brown); (b) betalains from red turnip (black) and wild prickly pear (red). LiI/I_2 0.5 M/0.05 M in ACN was used as a redox electrolyte.

cation recombination can also be critical compared to ruthenium sensitizers, in which the hole is confined into a metal centred d orbital relatively decoupled from the semiconductor surface. Electron recapture by smaller flat organic molecules is expected to be faster, since the hole is probably located in closer proximity to the nanoparticle surface. Indeed the spectroscopic investigation of series of cyanine dyes showed electron/hole recombination lifetimes lower than 200 ns.

3. Electron Mediators Based on Coordination Compounds

So far the I_3^-/I^- couple has been the most efficient and commonly used redox mediator in DSSCs, due to the fast regeneration of the oxidized dye provided by I^- on a nanosecond time scale [33, 34] (Figure 5). The reduction of I_3^- is a complex multistep reaction involving the breaking of chemical bonds: some authors [35, 36] have studied it in great detail and suggested a first dissociation of I_3^- in I^- and I_2 , a subsequent reduction of I_2 to I_2^- followed by the rate limiting dismutation of two I_2^- to give I^- and I_3^- . The same authors suggested that the reduction of I_2 occurs only with adsorbed I_2 molecules and the overall process is further slowed down by its relatively low concentration compared to I_3^- in solution; moreover it is efficiently catalyzed by the presence of Pt at the counter electrode.

The electronic recapture involving I_3^- is kinetically so slow on both TiO_2 and FTO surfaces that, under short circuit conditions, most of electrons survive the transit through the mesoporous film and the FTO surface and appear in the external circuit. In summary, the forward electron donation by I^- is a facile mono-electronic process which

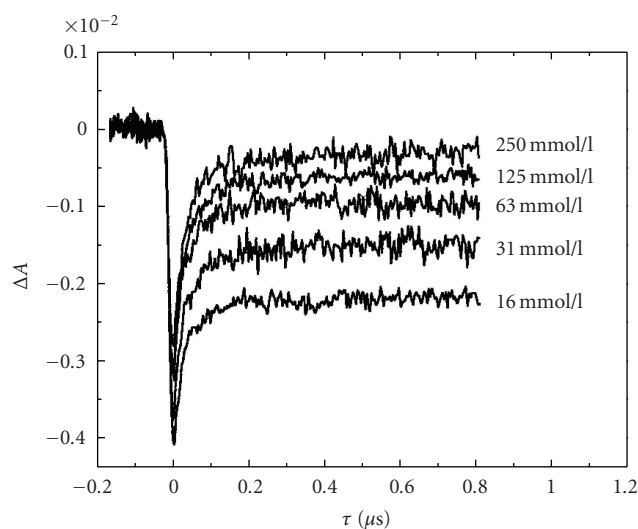


FIGURE 5: N3 recovery in presence of increasing concentration of NaI in acetonitrile.

ensures an efficient dye recovery (k_4 in Figure 1), while the reduction of I_3^- appears to be largely inefficient allowing for a minimization of the interfacial back recombination (k_6 in Figure 1).

In other respects the I_3^-/I^- redox couple is less than ideal for a number of reasons: I_2 in equilibrium with I_3^- is volatile, complicating long-term cell sealing; I_3^- is darkly colored and limits the light harvesting efficiency of the dye; DSSC cathodes require platinum coatings to effectively catalyze the I_3^- reduction. Most importantly, I_3^-/I^- is corrosive towards many highly conductive metals, posing a serious problem for the scaling up of the solar cells to large areas which

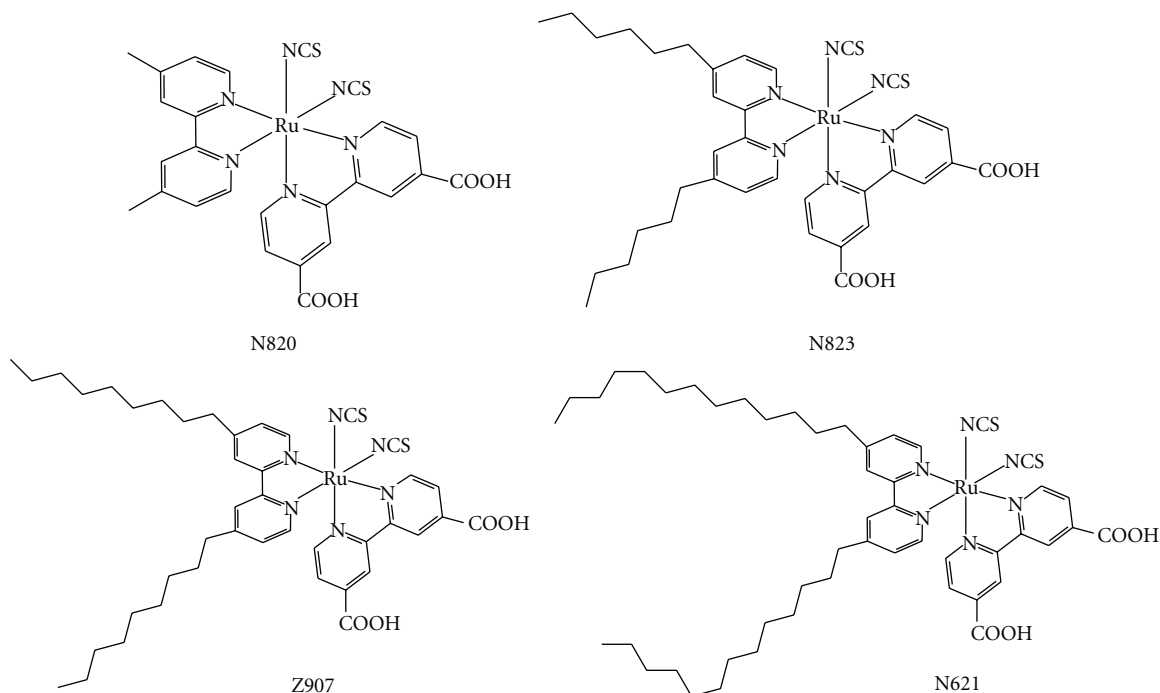


FIGURE 6: Heteroleptic dyes used in conjunction to cobalt electron transfer mediators.

requires the use of metallic grids deposited on FTO in order to minimize ohmic losses due to the high sheet resistance of the transparent conductive substrate. Besides these practical problems the search for new electron transfer mediators potentially capable of replacing the I_3^-/I^- couple is challenging for a number of reasons related to the strict requirements that must be fulfilled by an efficient electron mediator: it has to intercept efficiently the oxidized form of the dye, recombine slowly with photoinjected electrons on both TiO_2 and FTO substrates, and allow for an efficient mass transport in solution and into the TiO_2 mesopores. To our knowledge, there is no certain a priori indication that such requirements would be satisfied by a given chemical species on a specific substrate; however, in principle, every system characterized by a high reorganization energy associated to the electron transfer should exhibit a slow kinetics. In the following we report on the main attempts made to develop and improve new redox systems for DSSCs based on coordination compounds and on conductive polymers.

The electrochemical properties of coordination compounds can be tuned through a rational choice of the metal and an appropriate design of the coordination sphere. These features might guarantee the necessary flexibility to project an electron transfer mediator capable of meeting the kinetic requirements outlined above. In principle, to minimize recombination, kinetically slow couples have to be privileged. The relatively high concentration of electrolyte employed in photoelectrochemical cells (0.1–0.5 M in redox active species) demands for inexpensive and available metals, like the elements of the first transition row, and easily synthesizable ligands. To date, the most successful attempts have been based on octahedral cobalt(II) and tetrahedral copper(I) complexes. The Co(II)/(III) couple is usually

characterized by a high inner sphere reorganization energy associated to the electron transfer, essentially due to the involvement of a metal centred e_g redox orbital with antibonding characteristics.

One of the first reports by Graetzel and coworkers was focused on the use of a one-electron Co(II) redox mediator based on the Co(II)-bis-[2,6-bis(1'-butylbenzimidazol-2'-yl)pyridine] [37] (dbbip) complex. The Co(III)(dbbip) $_2^{3+}$ /Co(II)(dbbip) $_2^{2+}$ potential was of 0.36 V versus SCE, a value comparable with that of the I_3^-/I^- couple. Used in conjunction with a compact blocking TiO_2 underlayer, whose function is devoted to the minimization of the dark current (recombination with Co(III)), Co(dbbip) $_2$ appeared to rival the I_3^-/I^- performances in terms of IPCE and global cell efficiency. Encouraging was also the weak coloration of the complex which exhibited a moderate absorption in the visible region with an extinction coefficient of the order of $10^2 \text{ mol}^{-1} \text{ cm}^{-1}$ at 450 nm. The best results with this type of cobalt mediators were obtained using heteroleptic complexes like Z907 and N 621 bearing long alkyl chains (Figure 6).

The use of heteroleptic dyes [38, 39] brings two main advantages: reduction of the ion pairing effect due to a smaller negative ζ potential and suppression of the electron tunnelling to Co(III) acceptors caused by the steric hindrance of the long alkyl chains, which limit the access of the cobalt complex to the exposed TiO_2 surface, thus reducing the probability of electron recapture as evident from the cell dark current measurements. For similar reasons the cografting of long alkyl chain carboxylic acids like hexadecylmalonic acid allowed for an enhancement of the photovoltaic response of cobalt-mediated cells [39]. One of the limitations of Co(II) benzimidazol complexes is related to the multistep synthetic procedure for the ligand preparation.

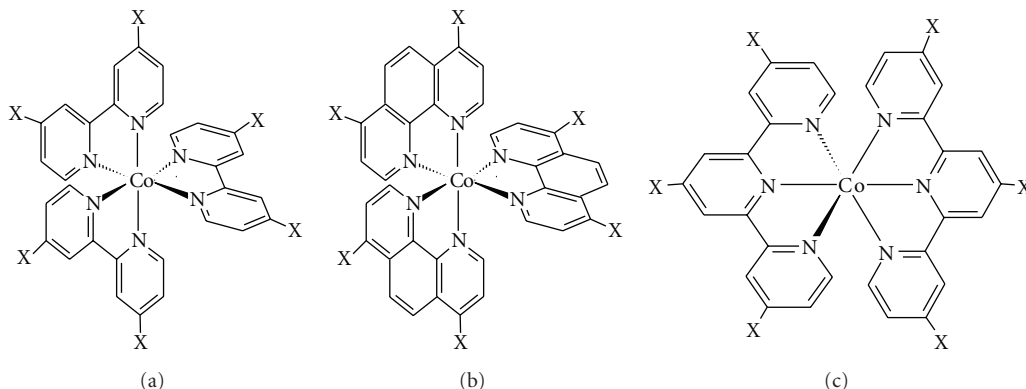


FIGURE 7: Structure of polypyridilic Co(II) complexes: (a) X = Tert-butyl (DTB), Methyl (DMB), H (bpy). (b) X = H (phen). (c) X = Tert-butyl (tTbterpy), Ethyl (tEterpy).

Almost contemporarily to the efforts made at the Swiss Federal Institute of Technology of Lausanne, it was found that particular cobalt polypyridine complexes, formed from structurally simple ligands, did function as efficient electron-transfer mediators in DSSCs [40].

The main focus of the investigation was thus to identify which structural and thermodynamic motifs generate the best mediators, allowing for the assembly of cells with the closest match to the performance of the I_3^-/I^- mediator.

The cobalt complexes reported in Figure 7 can be easily produced by mixing 1 equivalent of $[Co(H_2O)_6]^{2+}$ with 3 equivalents of a bidentate ligand or 2 equivalents of a tridentate ligand under magnetic stirring in refluxing methanol for 2 hours. Addition of ethyl ether results in the precipitation and isolation of the product which is then usually used without any further purification.

All of the complexes under consideration exhibit similar UV-Vis absorption spectra characterized by a weak absorption band centred at ca. 440–450 nm and a ligand-based $\pi-\pi^*$ transition above 350–380 nm.

The most intense visible absorption is for $Co(tTbterpy)_3^{2+}$ with $\epsilon_{450} = 1.4 \times 10^3 \text{ M}^{-1} \text{ cm}^{-1}$ while the other complexes exhibit $\epsilon_{440-450}$ values that are approximately an order of magnitude smaller. For the sake of comparison, the $\epsilon_{440-450}$ value for I_3^- is ca. $2 \times 10^3 \text{ M}^{-1} \text{ cm}^{-1}$; therefore, except $Co(tTbterpy)_3^{2+}$ that has a comparable absorbance, considerably less visible light is absorbed by all of the remaining cobalt complexes at similar concentrations.

Electrochemical characterization of these complexes revealed an unexpected electrode material dependence to the electron-transfer kinetics. In the case of 4-4' substituted polypyridine Co(II) complexes, gold electrodes exhibit the most reversible and ideally shaped CVs. Glassy carbon and platinum electrodes also produce quasireversible voltammograms, although less reversible than gold. In general, the shapes of the quasireversible waves indicate that, in cases where the heterogeneous electron transfer is slow, the transfer coefficient, α , is considerably greater than 0.5. In other words, for equivalent overpotentials the heterogeneous reduction of the Co(III) complex is considerably faster than the corresponding oxidation of the Co(II) species. The

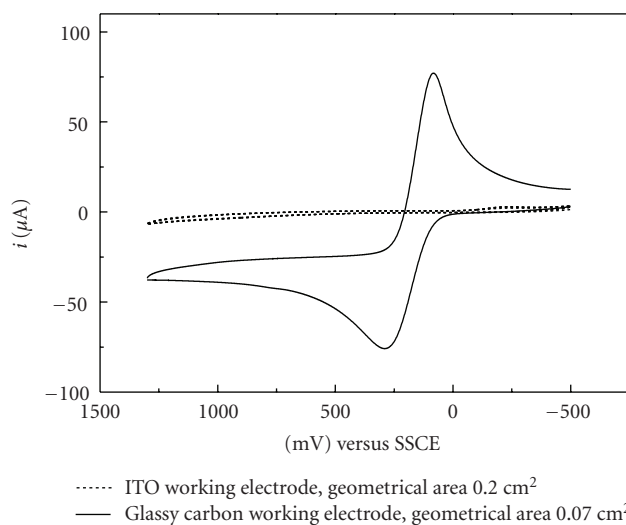


FIGURE 8: Cyclic voltammetry of approximately $1 \times 10^{-3} \text{ M}$ $Co(DTB)_3^{2+}$ recorded in ACN/TBAPF₆ 0.1 M on GC (solid line) and on ITO (dotted line).

voltammetric results also suggest that while platinum is the cathode of choice for the I_3^-/I^- redox mediator, it should *not* be the optimal choice for cobalt complex-based mediators. Likewise, while carbon has long been considered a poor cathode for I_3^-/I^- , it should be acceptable for any of the cobalt systems considered here. It should be considered that only very recently significant results concerning alternative high-performance counter electrodes for the I_3^-/I^- couple, based on particular carbonaceous materials (nanotubes, graphene, carbon black), have been reported [41–44]. It must be noted that, among the series of Figure 7, one of the most promising cobalt complexes ($Co(DTB)_3^{2+}$) is nearly *electrochemically inactive* on FTO and ITO electrodes (Figure 8), meaning that the unwanted Co(III) to Co(II) reduction at the photoanode requires high overpotentials to be effective.

The dramatic dependence of the $Co(DTB)_3^{2+/3+}$ heterogeneous electron transfer rate on the chemical nature of the electrode surface is most probably consequence of specific

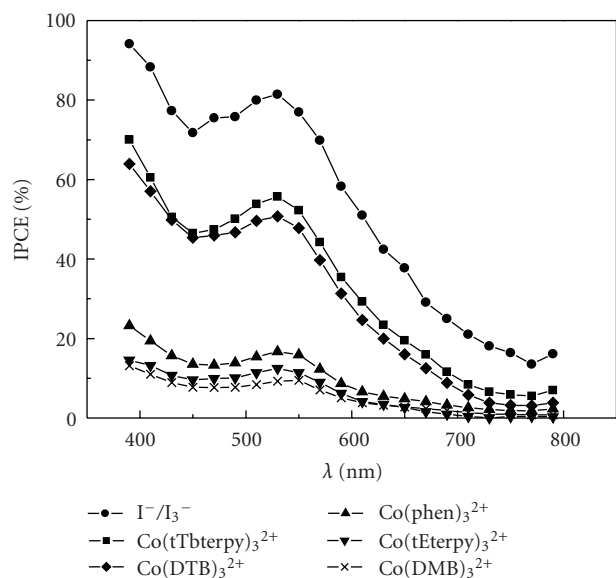


FIGURE 9: Photoaction spectra of N3 bound to nanocrystalline TiO₂ films in the presence of different electron mediators in MPN solutions: 0.25 M LiI/25 mM I₂ (circles), 0.25 M Co(tTBterpy)₂²⁺/25 mM NOBF₄ (squares), 0.25 M Co(DTB)₃²⁺/25 mM NOBF₄ (diamonds), 0.25 M Co(phen)₃²⁺/25 mM NOBF₄ (triangles), 0.25 M Co(tEterpy)₂²⁺/25 mM NOBF₄ (upside down triangles), and saturated (<0.15 M) Co(DMB)₃²⁺/25 mM NOBF₄ (crosses). 0.25 M LiClO₄ was added to all solutions containing a cobalt mediator.

interactions between the surface and the electroactive species which modify the electronic coupling and/or the activation barrier for the heterogeneous electron-transfer reaction. The electrochemical behaviour on metal oxide surfaces is in this case similar to that of the I₃⁻/I⁻ couple for which the electron transfer from the FTO substrate to I₃⁻ is a very slow multistep process [45].

The performances of the photoelectrochemical cells are strongly dependent on the composition of the electrolyte solution (Figure 9).

A maximum conversion efficiency of ca. 80%, in correspondence to the metal-to-ligand charge transfer absorption maximum of N3, was obtained in the presence of 0.25 M LiI/0.025 M I₂, whereas, with the cobalt based mediators, the best performances (IPCE ca. 50%–55%) were observed when solutions of Co(DTB)₃^{2+/3+} and Co(tTBterpy)₂^{2+/3+} were used. Co(phen)₃^{2+/3+}, Co(tEterpy)₂^{2+/3+} and Co(DMB)₃^{2+/3+} mediators exhibited much lower conversions, with maximum IPCE values in the range of 10%–20%.

Generally, cobalt complexes of unsubstituted and methylsubstituted bipyridine or terpyridine ligands are poor electron transfer mediators in the type of DSSCs considered herein. In contrast, if the ligand contains a tertiary butyl substituent in the para position, the resulting cobalt-based cells yield quite good IPCE. The observed substituent effect cannot be related to an electronic perturbation of the Co(II) redox orbitals and to a consequent modification of the electrochemical properties of the coordination compound, since the electron-donating effect of all simple alkyl

substituents (e.g., methyl, ethyl, *tert*-butyl, etc.) is essentially the same [46] and all of the complexes of a given ligand-type (i.e., bipyridine, phenanthroline, or terpyridine) were expected and found to have very similar $E_{1/2}$ (100–200 mV versus SCE) values for the relevant Co(II/III) couple.

Nanosecond transient absorption experiments allowed for the rationalization of the lower efficiency of the Co-based couples with respect to I₃⁻/I⁻ and for the clarification of their structure-dependent performance. Figure 10(a) shows the decay of the photogenerated N3 dye cation, observed at 480 nm in the presence of Co(DTB)₃²⁺ 0.1 M and TBAI 0.1 M: in both cases a $\tau_{2/3}$ of about 0.35 μ s indicates that dye regeneration by I⁻ and by Co(II) occurs at a very similar rate.

Upon Li⁺ addition (Figure 10(b)) an increased reduction rate by iodide is observed ($\tau_{2/3}$ = 0.12 μ s), whereas regeneration of the oxidized dye by Co(II) is substantially unchanged. Indeed, TiO₂ surface adsorption/intercalation by Li⁺ creates a positive polarization which attracts a surface excess of iodide in close proximity of the dye sites, allowing for a faster interception of the oxidized sensitizer. The same effect is obviously absent in the case of positively charged Co(II) complexes which do not experience any attraction with a positively polarized photoelectrode.

Recombination of injected electrons with the oxidized mediator could be particularly serious in the case of Co(II)/(III) electron transfer mediators in which the outer sphere mono-electronic Co(III) reduction at the photoanode could be considerably more efficient than the multistep I₃⁻ reduction.

The process can be probed by means of transient spectroscopy following the time evolution of dye-cation bleaching. Reduction of the oxidized mediator by photo-injected electrons results in a slowing down of dye absorption recovery.

From Figure 11(a) it is evident that I₃⁻ gives rise to the smallest increase in $\tau_{2/3}$ of the oxidized sensitizer, meaning that the CB electron interception has the lowest efficiency within the series of mediators explored so far. On the other hand Co(III) complexes produce a consistent increase in the recovery time of N3⁺ (Figures 10(a) and 10(b)), showing that the back electron transfer from TiO₂ (or from the exposed SnO₂ back contact) is more efficient than in the case of I₃⁻. It is also evident that Co(bpy)₃³⁺ is by far more effective than Co(DTB)₃³⁺ in recombining with photo-injected electrons. This behaviour is a convincing evidence that Co(II)/(III) mediators need bulky substituents to minimize the undesired recombination with CB electrons. On the other hand, ligand-mediated recombination can be safely excluded, since their reduction potential is generally too negative (about -1 V versus SCE) to be accessible for TiO₂ conduction band electrons.

In the effort of improving the performance of such mediators the possibility of using kinetically fast couples in conjunction with the best Co(II) mediators has been explored [47].

Kinetically fast couples efficiently reduce the oxidized dye, but due to the fast recombination with injected electrons, are totally unsuccessful as mediators in DSSCs. However, when mixed with an excess of cobalt mediator, if

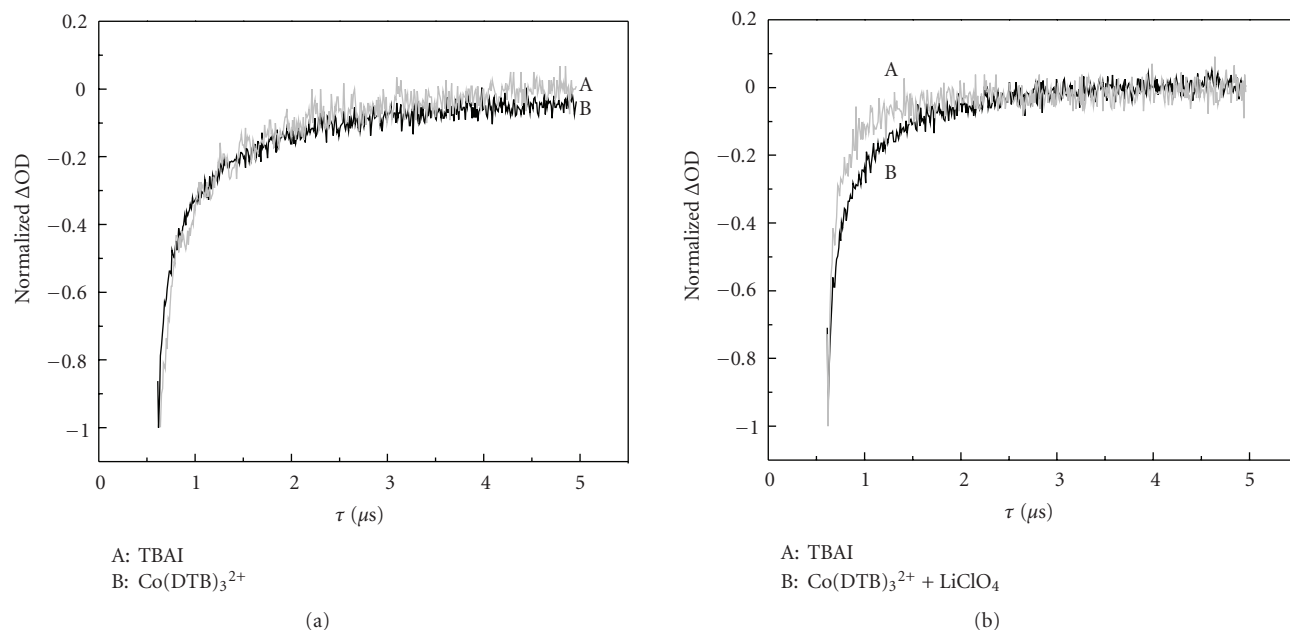


FIGURE 10: 480 nm $\text{Ru(III)(H}_2\text{DCB)}_2(\text{NCS})_2^+$ recovery in the presence of (a) Tetrabutyl-ammonium iodide (A) and Co(DTB)_3^{2+} (B) 0.1 M; (b) Tetrabutyl-ammonium iodide (A) and Co(DTB)_3^{2+} (B) 0.1 M + LiClO_4 0.1 M. Pulse energy $\approx 1 \text{ mJ/cm}^2$.

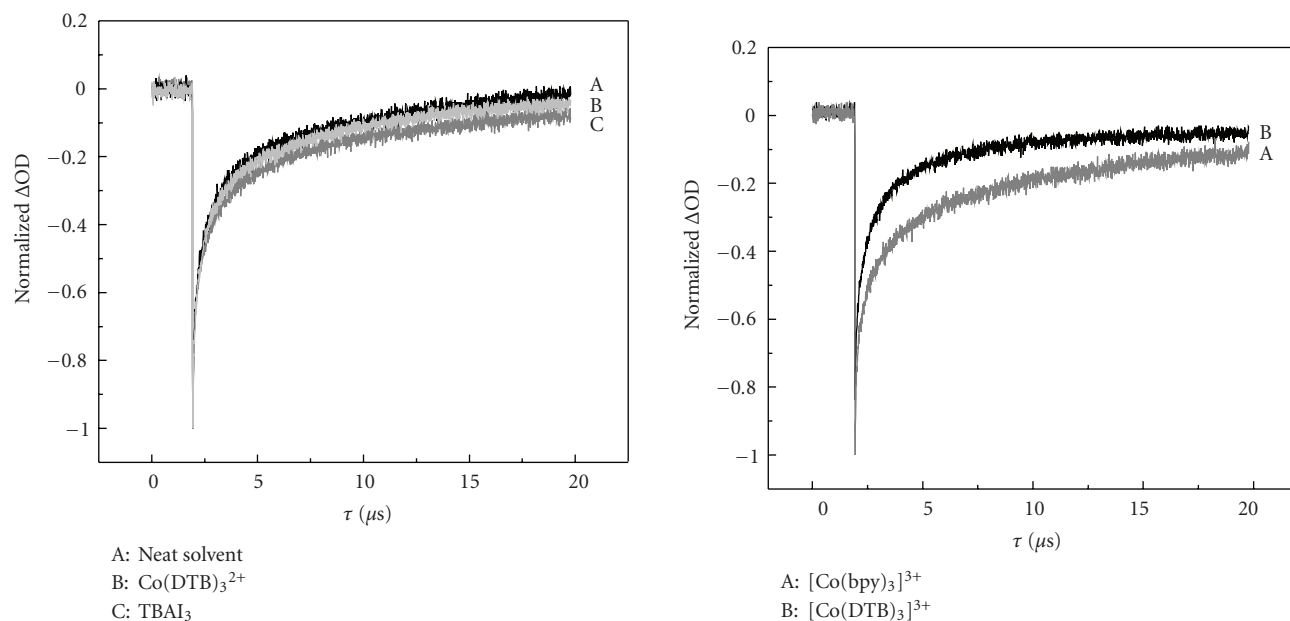


FIGURE 11: 480 nm $\text{Ru(III)(H}_2\text{DCB)}_2(\text{NCS})_2^+$ recovery in the presence of (a) neat solvent (γ butyrolactone) (A), 0.1 M Co(DTB)_3^{3+} (C), and Tetrabutyl-ammonium triiodide (B); (b) Co(DTB)_3^{3+} (B) and Co(bpy)_3^{3+} (A). Pulse energy $\approx 1 \text{ mJ/cm}^2$.

their redox potential is appropriate (i.e., more positive than the Co(III)/(II) couple), a cascade of electron transfer events allows to confine the hole on Co(III) (Figure 12) which, by virtue of its very slow heterogeneous electron transfer on semiconductor oxides, gives rise to a very inefficient electron recapture. As a consequence, the large majority of Co(III) created in the second electron transfer step is free to diffuse to the counter electrode of the cell, whereupon it is reduced.

The use of a long alkyl chain dyes like Z907, for example, is beneficial to the system allowing to further reduce back recombination enhancing the electron collection efficiency.

Phenothiazine (PTZ) and ferrocene (Fc), both having a small reorganization energy associated to the electron transfer, are the first comediators that have been considered. Each has a potential which falls between that of the $\text{Co(DTB)}_3^{3+/2+}$ (0.22 V versus SCE) and of the

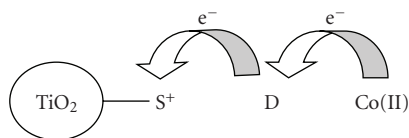


FIGURE 12: Sequence of electron transfer events involving the oxidized dye (S^+) the mediator (D) and the cobalt complex (Co(II)).

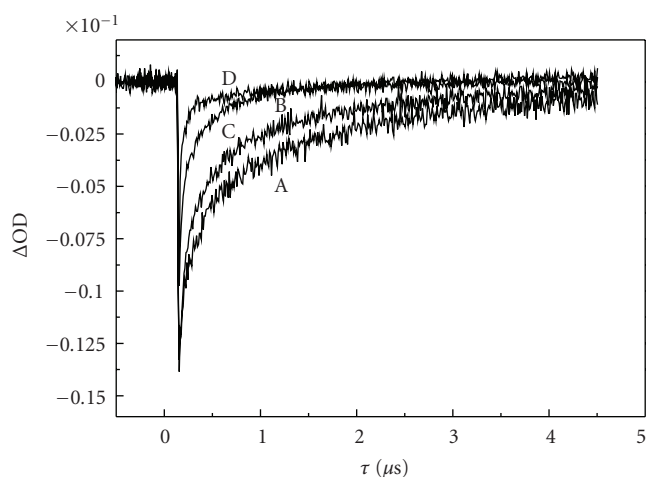


FIGURE 13: Decay kinetic of photooxidized Z907 adsorbed on TiO_2 in the presence of various electron mediators: (A) no mediator; (B) 0.1 M $Co(DTB)_3^{2+}$; (C) 0.1 M PTZ; (D) 0.1 M Fc. Differential absorbance changes are measured at 480 nm. Pulse energy: 5 mJ/cm².

dye $[Ru(H_2DCB)(dnbpy)(NCS)_2]^{+0}$ (0.75 V versus SCE). Because of the facile electron transfer the photooxidized dye would be predominantly reduced by the mediator. Its oxidized form (PTZ^+ and Fc^+) can be then rapidly intercepted by Co(II), preventing the direct charge recombination between the oxidized mediator and the electrons in the TiO_2 . Nanosecond transient absorption measurements confirmed a faster dye regeneration by both PTZ and Fc relative to $Co(DTB)_3^{2+}$, despite their higher redox potential (Figure 13).

The best results were observed using a mediator/Co(II) ratio of 1 : 2 with 0.15 M $Co(DTB)_3^{2+}$ in acetonitrile. Addition of 0.5 M Li^+ and 0.1 M *tert*-butyl-pyridine generally improved the open circuit photovoltage. In the presence of the PTZ/Co(II) mixture cell IPCE% reached more than 80% (Figure 14(b)), a value well comparable to the best I_3^-/I^- cells. Under white light irradiation J_{sc} was also comparable, with the advantage of a better fill factor and higher V_{oc} for the cobalt-based cell (Figure 14(a)).

In general the Fc/Co(II) mixture gave poorer overall photovoltaic performances than the equivalent PTZ/Co(II) system, notably a poorer V_{oc} and fill factor. Since ferrocene was found to be faster in dye regeneration, an explanation can lie in a less efficient interception of Fc^+ by Co(II) centres,

resulting in a larger steady state concentration of Fe(III) which undergoes recombination on the TiO_2 surface. Indeed, chronocoulometry and cyclic voltammetry experiments at FTO electrodes allowed to verify that PTZ^+ was from 1.5 to 2 times more effective than Fc^+ in the oxidation of Co(II), thus having a smaller probability of recombining with photoinjected electrons.

An analogous behaviour extends to other species having small reorganization energies and appropriate potentials such as the iron(II) complexes $Fe(DMB)_3^{2+}$ and $Fe(DTB)_3^{2+}$ ($E_{1/2} \approx 0.95$ V versus SCE). When used in the presence of an excess of $Co(DTB)_3^{2+}$ and in conjunction with suitable sensitizers like the heteroleptic dye $Ru(dnbpy)(H_2DCB)_2^{2+}$ ($E_{1/2} = 1.25$ V versus SCE) (Figure 15) the Fe(II) mediators clearly enhance the performance of the $Co(DTB)_3^{2+}$ and outperform the I_3^-/I^- redox couple, at least in terms of IPCE, with maximum values close to 85%.

Interestingly, the polypyridine Fe(II)/Co(II) mediator mixtures were rather insensitive to variations of the Fe(II) to Co(II) concentration ratio ranging from 0.1 to 0.5, with the optimum at 0.1. For higher Fe(II)/Co(II) ratios the cell performance dropped, ostensibly due to the formation of an excess of Fe(III) which was no longer effectively intercepted by Co(II) and recombined on the TiO_2 surface. In the case of electron mediator mixtures characterized by the presence of a kinetically fast couple, the decrease in ζ potential and the blocking effect obtained by using heteroleptic dyes with hindering chains is more than ever important for controlling electron recapture: meaningfully, the performances of the Fe(II)/Co(II) mixtures used in conjunction with the homoleptic $Ru(H_2DCB)_3^{2+}$ (where DCB is the 4,4'-dicarboxylic acid 2,2'-bipyridine) were rather poor, not exceeding a maximum IPCE% of 30%, whereas the I_3^-/I^- couple produced almost identical conversions (ca. 40%) to those reported with the heteroleptic $Ru(dnbpy)(H_2DCB)_2^{2+}$.

The Fe(II)/Co(II) mediators displayed an interesting behaviour in conjunction with bisterpyridine complexes (formula in Figure 16) which, when used with the I^-/I_2 couple, have been known to be rather poor sensitizers. The IPCE% improved from the 20% obtained in the presence of LiI/I_2 to 30% with $Co(DTB)_3^{2+}$ alone, to more than 60% using the $Fe(DMB)_3^{2+}/Co(DTB)_3^{2+}$ system (Figure 16).

Spectroscopic investigation evidenced that this enhanced performance could not be explained by an improved dye regeneration by the cobalt-based mediators: despite giving rise to an efficient dye recovery (14 ns and 9 ns for the Co(II) and the Fe(II)/Co(II) mixture, resp.) these metal-based mediators were still slower than iodide, which produced an instrument response-limited (≤ 7 ns) Ru(II) regeneration. Further investigations indicated, however, that the oxidized form of the iodide-based mediator, namely, triiodide, was consistently more effective than Co(III) in capturing conduction band electrons, producing a notable increase in the Ru(III) lifetime (Figure 17).

Thus the relatively low IPCE% observed with I_3^-/I^- appeared to be essentially determined by an efficient electron recombination with triiodide. This phenomenon, surprising at first, could be caused by a number of factors ranging

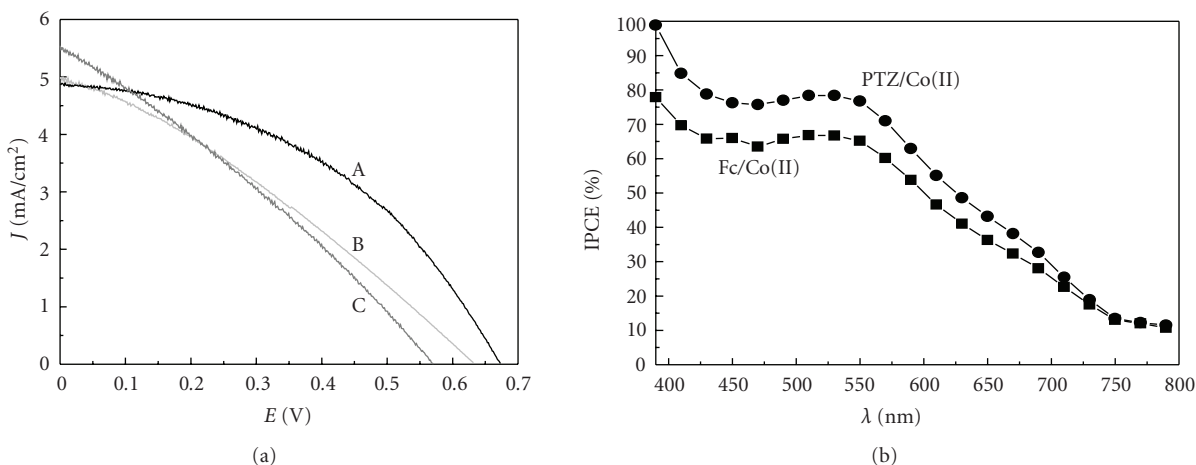


FIGURE 14: (a) J-V curves obtained in the presence of Co(II)/PTZ (A), I₃⁻/I⁻ (B), and Co(II)/Fc (C) in methoxypropionitrile. (b) Photoaction spectra. Incident irradiance ≈ 0.1 W/cm².

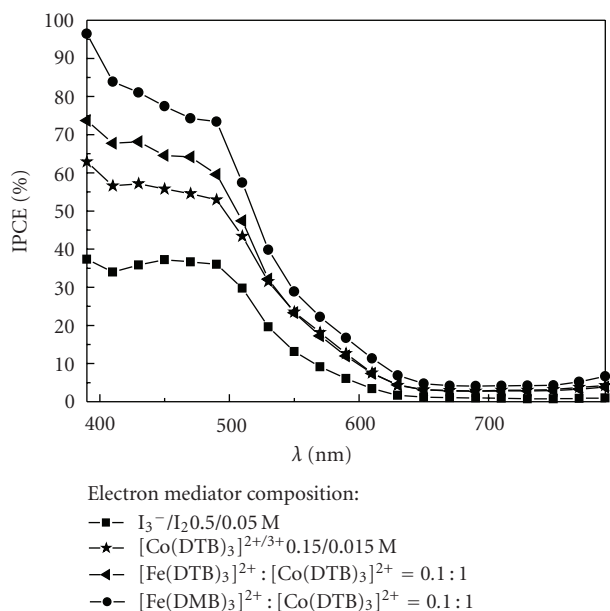
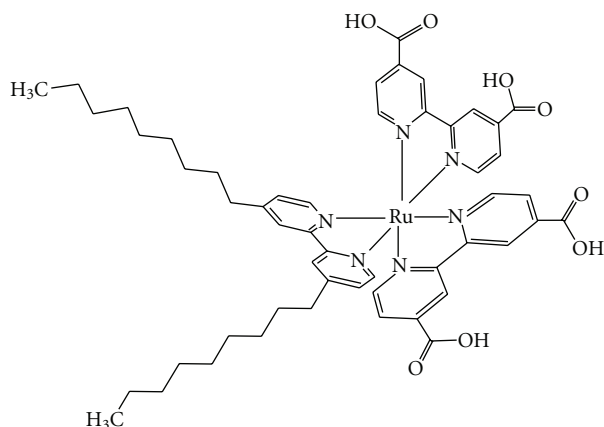


FIGURE 15: IPCE spectra of Ru(dnbpy)₂²⁺ obtained in the presence different electron transfer mediators.



from an insufficient TiO₂ surface passivation by the dye against the small I₃⁻ ions, to specific interactions between the complex and I₃⁻ which lead to iodine association via the sulphur atom of the thiophene ring and to the induction of a positive surface charge upon adsorption of the cationic Ru(II) dye possessing only one carboxylic function. The positively charged surface might attract I₃⁻ favouring recombination and, on the contrary, might repel Co(III), ultimately reducing the probability of electron recapture in the latter case. Thus it seems that, depending on their structure and charge, each dye interacts specifically with different electron mediators in ways that are worth to be studied, since they may lead to both fundamental and practical advances in DSSC design in the future.

4. Solid State Conductive Polymers

Conductive polymers based on polythiophenes and polypyrroles could be interesting candidates for replacing the liquid electrolyte in DSSC, due to their low cost, thermal stability, and good conductivity [48]. Thanks to these properties, these systems have already found application in the OLED technology as charge transporting matrices. PEDOP (poly-ethylene-dioxy-pyrrole) can be deposited on a sensitized TiO₂ photoanode via a photoassisted electropolymerization [49] initiated by the purpose built ruthenium complex [Ru(H₂DCB)(pyrr-bpy)₂]²⁺ [50] (Figure 18): the oxidized dye, [Ru^{III}(H₂DCB)(pyrr-bpy)₂]³⁺, created after the charge injection into TiO₂, is a sufficiently

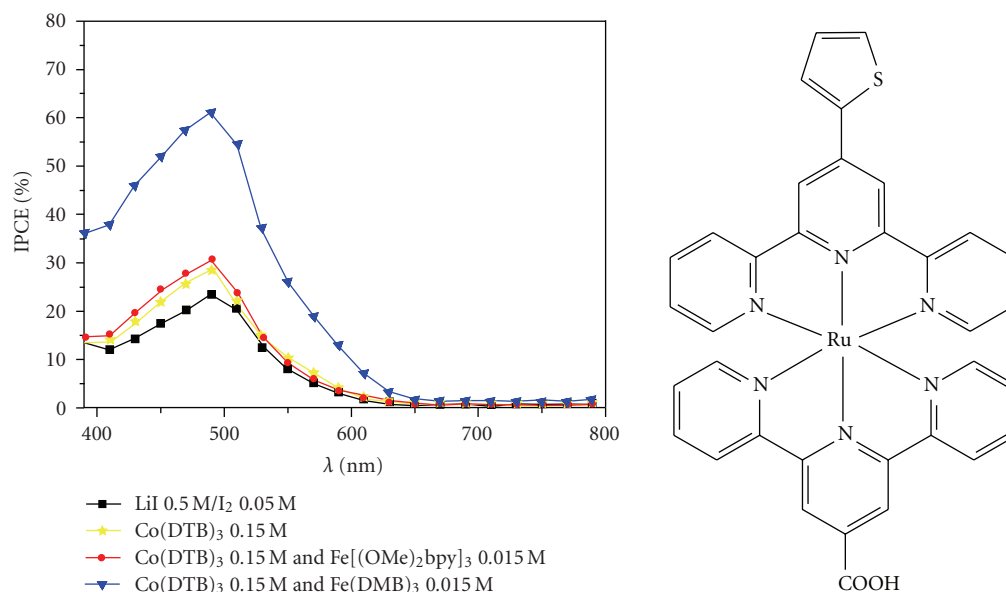


FIGURE 16: IPCE spectra in the presence of various electron mediators obtained by using the $[\text{Ru}(\text{II})(\text{terpy})(\text{Thtperty})]^{2+}$ dye as a TiO_2 photosensitizer. Thtperty stands for the 4'-thiophene terpyridine.

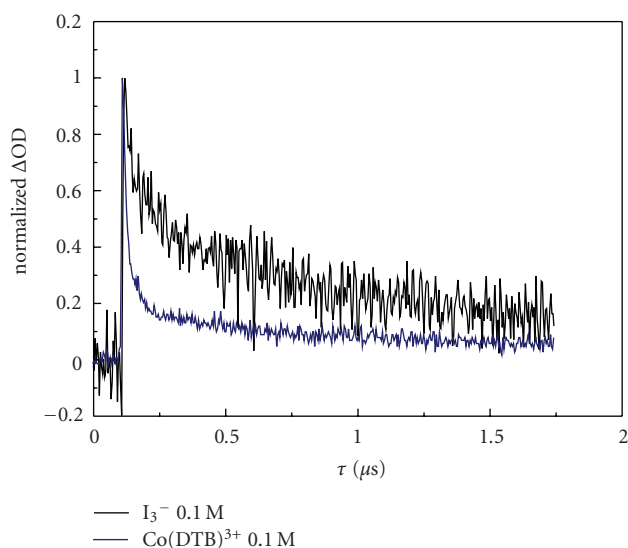


FIGURE 17: Differential absorption decays for $\text{Ru}(\text{III})$ recovery observed at 750 nm in the presence of equimolar amounts of I_3^- and $\text{Co}(\text{III})$ in acetonitrile +0.5 M Li^+ . Excitation energy density $\approx 1 \text{ mJ}/\text{cm}^2/\text{pulse}$.

strong oxidizer, with a potential of 1.19 V/SCE, to oxidize EDOP monomers and induce their cationic polymerization, leading to the growth of polymeric chains chemically attached to the dye with a possible advantage in terms of electronic coupling and charge transfer rate between electron donor (PEDOP) and acceptor (oxidized dye).

A typical solar cell assembled according to this approach is comprised of a photoanode, functionalized with PEDOP, firmly clamped together with a gold-coated FTO counter

electrode. A 0.3 M LiClO_4 solution in γ -butyrolactone is eventually drawn inside the cell by capillarity.

Our results on these types of cells showed very low efficiencies mostly due to small J_{sc} ($< 200 \mu\text{A}$) and poor fill factors (≤ 0.31). The J-V characteristics of solid state PEDOP cells (Figure 19) indicate a strong recombination and a high serial resistance.

Dark current measurements performed under direct voltage bias showed a marked increase in recombination efficiency as the bias approached -0.4 V , near the onset of PEDOP reduction, suggesting that higher lying states of TiO_2 were filled promoting recombination with PEDOP holes.

While the dark current suggested a possible photocurrent loss mechanism through PEDOP reduction, a relevant recombination with the oxidized dye could not be ruled out. Dark current simply could not provide information on the latter process since, in the dark, after equilibrium was attained, no oxidized $\text{Ru}(\text{III})$ centres should be present at the $\text{TiO}_2/\text{Dye}/\text{polymer}$ interface.

Indications of efficient recombination were also gained from cell photocurrent transients under short circuit conditions, showing cathodic spikes due to recombination of photoinjected electrons with PEDOP holes and oxidized $\text{Ru}(\text{III})$ centres.

The cathodic current dropped to zero on a very short time scale suggesting that recombination was kinetically fast, at least for the time scale (0.1 s sampling time) of the experiment. Passivation of the TiO_2 surface via the application of a nanometric insulating Al_2O_3 overlayer [51] was instrumental in reducing the electronic recapture, allowing for an IPCE% doubling (from 3% to 6%) (Figure 20). Cell J_{sc} and V_{oc} measured under $0.05 \text{ W}/\text{cm}^2$ white light irradiation were also significantly improved (from 50 to $100 \mu\text{A}/\text{cm}^2$ and from 0.4 to 0.7 V, resp.).

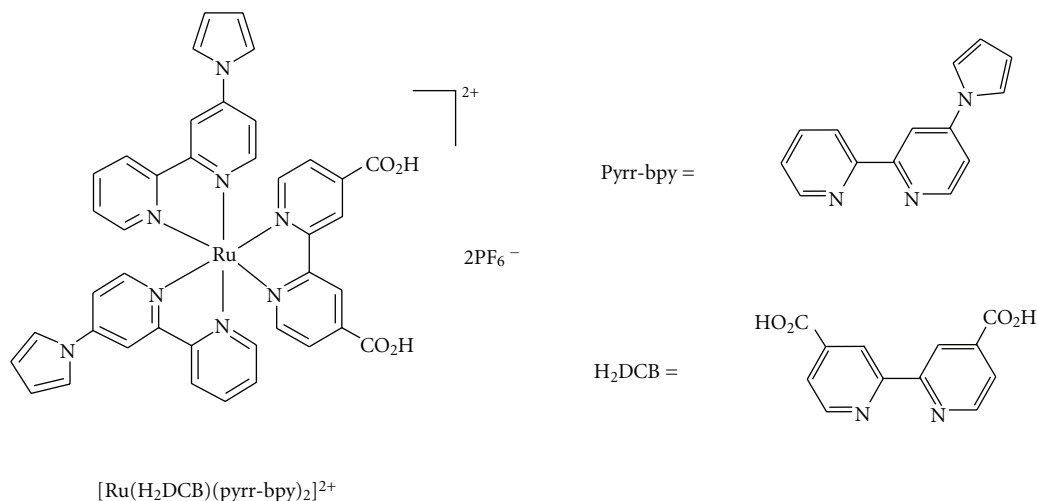
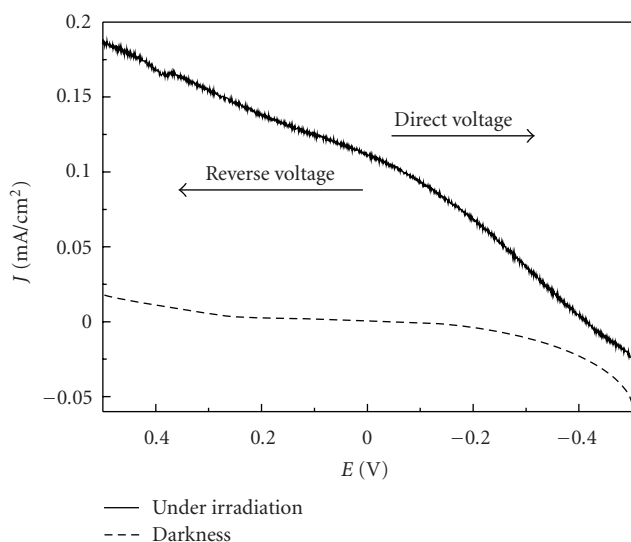
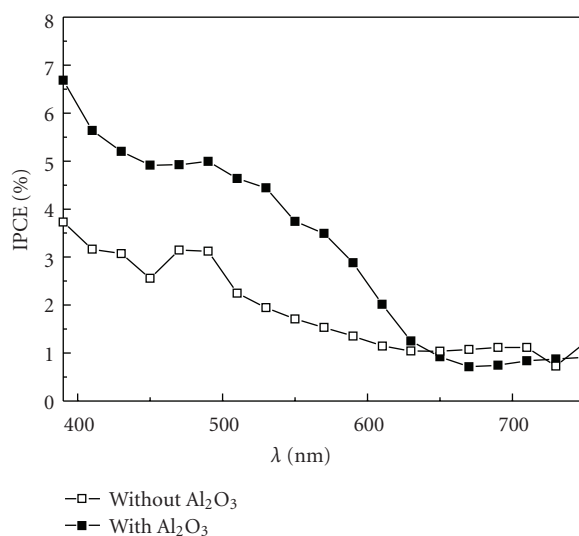


FIGURE 18: Ru(II) complex uses for in situ photoassisted PEDOP growth.

FIGURE 19: J-V characteristic obtained on PEDOP-based DSSC in the presence of Li^+ 0.3 M. 10 seconds polymerization time.FIGURE 20: Photoaction spectra of a $\text{TiO}_2/\text{Dye}/\text{PEDOP}/\text{Au}$ cell (white squares) compared to a $\text{TiO}_2/\text{Al}_2\text{O}_3/\text{Dye}/\text{PEDOP}/\text{Au}$ system (black squares).

Besides strong back recombination and despite the intimate contact between the dye and the hole transporting layer, the low efficiencies could also be explained by a nonoptimal hole injection into the PEDOP matrix, as evidenced by the slow oxidized dye recovery observed in transient absorbance experiments at 450 nm.

A better photovoltaic response has been recently obtained by using the excellent properties of PEDOT as a hole transporting material. As previously described, PEDOT can be in situ photo-electropolymerized from bis-EDOT monomers by exploiting the oxidizing power of a dye like Z907 [52]. The hydrophobic properties of Z907 allow for a good affinity for the scarcely polar polymeric matrix, ensuring a good electrical contact between the p-type material and the dye. The presence of

a coadsorbate like deoxycholic acid (DCA) in an optimal 2:1 ratio with respect to the dye enhanced the global photovoltaic response by reducing dye aggregates. This function seems to be particularly relevant for polymer mediated DSSC, since aggregated dye clusters reduce the number of available polymer growth sites and leave less effective space for polymerization initiation and propagation. In order to optimize the contact between the hole transporting layer and the counter electrode, a PEDOT-functionalized FTO was used as the cathode and, to achieve optimal performances, a drop of BMImTFSI (1-butyl-3-methylimidazolium bis(trifluoromethanesulfonyl)imide) containing 0.2 M LiTFSI and 0.2 M Tbpv was cast onto the $\text{TiO}_2/\text{dye}/\text{PEDOP}$ junction. The ionic liquid may improve the charge transporting capabilities of the heterointerface

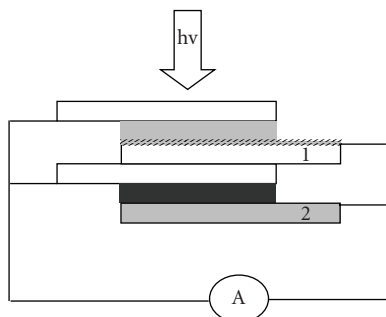


FIGURE 21: In parallel connected stacked cell based on the Co(II)/(III) couple. 1 is a transparent FTO cathode modified via chemisorption of an electroactive molecule. 2 is a conventional gold cathode. The red and the blue dyes, absorbing in complementary spectral regions, result in a panchromatic sensitization.

through screening of space charge effects, lithium cations assist electron injection and percolation through the n-type semiconductor, and, as usual, tppy increases the open circuit photovoltage via suppression of the back recombination. With such a treatment FTO/TiO₂/dye/PEDOT-PEDOT/FTO sandwich cells afforded efficiencies of the order of 2.6%, one of the highest results so far recorded with solid state DSSCs based on hole conducting polymers.

5. Catalytic Materials for Cathodes of DSSCs

A kinetically fast reduction of the oxidized redox mediator at the cathodic surface of the cell is required to maintain a sufficiently high concentration of electron donor thus ensuring an efficient dye regeneration. With the I₃⁻/I⁻ couple the use of a catalytic platinum coating is almost mandatory to achieve a satisfactory electrochemical kinetics, but the use of redox mediators alternative to the I₃⁻/I⁻ couple opens the way to the search for new, less expensive, more flexible, and available catalytic materials and to their application in new cell configurations. Many electrode materials (carbon, gold, platinum) function adequately in the case of Co(II)/(III) mediators but are generally opaque. In contrast, optically transparent conductive oxides (TCOs) are very poor cathodes for the Co(DTB)₃^{2+/3+} couple, unless they are chemically modified by surface chemisorption of certain metal complexes. This allows to obtain optically transparent cathodes with a good electrochemical response which can be employed to build stacked cells either serially or in parallel (Figure 21) connected in which, for example, two spectrally complementary dye can work in their optimal absorption region, improving the spectral responsivity of the modules.

In a first study [53] it was demonstrated that ITO and FTO electrodes modified by irreversibly adsorbing a monolayer of Fe(H₂DCB)₃²⁺ electrocatalyze efficiently the Co(DTB)₃²⁺ oxidation via an EC' mechanism. However, while electrogenerated Fe(III) has an ample driving force for oxidizing Co(II), Fe(II) is a thermodynamically too weak reductant for catalyzing Co(III) reduction, and the

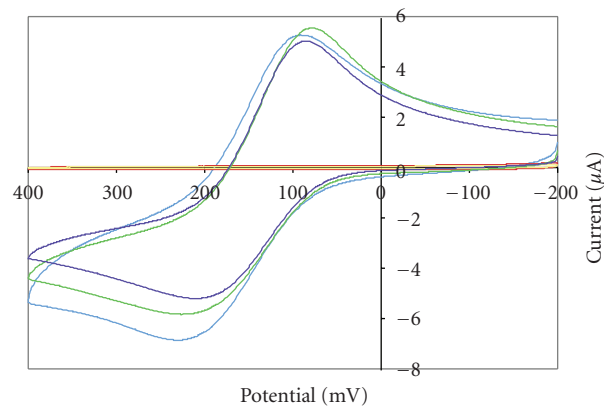


FIGURE 22: CV on gold (A), FTO (B), ITO (C), and osmium modified FTO (D) and ITO (E) working electrodes in the presence of ca. 0.1 mM Co(DTB)₃ClO₄. Potential referred to ferrocene.

Fe(II)/(III) couple is of no value for building transparent cathodes.

Nevertheless it was found that the electrocatalysis of the Co(II)/(III) redox chemistry promoted by surface bound electroactive species is a relatively general phenomenon and a number of molecular species with appropriate potential can promote the desired catalytic effect. For example, the osmium complex Os(H₂DCB)₂Cl₂ can be strongly adsorbed on FTO and, with its potential (-310 mV versus Ferrocene) slightly negative of the Co(II)/(III) couple, proved to efficiently catalyze both the oxidation and reduction of Co(DTB)₃^{2+/3+}. Indeed, the cyclic voltammetry of Co(II)/(III) (Figure 22) recorded at osmium-modified electrodes showed well-defined quasireversible waves ($\Delta E_p \approx 140$ mV), nearly identical to those obtained on gold, whereas on the unmodified FTO or ITO it was almost impossible to observe the analogous charge transfer process. Cyclic voltammetry results were substantially confirmed by thin layer photoelectrochemical experiments which demonstrated that the osmium-modified transparent cathodes gave rise to a very small overpotential (ca. 12 mV under cell short circuit conditions) for Co(III) reduction, indicative of a facile heterogeneous electron transfer [54].

The stacked cell configuration, employing N3 and a red absorbing cyanine dye which absorbs photons in a region where N3 does not, showed a J_{sc} improvement of about 15% over a single N3 cell. It must be considered that the blue dye is relatively inefficient, generating very modest IPCE% (ca. 5%–8%) due to less than ideal redox properties and electronic coupling with the TiO₂. Nevertheless the results confirmed the principle and with a better performing dye substantial performance improvements are expected.

Conductive polymers like PEDOP and PEDOT were also found effective in promoting the Co(II)/(III) electrochemical response. Both PEDOP and PEDOT can be electrodeposited on a transparent conductive substrate by an anodic potentiostatic (ca. +1.3 V versus SCE) or potentiodynamic electrolysis of the appropriate precursor solution in the presence of a perchlorate containing supporting electrolyte. Co(II)/(III)

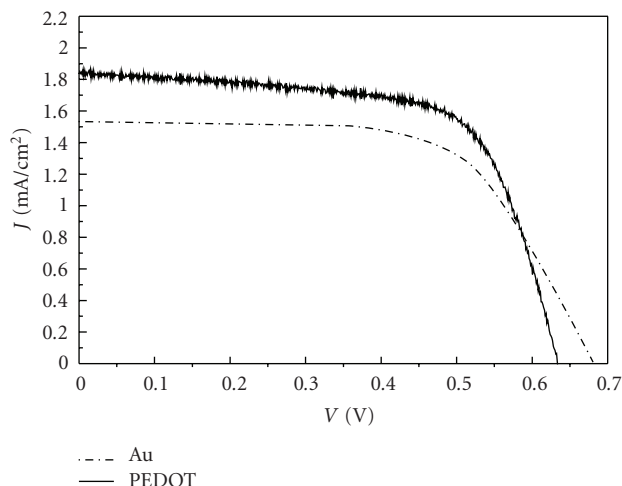


FIGURE 23: J-V curves of Co(II)/(III)-mediated cell employing a gold (dashed line) and a PEDOT counter electrode (solid line). Electrolyte composition is 0.15 M Co(II)/0.5 M Li⁺/0.1 M Tbp in acetonitrile. Cell is equipped with a 120 μ m spacer. Photosensitizer Z907.

appeared to have a clearly diffusion-limited electrochemical behaviour on both PEDOP- and PEDOT- functionalized cathodes. PEDOT gave rise to a more ideal behaviour associated to a smaller separation of the catalytic waves, with a peak separation of the order of 200 mV, substantially independent from Co(II) concentration, the slight peak shift at higher cobalt concentration being essentially determined by uncompensated cell resistance.

The electrodeposition offers the advantage of a fine control of the thickness of the catalytic layer, thus optimizing the electroactive area and the transparency of the cathode. A cathode which possesses both a remarkable catalytic activity and a partially porous structure with a large active area is important for limiting the concentration overpotential which may develop at the counter electrode of the cell under strong illumination, allowing for the consequent reduction of the photocell series resistance. An improvement in cell fill factor and global efficiency is therefore expected and found (Figure 23).

6. Conclusions

DSSCs are photoelectrochemical solar devices, currently subject of intense research in the framework of renewable energies as a low-cost photovoltaic device.

Researches on dye sensitizers are mainly focused on transition metal complexes, but a considerable amount of work is now directed towards the optimization of organic sensitizers and of natural sensitizers extracted from fruits.

Concerning the electron mediators, iodide/iodine has been so far the most efficient and commonly used redox system, due to the fact that I⁻ allows for a fast regeneration of the oxidized dye. The use of alternative redox couples as electron mediators has been addressed, so far, by a limited number of research groups but the results are promising.

To date, the most successful attempts have been based on octahedral cobalt(II) complexes and the best results obtained in combination with specific heteroleptic complexes. The development of efficient and noncorrosive electron mediators is considered of particular relevance since it may allow building large area modules where the different components are in parallel interconnected, increasing the single module short circuit photocurrent and allowing for a more flexible solar panel production.

The search for suitable solid materials that can replace the liquid electrolyte is an additional interesting and active area of research. Organic hole conductors like conductive polymers based on polythiophenes and polypyrroles have demonstrated some promise for application in dye-sensitized solar cells. In particular it has been reported that the presence of ionic liquids may improve the charge transporting capabilities of the heterointerface through screening of space charge effects.

Some efforts towards the modification of the counter electrode with inexpensive and transparent conductive materials have been discussed. In these studies it has been found that osmium complexes as well as electrodeposited conductive polymers like PEDOP and PEDOT are effective in promoting the electrochemical response of Co(II) electron mediators.

Acknowledgment

Financial support from the Polo Solare Organico, CHOSE, Regione Lazio is gratefully acknowledged.

References

- [1] R. Memming, "Electron transfer processes with excited molecules at semiconductor electrodes," *Progress in Surface Science*, vol. 17, no. 1, pp. 7–73, 1984.
- [2] B. O'Regan and M. Grätzel, "A low-cost, high-efficiency solar cell based on dye-sensitized colloidal TiO₂ films," *Nature*, vol. 353, no. 6346, pp. 737–740, 1991.
- [3] M. Grätzel, "Solar energy conversion by dye-sensitized photovoltaic cells," *Inorganic Chemistry*, vol. 44, no. 20, pp. 6841–6851, 2005.
- [4] M. K. Nazeeruddin, P. Péchy, T. Renouard, et al., "Engineering of efficient panchromatic sensitizers for nanocrystalline TiO₂-based solar cells," *Journal of the American Chemical Society*, vol. 123, no. 8, pp. 1613–1624, 2001.
- [5] C. Bauer, G. Boschloo, E. Mukhtar, and A. Hagfeldt, "Ultrafast studies of electron injection in Ru dye sensitized SnO₂ nanocrystalline thin film," *International Journal of Photoenergy*, vol. 4, no. 1, pp. 17–20, 2002.
- [6] Y. Fukai, Y. Kondo, S. Mori, and E. Suzuki, "Highly efficient dye-sensitized SnO₂ solar cells having sufficient electron diffusion length," *Electrochemistry Communications*, vol. 9, no. 7, pp. 1439–1443, 2007.
- [7] M. Quintana, T. Edvinsson, A. Hagfeldt, and G. Boschloo, "Comparison of dye-sensitized ZnO and TiO₂ solar cells: studies of charge transport and carrier lifetime," *Journal of Physical Chemistry C*, vol. 111, no. 2, pp. 1035–1041, 2007.
- [8] M. Saito and S. Fujihara, "Large photocurrent generation in dye-sensitized ZnO solar cells," *Energy & Environmental Science*, vol. 1, pp. 280–283, 2008.

- [9] K. Sayama, H. Sugihara, and H. Arakawa, "Photoelectrochemical properties of a porous Nb₂O₅ electrode sensitized by a ruthenium dye," *Chemistry of Materials*, vol. 10, no. 12, pp. 3825–3832, 1998.
- [10] A. Kay and M. Graetzel, "Artificial photosynthesis. 1. Photosensitization of TiO₂ solar cells with chlorophyll derivatives and related natural porphyrins," *The Journal of Physical Chemistry*, vol. 97, no. 23, pp. 6272–6277, 1993.
- [11] F. Odobel, E. Blart, M. Lagrée, et al., "Porphyrin dyes for TiO₂ sensitization," *Journal of Materials Chemistry*, vol. 13, no. 3, pp. 502–510, 2003.
- [12] M. K. Nazeeruddin, R. Humphry-Baker, M. Grätzel, et al., "Efficient near-IR sensitization of nanocrystalline TiO₂ films by zinc and aluminum phthalocyanines," *Journal of Porphyrins and Phthalocyanines*, vol. 3, no. 3, pp. 230–237, 1999.
- [13] J. He, A. Hagfeldt, S. E. Lindquist, et al., "Phthalocyanine-sensitized nanostructured TiO₂ electrodes prepared by a novel anchoring method," *Langmuir*, vol. 17, no. 9, pp. 2743–2747, 2001.
- [14] W. Paw, S. D. Cummings, M. A. Mansour, W. B. Connick, D. K. Geiger, and R. Eisenberg, "Luminescent platinum complexes: tuning and using the excited state," *Coordination Chemistry Reviews*, vol. 171, no. 1, pp. 125–150, 1998.
- [15] A. Islam, H. Sugihara, K. Hara, et al., "Dye sensitization of nanocrystalline titanium dioxide with square planar platinum(II) diimine dithiolate complexes," *Inorganic Chemistry*, vol. 40, no. 21, pp. 5371–5380, 2001.
- [16] J. M. Rehm, G. L. McLendon, Y. Nagasawa, K. Yoshihara, J. Moser, and M. Grätzel, "Femtosecond electron-transfer dynamics at a sensitizing dye-semiconductor (TiO₂) interface," *Journal of Physical Chemistry*, vol. 100, no. 23, pp. 9577–9578, 1996.
- [17] P. V. Kamat and W. E. Ford, "Photochemistry on surfaces: triplet-triplet energy transfer on colloidal TiO₂ particles," *Chemical Physics Letters*, vol. 135, no. 4-5, pp. 421–426, 1987.
- [18] S. Das, C. S. Rajesh, C. H. Suresh, et al., "Photophysical and photoelectrochemical behavior of poly[styrene-co-3-(acrylamido)-6-aminoacridine]," *Macromolecules*, vol. 28, no. 12, pp. 4249–4254, 1995.
- [19] D. Liu and P. V. Kamat, "Photoelectrochemical behavior of thin CdSe and coupled TiO₂/CdSe semiconductor films," *Journal of Physical Chemistry*, vol. 97, no. 41, pp. 10769–10773, 1993.
- [20] M. K. Nazeeruddin, A. Kay, I. Rodicio, et al., "Conversion of light to electricity by cis-Xbis(2,2'-bipyridyl-4,4'-dicarboxylate)ruthenium(II) charge-transfer sensitizers (X = Cl, Br, I, CN, and SCN) on nanocrystalline TiO₂ electrodes," *Journal of the American Chemical Society*, vol. 115, no. 14, pp. 6382–6390, 1993.
- [21] G. Sauvé, M. E. Cass, G. Coia, et al., "Dye sensitization of nanocrystalline titanium dioxide with osmium and ruthenium polypyridyl complexes," *Journal of Physical Chemistry B*, vol. 104, no. 29, pp. 6821–6836, 2000.
- [22] P. Wang, C. Klein, R. Humphry-Baker, S. M. Zakeeruddin, and M. Grätzel, "A high molar extinction coefficient sensitizer for stable dye-sensitized solar cells," *Journal of the American Chemical Society*, vol. 127, no. 3, pp. 808–809, 2005.
- [23] A. Hagfeldt and M. Grätzel, "Molecular photovoltaics," *Accounts of Chemical Research*, vol. 33, no. 5, pp. 269–277, 2000.
- [24] F. Cecchet, A. M. Gioacchini, M. Marcaccio, et al., "Solvent effects on the oxidative electrochemical behavior of cis-bis(isothiocyanato)ruthenium(II)-bis-2,2'-bipyridine-4,4'-dicarb oxylate," *Journal of Physical Chemistry B*, vol. 106, no. 15, pp. 3926–3932, 2002.
- [25] S. Altobello, R. Argazzi, S. Caramori, et al., "Sensitization of nanocrystalline TiO₂ with black absorbers based on Os and Ru polypyridine complexes," *Journal of the American Chemical Society*, vol. 127, no. 44, pp. 15342–15343, 2005.
- [26] C. W. Lee, H. P. Lu, C. M. Lan, et al., "Novel zinc porphyrin sensitizers for dye-sensitized solar cells: synthesis and spectral, electrochemical, and photovoltaic properties," *Chemistry: A European Journal*, vol. 15, no. 6, pp. 1403–1412, 2009.
- [27] X.-F. Wang, O. Kitao, H. Zhou, H. Tamiaki, and S.-I. Sasaki, "Efficient dye-sensitized solar cell based on oxobacteriochlorin sensitizers with broadband absorption capability," *Journal of Physical Chemistry C*, vol. 113, no. 18, pp. 7954–7961, 2009.
- [28] W. M. Campbell, K. W. Jolley, P. Wagner, et al., "Highly efficient porphyrin sensitizers for dye-sensitized solar cells," *Journal of Physical Chemistry C*, vol. 111, no. 32, pp. 11760–11762, 2007.
- [29] B. C. O'Regan, I. López-Duarte, M. V. Martínez-Díaz, et al., "Catalysis of recombination and its limitation on open circuit voltage for dye sensitized photovoltaic cells using phthalocyanine dyes," *Journal of the American Chemical Society*, vol. 130, no. 10, pp. 2906–2907, 2008.
- [30] J.-H. Yum, P. Walter, S. Huber, et al., "Efficient far red sensitization of nanocrystalline TiO₂ films by an unsymmetrical squaraine dye," *Journal of the American Chemical Society*, vol. 129, no. 34, pp. 10320–10321, 2007.
- [31] C. G. Garcia, A. Sarto Polo, and N. Y. Murakami Iha, "Fruit extracts and ruthenium polypyridinic dyes for sensitization of TiO₂ in photoelectrochemical solar cells," *Journal of Photochemistry and Photobiology A*, vol. 160, no. 1-2, pp. 87–91, 2003.
- [32] G. Calogero and G. Di Marco, "Red Sicilian orange and purple eggplant fruits as natural sensitizers for dye-sensitized solar cells," *Solar Energy Materials and Solar Cells*, vol. 92, no. 11, pp. 1341–1346, 2008.
- [33] T. A. Heimer, E. J. Heilweil, C. A. Bignozzi, and G. J. Meyer, "Electron injection, recombination, and halide oxidation dynamics at dye-sensitized metal oxide interfaces," *Journal of Physical Chemistry A*, vol. 104, no. 18, pp. 4256–4262, 2000.
- [34] I. Montanari, J. Nelson, and J. R. Durrant, "Iodide electron transfer kinetics in dye-sensitized nanocrystalline TiO₂ films," *Journal of Physical Chemistry B*, vol. 106, no. 47, pp. 12203–12210, 2002.
- [35] G. Schlichthörl, S. Y. Huang, J. Sprague, and A. J. Frank, "Band edge movement and recombination kinetics in dye-sensitized nanocrystalline TiO₂ solar cells: a study by intensity modulated photovoltage spectroscopy," *Journal of Physical Chemistry B*, vol. 101, no. 41, pp. 8141–8155, 1997.
- [36] S. Y. Huang, G. Schlichthörl, A. J. Nozik, M. Grätzel, and A. J. Frank, "Charge recombination in dye-sensitized nanocrystalline TiO₂ solar cells," *Journal of Physical Chemistry B*, vol. 101, no. 14, pp. 2576–2582, 1997.
- [37] H. Nusbaumer, J. E. Moser, S. M. Zakeeruddin, M. K. Nazeeruddin, and M. Grätzel, "Co(dbbip) complex rivals triiodide/iodide redox mediator in dye-sensitized photovoltaic cells," *Journal of Physical Chemistry B*, vol. 105, no. 43, pp. 10461–10464, 2001.
- [38] C. Klein, M. K. Nazeeruddin, D. Di Censo, P. Liska, and M. Grätzel, "Amphiphilic ruthenium sensitizers and their applications in dye-sensitized solar cells," *Inorganic Chemistry*, vol. 43, no. 14, pp. 4216–4226, 2004.

- [39] P. Wang, S. M. Zakeeruddin, P. Comte, R. Charvet, R. Humphry-Baker, and M. Grätzel, "Enhance the performance of dye-sensitized solar cells by Co-grafting amphiphilic sensitizer and hexadecylmalonic acid on TiO₂ nanocrystals," *Journal of Physical Chemistry B*, vol. 107, no. 51, pp. 14336–14341, 2003.
- [40] S. A. Sapp, C. M. Elliott, C. Contado, S. Caramori, and C. A. Bignozzi, "Substituted polypyridine complexes of cobalt(II/III) as efficient electron-transfer mediators in dye-sensitized solar cells," *Journal of the American Chemical Society*, vol. 124, no. 37, pp. 11215–11222, 2002.
- [41] T. N. Murakami, S. Ito, Q. Wang, et al., "Highly efficient dye-sensitized solar cells based on carbon black counter electrodes," *Journal of the Electrochemical Society*, vol. 153, no. 12, pp. A2255–A2261, 2006.
- [42] E. Ramasamy, W. J. Lee, D. Y. Lee, and J. S. Song, "Spray coated multi-wall carbon nanotube counter electrode for tri-iodide (I₃⁻) reduction in dye-sensitized solar cells," *Electrochemistry Communications*, vol. 10, no. 7, pp. 1087–1089, 2008.
- [43] T. Denaro, V. Baglio, M. Girolamo, et al., "Investigation of low cost carbonaceous materials for application as counter electrode in dye-sensitized solar cells," *Journal of Applied Electrochemistry*, vol. 39, no. 11, pp. 2173–2179, 2009.
- [44] C.-S. Chou, R.-Y. Yang, M.-H. Weng, and C.-I. Huang, "The applicability of SWCNT on the counter electrode for the dye-sensitized solar cell," *Advanced Powder Technology*, vol. 20, no. 4, pp. 310–317, 2009.
- [45] P. J. Cameron and L. M. Peter, "Characterization of titanium dioxide blocking layers in dye-sensitized nanocrystalline solar cells," *Journal of Physical Chemistry B*, vol. 107, no. 51, pp. 14394–14400, 2003.
- [46] L. G. Wade, *Organic Chemistry*, Prentice Hall, Englewood Cliffs, NJ, USA, 1991.
- [47] S. Cazzanti, S. Caramori, R. Argazzi, C. M. Elliott, and C. A. Bignozzi, "Efficient non-corrosive electron-transfer mediator mixtures for dye-sensitized solar cells," *Journal of the American Chemical Society*, vol. 128, no. 31, pp. 9996–9997, 2006.
- [48] K. Murakoshi, R. Kogure, Y. Wada, and S. Yanagida, "Fabrication of solid-state dye-sensitized TiO₂ solar cells combined with polypyrrole," *Solar Energy Materials and Solar Cells*, vol. 55, no. 1-2, pp. 113–125, 1998.
- [49] S. Caramori, S. Cazzanti, L. Marchini, et al., "Dye-sensitized solar cells based on PEDOP as a hole conductive medium," *Inorganica Chimica Acta*, vol. 361, no. 3, pp. 627–634, 2008.
- [50] D. Martineau, M. Beley, P. C. Gros, S. Cazzanti, S. Caramori, and C. A. Bignozzi, "Tuning of ruthenium complex properties using pyrrole- and pyrrolidine-containing polypyridine ligands," *Inorganic Chemistry*, vol. 46, no. 6, pp. 2272–2277, 2007.
- [51] E. Palomares, J. N. Clifford, S. A. Haque, T. Lutz, and J. R. Durrant, "Slow charge recombination in dye-sensitized solar cells (DSSC) using Al₂O₃ coated nanoporous TiO₂ films," *Chemical Communications*, no. 14, pp. 1464–1465, 2002.
- [52] Y. Kim, Y. E. Sung, J. B. Xia, M. Lira-Cantu, N. Masaki, and S. Yanagida, "Solid-state dye-sensitized TiO₂ solar cells using poly(3,4-ethylenedioxythiophene) as substitutes of iodine/iodide electrolytes and noble metal catalysts on FTO counter electrodes," *Journal of Photochemistry and Photobiology A*, vol. 193, no. 2-3, pp. 77–80, 2008.
- [53] C. M. Elliott, S. Caramori, and C. A. Bignozzi, "Indium tin oxide electrodes modified with tris(2,2'-bipyridine-4,4'-dicarboxylic acid) iron(II) and the catalytic oxidation of tris(4,4'-di-tert-butyl-2,2'-bipyridine) cobalt(II)," *Langmuir*, vol. 21, no. 7, pp. 3022–3027, 2005.
- [54] M. J. Scott, J. J. Nelson, S. Caramori, C. A. Bignozzi, and C. M. Elliott, "cis-dichloro-bis(4,4'-dicarboxy-2,2'-bipyridine)osmium(II)-modified optically transparent electrodes: application as cathodes in stacked dye-sensitized solar cells," *Inorganic Chemistry*, vol. 46, no. 24, pp. 10071–10078, 2007.

Review Article

Progress in Polycrystalline Thin-Film Cu(In,Ga)Se₂ Solar Cells

Udai P. Singh and Surya P. Patra

School of Electronics Engineering, KIIT University, Campus-3 (Kathjodi), Patia Bhubaneswar 751024, India

Correspondence should be addressed to Udai P. Singh, singhup@kiit.ac.in

Received 7 January 2010; Revised 21 May 2010; Accepted 30 June 2010

Academic Editor: Gaetano Di Marco

Copyright © 2010 U. P. Singh and S. P. Patra. This is an open access article distributed under the Creative Commons Attribution License, which permits unrestricted use, distribution, and reproduction in any medium, provided the original work is properly cited.

For some time, the chalcopyrite semiconductor CuInSe₂ and its alloy with Ga and/or S [Cu(InGa)Se₂ or Cu(InGa)(Se,S)₂], commonly referred as CIGS, have been leading thin-film material candidates for incorporation in high-efficiency photovoltaic devices. CuInSe₂-based solar cells have shown long-term stability and the highest conversion efficiencies among all thin-film solar cells, reaching 20%. A variety of methods have been reported to prepare CIGS thin film. Efficiency of solar cells depends upon the various deposition methods as they control optoelectronic properties of the layers and interfaces. CIGS thin film grown on glass or flexible (metal foil, polyimide) substrates require p-type absorber layers of optimum optoelectronic properties and n-type wideband gap partner layers to form the p-n junction. Transparent conducting oxide and specific metal layers are used for front and back contacts. Progress made in the field of CIGS solar cell in recent years has been reviewed.

1. Introduction

Current trends suggest solar energy will play an important role in future energy production [1]. Silicon has been and remains the traditional solar cell material of choice. Although silicon is a highly abundant material, it requires an energy intensive process to purify and crystallize. Furthermore, installations of silicon cells require heavy glass protection plates, which reduce residential applications [2].

Recently, commercial interest is beginning to shift towards thin-film cells [3]. Material, manufacturing time, and weight savings are driving the increase in thin-film cells. Cu(In,Ga)Se₂ (CIGS) is one of the most promising semiconductors for the absorber-layer of thin-film solar cells [4]. The conversion efficiency of such cells on glass substrates is approaching 20% [5]. Chalcopyrite-based solar modules are uniquely combining advantages of thin-film technology with the efficiency and stability of conventional crystalline silicon cells. Copper indium gallium selenide (CIGS) solar cells have the highest production among thin film technologies. Advances in preparation and efficiency have allowed these cells to be produced rapidly and are approaching market values for carbon-based energy production [6].

The first report on chalcopyrite-based solar cell was published in 1974 [7]. The cell was prepared from a p-type CuInSe₂ (CISe) single crystal onto which a CdS film was evaporated in vacuum. This combination of a p-type chalcopyrite absorber and a wide-gap n-type window layer still is the basic concept upon which current cell designs are based. The typical design, first described in 1985 [8] is shown in Figure 1 and a typical cross-section CIGS device structure is shown in Figure 2. The CuInSe₂ crystal was replaced by a polycrystalline thin film of the more general composition Cu(In,Ga)(S,Se)₂.

Many groups across the world have developed CIGS solar cells with efficiencies in the range of 15–19%, depending on different growth procedures. Glass is the most commonly used substrate, but now efforts are being made to develop flexible solar cells on polyimide [9–17] and metal foils [2, 18–29]. Highest efficiencies of 14.1% and 17.6% have been reported for CIGS cells on polyimide [30] and metal foils [31], respectively. Recently a slight increase in efficiency of 14.7% and 17.7% has been reported for CIGS cells on polyimide and metal foils [32], respectively.

CIGS solar cells also attract considerable interest for space applications due to their two main advantages. It offers

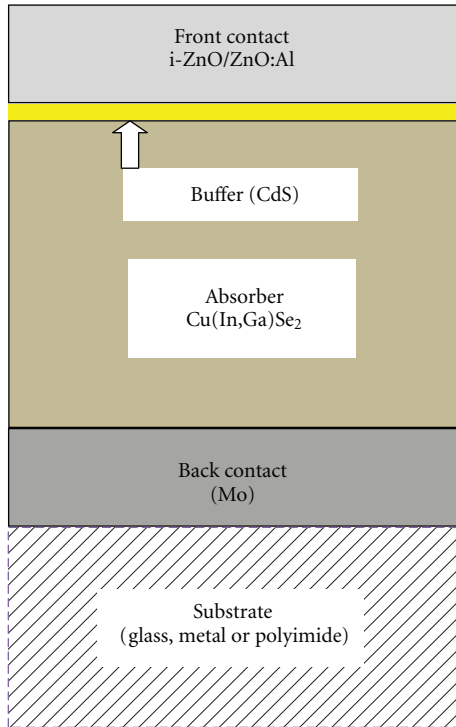


FIGURE 1: Schematic cross-section of a chalcopyrite-based thin-film solar cell. Typical materials for the individual parts of the cell are given in brackets.

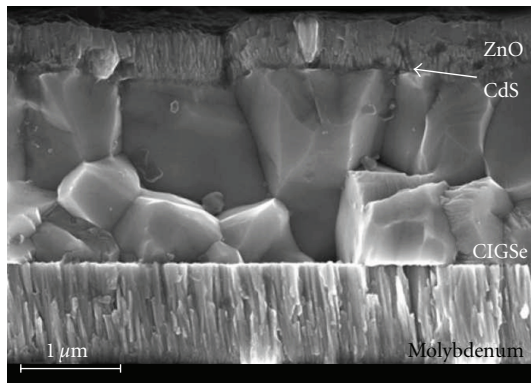


FIGURE 2: Scanning electron micrograph of the cross-section of a typical chalcopyrite solar cell with Cu(In,Ga)Se_2 (CIGSe) absorber (substrate now shown). Taken from [34].

specific power up to 919 W/Kg, the highest for any solar cell [23]. CIGS cells are also superior to GaAs cells in radiation hardness [33]. Moreover, the flexibility of these cells allows for novel storage and deployment options [23].

There are several reviews available dealing with different aspects of CIGS solar cells [35–39]. The emphasis of the present paper is placed on the progress made in different aspects of CIGS solar cells in the recent times.

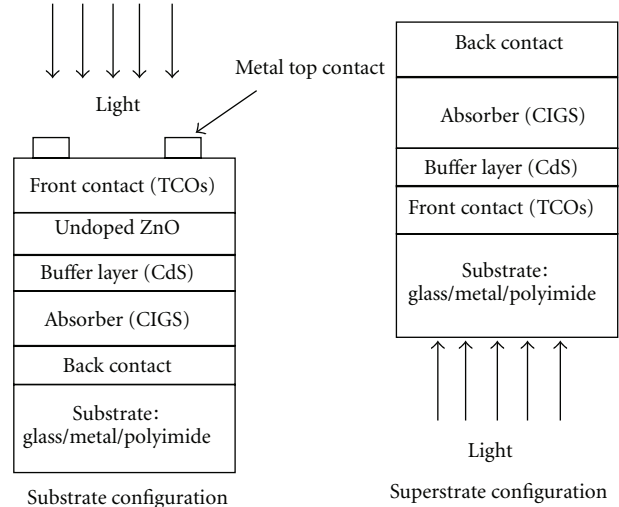


FIGURE 3: Schematic cross-section of “substrate” and “superstrate” configuration of CIGS solar cell.

2. CIGS Cell Configuration

The Cu-chalcopyrites exhibit the highest efficiencies among the thin-film solar cells with a record lab-scale efficiency reaching nearly 20% [5]. Most commonly CIGS solar cells are grown in substrate configuration (see Figure 3). This configuration gives the highest efficiency owing to favourable process conditions and material compatibility. Cell preparation starts with the deposition of back contact, usually Mo, on glass, followed by the p-type CIGS absorber, CdS or other weakly n-type buffer layer, undoped ZnO, n-type transparent conductor (usually doped ZnO or In_2O_3), metal grid, and antireflection coating. It requires an additional encapsulation layer and/or glass to protect the cell surface.

The structure of a CIGS solar cell is quite complex because it contains several compounds as stacked films that may react with each other. Fortunately, all detrimental interface reactions are either thermodynamically or kinetically inhibited at ambient temperature [40]. The cover glass used in substrate configuration is not required for the cells grown in the superstrate configuration (see Figure 3). CIS-based superstrate solar cells were investigated by Duchemin et al. [41] using spray pyrolysis deposition, but efficiencies did not exceed 5%. The main reason for this low efficiency in CdS/CIGS superstrate cells is the undesirable interdiffusion of Cd into CIS (or CIGS) during the elevated temperatures required for absorber deposition on CdS buffer layers [42]. To overcome this problem of interdiffusion more stable buffer materials and low-temperature deposition processes such as electrodeposition (ED), low-substrate temperature coevaporation and screen printing were investigated. Nakada and Mise [43] achieved a breakthrough by replacing CdS with undoped ZnO and coevaporating Na_xSe during CIGS deposition. With the additional introduction of composition grading in absorber layer, 12.8% efficiency cells were developed [43].

TABLE 1: Superstrate Cells.

Efficiency	TCO	Buffer	Absorber	Reference
($V_{oc} > 800$ mV) 3%	ZnO	None	CuGaSe ₂	Klenk et al. [48]
2.8%	ITO	In ₂ Se ₃	CuInSe ₂	Kampmann [49]
6.6%	ITO	CdS	CuInSe ₂	Yoshida and Birkmire [50]
6.7%	ZnO	CdS	CuInSe ₂	Negami et al. [51]
8.1%	ZnO	CdS	CuInSe ₂	Nakada et al [52]
11.2%	ZnO	None	Cu(In,Ga)Se ₂	Haug et al. [47]
12.8%	ZnO	None	Cu(In,Ga)Se ₂	Nakada and Mise [43]

This coevaporation of Na_xSe for incorporation of sodium in CIGS is essential for high-efficiency cells, as the ZnO front contact acts as diffusion barrier for Na from the glass substrate and leads to a low net carrier density in CIGS and cells with low open-circuit voltage (V_{OC}) and fill factor (FF) [44]. (*The influence of Na on CIGS optoelectronic properties is discussed in Section 6*) Investigations of the interface between the ZnO buffer layer and CIGS revealed the presence of a thin layer of Ga₂O₃ which acts as barrier against photocurrent transport [43, 45, 46]. However, Na-free superstrate solar cells with efficiencies up to 11.2% was obtained, but a strong light-soaking treatment was necessary [47].

Preparing a blocking contact in superstrate structure has been difficult. Only small-area cells have been demonstrated so far and even those show limited performance (see Table 1). It is interesting to note that approaches not using buffer layers have resulted in higher efficiency than those using CdS buffers prepared by various methods.

Another interesting application for superstrate solar cells are tandem solar cells. These solar cells employ two separate solar cell structures for a more efficient conversion of the illumination. Superstrate solar cells are then required as top cell for the short wavelength part of the solar irradiation. Tandem solar cell will not be the part of present discussion. The details can be referred to in the following articles [53–56].

3. Back Contact

Molybdenum (Mo) is the most common metal used as a back contact for CIGS solar cells. Several metals, Pt, Au, Ag, Cu, and Mo, have been investigated for using as an electrical contact of CIS- and CIGS-based solar cells [57–59]. Mo emerged as the dominant choice for back contact due to its relative stability at the processing temperature, resistance to alloying with Cu and In, and its low contact resistance to CIGS. The typical value of resistivity of Mo is nearly $5 \times 10^{-5} \Omega \text{ cm}$ or less. The preferred contact resistivity value is $\leq 0.3 \Omega \text{ cm}$. Results have been reported in several papers [57, 60, 61] concerning the influence of the mechanical and electrical properties of the Mo films on the performance of the photovoltaic devices. Molybdenum is typically deposited by e-gun evaporation [61, 62] or sputtering [63–65] on soda-lime glass which ideally provides

an inexpensive, inert, and mechanical durable substrate at temperatures below 500–600°C. Intrinsic stresses in molybdenum films depend on the experimental deposition parameters [61–66], inducing significant changes in the structural and electrical properties. Films with compressive stresses have near bulk like values of the electrical resistivity and a dense microstructure, but films under tensile stresses exhibit altered physical properties and a more open porous structure [61–64]. Gross stress may be determined by visual inspection in that highly compressed films tend to buckle up, frequently in zigzag patterns, whereas films under extreme tensile stress develop a system of stress lines that look scratches. Orgassa et al. [67] fabricated CIGS solar cells with different back-contact materials, emphasizing the role of the back contact as an optical reflector. Early results by Russell et al. [68] and Jaegaermann et al. [69] suggested that Mo back contacts for CIS form a Schottky-type barrier with a barrier height of 0.8 eV for the intimate p-doped CIS/Mo contact. The work of Shafarman et al. [70], who analyzed the Mo/CIS interface separately from the cell, shows the contact to be ohmic.

The influence of MoSe₂ on the ohmic contact behaviour at the CIGS/Mo interface makes MoSe₂ formation an important issue. Fundamental work by Raud and Nicolet [71] on Mo/Se, Mo/In, and Mo/Cu diffusion couples showed Se to react with Mo, forming MoSe₂ in very small amounts after annealing at 600°C. Kohara et al. [72] have also shown the formation of nearly ideal ohmic contact between Mo and CIGS that occurs via an intermediate MoSe₂ layer. Jones et al. [73] investigated the interface properties of d.c.-sputtered Mo on CIS layers, deposited by coevaporation, and concluded that MoSe₂ does not form below 500°C and it might be an artifact of the sputtering process. Similar results have been obtained by Schmid et al. [74] they detected Mo–O and Mo–O–Se compounds, while selenizing the Mo-coated substrate prior to the CIS deposition at 600°C. They concluded that there should be a Schottky-type barrier at the CIS-Mo/MoO₂ interface. Wada et al. [75] have also suggested that CIGS/Mo heterocontact including a MoSe₂ layer is not Schottky type, but a favorable ohmic type contact. Nishiwaki et al. [76, 77] have also studied the formation of MoSe₂ layer at the CIGS/Mo interface during “3-stage” process.

Wada et al. [78] reported the formation of a MoSe₂ layer at the Mo/CIGS interface during the second stage of the three-stage process, yet only under (In,Ga)-rich growth and

for substrate temperatures higher than 550°C. They found Na to enhance the formation of MoSe₂. Assmann et al. [79] have also shown the presence of MoSe₂ at the Mo/CIGS interface; they conclude that mechanical stable MoSe₂ at the interface gives good adhesion. Recently, Shimizu et al. [80] have studied the variation of Mo thickness from 0.2 μm to 0.07 μm on the properties of CIGS solar cells. They conclude that there is a tradeoff between the decreased sodium diffusion for thicker Mo layers and decreased fill factor for thin layers. The optimum Mo thickness suggested was 0.2 μm. They have also found that water vapour introduced during CIGS growth improve the overall photovoltaic properties.

MoSe₂ layers were confirmed also in CuGaSe₂-based solar cells by Würz et al. [81]. Contrary to the above results, Ballif et al. [82] could not detect any intermediate compound within the Mo/CIGS interface. Mo back contact for flexible polyimide is also been investigated by Zhang et al. [83].

The properties of molybdenum thin films evaporated onto large area (30 cm × 30 cm) soda-lime glass substrates at different deposition rates have been investigated by Guillén and Herrero [84]. During the formation of films, Na ion diffuse from the soda lime glass substrate through the Mo back contact into the absorber layer. The diffusion of Na into absorber film depends on the deposition conditions of the Mo back contact [85–87]. Nowadays, Mo growth by sputtering or e-beam evaporation is the most commonly used back contact for CIGS solar cells.

Kim et al. [88] have tried Na-doped Mo/Mo bilayer on Alumina substrate and have shown improvement in photovoltaic properties. Nakada [89] has tried transparent conducting oxide as back contact. The TCO back contact deteriorated at high absorber deposition temperature. The formation of Ga₂O₃ was also reported at the CIGS/ITO and CIGS/ZnO:Al interfaces.

4. CIGS Absorber Layer—Deposition Methods

I–III–VI₂ semiconductors, such as CIS or CIGS are often simply referred to as chalcopyrites because of their crystal structure. These materials are easily prepared in a wide range of compositions and the corresponding phase diagrams are well investigated [90–92]. For the preparation of solar cells, only slightly Cu-deficient compositions of p-type conductivity are suited [93, 94]. The details of material properties will not be discussed here.

A wide variety of thin-film deposition methods has been used to deposit Cu(In,Ga)Se₂ thin films. To determine the most promising technique for the commercial manufacture of modules, the overriding criteria are that the deposition can be completed at low cost while maintaining high deposition or processing rate with high yield and reproducibility. Compositional uniformity over large areas is critical for high yield. Device considerations dictate that the Cu(In,Ga)Se₂ layer should be at least 1 μm thick and that the relative compositions of the constituents are kept within the bounds determined by the phase diagram.

The most promising deposition methods for the commercial manufacture of modules can be divided into two

general approaches that have both been used to demonstrate high device efficiencies and in pilot scale manufacturing. The first approach is vacuum coevaporation in which all the constituents, Cu, In, Ga, and Se, can be simultaneously delivered to a substrate heated at 400°C to 600°C and the Cu(In,Ga)Se₂ film is formed in a single growth process. The second approach is a two-step process that separates the delivery of the metals from the reaction to form device-quality films. Typically the Cu, Ga, and In are deposited using low-cost and low-temperature methods that facilitate uniform composition. Then, the films are annealed in a Se atmosphere, also at 400°C to 600°C. The reaction and anneal step often takes longer time than formation of films by coevaporation due to diffusion kinetics, but is amenable to batch processing.

4.1. Coevaporation. The most successful technique for deposition of CIGS absorber layers for highest-efficiency cells is the simultaneous evaporation [95] of the constituent elements from multiple sources in single processes where Se is offered in excess during the whole deposition process. The process uses line-of-sight delivery of the Cu, In, Ga, and Se from Knudsen-type effusion cells or open boat sources to the heated substrate. While a variation of the In-to-Ga ratio during the deposition process leads to only minor changes in the growth kinetics, variation of the Cu content strongly affects the film growth.

The sticking coefficients of Cu, In, and Ga are very high, so the film composition and growth rate are determined simply by the flux distribution and effusion rate from each source. Different deposition variations, using elemental fluxes deliberately varied over time, have been explored using coevaporation. Four different sequences that have been used to fabricate devices with efficiencies greater than 16% are shown in Figure 4.

The first process (Figure 4(a)) is the simplest stationary process in which all fluxes as well as substrate temperature is constant throughout the deposition process [96]. Advanced preparation sequences include a Cu-rich stage during the growth process and end up with an In-rich overall composition in order to combine the large grains of the Cu-rich stage with the otherwise more favourable electronic properties of In-rich composition. The use of this kind of procedure is called “Boeing or bilayer process” (Figure 4(b)) originates from the work of Mickelsen and Chen [97, 98].

This bilayer process yields larger grain sizes compared to the constant rate (single stage) process. This is attributed to the formation of a Cu_xSe phase during the Cu-rich first stage, which improves the mobility of group III atoms during growth [99–101]. Another possibility is the inverted process where first (In,Ga)₂Se₃ is deposited at a lower temperature (typically ~300°C). Then Cu and Se are evaporated at an elevated temperature until an overall composition close to stoichiometry is reached [102–104]. This process leads to smoother film morphology than bilayer process. The so-called “three-stage process” introduced by Gabor et al. [103] from NREL is shown in Figure 4(c).

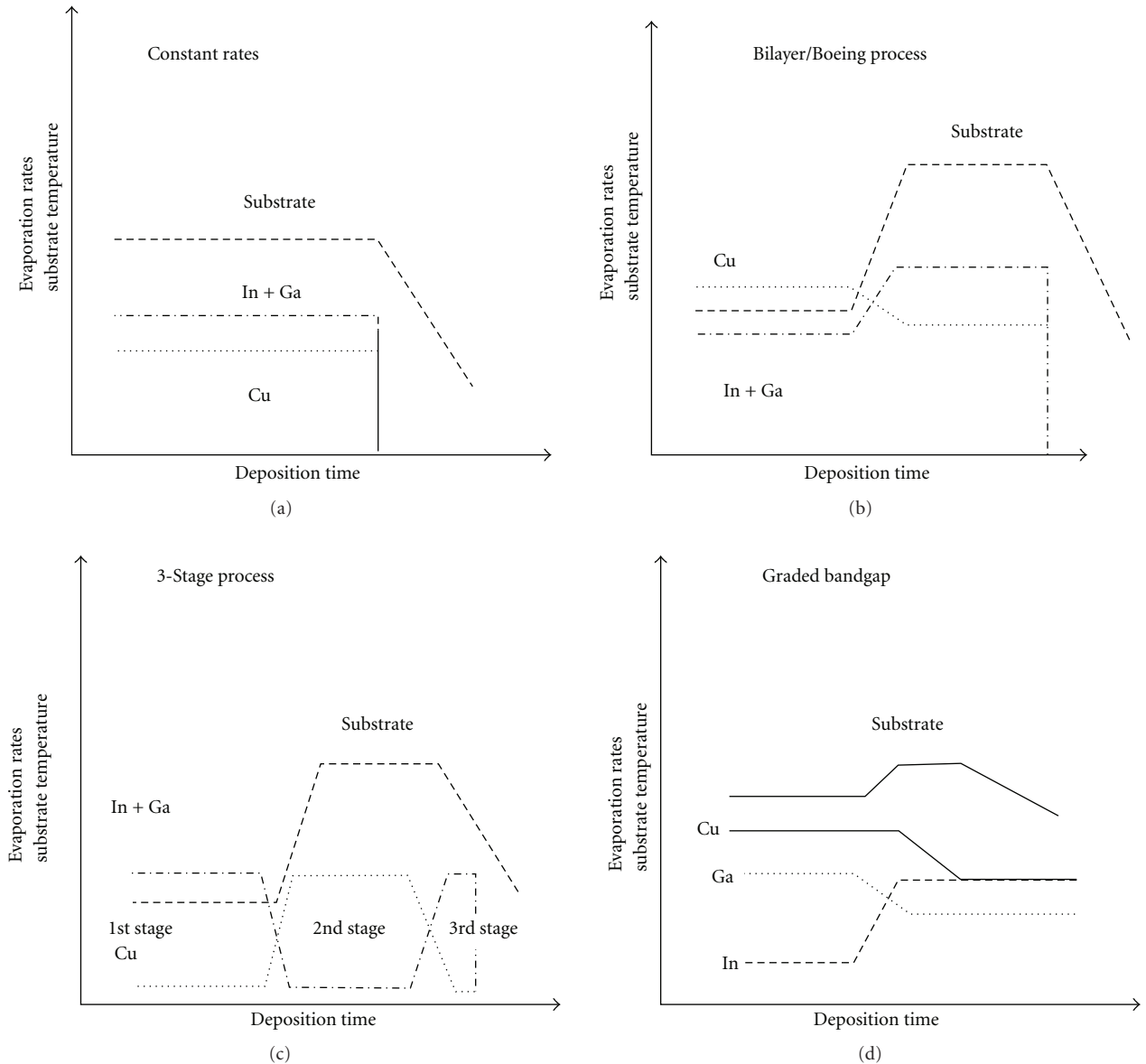


FIGURE 4: Schematic illustration of different coevaporation process. In all cases, a constant Se flux is also supplied.

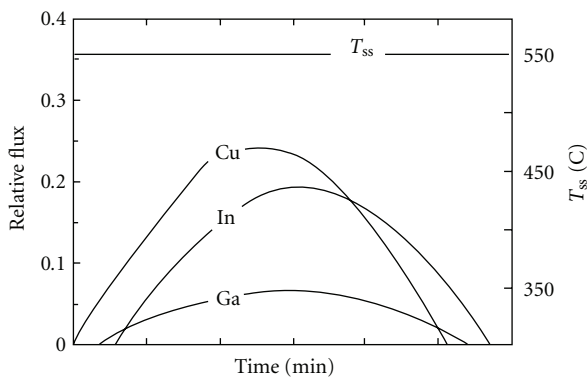


FIGURE 5: Flux distributions of different elements for in-line system. A constant Se flux is also supplied (from [35]).

This method leads, up to now, to the most efficient solar cells. The smoother surface obtained with three-stage process reduces the junction area and thereby is expected to reduce the number of defects at the junction and also facilitates the uniform conformal deposition of a thin buffer layer and prevents ion damage in CIGS during sputter deposition of ZnO/ZnO:Al. Variations of the Ga/In ratio during deposition (Figure 4(d)) allow the design of graded band-gap structures [105].

In one of the other process (shown in Figure 5) is an in-line process in which the flux distribution results from the substrate moving sequentially over the Cu, Ga, and In sources. This was first simulated in a stationary evaporation system [106] and demonstrated by Hanket et al. [107] and has subsequently been implemented by several groups in pilot manufacturing systems.

4.2. Sequential Approach—Selenization of Precursor Material.

The interest in sequential processes is sparked by its suitability for large-area film deposition with good control of the composition and film thickness. Such processes consist of the deposition of a precursor material, followed by thermal annealing in controlled reactive or inert atmosphere for optimum compound formation via the chalcogenization reaction. This is commonly referred as selenization of stacked metal or alloy layers. The metals and alloys can be deposited by variety of methods which involve vacuum or no vacuum. The most common of vacuum process is sputtering [108–114] and thermal evaporation [113, 115–131]. The two step process has many variations in both the precursor deposition and the Se reaction step.

4.2.1. Vacuum-Based Approach. This general approach was first demonstrated by Grindle et al. [132] who sputtered Cu/In layers and reacted them in hydrogen sulfide to form CuInS_2 . This was first adapted to CuInSe_2 by Chu et al. [121]. The highest-efficiency Cu(InGa)Se_2 cell reported using the reaction in H_2Se is 16.2%, on the basis of the active area [133], but there have been less effort at optimizing laboratory-scale cell efficiencies than with coevaporated Cu(InGa)Se_2 . Using the two-step selenization/sulfurization approach, some groups have reported CIGSS-solar cells with V_{OC} and efficiency above 600 mV [134] and 14%, respectively, [135]. Lately, an efficiency of 13% [136] has been achieved on 30×30 cm large modules. Recently 14.3% has been reported on 30×30 cm large modules [137] and 14.7% on 10×10 cm minimodules [138]. In both cases, sulphur as well as selenium is used for absorber preparation.

The precursor films are typically reacted in either H_2Se or Se vapor at 400°C to 500°C for 30 to 60 min to form the best device quality material. Poor adhesion [139] and formation of a MoSe_2 layer [140] at the Mo/CuInSe_2 interface may limit the reaction time and temperature. Reaction in H_2Se has the advantage that it can be done at atmospheric pressure and can be precisely controlled, but the gas is highly toxic and requires special precautions for its use. The precursor films can also be reacted in a Se vapor, which might be obtained by thermal evaporation, to form the CuInSe_2 film [141]. A third reaction approach is rapid thermal processing (RTP) of either elemental layers, including Se [142, 143] or amorphous evaporated Cu-In-Se layers [144]. Recently, Chen et al. had tried one step sputtering using Cu-In-Ga alloy target followed by selenization [145].

4.2.2. Nonvacuum-Based Approach. Vacuum-evaporated, polycrystalline copper indium gallium diselenide (CIGS) thin films are used as the absorber layers in the highest efficiency thin film photovoltaic (PV) cells reported to date [5, 146]. However, the high cost and low material utilisation of the equipment used to produce these layers may be a barrier to their commercialization and will increase the cost of the electricity generated by CIGS based systems [147]. Nonvacuum techniques for CIGS deposition offer potential reductions in capital cost and many such techniques have been investigated [148]. These techniques generally split

CIGS formation into two stages, one in which the precursor is deposited and one in which the precursor is converted into CIGS.

Nonvacuum approaches to CIGS deposition can be divided into the following categories depending on the deposition method and the scale of mixing of the precursor materials:

- (1) electrochemical process,
- (2) particulate process,
- (3) solution based process.

A detailed review on nonvacuum process dealing with above process is recently published [149]. In view of this, the present section will only update the recent work done in this area, so as not to duplicate the recently published work. In the recent development, Kang et al. [150] have prepared CIGS absorber by selenizing electrodeposited precursor with rich Se and poor Se content. The Se-poor electrodeposited precursor had better crystallinity and increased Ga content. The best cell obtained has efficiency of 1.63% only. In another study, Lai et al. [151] investigated the electrodeposition of CIGS using cyclic voltammetry in a DMF-aqueous solution containing citrate as complexing agent. They performed the cyclic voltammetry study on a ternary Cu-In-Se system, a quaternary system Cu-In-Ga-Se and binary Cu-Se, In-Se, and Ga-Se systems.

Nanoparticle-based approach was carried out by Yoon et al. [152] for the formation of CIS solar cells. They concluded that the Se loss can be minimized by using high heating rate and core-shell structure with a binary compound. The highest efficiency reported was 1.11%. Park et al. [153] have synthesized CIGS absorber using a paste of a Cu, In, Ga, and Se with an aim to develop a simpler and lower cost method of fabricating the absorber layer. Kaigawa et al. [154] have also reported the absorber formation using spray and sintering the film using spot welding machine. Recently a nonvacuum process for preparing nanocrystalline CIGS materials involving an open-air solvothermal route has been demonstrated [155]. In continuation of their earlier work [156, 157], that is, hydrazine-based processor approach for the depositing CIGS and related chalcogenide-based absorber layer, Liu et al. have recently reported 12% efficient CuIn(SeS)_2 solar cell [158]. Hou et al. [159] have also reported the formation of hydrazine-based CuIn(SeS)_2 thin film solar cell.

5. Alternative CIS or CIGS Growth Process

The CIS or CIGS compound has been reported using other alternative techniques. In one of the studies, Ahmed et al. [160] have studied the thermal annealing of flash evaporated CIGS thin films. In another approach [161], efficiency as high as 15.4% was achieved using additional deposition of In, Ga, and Se at high temperatures. In spray pyrolysis, metal salts with a chalcogen reactant are sprayed on heated substrate to form CIS layer. However, a subsequent heat treatment in a reducing atmosphere is still required to improve crystallinity and purity [162–164]. Different other

approaches have also been successfully adopted for the fabrication of CIGS absorber layers. Flash evaporation has also been used to prepare CIGS film [165]. MOCVD has also been investigated [166] for the deposition of CGS layers as part of a tandem structure, but the growth rate and cell efficiency is rather low. CuInGaSe₂ thin films have been prepared by a low pressure metalorganic chemical vapor deposition technique using three precursors without additional Se [167]. A plasma-enhanced CVD has also been reported for fabricating stoichiometric CIS film [168]. CIS thin film has also been deposited by atmospheric pressure metal organic chemical vapor deposition (AP- MOCVD) [169, 170]. Brien et al. [171–173] have deposited CuInSe₂, CuInS₂ and CuGaSe₂ thin film by low pressure MOCVD. Recently deposition of CuInSe₂ thin film on CuGaSe₂ thin film and vice versa has been achieved by a low pressure metal organic chemical vapor deposition technique with three precursors without additional Se [174]. No devices have been attempted by the authors.

Few different techniques have also been used to deposit and characterize CIGS thin film. The technique used are closed-spaced vapor transport [175–177] electrodeposition of CIS using ethylene glycol at 150°C [178] CIGSS films by sol-gel route [179] electron beam evaporated CIGS film [180–185] CuInSe₂ thin films prepared using sequential vacuum evaporation of In, Se, and Cu at moderately low substrate temperatures, avoiding any treatment using toxic H₂Se gas [186], CIS using hot wall vacuum evaporation [187], MBE grown CIGS, CIS [188, 189] CIGS using ion-beam plasma evaporation in vacuum [190] and CIGS using a two-stage hybrid sputtering/evaporation method [191].

6. Influence of Sodium

The most important effect of the soda lime glass substrate on Cu(InGa)Se₂ film growth is that it supplies sodium to the growing chalcopyrite material. It has been clearly shown that this effect is distinct from the thermal expansion match of soda lime glass [192]. The sodium diffuses through the Mo back contact, which also means that it is important to control the properties of the Mo [193]. Na, incorporated into CIGS absorber layers are widely known to have significantly beneficial effects that lead to enhanced CIGS-related photovoltaic cell efficiencies.

The effect of Na include an improvement in p-type conductivity due to an increase in the effective hole carrier density and improved open circuit voltage (V_{OC}) and fill factor for solar cells fabricated from Na doped CIGS [194, 195]. In addition to this, the effect of Na on the growth orientation of CIGS films results in an enhancement of (112) texture [194, 196, 197]. Among the various Na effects, variations in the electrical properties have been well discussed. The observed improvement in V_{OC} has been proposed to originate from an increase in the effective acceptor density [198]. Na in polycrystalline CIGS films is considered to act on the grain boundaries rather than in the bulk [199, 200]. Na substituting on a Cu site Na_{Cu} results in the formation of a stable compound NaInSe₂, which has a larger band

gap energy and in turn leads to a larger V_{OC} has also been proposed [201].

The correlation between the CIGS grain size and the presence of Na has been occasionally discussed. While some groups [192, 196, 202] have reported an increase of the grain size in CIGS films containing Na, others did not support these observations [203–206]. A decreasing grain size was observed for several Na incorporation methods in a direct comparison [200]. This may be due to the fact that the nature of the effects of Na on grain size depends on the CIGS growth method and the Na-doping process.

The CIS compound formation in rapid-thermal-processed layers was found to be delayed in the presence of Na, resulting in CIS growth at a higher mean temperature, which serves as an explanation for the observed increase in grain size [207]. In any case, the grain size of Na-doped CIGS films seems to have no critical role in solar cell performance [208, 209]. Higher doses of Na are shown to lead to smaller grain sizes, porous films and detrimental to the cell performance [204, 205]. The most obvious electronic effect of Na incorporation into CIGS films is a decrease in resistivity by up to two orders of magnitude [210–212]. In one of the recent studies [213] NaF was deposited prior to CIGS absorber and it reported that NaF precursors modify the CIGS growth kinetics: a reduction of the grain size and a slightly enhanced Ga-gradient through the absorber layer were observed. V_{OC} and FF (fill factor) increase when the Na content increases at $T_{sub, max} = 500^\circ\text{C}$ during the absorber deposition.

In other studies, Erslev et al. [214] have studied the role of sodium in CIGS solar cells using junction capacitance methods. The increase in solar cell efficiency with sodium was attributed to passivation of a defect state near the CdS/CIGS junction. Recently, Ishizuka et al. [215] have studied the variations in the structural, optical, and electrical properties of polycrystalline Cu(In,Ga)Se₂ thin films with Na doping level. Na incorporation into CIGS absorber was controlled using alkali-silicate glass thin layers. They found that the Ga composition gradient in CIGS films became larger and the grain size decreased with increasing Na concentration.

7. CdS Buffer Layers

Semiconductor compounds with n-type conductivity and band gaps between 2.0 and 3.6 eV have been applied as buffer for CIGS solar cells. However, CdS remains the most widely investigated buffer layer, as it has continuously yielded high-efficiency cells. CdS for high-efficiency CIGS cells is generally grown by a chemical bath deposition (CBD), which is a low-cost, large-area process. However, incompatibility with in-line vacuum-based production methods is a matter of concern. Physical vapor deposition- (PVD-) grown CdS layers yield lower efficiency cells, as thin layers grown by PVD do not show uniform coverage of CIGS and are ineffective in chemically engineering the interface properties. For a comprehensive review on CBD-deposited CdS see Ortega-Borges and Lincot [216] and Hodes [217].

The recent trend in buffer layers is to substitute CdS with “Cd-free” wide-bandgap semiconductors and to replace the CBD technique with in-line-compatible processes. The first approach has been to omit CdS and form a direct junction between CIGS and ZnO, but the plasma (ions) during ZnO deposition by RF sputtering can damage the CIGS surface and enhance interface recombination. Possible solutions include ZnO deposited by metal organic chemical vapor deposition (MOCVD), atomic layer deposition (ALD) or a novel technique, called ion layer gas reaction (ILGAR) [218–220]. CIS and CIGS solar cells have yielded highest efficiencies with CdS buffer layers deposited by chemical bath deposition (CBD). Omitting the buffer layer always resulted in lower efficiencies [221]. Also, as-grown CIGS cells with CdS buffers deposited by physical vapor deposition (PVD) have always shown significantly lower efficiencies than cells with CBD-CdS buffers [222, 223].

The role of the CdS buffer layer is twofold: it affects both the electrical properties of the junction and protects the junction against chemical reactions and mechanical damage. From the electric point of view the CdS layer optimizes the band alignment of the device [224, 225] and builds a sufficiently wide depletion layer that minimizes tunneling and establishes a higher contact potential that allows higher open circuit voltage value [225]. The buffer layer also play a very important role as a “mechanical buffer” because it protects the junction electrically and mechanically against the damage that may otherwise be caused by the oxide deposition (especially by sputtering). Moreover, in large-area devices the electric quality of the CIGS film is not necessarily the same over the entire area, and recombination may be enhanced at grain boundaries or by local shunts. Together with the undoped ZnO layer, CdS enables self-limitation of electric losses by preventing defective parts of the CIGS film from dominating the open circuit voltage of the entire device [226].

The thickness as well as the deposition method of the CdS layer has a large impact on device performance. During the early days, the device structure consisted of a CuInSe₂/CdS junction with a thick (about 1–3 μm) CdS layer [227–229]. The CdS layer of these devices were most often prepared by evaporation at substrate temperatures between RT and about 200°C or in some cases by sputtering [229]. Also CdS film was often doped with either In [229] or Ga [106] and in some cases a CdS bilayer was used [230, 231] consisting of a thinner high-resistive layer, prepared either by evaporation [143] or chemical bath deposition [194, 230, 231] and a thicker low-resistivity layer, doped with 2% In [231] or Ga [194]. Alternatively, evaporated CdS has been used also in combination with the transparent conducting oxide layer [232–234]. Nowadays chemical bath deposition (CBD) is used almost exclusively [235, 236].

In contrast to evaporated films [237], CBD films contain high amounts of oxygen-related impurities that originate from the deposition solution; the amount of oxygen in the films can be as high as at 10–15 at % [237, 238]. Most of the oxygen is present as OH⁻ and H₂O [237, 238]. Thus, the composition of the CBD-CdS films is more accurately stated as Cd(S,O,OH) [237]. Additional impurities such as C and

N containing compounds result from the side reactions of thiourea [238]. The amount and identity of the impurities, and consequently the performance of the solar cell, depend strongly on the CdS deposition conditions [225, 239–241]. Negami et al. [242] for instance, reported an increase of conversion efficiency from 17.6 to 18.5% when the CBD-CdS process was improved.

In addition to the CdS film deposition, the chemical bath also modifies the absorber surface region [235, 243]. Thus, the interface between CIGS and CBD-CdS is not abrupt, but the layers are intermixing to some extent [238, 244]. Both Cu and Cd diffusion play a role, and the intermixing is further enhanced during the post deposition air-annealing [226]. According to Nakada and Kunioka [238], Cu was substituted by Cd at the surface region of CIGS. The diffusion depth of Cd atoms was about 10 nm, which may be related to the thickness of the Cu-deficient surface layer (CuIn₃Se₅) of CIGS [238]. On the other hand, Heske et al. [244] observe diffusion of Se and In from CIGS into CdS and the diffusion of S from CdS into CIGS. The extent of interdiffusion depends on the structure of the absorber: (224/208) oriented CIGS films have been found to allow more Cd atoms to diffuse into the CIGS film [245].

One advantage of the CBD method as compared to evaporation is that a complete, conformal coverage of the CIGS surface can be obtained at very low thicknesses: already 10 nm has been reported to be sufficient [246]. The coverage depends on deposition conditions, particularly on the concentration ratio of the S and Cd precursors, being better with higher S/Cd precursor ratios [240].

Some studies have been conducted on the fundamental properties of CdS films deposited by an ammonia-free CBD process [247] and very few studies have used an ammonia-free buffer layer for the fabrication of a CIGS solar cell [248]. In a recent work, Mann et al. [249] has also deposited CdS by CBD and used optical reflectance-based measurement of the growing film to determine in situ film thickness.

8. Alternative Buffer Layer

As an alternative to CdS, various materials show promising results. The different buffer layer used and the deposition method for the same is tabulated in Table 2.

The Zn-based compounds tend to form a blocking barrier due to the band alignment with CIGS [253]. Using layers of less than 50 nm thickness, the barrier can be crossed by tunneling of charge carriers, but this poses high requirements on the quality of the deposition process and the CIGS surface to obtain a uniform coverage. The band offset can be reduced as well, if impurities such as hydroxides that can be present in a CBD are incorporated in the CIGS/buffer layer interface [281].

9. Front Contact

There are two main requirements for the electric front contact of a CIGS solar cell device: sufficient transparency in order to let enough light through to the underlying parts of

TABLE 2: Alternative buffer layers and their deposition methods.

Buffer Layer	Deposition Method	References
ZnS	CBD	[250–253]
ZnS	MBE	[254]
ZnS(O,OH)	CBD	[25]
ZnSe	MOCVD	[255, 256]
ZnSe	ALCVD	[257]
ZnSe	ALD	[258]
ZnSe	CBD	[259]
ZnIn ₂ Se ₄	PVD	[260]
ZnIn _x Se _y	Coevaporation	[261]
Zn _{x-y} Mg _x O	Co-sputtered	[262]
Zn _{x-y} Mg _x O	ALD	[263]
In ₂ S ₃	ALD	[264, 265]
In ₂ S ₃	ALCVD	[266]
In ₂ S ₃	MOCVD	[267]
In ₂ S ₃	PVD	[268, 269]
In ₂ S ₃	US	[270]
In ₂ S _x	Coevaporation	[271]
In _x S _y	Sputtered	[272]
In _x S _y	Coevaporation	[273, 274]
In _x (OH,S) _y	CBD	[275]
Zn(Se,OH)	CBD	[276]
Zn(S,O,OH)	CBD	[256, 277]
Zn(S,O)	CBD	[278]
	ALD	[279]
ZnS/Zn(S,O)	CBD	[280]
ZnMgO	CBD	[263]
	ALD	[278]

CBD-Chemical Bath Deposition, MBE-Molecular Beam Epitaxy, MOCVD-metalorganic chemical vapour deposition, ALCVD-Atomic Layer CVD, ALD-Atomic Layer Deposition, PVD-Physical Vapour Deposition, US-Ultrasonic spray.

the device, and sufficient conductivity to be able to transport the photo-generated current to the external circuit without too much resistance losses. Transparent conducting metal oxides (TCO) are used almost exclusively as the top contacts. Narrow lined metal grids (Ni–Al) are usually deposited on top of the TCO in order to reduce the series resistance. The quality of the front contact is thus a function of the sheet resistance, absorption and reflection of the TCO as well as the spacing of the metal grids [282].

During the early days of CIS and CIGS substrate cell development, a bilayer of undoped and doped CdS served as a buffer and front contact, respectively [283, 284]. High conductivity in doped CdS was achieved either by controlling the density of donor type defects or by extrinsic doping with Al or In [283, 284]. Spectral absorption loss in the conducting CdS layer was reduced by increasing the bandgap, alloying with ZnS or later replacing it with TCOs with bandgaps of above 3 eV [283]. Transmission spectra of various TCOs are shown in Figure 6.

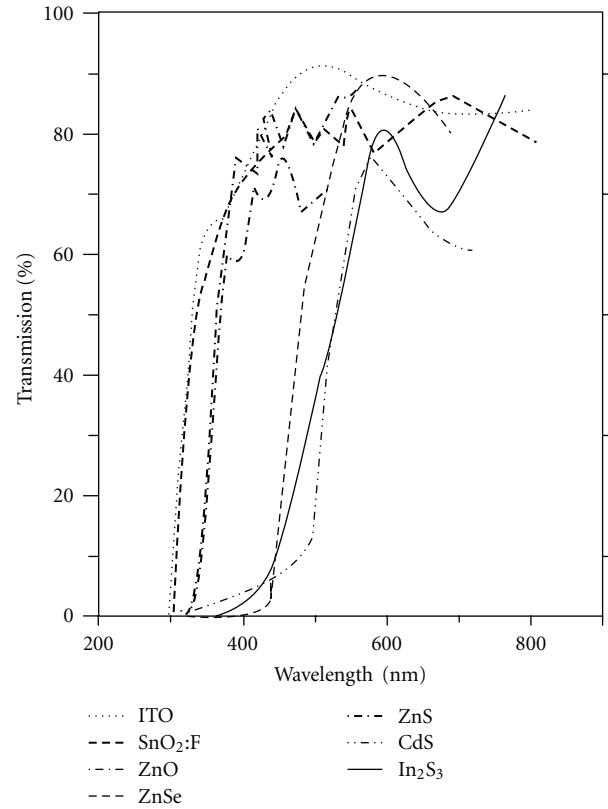


FIGURE 6: Optical transmission of different front contacts and buffer layers (from [38]).

Today, CIGS solar cells employ either tin doped In₂O₃ (In₂O₃: Sn, ITO) [285–287] or, more frequently, RF-sputtered Al-doped ZnO. A combination of an intrinsic and a doped ZnO layer is commonly used, although this double layer yields consistently higher efficiencies, the beneficial effect of intrinsic ZnO is still under discussion [226]. It has been shown that device performance increases due to the increase in V_{OC} by 20–40 mV [226]. It has been discussed that resistive oxide layer provides, together with buffer, a series resistance that protects the device from local electrical losses that may originate from inhomogeneities of the absorber [226]. Doping of the conducting ZnO layer is achieved by group III elements, particularly with aluminum [194, 288–298]. However, investigations show boron to be a feasible alternative, as it yields a high mobility of charge carriers [290, 299–304] and a higher transmission in the long-wavelength spectral region, giving rise to higher currents [305]. For high-efficiency cells the TCO deposition temperature should be lower than 150°C in order to avoid the detrimental interdiffusion across CdS/CIGS interface.

There had been some recent studies of i-ZnO and doped ZnO. Yu et al. [306] have studied the Ni and Al codoped ZnO grown by dc magnetron cosputtering. A comparative study of i-ZnO and ZnO:Al using rf magnetron sputtering and electrodeposition done by Wellings et al. [307] to be used for CIGS solar cells. Pawar et al. [308] have studied the Boron doped ZnO using spray pyrolysis.

Few [309, 310] have reported the deposition of ZnO:Al on polyimide substrate. Recently, Calnan and Tiwari have discussed in detail regarding High Mobility Transparent Conductor Oxide (HMTCO) [311].

10. Conclusion

Remarkable progress has been made in the development of high efficiency CIGS solar cells. CIGS PV modules have the potential to reach cost-effective PV-generated electricity. Transition from lab to manufacturing has been much more difficult than anticipated.

Each component of the solar cell structure and its manufacturing requires further investigation to simplify the processing and to have more efficient solar cell with lower cost. Few of the key issues related to development of CIGS solar cells are: higher module efficiency, columnar CIGS structures deposited by alternative process for high efficiency cells and modules, thinner absorber layer ($\leq 1 \mu\text{m}$), and CIGS absorber film stoichiometry and uniformity over large areas.

There is also a need to develop a robust and low temperature ($\sim 400^\circ\text{C}$) deposition process for CIGS for the flexible substrate (polyimide) to facilitate roll to roll manufacturing and to extend the application for space market.

Acknowledgments

The authors would like to thank Mr. Abdul Khader and Ms. Krishna Dalai, for their support during the work. This work has been supported by the Ministry of New & Renewable Energy (31/12/2009/PVSE), New Delhi, Department of Science & Technology (DST), New Delhi (SR/S2/CMP-30/2003), and AICTE, New Delhi (8023/BOR/RID/RPS-78/2007-08).

References

- [1] M. Kaelin, D. Rudmann, and A. N. Tiwari, "Low cost processing of CIGS thin film solar cells," *Solar Energy*, vol. 77, no. 6, pp. 749–756, 2004.
- [2] F. Kessler and D. Rudmann, "Technological aspects of flexible CIGS solar cells and modules," *Solar Energy*, vol. 77, no. 6, pp. 685–695, 2004.
- [3] D. Graham-Rowe, "Solar cells get flexible," *Nature Photonics*, vol. 1, no. 8, pp. 433–435, 2007.
- [4] M. A. Green, K. Emery, D. L. King, S. Igari, and W. Warta, "Solar cell efficiency tables (Version 22)," *Progress in Photovoltaics: Research and Applications*, vol. 11, no. 5, pp. 347–352, 2003.
- [5] I. Repins, M. A. Contreras, B. Egaas et al., "19.9%-efficient ZnO/CdS/CuInGaSe₂ solar cell with 81.2% fill factor," *Progress in Photovoltaics: Research and Applications*, vol. 16, no. 3, pp. 235–239, 2008.
- [6] B. Dimmler and R. Wächter, "Manufacturing and application of CIS solar modules," *Thin Solid Films*, vol. 515, no. 15, pp. 5973–5978, 2007.
- [7] S. Wagner, J. L. Shay, P. Migliorato, and H. M. Kasper, "CuInSe₂/CdS heterojunction photovoltaic detectors," *Applied Physics Letters*, vol. 25, no. 8, pp. 434–435, 1974.
- [8] R. R. Potter, C. Eberspacher, and L. B. Fabick, "Device analysis of CuInSe₂/(Cd,Zn)S/ZnO solar cells," in *Proceedings of the Conference Record of the 18th IEEE Photovoltaic Specialists Conference*, pp. 1659–1664, 1985.
- [9] B. M. Başol, V. K. Kapur, C. R. Leidholm, A. Halani, and K. Gledhill, "Flexible and light weight copper indium diselenide solar cells on polyimide substrates," *Solar Energy Materials and Solar Cells*, vol. 43, no. 1, pp. 93–98, 1996.
- [10] A. N. Tiwari, M. Krejci, F.-J. Haug, and H. Zogg, "12.8% efficiency Cu(In,Ga)Se₂ solar cell on a flexible polymer sheet," *Progress in Photovoltaics: Research and Applications*, vol. 7, no. 5, pp. 393–397, 1999.
- [11] G. M. Hanket, U. P. Singh, E. Eser, W. N. Shafarman, and R. W. Birkmire, "Pilot-scale manufacture of Cu(InGa)Se₂ films on a flexible polymer substrate," in *Proceedings of the 29th IEEE Photovoltaic Specialists Conference*, pp. 567–569, May 2002.
- [12] R. Birkmire, E. Eser, S. Fields, and W. Shafarman, "Cu(InGa)Se₂ solar cells on a flexible polymer web," *Progress in Photovoltaics: Research and Applications*, vol. 13, no. 2, pp. 141–148, 2005.
- [13] S. Ishizuka, H. Hommoto, N. Kido, K. Hashimoto, A. Yamada, and S. Niki, "Efficiency enhancement of Cu(In,Ga)Se₂ solar cells fabricated on flexible polyimide substrates using alkali-silicate glass thin layers," *Applied Physics Express*, vol. 1, no. 9, Article ID 092303, pp. 1–3, 2008.
- [14] P. Gečys, G. Račiukaitis, M. Gedvilas, and A. Selskis, "Laser structuring of thin-film solar cells on polymers," *EPJ Applied Physics*, vol. 46, no. 1, Article ID 12508, 2009.
- [15] L. Zhang, Q. He, W.-L. Jiang, C.-J. Li, and Y. Sun, "Flexible Cu(In,Ga)Se₂ thin-film solar cells on polyimide substrate by low-temperature deposition process," *Chinese Physics Letters*, vol. 25, no. 2, pp. 734–736, 2008.
- [16] R. Caballero, C. A. Kaufmann, T. Eisenbarth et al., "The influence of Na on low temperature growth of CIGS thin film solar cells on polyimide substrates," *Thin Solid Films*, vol. 517, no. 7, pp. 2187–2190, 2009.
- [17] H. Zachmann, S. Heinker, A. Braun et al., "Characterisation of Cu(In,Ga)Se₂-based thin film solar cells on polyimide," *Thin Solid Films*, vol. 517, no. 7, pp. 2209–2212, 2009.
- [18] T. Satoh, Y. Hashimoto, S. Shimakawa, S. Hayashi, and T. Negami, "Cigs solar cells on flexible stainless steel substrates," in *Proceedings of the Conference Record of the 28th IEEE Photovoltaic Specialists Conference*, p. 567, 2000.
- [19] K. Herz, F. Kessler, R. Wächter et al., "Dielectric barriers for flexible CIGS solar modules," *Thin Solid Films*, vol. 403–404, pp. 384–389, 2002.
- [20] D. Herrmann, F. Kessler, K. Herz et al., "High-performance barrier layers for flexible CIGS thin-film solar cells on metal foils," in *Proceedings of the Materials Research Society Symposium: Compound Semiconductor Photovoltaics*, vol. 763, pp. 287–292, San Francisco, Calif, USA, 2003.
- [21] D. R. Hollars, R. Dorn, P. D. Paulson, J. Titus, and R. Zubeck, "Large area Cu(In,Ga)Se₂ films and devices on flexible substrates made by sputtering," in *Proceedings of the Materials Research Society Spring Meeting*, pp. 477–482, April 2005, F14.34.1.
- [22] K. Otte, L. Makhova, A. Braun, and I. Konovalov, "Flexible Cu(In,Ga)Se₂ thin-film solar cells for space application," *Thin Solid Films*, vol. 511–512, pp. 613–622, 2006.
- [23] S. Ishizuka, A. Yamada, P. Fons, and S. Niki, "Flexible Cu(In,Ga)Se₂ solar cells fabricated using alkali-silicate glass thin layers as an alkali source material," *Journal of Renewable Sustainable Energy*, vol. 1, Article ID 013102, 8 pages, 2008.

- [24] R. Wuerz, A. Eicke, M. Frankenfeld et al., "CIGS thin-film solar cells on steel substrates," *Thin Solid Films*, vol. 517, no. 7, pp. 2415–2418, 2009.
- [25] T. Yagioka and T. Nakada, "Cd-free flexible Cu(In,Ga)Se₂ thin film solar cells with ZnS(O,OH) buffer layers on Ti foils," *Applied Physics Express*, vol. 2, no. 7, Article ID 072201, 3 pages, 2009.
- [26] D. Brémaud, D. Rudmann, M. Kaelin et al., "Flexible Cu(In,Ga)Se₂ on Al foils and the effects of Al during chemical bath deposition," *Thin Solid Films*, vol. 515, no. 15, pp. 5857–5861, 2007.
- [27] S. Ishizuka, A. Yamada, K. Matsubara, P. Fons, K. Sakurai, and S. Niki, "Development of high-efficiency flexible Cu(In,Ga)Se₂ solar cells: a study of alkali doping effects on CIS, CIGS, and CGS using alkali-silicate glass thin layers," *Current Applied Physics*, vol. 20, no. 2, supplement 1, pp. S154–S156, 2009.
- [28] C. Y. Shi, Y. Sun, Q. He, F. Y. Li, and J. C. Zhao, "Cu(In,Ga)Se₂ solar cells on stainless-steel substrates covered with ZnO diffusion barriers," *Solar Energy Materials and Solar Cells*, vol. 93, no. 5, pp. 654–656, 2009.
- [29] M. S. Kim, J. H. Yun, K. H. Yoon, and B. T. Ahn, "Fabrication of flexible CIGS solar cell on stainless steel substrate by co-evaporation process," *Diffusion and Defect Data B*, vol. 124–126, pp. 73–76, 2007.
- [30] D. Brémaud, D. Rudmann, G. Bilger, H. Zogg, and A. N. Tiwari, "Towards the development of flexible CIGS solar cells on polymer films with efficiency exceeding 15%," in *Proceedings of the 31st IEEE Photovoltaic Specialists Conference*, pp. 223–226, January 2005.
- [31] J. R. Tuttle, A. Szalaj, and J. Keane, "A 15.2 % AM0 / 1433 W/kg thin-film Cu(In,Ga)Se₂ solar cell for space applications," in *Proceedings of the 28th IEEE Photovoltaic Specialists Conference*, pp. 1042–1045, Anchorage, Alaska, 2000.
- [32] S. Ishizuka, "Flexible CIGS photovoltaic cell with energy conversion efficiency of 17.7%—enabling development of a sticker-type high-performance solar cell," *AIST Today*, vol. 8, no. 10, p. 20, 2008.
- [33] J. F. Guillemoles, "The puzzle of Cu(In,Ga)Se₂ (CIGS) solar cells stability," *Thin Solid Films*, vol. 403–404, pp. 405–409, 2002.
- [34] J. Poortmans and V. Archipov, *Thin Film Solar Cells*, John Wiley & Sons, New York, NY, USA, 2006.
- [35] A. Luque and S. Hegeds, Eds., *Handbook of Photovoltaic Science & Engineering*, John Wiley & Sons, New York, NY, USA, 2003.
- [36] T. Markvant and L. Castarier, Eds., *Practical handbook of Photovoltaics: Fundamentals and Applications*, Elsevier, Amsterdam, The Netherlands, 2003.
- [37] M. D. Archer and R. Hill, Eds., *Clean Electricity from Photovoltaics*, vol. 1, chapter 7 of *Series on Photoconversion of Solar Energy*, 2001.
- [38] A. Romeo, M. Terheggen, D. Abou-Ras et al., "Development of thin-film Cu(In,Ga)Se₂ and CdTe solar cells," *Progress in Photovoltaics: Research and Applications*, vol. 12, no. 2–3, pp. 93–111, 2004.
- [39] M. Kemell, M. Ritala, and M. Leskelä, "Thin film deposition methods for CuInSe₂ solar cells," *Critical Reviews in Solid State and Materials Science*, vol. 30, no. 1, pp. 1–31, 2005.
- [40] J.-F. Guillemoles, L. Kronik, D. Cahen, U. Rau, A. Jasenek, and H.-W. Schock, "Stability issues of Cu(In,Ga)Se₂-based solar cells," *Journal of Physical Chemistry B*, vol. 104, no. 20, pp. 4849–4862, 2000.
- [41] S. Duchemin, V. Chen, J. C. Yoyotte, J. Bougnot, and M. Savelli, "Backwall CdS(n)-CuInSe₂(p) sprayed solar cells," in *Proceedings of the 8th European Photovoltaic Solar Energy Conference*, pp. 1038–1042, Florence, Italy, 1988.
- [42] T. Nakada, N. Okano, Y. Tanaka, H. Fukuda, and A. Kunioka, "Superstrate-type CuInSe₂ with chemically deposited CdS window layers," in *Proceedings of the IEEE 1st World Conference on Photovoltaic Energy Conversion*, pp. 95–98, Hawaii, USA, 1994.
- [43] T. Nakada and T. Mise, "High-efficiency superstrate type cigs thin film solar cells with graded bandgap absorber layers," in *Proceedings of the 17th European Photovoltaic Solar Energy Conference*, pp. 1027–1030, Munich, Germany, 2001.
- [44] F.-J. Haug, D. Rudmann, G. Bilger, H. Zogg, and A. N. Tiwari, "Comparison of structural and electrical properties of Cu(In,Ga)Se₂ for substrate and superstrate solar cells," *Thin Solid Films*, vol. 403–404, pp. 293–296, 2002.
- [45] F.-J. Haug, M. Krejci, H. Zogg, A. N. Tiwari, M. Kirsch, and S. Siebentritt, "Characterization of CuGa_xSe_y/ZnO for superstrate solar cells," *Thin Solid Films*, vol. 361, pp. 239–242, 2000.
- [46] M. Terheggen, H. Heinrich, G. Kostorz, F.-J. Haug, H. Zogg, and A. N. Tiwari, "Ga₂O₃ segregation in Cu(In,Ga)Se₂/ZnO superstrate solar cells and its impact on their photovoltaic properties," *Thin Solid Films*, vol. 403–404, pp. 212–215, 2002.
- [47] F.-J. Haug, D. Rudmann, H. Zogg, and A. N. Tiwari, "Light soaking effects in Cu(In,Ga)Se₂ superstrate solar cells," *Thin Solid Films*, vol. 431–432, pp. 431–435, 2003.
- [48] R. Klenk, R. Mauch, R. Schäffler, D. Schmid, and H. W. Schock, "Progress in CuGaSe₂ based thin film solar cells," in *Proceedings of the 22nd IEEE Photovoltaic Specialists Conference*, pp. 1071–1076, October 1991.
- [49] A. Kampmann, A. Abken, G. Leimkühler et al., "Cadmium-free CuInSe₂ superstrate solar cell fabricated by electrodeposition using a ITO/In₂Se₃/CuInSe₂/Au structure," *Progress in Photovoltaics: Research and Applications*, vol. 7, no. 2, pp. 129–135, 1999.
- [50] T. Yoshida and R. W. Birkmire, "Fabrication of CuInSe₂ solar cells in a superstrate configuration," in *Proceedings of the 11th EC Photovoltaic Solar Energy Conference*, p. 811, 1992.
- [51] T. Negami, M. Nishitani, M. Ikeda, and T. Wada, "Preparation of CuInSe₂ films on large grain CdS films for superstrate-type solar cells," *Solar Energy Materials and Solar Cells*, vol. 35, no. C, pp. 215–222, 1994.
- [52] T. Nakada, Y. Hirabayashi, T. Tokado, D. Ohmori, and T. Mise, "Novel device structure for Cu(In,Ga)Se₂ thin film solar cells using transparent conducting oxide back and front contacts," *Solar Energy*, vol. 77, no. 6, pp. 739–747, 2004.
- [53] S. Nishiwaki, S. Siebentritt, P. Walk, and M. Ch. Lux-Steiner, "A stacked chalcopyrite thin-film tandem solar cell with 1.2 V open-circuit voltage," *Progress in Photovoltaics: Research and Applications*, vol. 11, no. 4, pp. 243–248, 2003.
- [54] S. A. Alagappan and S. Mitra, "Optimizing the design of CIGS-based solar cells: a computational approach," *Materials Science and Engineering B*, vol. 116, no. 3, pp. 293–296, 2005.
- [55] T. Nakada, S. Kijima, Y. Kuromiya et al., "Chalcopyrite thin-film tandem solar cells with 1.5 V open-circuit-voltage," in *Proceedings of the IEEE 4th World Conference on Photovoltaic Energy Conversion (WCPEC '06)*, vol. 1, pp. 400–403, May 2006.

- [56] M. W. Wang, "Novel CdSe-based PV structure for high efficiency CdSe/CIGS tandem solar cells," in *Proceedings of the 34th IEEE Photovoltaic Specialists Conference (PVSC '09)*, pp. 489–493, Philadelphia, Pa, USA, June 2009.
- [57] J. H. Scofield, A. Duda, D. Albin, B. L. Ballard, and P. K. Predecki, "Sputtered molybdenum bilayer back contact for copper indium diselenide-based polycrystalline thin-film solar cells," *Thin Solid Films*, vol. 260, no. 1, pp. 26–31, 1995.
- [58] R. J. Matson, O. Jamjoum, A. D. Buonaquisti et al., "Metal contacts to CuInSe₂," *Solar Cells*, vol. 11, no. 3, pp. 301–305, 1984.
- [59] E. Moons, T. Engelhard, and D. Cahen, "Ohmic contacts to p-CuInSe₂ crystals," *Journal of Electronic Materials*, vol. 22, no. 3, pp. 275–280, 1993.
- [60] M. Powalla and B. Dimmler, "Scaling up issues of CIGS solar cells," *Thin Solid Films*, vol. 361, pp. 540–546, 2000.
- [61] R. Menner, E. Gross, A. Eicke, et al., in *Proceedings of the 13th European Photovoltaic Solar Energy Conference*, p. 2067, Nice, France, 1995.
- [62] R. A. Hoffman, J. C. Lin, and J. P. Chambers, "The effect of ion bombardment on the microstructure and properties of molybdenum films," *Thin Solid Films*, vol. 206, no. 1-2, pp. 230–235, 1991.
- [63] K. Granath, A. Rockett, M. Bodegard, C. Nender, and L. Stolt, "Mechanical issues of Mo back contacts for Cu(In,Ga)Se₂ devices," in *Proceedings of the 13th European Photovoltaic Solar Energy Conference*, pp. 1983–1986, Nice, France, 1995.
- [64] G. Gordillo, M. Grizález, and L. C. Hernandez, "Structural and electrical properties of DC sputtered molybdenum films," *Solar Energy Materials and Solar Cells*, vol. 51, no. 3-4, pp. 327–337, 1998.
- [65] M. A. Martínez and C. Guillén, "Effect of r.f.-sputtered Mo substrate on the microstructure of electrodeposited CuInSe₂ thin films," *Surface and Coatings Technology*, vol. 110, no. 1-2, pp. 62–67, 1998.
- [66] K. H. Yoon, S. K. Kim, R. B. V. Chalapathy et al., "Characterization of a molybdenum electrode deposited by sputtering and its effect on Cu(In,Ga)Se₂ solar cells," *Journal of the Korean Physical Society*, vol. 45, no. 4, pp. 1114–1118, 2004.
- [67] K. Orgassa, H. W. Schock, and J. H. Werner, "Alternative back contact materials for thin film Cu(In,Ga)Se₂ solar cells," *Thin Solid Films*, vol. 431-432, pp. 387–391, 2003.
- [68] P. E. Russell, O. Jamjoum, R. K. Ahrenkiel, L. L. Kazmerski, R. A. Mickelsen, and W. S. Chen, "Properties of the Mo-CuInSe₂ interface," *Applied Physics Letters*, vol. 40, no. 11, pp. 995–997, 1982.
- [69] W. Jaegaermann, T. Löher, and C. Pettenkofer, "Surface properties of chalcopyrite semiconductors," *Crystal Research and Crystal Technology*, vol. 31, p. 273, 1996.
- [70] W. N. Shafarman and J. E. Phillips, "Direct current-voltage measurements of the Mo/CuInSe₂ contact on operating solar cells," in *Proceedings of the 25th IEEE Photovoltaic Specialists Conference*, pp. 917–919, Washington, DC, USA, May 1996.
- [71] S. Raud and M.-A. Nicolet, "Study of the CuInSe₂/Mo thin film contact stability," *Thin Solid Films*, vol. 201, no. 2, pp. 361–371, 1991.
- [72] N. Kohara, S. Nishiwaki, Y. Hashimoto, T. Negami, and T. Wada, "Electrical properties of the Cu(In,Ga)Se₂/MoSe₂/Mo structure," *Solar Energy Materials and Solar Cells*, vol. 67, no. 1-4, pp. 209–215, 2001.
- [73] K. M. Jones, L. L. Kazmerski, and B. G. Yacobi, "Transmission electron microscopy and X-ray photoelectron spectroscopy investigations of the MoCuInSe₂ interface," *Thin Solid Films*, vol. 116, no. 1-3, pp. L59–L62, 1984.
- [74] D. Schmid, M. Ruckh, and H. W. Schock, "A comprehensive characterization of the interfaces in Mo/CIS/CdS/ZnO solar cell structures," *Solar Energy Materials and Solar Cells*, vol. 41-42, pp. 281–294, 1996.
- [75] T. Wada, N. Kohara, S. Nishiwaki, and T. Negami, "Characterization of the Cu(In,Ga)Se₂/Mo interface in CIGS solar cells," *Thin Solid Films*, vol. 387, no. 1-2, pp. 118–122, 2001.
- [76] S. Nishiwaki, N. Kohara, T. Negami, M. Nishitani, and T. Wada, "Characterization of Cu(In,Ga)Se₂/Mo interface in CIGS solar cells," in *Materials Research Society Symposium Proceedings*, vol. 485, p. 139, 1997.
- [77] S. Nishiwaki, N. Kohara, T. Negami, and T. Wada, "MoSe₂ layer formation at Cu(In,Ga)Se₂/Mo interfaces in high efficiency Cu(In_{1-x}Ga_x)Se₂ Solar Cells," *Japanese Journal of Applied Physics. Part 2*, vol. 37, no. 1, pp. L71–L73, 1998.
- [78] T. Wada, N. Kohara, T. Negami, and M. Nishitani, "Chemical and structural characterization of Cu(In, Ga)Se₂/Mo interface in Cu(In, Ga)Se₂ solar cells," *Japanese Journal of Applied Physics*, vol. 35, no. 10, pp. L1253–L1256, 1996.
- [79] L. Assmann, J. C. Bernède, A. Drici, C. Amory, E. Halgand, and M. Morsli, "Study of the Mo thin films and Mo/CIGS interface properties," *Applied Surface Science*, vol. 246, no. 1–3, pp. 159–166, 2005.
- [80] Y. K. Shimizu, S. Shimada, M. Watanabe et al., "Effects of Mo back contact thickness on the properties of CIGS solar cells," *Physica Status Solidi A*, vol. 206, no. 5, pp. 1063–1066, 2009.
- [81] R. Würz, D. Fuertes Marwón, A. Meeder et al., "Formation of an interfacial MoSe₂ layer in CVD grown CuGaSe₂ based thin film solar cells," *Thin Solid Films*, vol. 431-432, pp. 398–402, 2003.
- [82] C. Ballif, H. R. Moutinho, F. S. Hasoon, R. G. Dhere, and M. M. Al-Jassim, "Cross-sectional atomic force microscopy imaging of polycrystalline thin films," *Ultramicroscopy*, vol. 85, no. 2, pp. 61–71, 2000.
- [83] L. Zhang, Q. He, W.-L. Jiang, F.-F. Liu, C.-J. Li, and Y. Sun, "Mo back contact for flexible polyimide substrate Cu(In, Ga)Se₂ thin-film solar cells," *Chinese Physics Letters*, vol. 25, no. 9, pp. 3452–3454, 2008.
- [84] C. Guillén and J. Herrero, "Low-resistivity Mo thin films prepared by evaporation onto 30 cm × 30 cm glass substrates," *Journal of Materials Processing Technology*, vol. 143-144, no. 1, pp. 144–147, 2003.
- [85] B. M. Basol, V. K. Kapur, C. R. Leidholm, A. Minnickand, and A. Halani, "Studies on substrates and contacts for CIS films and devices," in *Proceedings of the IEEE 1st World Conference on Photovoltaic Energy Conversion*, pp. 148–151, Hawaii, USA, 1994.
- [86] D. C. Fishor, I. L. Repins, J. Schafor, et al., "The effect of Mo morphology on the performance of Cu(In,Ga)Se₂ thin films," in *Proceedings of the 31st IEEE Photovoltaic Specialists Conference (PVSEC '05)*, p. 371, 2005.
- [87] V. Mohanakrishnaswamy, H. Sankaranarayanan, S. Pethe, C. S. Ferekides, and D. L. Morel, "The effect of Mo deposition conditions on defect formation and device performance for CIGS solar cells," in *Proceedings of the 31st IEEE Photovoltaic Specialists Conference (PVSEC '05)*, pp. 422–425, Tampa, Fla, USA, 2005.
- [88] J. H. Y., K. H. Kim, Y. T. Ahn, and K. H. Yoon, "Effect of Na-doped Mo/Mo bilayer on CIGS cells and its photovoltaic properties," in *Proceedings of the IEEE 4th World Conference on Photovoltaic Energy Conversion (WCPEC '06)*, pp. 509–511, May 2006.

- [89] T. Nakada, "Microstructural and diffusion properties of CIGS thin film solar cells fabricated using transparent conducting oxide back contacts," *Thin Solid Films*, vol. 480-481, pp. 419-425, 2005.
- [90] T. Haalboom, T. Godecke, F. Ernst, M. Ruhle, R. Herberholz, and H. W. Schock, "Phase relations and microstructure in bulk materials and thin films of the ternary system Cu-In-Se," in *Proceedings of the 11th International Conference on Ternary and Multinary Compounds*, pp. 249-252, Salford, UK, 1998.
- [91] J. C. Mikkelsen, "Ternary phase relations of the chalcopyrite compound CuGaSe_2 ," *Journal of Electronic Materials*, vol. 10, no. 3, pp. 541-558, 1981.
- [92] H. Jitsukawa, H. Matsushita, and T. Takizawa, "Phase diagrams of the $(\text{Cu}_2\text{Se}, \text{CuSe})\text{-CuGaSe}_2$ system and the crystal growth of CuGaSe_2 by the solution method," *Journal of Crystal Growth*, vol. 186, no. 4, pp. 587-593, 1998.
- [93] U. Rau, M. Schmitt, J. Parisi, W. Riedl, and F. Karg, "Persistent photoconductivity in $\text{Cu}(\text{In,Ga})\text{Se}_2$ heterojunctions and thin films prepared by sequential deposition," *Applied Physics Letters*, vol. 73, no. 2, pp. 223-225, 1998.
- [94] V. Nadenau, D. Hariskos, H.-W. Schock et al., "Microstructural study of the $\text{CdS}/\text{CuGaSe}_2$ interfacial region in CuGaSe_2 thin film solar cells," *Journal of Applied Physics*, vol. 85, no. 1, pp. 534-542, 1999.
- [95] D. Mattox, *Handbook of Physical Vapor Deposition (PVD) Processing*, Noyes, Park Ridge, NJ, USA, 1998.
- [96] W. N. Shafarman and J. Zhu, "Effect of substrate temperature and deposition profile on evaporated $\text{Cu}(\text{In,Ga})\text{Se}_2$ films and devices," *Thin Solid Films*, vol. 361, pp. 473-477, 2000.
- [97] R. A. Mickelsen and W. S. Chen, "High photocurrent polycrystalline thin-film $\text{CdS}/\text{CuInSe}_2$ solar cell," *Applied Physics Letters*, vol. 36, no. 5, pp. 371-373, 1980.
- [98] R. A. Mickelsen and W. S. Chen, "Development of a 9.4% efficient thin-film $\text{CuInSe}/2/\text{CdS}$ solar cell," in *Proceedings of the 15th IEEE Photovoltaic Specialists Conference*, pp. 800-804, 1981.
- [99] R. Klenk, T. Walter, H.-W. Schock, and D. Cahen, "A model for the successful growth of polycrystalline films of CuInSe_2 by multisource physical vacuum evaporation," *Advanced Materials*, vol. 5, no. 2, pp. 114-119, 1993.
- [100] J. R. Tuttle, M. Contreras, A. Tennant, D. Albin, and R. Noufi, "High efficiency thin-film $\text{Cu}(\text{In,Ga})\text{Se}_2$ -based photovoltaic devices: progress towards a universal approach to absorber fabrication," in *Proceedings of the 23rd IEEE Photovoltaic Specialists Conference*, pp. 415-421, New York, NY, USA, May 1993.
- [101] J. S. Park, Z. Dong, S. Kim, and J. H. Perepezko, " CuInSe_2 phase formation during $\text{Cu}_2\text{Se}/\text{In}_2\text{Se}_3$ interdiffusion reaction," *Journal of Applied Physics*, vol. 87, no. 8, pp. 3683-3690, 2000.
- [102] J. Kessler, K. O. Velthaus, M. Ruekh, et al., in *Proceedings of the 6th Photovoltaic Science and Engineering Conference (PVSEC '92)*, pp. 1005-1010, New Delhi, India, 1992.
- [103] A. Gabor, J. Tuttle, D. Albin, et al., "High efficiency polycrystalline $\text{Cu}(\text{In,Ga})\text{Se}_2$ -based solar cells," in *Proceedings of the 12th NREL Photovoltaic Program Review*, pp. 59-66, Denver, Colo, USA, 1993.
- [104] S. Zweigart, T. Walter, C. Koble, S. M. Sun, U. Ruhle, and H. W. Schock, "Sequential deposition of $\text{Cu}(\text{In,Ga})(\text{S,Se})_2$," in *Proceedings of the IEEE 1st World Conference on Photovoltaic Energy Conversion*, vol. 1, pp. 60-67, Hawaii, USA, 1994.
- [105] A. M. Gabor, J. R. Tuttle, M. H. Bode et al., "Band-gap engineering in $\text{Cu}(\text{In,Ga})\text{Se}_2$ thin films grown from $(\text{In,Ga})_2\text{Se}_3$ precursors," *Solar Energy Materials and Solar Cells*, vol. 41-42, pp. 247-260, 1996.
- [106] L. Stolt, J. Hedström, J. Kessler, M. Ruckh, K.-O. Velthaus, and H.-W. Schock, " $\text{ZnO}/\text{CdS}/\text{CuInSe}_2$ thin-film solar cells with improved performance," *Applied Physics Letters*, vol. 62, no. 6, pp. 597-599, 1993.
- [107] G. M. Hanket, P. D. Paulson, U. P. Singh, et al., "Fabrication of graded $\text{Cu}(\text{In,Ga})\text{Se}_2$ films by inline evaporation," in *Proceedings of the IEEE Photovoltaic Specialists Conference (PVSC '00)*, p. 499, 2000.
- [108] M. Marudachalam, H. Hichri, R. Klenk, R. W. Birkmire, W. N. Shafarman, and J. M. Schultz, "Preparation of homogeneous $\text{Cu}(\text{In,Ga})\text{Se}_2$ films by selenization of metal precursors in H_2Se atmosphere," *Applied Physics Letters*, vol. 67, p. 3978, 1995.
- [109] A. M. Hermann, C. Gonzalez, P. A. Ramakrishnan et al., "Fundamental studies on large area $\text{Cu}(\text{In,Ga})\text{Se}_2$ films for high efficiency solar cells," *Solar Energy Materials and Solar Cells*, vol. 70, no. 3, pp. 345-361, 2001.
- [110] J. Zank, M. Mehlin, and H. P. Fritz, "Electrochemical codeposition of indium and gallium for chalcopyrite solar cells," *Thin Solid Films*, vol. 286, no. 1-2, pp. 259-263, 1996.
- [111] K. T. Ramakrishna Reddy, P. K. Datta, and M. J. Carter, "Detection of crystalline phases in CuInSe_2 films grown by selenization process," *Physica Status Solidi A*, vol. 182, no. 2, pp. 679-685, 2000.
- [112] F. O. Adurodija, J. Song, S. D. Kim et al., "Growth of CuInSe_2 thin films by high vapour Se treatment of co-sputtered Cu-In alloy in a graphite container," *Thin Solid Films*, vol. 338, no. 1-2, pp. 13-19, 1999.
- [113] M. Marudachalam, R. W. Birkmire, H. Hichri, J. M. Schultz, A. Swartzlander, and M. M. Al-Jassim, "Phases, morphology, and diffusion in $\text{Cu}(\text{In}_{1-x}\text{Ga}_x)\text{Se}_2$ thin films," *Journal of Applied Physics*, vol. 82, no. 6, pp. 2896-2905, 1997.
- [114] C. Guillén, M. A. Martínez, and J. Herrero, " CuInSe_2 thin films obtained by a novel electrodeposition and sputtering combined method," *Vacuum*, vol. 58, no. 4, pp. 594-601, 2000.
- [115] R. Caballero and C. Guillén, "Comparative studies between Cu-Ga-Se and Cu-In-Se thin film systems," *Thin Solid Films*, vol. 403-404, pp. 107-111, 2002.
- [116] Ö. F. Yüksel, B. M. Basol, H. Safak, and H. Karabiyik, "Optical characterisation of CuInSe_2 thin films prepared by two-stage process," *Applied Physics A*, vol. 73, no. 3, pp. 387-389, 2001.
- [117] A. G. Chowles, J. H. Neethling, H. Van Niekerk, J. A. A. Engelbrecht, and V. J. Watters, "Deposition and characterization of CuInSe_2 ," *Renewable Energy*, vol. 6, no. 5-6, pp. 613-618, 1995.
- [118] S. Bandyopadhyaya, S. Roy, S. Chaudhuri, and A. K. Pal, " $\text{CuIn}(\text{S}_x\text{Se}_{1-x})_2$ films prepared by graphite box annealing of In/Cu stacked elemental layers," *Vacuum*, vol. 62, no. 1, pp. 61-73, 2001.
- [119] C. Guillén and J. Herrero, "Structure, morphology and photoelectrochemical activity of CuInSe_2 thin films as determined by the characteristics of evaporated metallic precursors," *Solar Energy Materials and Solar Cells*, vol. 73, no. 2, pp. 141-149, 2002.
- [120] M. S. Sadigov, M. Özkan, E. Bacaksiz, M. Altunbaş, and A. I. Kopya, "Production of CuInSe_2 thin films by a sequential processes of evaporations and selenization," *Journal of Materials Science*, vol. 34, no. 18, pp. 4579-4584, 1999.

- [121] T. L. Chu, S. S. Chu, S. C. Lin, and J. Yue, "Large grain copoer indium diselenide films," *Journal of the Electrochemical Society*, vol. 131, no. 9, pp. 2182–2185, 1984.
- [122] J. Bekker, V. Alberts, and M. J. Witcomb, "Influence of selenization techniques on the reaction kinetics of chalcopyrite thin films," *Thin Solid Films*, vol. 387, no. 1-2, pp. 40–43, 2001.
- [123] S. F. Chichibu, M. Sugiyama, M. Ohbasami et al., "Use of diethylselenide as a less-hazardous source for preparation of CuInSe₂ photo-absorbers by selenization of metal precursors," *Journal of Crystal Growth*, vol. 243, no. 3-4, pp. 404–409, 2002.
- [124] A. Garg, K. S. Balakrishnan, and A. C. Rastogi, "Structural properties and growth mechanism of copper and indium selenide films prepared by electrochemical selenization of metal layers," *Journal of the Electrochemical Society*, vol. 141, no. 6, pp. 1566–1572, 1994.
- [125] A. C. Rastogi, K. S. Balakrishnan, R. K. Sharma, and K. Jain, "Growth phases during electrochemical selenization of vacuum deposited CuIn metal layers for the formation of semiconducting CuInSe₂ films," *Thin Solid Films*, vol. 357, no. 2, pp. 179–188, 1999.
- [126] C. Guillén and J. Herrero, "New approaches to obtain CuIn_{1-x}Ga_xSe₂ thin films by combining electrodeposited and evaporated precursors," *Thin Solid Films*, vol. 323, no. 1-2, pp. 93–98, 1998.
- [127] V. Alberts, M. Klenk, and E. Bucher, "Phase separation and compositional changes in two-stage processed chalcopyrite thin films," *Thin Solid Films*, vol. 387, no. 1-2, pp. 44–46, 2001.
- [128] F. B. Dejene, "The structural and material properties of CuInSe₂ and Cu(In,Ga)Se₂ prepared by selenization of stacks of metal and compound precursors by Se vapor for solar cell applications," *Solar Energy Materials and Solar Cells*, vol. 93, no. 5, pp. 577–582, 2009.
- [129] F. B. Dejene, "Material and device properties of Cu(In,Ga)Se₂ absorber films prepared by thermal reaction of InSe/Cu/GaSe alloys to elemental Se vapor," *Current Applied Physics*, vol. 10, no. 1, pp. 36–40, 2010.
- [130] N. M. Shah, C. J. Panchal, V. A. Kheraj, J. R. Ray, and M. S. Desai, "Growth, structural and optical properties of copper indium diselenide thin films deposited by thermal evaporation method," *Solar Energy*, vol. 83, no. 5, pp. 753–760, 2009.
- [131] N. M. Shah, J. R. Ray, K. J. Patel et al., "Structural, electrical, and optical properties of copper indium diselenide thin film prepared by thermal evaporation method," *Thin Solid Films*, vol. 517, no. 13, pp. 3639–3644, 2009.
- [132] S. P. Grindle, C. W. Smith, and S. D. Mittleman, "Preparation and properties of CuInS₂ thin films produced by exposing sputtered Cu-In films to an H₂S atmosphere," *Applied Physics Letters*, vol. 35, no. 1, pp. 24–26, 1979.
- [133] R. Gay, et al., "Efficiency and process improvements in CuInSe₂-based modules," in *Proceedings of the 12th European Photovoltaic Solar Energy Conference*, pp. 935–938, 1994.
- [134] V. Alberts, J. Titus, and R. W. Birkmire, "Material and device properties of single-phase Cu(In,Ga)(Se,S)₂ alloys prepared by selenization/sulfurization of metallic alloys," *Thin Solid Films*, vol. 451–452, pp. 207–211, 2004.
- [135] K. Kushiya, M. Tachiyuki, T. Kase et al., "Fabrication of graded band-gap Cu(InGa)Se₂ thin-film mini-modules with a Zn(O,S,OH)_x buffer layer," *Solar Energy Materials and Solar Cells*, vol. 49, no. 1–4, pp. 277–283, 1997.
- [136] Y. Tanaka, N. Akema, T. Morishita, D. Okumura, and K. Kushiya, "Improvement of V_{oc} upward of 600 mV/cell with CIGS-based absorber prepared by Selenization/Sulfurization," in *Proceedings of the 17th European Photovoltaic Solar Energy Conference*, pp. 989–994, Munich, Germany, 2001.
- [137] Y. Goushi, H. Hakuma, K. Tabuchi, S. Kijima, and K. Kushiya, "Fabrication of pentanary Cu(InGa)(SeS)₂ absorbers by selenization and sulfurization," *Solar Energy Materials and Solar Cells*, vol. 93, no. 8, pp. 1318–1320, 2009.
- [138] V. Probst, W. Stetter, W. Riedl et al., "Rapid CIS-process for high efficiency PV-modules: development towards large area processing," *Thin Solid Films*, vol. 387, no. 1-2, pp. 262–267, 2001.
- [139] V. K. Kapur, B. M. Basol, and E. S. Tseng, "Low cost methods for the production of semiconductor films for CuInSe₂/CdS solar cells," *Solar Cells*, vol. 21, no. 1–4, pp. 65–72, 1987.
- [140] H. Sato, et al., "Fabrication of high efficiency CuIn(Ga)Se₂ thin film solar cell by selenization with H₂Se," in *Proceedings of the 23rd IEEE Photovoltaic Specialist Conference*, p. 521, 1993.
- [141] J. Kessler, H. Dittrich, F. Grunwald, and H. Schock, in *Proceedings of the 10th European Conference on Photovoltaic Solar Energy Conversion*, p. 879, 1991.
- [142] H. Oumous, in *Proceedings of the 9th European Conference on Photovoltaic Solar Energy Conversion*, p. 153, 1992.
- [143] F. Karg, et al., "Novel rapid-thermal-processing for CIS thin-film solar cells," in *Proceedings of the 23rd IEEE Photovoltaic Specialists Conference*, pp. 441–446, 1993.
- [144] G. D. Mooney, A. M. Hermann, J. R. Tuttle, D. S. Albin, and R. Noufi, "Formation of CuInSe₂ thin films by rapid thermal recrystallization," *Applied Physics Letters*, vol. 58, no. 23, pp. 2678–2680, 1991.
- [145] G. S. Chen, J. C. Yang, Y. C. Chan, L. C. Yang, and W. Huang, "Another route to fabricate single-phase chalcogenides by post-selenization of Cu-In-Ga precursors sputter deposited from a single ternary target," *Solar Energy Materials and Solar Cells*, vol. 93, no. 8, pp. 1351–1355, 2009.
- [146] M. A. Green, K. Emery, Y. Hishikawa, and W. Warta, "Solar cell efficiency tables (version 31)," *Progress in Photovoltaics: Research and Applications*, vol. 16, no. 1, pp. 61–67, 2008.
- [147] K. Zweibel, "Issues in thin film PV manufacturing cost reduction," *Solar Energy Materials and Solar Cells*, vol. 59, no. 1, pp. 1–18, 1999.
- [148] M. Kaelin, D. Rudmann, and A. N. Tiwari, "Low cost processing of CIGS thin film solar cells," *Solar Energy*, vol. 77, no. 6, pp. 749–756, 2004.
- [149] C. J. Hibberd, E. Chassaing, W. Liu, D. B. Mitzi, D. Lincot, and A. N. Tiwari, "Non-vacuum methods for formation of Cu(In,Ga)(Se,S)₂ thin film photovoltaic absorbers," *Progress in Photovoltaics: Research and Applications*.
- [150] F. Kang, J. Ao, G. Sun, Q. He, and Y. Sun, "Properties of CuIn_xGa_{1-x}Se₂ thin films grown from electrodeposited precursors with different levels of selenium content," *Current Applied Physics*, vol. 10, no. 3, pp. 886–888, 2010.
- [151] Y. Lai, F. Liu, Z. Zhang et al., "Cyclic voltammetry study of electrodeposition of Cu(In,Ga)Se₂ thin films," *Electrochimica Acta*, vol. 54, no. 11, pp. 3004–3010, 2009.
- [152] S. Yoon, T. Yoon, K.-S. Lee, S. Yoon, J. M. Ha, and S. Choe, "Nanoparticle-based approach for the formation of CIS solar cells," *Solar Energy Materials and Solar Cells*, vol. 93, no. 6-7, pp. 783–788, 2009.

- [153] J. W. Park, Y. W. Choi, E. Lee, O. S. Joo, S. Yoon, and B. K. Min, "Synthesis of CIGS absorber layers via a paste coating," *Journal of Crystal Growth*, vol. 311, no. 9, pp. 2621–2625, 2009.
- [154] R. Kaigawa, T. Uesugi, T. Yoshida, S. Merdes, and R. Klenk, "Instantaneous preparation of CuInSe₂ films from elemental In, Cu, Se particles precursor films in a non-vacuum process," *Thin Solid Films*, vol. 517, no. 7, pp. 2184–2186, 2009.
- [155] J. Olejníček, C. A. Kamler, A. Mirasano et al., "A non-vacuum process for preparing nanocrystalline CuIn_{1-x}Ga_xSe₂ materials involving an open-air solvothermal reaction," *Solar Energy Materials and Solar Cells*, vol. 94, no. 1, pp. 8–11, 2010.
- [156] D. B. Mitzi, M. Yuan, W. Liu et al., "A high-efficiency solution-deposited thin-film photovoltaic device," *Advanced Materials*, vol. 20, no. 19, pp. 3657–3662, 2008.
- [157] D. B. Mitzi, M. Yuan, W. Liu et al., "Hydrazine-based deposition route for device-quality CIGS films," *Thin Solid Films*, vol. 517, no. 7, pp. 2158–2162, 2009.
- [158] W. Liu, D. B. Mitzi, M. Yuan, A. J. Kellock, S. J. Chey, and O. Gunawan, "12% efficiency CuIn(S₂)₂ photovoltaic device prepared using a hydrazine solution process," *Chemistry of Materials*, vol. 22, no. 3, pp. 1010–1014, 2010.
- [159] W. W. Hou, B. Bob, S.-h. Li, and Y. Yang, "Low-temperature processing of a solution-deposited CuInSSe thin-film solar cell," *Thin Solid Films*, vol. 517, no. 24, pp. 6853–6856, 2009.
- [160] E. Ahmed, A. Zegadi, A. E. Hill, R. D. Pilkington, R. D. Tomlinson, and W. Ahmed, "Thermal annealing of flash evaporated Cu(In, Ga)Se₂ thin films," *Journal of Materials Processing Technology*, vol. 300, no. 3-4, pp. 260–265, 1998.
- [161] R. N. Bhattacharya, J. F. Hiltner, W. Batchelor, M. A. Contreras, R. N. Noufi, and J. R. Sites, "15.4% CuIn_{1-x}Ga_xSe₂-based photovoltaic cells from solution-based precursor films," *Thin Solid Films*, vol. 361, pp. 396–399, 2000.
- [162] M. Krunk, O. Kijatkina, H. Rebane, I. Oja, V. Mikli, and A. Mere, "Composition of CuInS₂ thin films prepared by spray pyrolysis," *Thin Solid Films*, vol. 403-404, pp. 71–75, 2002.
- [163] A. Katerski, A. Mere, V. Kazlauskienė et al., "Surface analysis of spray deposited copper indium disulfide films," *Thin Solid Films*, vol. 516, no. 20, pp. 7110–7115, 2008.
- [164] K. T. R. Reddy and R. W. Miles, "Surface characterization of sprayed CuGa_xIn_{1-x}Se₂ layers," *Journal of Materials Science: Materials in Electronics*, vol. 14, no. 9, pp. 529–532, 2003.
- [165] N. Romeo, V. Canevari, G. Sberveglieri, O. Vigil, and L. Zanotti, "CuGa_xIn_{1-x}Se₂ thin films for solar cells prepared by flash-evaporation," *Solar Energy Materials*, vol. 3, no. 3, pp. 367–370, 1980.
- [166] A. Bauknecht, S. Siebentritt, A. Gerhard et al., "Defects in CuGaSe₂ thin films grown by MOCVD," *Thin Solid Films*, vol. 361, pp. 426–431, 2000.
- [167] I. H. Choi and D. H. Lee, "Preparation of CuIn_{1-x}Ga_xSe₂ films by metalorganic chemical vapor deposition using three precursors," *Thin Solid Films*, vol. 515, no. 11, pp. 4778–4782, 2007.
- [168] P. A. Jones, A. D. Jackson, P. D. Lickiss, R. D. Pilkington, and R. D. Tomlinson, "The plasma enhanced chemical vapour deposition of CuInSe₂," *Thin Solid Films*, vol. 238, no. 1, pp. 4–7, 1994.
- [169] S. Duchemin, M. C. Artaud, F. Ouchen, and J. Bougnot, "Growth of CuInSe₂ by metallorganic chemical vapour deposition (MOCVD): new copper precursor," *Journal of Materials Science: Materials in Electronics*, vol. 7, no. 3, pp. 201–205, 1996.
- [170] M. C. Artaud, F. Ouchen, L. Martin, and S. Duchemin, "CuInSe₂ thin films grown by MOCVD: characterization, first devices," *Thin Solid Films*, vol. 324, no. 1-2, pp. 115–123, 1998.
- [171] J. M. Aleese, P. O. Brien, and D. J. Otway, *Chemical Vapor Deposition*, vol. 4, p. 94, 1998.
- [172] J.-H. Park, M. Afzaal, M. Kemmler et al., "The deposition of thin films of CuME₂ by CVD techniques (M = In, Ga and E = S, Se)," *Journal of Materials Chemistry*, vol. 13, no. 8, pp. 1942–1949, 2003.
- [173] M. Afzaal, D. J. Crouch, P. O. Brien, et al., "The synthesis, X-ray structures and Cvd studies of some group 11 complexes of imino-bis(diisopropylphosphine selenides) and their use in the deposition of I/iii/vi photovoltaic materials," *Journal of Materials Chemistry*, vol. 14, pp. 233–237, 2004.
- [174] I.-H. Choi and P. Y. Yu, "Preparation of CuInSe₂/CuGaSe₂ two layers absorber film by metal-organic chemical vapor deposition," *Current Applied Physics*, vol. 9, no. 1, pp. 151–154, 2009.
- [175] A. Bouloufa, K. Djessas, and D. Todorovic, "Structural and optical properties of Cu(In,Ga)Se₂ grown by close-spaced vapor transport technique," *Materials Science in Semiconductor Processing*, vol. 12, no. 1-2, pp. 82–87, 2009.
- [176] G. W. El Haj Moussa, Ariswan, A. Khoury, F. Guastavino, and C. Llinarés, "Fabrication and study of photovoltaic material CuIn_{1-x}Ga_xSe₂ bulk and thin films obtained by the technique of close-spaced vapor transport," *Solid State Communications*, vol. 122, no. 3-4, pp. 195–199, 2002.
- [177] G. Massé, K. Djessas, C. Monty, and F. Sibieude, "Morphology of Cu(In,Ga)Se₂ thin films grown by close-spaced vapor transport from sources with different grain sizes," *Thin Solid Films*, vol. 414, no. 2, pp. 192–198, 2002.
- [178] J. S. Wellings, A. P. Samantilleke, S. N. Heavens, P. Warren, and I. M. Dharmadasa, "Electrodeposition of CuInSe₂ from ethylene glycol at 150 °C," *Solar Energy Materials and Solar Cells*, vol. 93, no. 9, pp. 1518–1523, 2009.
- [179] L. Oliveira, T. Todorov, E. Chassaing, D. Lincot, J. Carda, and P. Escribano, "CIGSS films prepared by sol-gel route," *Thin Solid Films*, vol. 517, no. 7, pp. 2272–2276, 2009.
- [180] B. M. Basol, V. K. Kapur, A. Halani, et al., "Cu(In,Ga)Se₂ thin films and solar cells prepared by selenization of metallic precursors," *The Journal of Vacuum Science and Technology A*, vol. 14, pp. 2251–2256, 1996.
- [181] R. Caballero, C. Guillén, M. T. Gutiérrez, and C. A. Kaufmann, "CuIn_{1-x}Ga_xSe₂-based thin-film solar cells by the selenization of sequentially evaporated metallic layers," *Progress in Photovoltaics: Research and Applications*, vol. 14, no. 2, pp. 145–153, 2006.
- [182] R. Caballero and C. Guillen, in *Proceedings of the International Conference on Advances in Materials and Processing Technologies*, p. 583, Madrid, Spain, 2001.
- [183] R. Caballero and C. Guillén, "CuInSe₂ Formation by selenization of sequentially evaporated metallic layers," *Solar Energy Materials and Solar Cells*, vol. 86, no. 1, pp. 1–10, 2005.
- [184] H. Sato, T. Hama, E. Niemi, Y. Ichikawa, and H. Sakai, *Japanese Journal of Applied Physics*, vol. 32, p. 50, 1993.
- [185] M. Venkatachalam, M. D. Kannan, N. Muthukumarasamy et al., "Investigations on electron beam evaporated Cu(In_{0.85}Ga_{0.15})Se₂ thin film solar cells," *Solar Energy*, vol. 83, no. 9, pp. 1652–1655, 2009.
- [186] K. G. Deepa, R. Jayakrishnan, K. P. Vijayakumar, C. Sudha Kartha, and V. Ganesan, "Sub-micrometer thick CuInSe₂ films for solar cells using sequential elemental evaporation," *Solar Energy*, vol. 83, no. 7, pp. 964–968, 2009.

- [187] S. Agilan, D. Mangalaraj, S. A. K. Narayandass, S. Velumani, and A. Ignatiev, "Structural and optical characterization of CuInSe₂ films deposited by hot wall vacuum evaporation method," *Vacuum*, vol. 81, no. 7, pp. 813–818, 2007.
- [188] M. M. Islam, T. Sakurai, S. Ishizuka et al., "Effect of Se/(Ga+In) ratio on MBE grown Cu(In,Ga)Se₂ thin film solar cell," *Journal of Crystal Growth*, vol. 311, no. 7, pp. 2212–2214, 2009.
- [189] S. Niki, P. J. Fons, A. Yamada, et al., "High quality CuInSe₂ epitaxial films—molecular beam epitaxial growth and intrinsic properties," *Institute of Physics Conference Series*, vol. 152E, p. 221, 1994.
- [190] E. P. Zaretskaya, V. F. Gremenok, V. B. Zalesski, K. Bente, S. Schorr, and S. Zukotynski, "Properties of Cu(In,Ga)(S,Se)₂ thin films prepared by selenization/sulfurization of metallic alloys," *Thin Solid Films*, vol. 515, no. 15, pp. 5848–5851, 2007.
- [191] A. F. da Cunha, F. Kurdesau, D. Rudmann, and P. M. P. Salomé, "Performance comparison of hybrid sputtering/evaporation CuIn_{1-x}Ga_xSe₂ solar cells with different transparent conducting oxide window layers," *Journal of Non-Crystalline Solids*, vol. 352, no. 9–20, pp. 1976–1980, 2006.
- [192] M. Bodegard, L. Stolt, and J. Hedstrom, "The influence of sodium on the grain structure of CuInSe₂ films for photovoltaic applications," in *Proceedings of the 12th European Conference on Photovoltaic Solar Energy Conversion*, pp. 1743–1746, 1994.
- [193] M. Bodegård, K. Granath, L. Stolt, and A. Rockett, "Behaviour of Na implanted into Mo thin films during annealing," *Solar Energy Materials and Solar Cells*, vol. 58, no. 2, pp. 199–208, 1999.
- [194] J. Hedstrom, H. Ohlsen, M. Bodegard et al., "ZnO/CdS/Cu(In,Ga)Se₂ thin film solar cells with improved performance," in *Proceedings of the 23rd IEEE Photovoltaic Specialists Conference*, pp. 364–371, New York, NY, USA, May 1993.
- [195] M. Ruckh, D. Schmid, M. Kaiser, R. Schaffler, T. Walter, and H. W. Schock, "Influence of substrates on the electrical properties of Cu(In,Ga)Se₂ thin films," in *Proceedings of the Conference Record of the IEEE 1st World Conference on Photovoltaic Energy Conversion*, pp. 156–159, Hawaii, USA, 1994.
- [196] M. Bodegård, K. Granath, and L. Stolt, "Growth of Cu(In,Ga)Se₂ thin films by coevaporation using alkaline precursors," *Thin Solid Films*, vol. 361, pp. 9–16, 2000.
- [197] D. Rudmann, G. Bilger, M. Kaelin, F.-J. Haug, H. Zogg, and A. N. Tiwari, "Effects of NaF coevaporation on structural properties of Cu(In,Ga)Se₂ thin films," *Thin Solid Films*, vol. 431–432, pp. 37–40, 2003.
- [198] T. Nakada, D. Iga, H. Ohbo, and A. Kunioka, "Effects of sodium on Cu(In, Ga)Se₂-based thin films and solar cells," *Japanese Journal of Applied Physics. Part 1*, vol. 36, no. 2, pp. 732–737, 1997.
- [199] D. W. Niles, M. Al-Jassim, and K. Ramanathan, "Direct observation of Na and O impurities at grain surfaces of CuInSe₂ thin films," *Journal of Vacuum Science and Technology A*, vol. 17, no. 1, pp. 291–296, 1999.
- [200] D. Rudmann, A. F. Da Cunha, M. Kaelin et al., "Efficiency enhancement of Cu(In,Ga)Se₂ solar cells due to post-deposition Na incorporation," *Applied Physics Letters*, vol. 84, no. 7, pp. 1129–1131, 2004.
- [201] S.-H. Wei, S. B. Zhang, and A. Zunger, "Effects of Na on the electrical and structural properties of CuInSe₂," *Journal of Applied Physics*, vol. 85, no. 10, pp. 7214–7218, 1999.
- [202] V. Probst, J. Rimmasch, W. Riedl, et al., "The impact of controlled sodium incorporation on rapid thermal processed Cu(In,Ga)Se₂-thin films and devices," in *Proceedings of the Conference Record of the IEEE 1st World Conference on Photovoltaic Energy Conversion*, p. 144, New York, NY, USA, 1994.
- [203] A. Rockett, J. S. Britt, T. Gillespie et al., "Na in selenized Cu(In,Ga)Se₂ on Na-containing and Na-free glasses: distribution, grain structure, and device performances," *Thin Solid Films*, vol. 372, no. 1, pp. 212–217, 2000.
- [204] J. E. Granata and J. R. Sites, "Impact of sodium in the bulk and in grain boundaries of CuInSe₂," in *Proceedings of the 2nd World Conference on Photovoltaic Solar Energy Conversion*, vol. 1, pp. 604–607, Vienna, Austria, July 1998.
- [205] R. J. Matson, J. E. Granata, S. E. Asher, and M. R. Young, "Effects of substrate and Na concentration on device properties, junction formation, and film microstructure in CuInSe₂ PV devices," in *Proceedings of the 15th NCPV Photovoltaic Program Review*, vol. 462, pp. 542–552, Denver, Colo, USA, March 1999.
- [206] T. Nakada, H. Ohbo, M. Fukuda, and A. Kunioka, "Improved compositional flexibility of Cu(In,Ga)Se₂-based thin film solar cells by sodium control technique," *Solar Energy Materials and Solar Cells*, vol. 49, no. 1–4, pp. 261–267, 1997.
- [207] D. Wolf, G. Muller, W. Stetter, and F. Karg, "In-situ investigation of Cu-In-Se reactions: impact of Na on CIS formation," in *Proceedings of the 2nd World Conference on Photovoltaic Solar Energy Conversion*, pp. 2426–2430, Vienna, Austria, 1998.
- [208] W. N. Shafarman and J. Zhu, "Effect of substrate temperature and deposition profile on evaporated Cu(In,Ga)Se₂ films and devices," *Thin Solid Films*, vol. 361, pp. 473–477, 2000.
- [209] S. Ishizuka, H. Shibata, A. Yamada et al., "Growth of polycrystalline Cu (In,Ga) Se₂ thin films using a radio frequency-cracked Se-radical beam source and application for photovoltaic devices," *Applied Physics Letters*, vol. 91, no. 4, Article ID 041902, 2007.
- [210] J. Holz, F. Karg, and H. V. Philipsborn, "The effect of substrate impurities on the electronic conductivity in CIS thin films," in *Proceedings of the 12th European Photovoltaic Solar Energy Conference*, pp. 1592–1595, Amsterdam, The Netherlands, 1994.
- [211] R. Kirmura, T. Mouri, T. Nakada, et al., "Photoluminescence properties of sodium incorporated in CuInSe₂ thin films," *Japanese Journal of Applied Physics*, vol. 38, pp. L289–L291, 1999.
- [212] M. Lammer, U. Klemm, and M. Powalla, "Sodium coevaporation for low temperature Cu(In,Ga)Se₂ deposition," *Thin Solid Films*, vol. 387, no. 1–2, pp. 33–36, 2001.
- [213] R. Caballero, C. A. Kaufmann, T. Eisenbarth et al., "The influence of Na on low temperature growth of CIGS thin film solar cells on polyimide substrates," *Thin Solid Films*, vol. 517, no. 7, pp. 2187–2190, 2009.
- [214] P. T. Erslev, J. W. Lee, W. N. Shafarman, and J. D. Cohen, "The influence of Na on metastable defect kinetics in CIGS materials," *Thin Solid Films*, vol. 517, no. 7, pp. 2277–2281, 2009.
- [215] S. Ishizuka, A. Yamada, M. M. Islam et al., "Na-induced variations in the structural, optical, and electrical properties of Cu (In,Ga) Se₂ thin films," *Journal of Applied Physics*, vol. 106, no. 3, Article ID 034908, 2009.

- [216] R. Ortega-Borges and D. Lincot, "Mechanism of chemical bath deposition of cadmium sulfide thin films in the ammonia-thiourea system," *Journal of the Electrochemical Society*, vol. 140, no. 12, pp. 3464–3473, 1993.
- [217] G. Hodes, *Chemical Solution Deposition of Semiconductor Films*, Marcel Dekker, New York, NY, USA, 2002.
- [218] L. Olsen, P. Eschbach, and S. Kundu, "Role of buffer layers in CIS based solar cells," in *Proceedings of the 29th IEEE Photovoltaic Specialists Conference*, p. 652, New York, NY, USA, 2002.
- [219] S. Chaisitsak, A. Yamada, and M. Konagai, "Comprehensive study of light-soaking effect in ZnO/Cu(InGa)Se₂ Solar Cells with Zn-Based Buffer Layers," in *Proceedings of the Materials Research Society Spring Meeting*, San Francisco, Calif, USA, 2001, v.668:H9.10.1.5.
- [220] M. Bär, Ch.-H. Fischer, and H.-J. Muffier, in *Proceedings of the 29th IEEE Photovoltaic Specialists Conference*, p. 636, New Orleans, La, USA, 2002.
- [221] J. Kessler, M. Ruckh, D. Hariskos, U. Ruhle, R. Menner, and H. W. Schock, "Interface engineering between CuInSe₂ and ZnO," in *Proceedings of the 23rd IEEE Photovoltaic Specialists Conference*, pp. 447–452, Louisville, Ky, USA, May 1993.
- [222] A. Romeo, R. Gysel, and S. Buzzi, "Properties of CIGS solar cells developed with evaporated II–VI buffer layers," in *Proceedings of the Technical Digest of the 14th International Photovoltaic Science and Engineering Conference*, p. 705, Bangkok, Thailand, 2004.
- [223] M. Rusu, T. Glatzel, C. A. Kaufmann et al., "High-efficient ZnO/PVD-CdS/Cu(In,Ga)Se₂ thin film solar cells: formation of the buffer-absorber interface and transport properties," in *Proceedings of the Materials Research Society Symposium: Thin-Film Compound Semiconductor Photovoltaics*, vol. 865, pp. F14.25.1–F14.25.7, San Francisco, Calif, USA, April 2005.
- [224] D. Schmid, M. Ruckh, and H. W. Schock, "A comprehensive characterization of the interfaces in Mo/CIS/CdS/ZnO solar cell structures," *Solar Energy Materials and Solar Cells*, vol. 41–42, pp. 281–294, 1996.
- [225] M. A. Contreras, M. J. Romero, B. To et al., "Optimization of CBD CdS process in high-efficiency Cu(In,Ga)Se₂-based solar cells," *Thin Solid Films*, vol. 403–404, pp. 204–211, 2002.
- [226] U. Rau and M. Schmidt, "Electronic properties of ZnO/CdS/Cu(In,Ga)Se₂ solar cells—aspects of heterojunction formation," *Thin Solid Films*, vol. 387, no. 1–2, pp. 141–146, 2001.
- [227] P. Garg, A. Garg, A. C. Rastogi, and J. C. Garg, "Growth and characterization of electrodeposited CuInSe₂ thin films from seleno-sulphate solution," *Journal of Physics D*, vol. 24, no. 11, pp. 2026–2031, 1991.
- [228] S. N. Sahu, R. D. L. Kristensen, and D. Haneman, "Electrodeposition of CuInSe₂ thin films from aqueous solution," *Solar Energy Materials*, vol. 18, no. 6, pp. 385–397, 1989.
- [229] C. X. Qiu and I. Shih, "Investigation of electrodeposited CuInSe₂ films," *Canadian journal of physics*, vol. 65, no. 8, pp. 1011–1014, 1987.
- [230] V. K. Kapur, B. M. Basol, and E. S. Tseng, "Low cost methods for the production of semiconductor films for CuInSe₂/CdS solar cells," *Solar Cells*, vol. 21, no. 1–4, pp. 65–72, 1987.
- [231] S. N. Qiu, L. Li, C. X. Qiu, I. Shih, and C. H. Champness, "Study of CuInSe₂ thin films prepared by electrodeposition," *Solar Energy Materials and Solar Cells*, vol. 37, no. 3–4, pp. 389–393, 1995.
- [232] A. Rockett and R. W. Birkmire, "CuInSe₂ for photovoltaic applications," *Journal of Applied Physics*, vol. 70, no. 7, pp. R81–R97, 1991.
- [233] D. Schmid, M. Ruckh, F. Grunwald, and H. W. Schock, "Chalcopyrite/defect chalcopyrite heterojunctions on the basis of CuInSe₂," *Journal of Applied Physics*, vol. 73, no. 6, pp. 2902–2909, 1993.
- [234] Y. Sudo, S. Endo, and T. Irie, "Preparation and characterization of electrodeposited CuInSe₂ thin films," *Japanese Journal of Applied Physics. Part 1*, vol. 32, no. 4, pp. 1562–1567, 1993.
- [235] R. W. Birkmire and E. Eser, "Polycrystalline thin film solar cells: present status and future potential," *Annual Review of Materials Science*, vol. 27, no. 1, pp. 625–653, 1997.
- [236] H.-W. Schock and R. Noufi, "CIGS-based solar cells for the next millennium," *Progress in Photovoltaics: Research and Applications*, vol. 8, no. 1, pp. 151–160, 2000.
- [237] A. Kylner, A. Rockett, and L. Stolt, "Oxygen in solution grown CdS films for thin film solar cells," *Diffusion and Defect Data B*, vol. 51–52, pp. 533–540, 1996.
- [238] T. Nakada and A. Kunioka, "Direct evidence of Cd diffusion into Cu(In,Ga)Se₂ thin films during chemical-bath deposition process of CdS films," *Applied Physics Letters*, vol. 74, no. 17, pp. 2444–2446, 1999.
- [239] Y. Hashimoto, N. Kohara, T. Negami, N. Nishitani, and T. Wada, "Chemical bath deposition of CdS buffer layer for CIGS solar cells," *Solar Energy Materials and Solar Cells*, vol. 50, no. 1–4, pp. 71–77, 1998.
- [240] C. Guillén, M. A. Martínez, C. Maffiotte, and J. Herrero, "Chemistry of CdS/CuInSe₂ structures as controlled by the CdS deposition bath," *Journal of the Electrochemical Society*, vol. 148, no. 11, pp. G602–G606, 2001.
- [241] A. Kylner, "Effect of impurities in the CdS buffer layer on the performance of the Cu(In, Ga)Se₂ thin film solar cell," *Journal of Applied Physics*, vol. 85, no. 9, pp. 6858–6865, 1999.
- [242] T. Negami, Y. Hashimoto, and S. Nishiwaki, "Cu(In,Ga)Se₂ thin-film solar cells with an efficiency of 18%," *Solar Energy Materials and Solar Cells*, vol. 67, no. 1–4, pp. 331–335, 2001.
- [243] L. Kronik, U. Rau, J.-F. Guillemoles, D. Braunger, H.-W. Schock, and D. Cahen, "Interface redox engineering of Cu(In,Ga)Se₂-based solar cells: oxygen, sodium, and chemical bath effects," *Thin Solid Films*, vol. 361, pp. 353–359, 2000.
- [244] C. Heske, D. Eich, R. Fink et al., "Observation of intermixing at the buried CdS/Cu(In, Ga)Se₂ thin film solar cell heterojunction," *Applied Physics Letters*, vol. 74, no. 10, pp. 1451–1453, 1999.
- [245] S. Chaisitsak, A. Yamada, and M. Konagai, "Preferred orientation control of Cu(In_{1-x}Ga_x)Se₂ (x ≈ 0.28) thin films and its influence on solar cell characteristics," *Japanese Journal of Applied Physics. Part 1*, vol. 41, no. 2, pp. 507–513, 2002.
- [246] T. M. Friedlmeier, D. Braunger, D. Hariskos, M. Kaiser, H. N. Wanka, and H. W. Schock, "Nucleation and growth of the CdS buffer layer on Cu(In,Ga)Se₂ thin films," in *Proceedings of the 25th IEEE Photovoltaic Specialists Conference*, pp. 845–848, May 1996.
- [247] M. G. Sandoval-Paz, M. Sotelo-Lerma, A. Mendoza-Galvan, and R. Ramírez-Bon, "Optical properties and layer microstructure of CdS films obtained from an ammonia-free chemical bath deposition process," *Thin Solid Films*, vol. 515, no. 7–8, pp. 3356–3362, 2007.
- [248] H. Komaki, A. Yamada, K. Sakurai et al., "CIGS solar cell with CdS buffer layer deposited by ammonia-free process," *Physica Status Solidi A*, vol. 206, no. 5, pp. 1072–1075, 2009.
- [249] J. R. Mann, N. Vora, and I. L. Repins, "In Situ thickness measurements of chemical bath-deposited CdS," *Solar Energy Materials and Solar Cells*, vol. 94, no. 2, pp. 333–337, 2010.

- [250] N. Naghavi, C. Hubert, O. Kerrec, et al., in *Proceedings of the 22nd European Photovoltaic Solar Energy Conference*, p. 2304, 2007.
- [251] M. Powalla, G. Voorwinden, D. Hariskos, P. Jackson, and R. Kniese, "Highly efficient CIS solar cells and modules made by the co-evaporation process," *Thin Solid Films*, vol. 517, no. 7, pp. 2111–2114, 2009.
- [252] T. Nakada and M. Mizutani, "18% efficiency Cd-free Cu(In, Ga)Se₂ thin-film solar cells fabricated using chemical bath deposition (CBD)-ZnS buffer layers," *Japanese Journal of Applied Physics. Part 2*, vol. 41, no. 2 B, pp. L165–L167, 2002.
- [253] A. J. Nelson, C. R. Schwerdtfeger, S.-H. Wei et al., "Theoretical and experimental studies of the ZnSe/CuInSe₂ heterojunction band offset," *Applied Physics Letters*, vol. 62, no. 20, pp. 2557–2559, 1993.
- [254] M. M. Islam, S. Ishizuka, A. Yamada et al., "CIGS solar cell with MBE-grown ZnS buffer layer," *Solar Energy Materials and Solar Cells*, vol. 93, no. 6-7, pp. 970–972, 2009.
- [255] S. Siebentritt, T. Kampschulte, A. Bauknecht et al., "Cd-free buffer layers for CIGS solar cells prepared by a dry process," *Solar Energy Materials and Solar Cells*, vol. 70, no. 4, pp. 447–457, 2002.
- [256] F. Engelhardt, M. Schmidt, Th. Meyer, O. Seifert, and J. Parisi, in *Proceedings of the 2nd World Conference on PV Solar Energy Conversion*, 1998.
- [257] Y. Ohtake, K. Kushiya, A. Yamada, and M. Konagai, "Development of ZnO/ZnSe/CuIn_{1-x}Ga_xSe₂ thin-film solar cells with band gap of 1.3 to 1.5 eV," in *Proceedings of the 1st World Conference on Photovoltaic Solar Energy Conversion*, p. 218, 1994.
- [258] Y. Ohtake, K. Kushiya, M. Ichikawa, A. Yamada, and M. Konagai, "Polycrystalline Cu(InGa)Se₂ thin-film solar cells with ZnSe buffer layers," *Japanese Journal of Applied Physics. Part 1*, vol. 34, no. 11, pp. 5949–5955, 1995.
- [259] A. Ennaoui, S. Siebentritt, M. Ch. Lux-Steiner, W. Riedl, and F. Karg, "High-efficiency Cd-free CIGSS thin-film solar cells with solution grown zinc compound buffer layers," *Solar Energy Materials and Solar Cells*, vol. 67, no. 1–4, pp. 31–40, 2001.
- [260] Y. Ohtake, S. Chaisitsak, A. Yamada, and M. Konagai, "Characterization of ZnIn_xSe_y thin films as a buffer layer for high efficiency Cu(InGa)Se₂ thin-film solar cells," *Japanese Journal of Applied Physics. Part 1*, vol. 37, no. 6, pp. 3220–3225, 1998.
- [261] Y. Ohtake, T. Okamoto, A. Yamada, M. Konagai, and K. Saito, "Improved performance of Cu(InGa)Se₂ thin-film solar cells using evaporated Cd-free buffer layers," *Solar Energy Materials and Solar Cells*, vol. 49, no. 1–4, pp. 269–275, 1997.
- [262] T. Negami, T. Aoyagi, T. Satoh, et al., "Cd free CIGS solar cells fabricated by dry processes," in *Proceedings of the 29th IEEE Photovoltaic Specialists Conference*, p. 656, 2002.
- [263] D. Hariskos, B. Fuchs, R. Menner et al., "The Zn(S,O,OH)/ZnMgO buffer in thin-film Cu(In,Ga)(Se,S)₂-based solar cells part II: magnetron sputtering of the ZnMgO buffer layer for in-line co-evaporated Cu(In,Ga)Se₂ solar cells," *Progress in Photovoltaics: Research and Applications*, vol. 17, no. 7, pp. 479–488, 2009.
- [264] E. B. Yousfi, B. Weinberger, F. Donsanti, P. Cowache, and D. Lincot, "Atomic layer deposition of zinc oxide and indium sulfide layers for Cu(In,Ga)Se₂ thin-film solar cells," *Thin Solid Films*, vol. 387, no. 1-2, pp. 29–32, 2001.
- [265] S. Spiering, D. Hariskos, M. Powalla, N. Naghavi, and D. Lincot, "CD-free Cu(In,Ga)Se₂ thin-film solar modules with In₂S₃ buffer layer by ALCVD," *Thin Solid Films*, vol. 431-432, pp. 359–363, 2003.
- [266] J.-F. Guillemoles, B. Canava, E. B. Yousfi et al., "Indium-based interface chemical engineering by electrochemistry and atomic layer deposition for copper indium diselenide solar cells," *Japanese Journal of Applied Physics. Part 1*, vol. 40, no. 10, pp. 6065–6068, 2001.
- [267] S. Spiering, L. Bürkert, D. Hariskos et al., "MOCVD indium sulphide for application as a buffer layer in CIGS solar cells," *Thin Solid Films*, vol. 517, no. 7, pp. 2328–2331, 2009.
- [268] F. Couzinié-Devy, N. Barreau, and J. Kessler, "Influence of absorber copper concentration on the Cu(In,Ga)Se₂/(PVD)In₂S₃ and Cu(In,Ga)Se₂/(CBD)CdS based solar cells performance," *Thin Solid Films*, vol. 517, no. 7, pp. 2407–2410, 2009.
- [269] A. Darga, D. Mencaraglia, Z. Djebbour et al., "Comparative study of Cu(In,Ga)Se₂/(PVD)In₂S₃ and Cu(In,Ga)Se₂/(CBD)CdS heterojunction based solar cells by admittance spectroscopy, current-voltage and spectral response measurements," *Thin Solid Films*, vol. 517, no. 7, pp. 2423–2426, 2009.
- [270] S. Buecheler, D. Corica, D. Guettler et al., "Ultrasonically sprayed indium sulfide buffer layers for Cu(In,Ga)(S,Se)₂ thin-film solar cells," *Thin Solid Films*, vol. 517, no. 7, pp. 2312–2315, 2009.
- [271] A. Eicke, S. Spiering, A. Dresel, and M. Powalla, "Chemical characterisation of evaporated In₂S_x buffer layers in Cu(In,Ga)Se₂ thin-film solar cells with SNMS and SIMS," *Surface and Interface Analysis*, vol. 40, no. 3-4, pp. 830–833, 2008.
- [272] D. Abou-Ras, G. Kostorz, D. Hariskos et al., "Structural and chemical analyses of sputtered In_xS_y buffer layers in Cu(In,Ga)Se₂ thin-film solar cells," *Thin Solid Films*, vol. 517, no. 8, pp. 2792–2798, 2009.
- [273] Y. Ohtake, M. Ichikawa, T. Okamoto, A. Yamada, M. Konagai, and K. Saito, "Cu(InGa)Se₂ thin-film solar cells with continuously evaporated Cd-free buffer layers," in *Proceedings of the 25th IEEE Photovoltaic Specialists Conference*, pp. 793–796, May 1996.
- [274] N. Barreau, A. Mokrani, F. Couzinié-Devy, and J. Kessler, "Bandgap properties of the indium sulfide thin-films grown by co-evaporation," *Thin Solid Films*, vol. 517, no. 7, pp. 2316–2319, 2009.
- [275] D. Hariskos, R. Herberholz, M. Ruckh, et al., in *Proceedings of the 3th European Photovoltaic Solar Energy Conference*, p. 1995, France, 1995.
- [276] A. Ennaoui, U. Blieske, and M. CH. Lux-Steiner, "13.7%-efficient Zn(Se,OH)_x/Cu(In,Ga)(S,Se)₂ thin-film solar cell," *Progress in Photovoltaics: Research and Applications*, vol. 6, no. 6, pp. 447–451, 1998.
- [277] C. Hubert, N. Naghavi, O. Roussel et al., "The Zn(S,O,OH)/ZnMgO buffer in thin film Cu(In,Ga)(S,Se)₂-based solar cells part I: fast chemical bath deposition of Zn(S,O,OH) buffer layers for industrial application on co-evaporated Cu(In,Ga)Se₂ and electrodeposited CuIn(S,Se)₂ solar cells," *Progress in Photovoltaics: Research and Applications*, vol. 17, no. 7, pp. 470–478, 2009.
- [278] R. Sáez-Araoz, A. Ennaoui, T. Kropp, E. Veryaeva, T. P. Niesen, and M. CH. Lux-Steiner, "Use of different Zn precursors for the deposition of Zn(S,O) buffer layers by chemical bath for chalcopyrite based Cd-free thin-film solar

- cells," *Physica Status Solidi A*, vol. 205, no. 10, pp. 2330–2334, 2008.
- [279] A. Hultqvist, C. Platzer-Björkman, J. Pettersson, T. Törndahl, and M. Edoff, "CuGaSe₂ solar cells using atomic layer deposited Zn(O,S) and (Zn,Mg)O buffer layers," *Thin Solid Films*, vol. 517, no. 7, pp. 2305–2308, 2009.
- [280] R. Sáez-Araoz, D. Abou-Ras, T. P. Niesen et al., "In situ monitoring the growth of thin-film ZnS/Zn(S,O) bilayer on Cu-chalcopyrite for high performance thin film solar cells," *Thin Solid Films*, vol. 517, no. 7, pp. 2300–2304, 2009.
- [281] T. Nakada, M. Hongo, and E. Hayashi, "Band offset of high efficiency CBD-ZnS/CIGS thin film solar cells," *Thin Solid Films*, vol. 431–432, pp. 242–248, 2003.
- [282] W. E. Devaney, W. S. Chen, J. M. Stewart, and R. A. Mickelsen, "Structure and properties of high efficiency ZnO/CdZnS/CuInGaSe₂ solar cells," *IEEE Transactions on Electron Devices*, vol. 37, no. 2, pp. 428–433, 1990.
- [283] Rothwarf, "A p-i-n heterojunction model for the thin-film CuInSe₂/CdS solar cell," *IEEE Transactions on Electron Devices*, vol. 29, no. 10, pp. 1513–1515, 1982.
- [284] N. Romeo, A. Bosio, and V. Canevari, "R.F. sputtered CuInSe₂ thin films for photovoltaic applications," in *Proceedings of the 8th European Photovoltaic Solar Energy Conference*, vol. 2, pp. 1092–1096, Florence, Italy, 1988.
- [285] S. H. Kwon, S. C. Park, B. T. Ahn, K. H. Yoon, and J. Song, "Effect of CuIn₃Se₅ layer thickness on CuInSe₂ thin films and devices," *Solar Energy*, vol. 64, no. 1–3, pp. 55–60, 1998.
- [286] T. Negami, Y. Hashimoto, and S. Nishiwaki, "Cu(In,Ga)Se₂ thin-film solar cells with an efficiency of 18%," *Solar Energy Materials and Solar Cells*, vol. 67, no. 1–4, pp. 331–335, 2001.
- [287] T. Negami, T. Satoh, Y. Hashimoto et al., "Production technology for CIGS thin film solar cells," *Thin Solid Films*, vol. 403–404, pp. 197–203, 2002.
- [288] T. Minami, H. Sato, H. Nanto, and S. Takata, "Group III impurity doped zinc oxide thin films prepared by RF magnetron sputtering," *Japanese Journal of Applied Physics. Part 2*, vol. 24, no. 10, pp. L781–L784, 1985.
- [289] M. A. Contreras, B. Egaas, K. Ramanathan et al., "Progress toward 20% efficiency in Cu(In,Ga)Se₂ polycrystalline thin-film solar cells," *Progress in Photovoltaics: Research and Applications*, vol. 7, no. 4, pp. 311–316, 1999.
- [290] Y. Hagiwara, T. Nakada, and A. Kunioka, "Improved J_{sc} in CIGS thin film solar cells using a transparent conducting ZnO:B window layer," *Solar Energy Materials and Solar Cells*, vol. 67, no. 1–4, pp. 267–271, 2001.
- [291] M. A. Contreras, J. Tuttle, A. Gabor, et al., "High efficiency Cu(In,Ga)Se₂ based solar cells: processing of novel absorber structures," in *Proceedings 1st World conference on Photovoltaic Solar Energy Conversion*, pp. 68–75, IEEE, Hawaii, USA, 1994.
- [292] K. Granath, M. Bodegård, and L. Stolt, "Effect of NaF on Cu(In,Ga)Se₂ thin film solar cells," *Solar Energy Materials and Solar Cells*, vol. 60, no. 3, pp. 279–293, 2000.
- [293] M. Klenk, O. Schenker, V. Albers, and E. Bucher, "Preparation of device quality chalcopyrite thin films by thermal evaporation of compound materials," *Semiconductor Science and Technology*, vol. 17, no. 5, pp. 435–439, 2002.
- [294] M. Powalla and B. Dimmler, "Scaling up issues of CIGS solar cells," *Thin Solid Films*, vol. 361, pp. 540–546, 2000.
- [295] F. H. Karg, "Development and manufacturing of CIS thin film solar modules," *Solar Energy Materials and Solar Cells*, vol. 66, no. 1–4, pp. 645–653, 2001.
- [296] C. Eberspacher, C. Fredric, K. Pauls, and J. Serra, "Thin-film CIS alloy PV materials fabricated using non-vacuum, particles-based techniques," *Thin Solid Films*, vol. 387, no. 1–2, pp. 18–22, 2001.
- [297] S. Siebentritt, T. Kampschulte, A. Bauknecht et al., "Cd-free buffer layers for CIGS solar cells prepared by a dry process," *Solar Energy Materials and Solar Cells*, vol. 70, no. 4, pp. 447–457, 2002.
- [298] Z. A. Wang, J. B. Chu, H. B. Zhu, Z. Sun, Y. W. Chen, and S. M. Huang, "Growth of ZnO:Al films by RF sputtering at room temperature for solar cell applications," *Solid-State Electronics*, vol. 53, no. 11, pp. 1149–1153, 2009.
- [299] T. Nakada, N. Murakami, and A. Kunioka, "Transparent conducting Al-, AlB12-, and B-doped ZnO films for solar cells by dc magnetron sputtering," in *Proceedings of the 12th European Photovoltaic Solar Energy Conference*, pp. 1507–1610, Amsterdam, The Netherlands, 1994.
- [300] S. Chaisitsak, A. Yamada, and M. Konagai, "Preferred orientation control of Cu(In_{1-x}Ga_x)Se₂ (x ≈ 0.28) thin films and its influence on solar cell characteristics," *Japanese Journal of Applied Physics*, vol. 41, pp. 507–513, 2002.
- [301] V. Probst, W. Stetter, W. Riedl et al., "Rapid CIS-process for high efficiency PV-modules: development towards large area processing," *Thin Solid Films*, vol. 387, no. 1–2, pp. 262–267, 2001.
- [302] B. M. Basol, V. K. Kapur, G. Norsworthy, A. Halani, C. R. Leidholm, and R. Roe, "Efficient CuInSe₂ solar cells fabricated by a novel ink coating approach," *Electrochemical and Solid-State Letters*, vol. 1, no. 6, pp. 252–254, 1998.
- [303] T. Sugiyama, S. Chaisitsak, A. Yamada et al., "Formation of pn homojunction in Cu(InGa)Se₂ thin film solar cells by Zn doping," *Japanese Journal of Applied Physics. Part 1*, vol. 39, no. 8, pp. 4816–4819, 2000.
- [304] N. F. Cooray, K. Kushiya, A. Fujimaki et al., "Large area ZnO films optimized for graded band-gap Cu(InGa)Se₂-based thin-film mini-modules," *Solar Energy Materials and Solar Cells*, vol. 49, no. 1–4, pp. 291–297, 1997.
- [305] Y. Hagiwara, T. Nakada, and A. Kunioka, "Improved J_{sc} in CIGS thin film solar cells using a transparent conducting ZnO:B window layer," *Solar Energy Materials and Solar Cells*, vol. 67, no. 1–4, pp. 267–271, 2001.
- [306] M. Yu, H. Qiu, X. Chen, H. Liu, and M. Wang, "Structural and physical properties of Ni and Al co-doped ZnO films grown on glass by direct current magnetron co-sputtering," *Physica B*, vol. 404, no. 12–13, pp. 1829–1834, 2009.
- [307] J. S. Wellings, A. P. Samantilleke, P. Warren, S. N. Heavens, and I. M. Dharmadasa, "Comparison of electrodeposited and sputtered intrinsic and aluminium-doped zinc oxide thin films," *Semiconductor Science and Technology*, vol. 23, no. 12, Article ID 125003, 2008.
- [308] B. N. Pawar, G. Cai, D. Ham et al., "Preparation of transparent and conducting boron-doped ZnO electrode for its application in dye-sensitized solar cells," *Solar Energy Materials and Solar Cells*, vol. 93, no. 4, pp. 524–527, 2009.
- [309] X.-T. Hao, J. Ma, D.-H. Zhang et al., "Comparison of the properties for ZnO:Al films deposited on polyimide and glass substrates," *Materials Science and Engineering B*, vol. 90, no. 1–2, pp. 50–54, 2002.
- [310] S. Fernández, A. Martínez-Steele, J. J. Gandía, and F. B. Naranjo, "Radio frequency sputter deposition of high-quality conductive and transparent ZnO:Al films on polymer substrates for thin film solar cells applications," *Thin Solid Films*, vol. 517, no. 10, pp. 3152–3156, 2009.
- [311] S. Calnan and A. N. Tiwari, "High mobility transparent conducting oxides for thin film solar cells," *Thin Solid Films*, vol. 518, no. 7, pp. 1839–1849, 2010.

Research Article

Preparation and Characterization of Sb_2Te_3 Thin Films by Coevaporation

Bin Lv, Songbai Hu, Wei Li, Xia Di, Lianghuan Feng, Jingquan Zhang, Lili Wu, Yaping Cai, Bing Li, and Zhi Lei

College of Materials Science and Engineering, Sichuan University, Chengdu 610064, China

Correspondence should be addressed to Wei Li, waylee2000@sohu.com

Received 3 April 2010; Accepted 23 June 2010

Academic Editor: Leonardo Palmisano

Copyright © 2010 Bin Lv et al. This is an open access article distributed under the Creative Commons Attribution License, which permits unrestricted use, distribution, and reproduction in any medium, provided the original work is properly cited.

Deposition of Sb_2Te_3 thin films on soda-lime glass substrates by coevaporation of Sb and Te is described in this paper. Sb_2Te_3 thin films were characterized by x-ray diffraction (XRD), x-ray fluorescence (XRF), atomic force microscopy (AFM), x-ray photoelectron spectroscopy (XPS), electrical conductivity measurements, and Hall measurements. The abnormal electrical transport behavior occurred from *in situ* electrical conductivity measurements. The results indicate that as-grown Sb_2Te_3 thin films are amorphous and undergo an amorphous-crystalline transition after annealing, and the posttreatment can effectively promote the formation of Sb-Te bond and prevent oxidation of thin film surface.

1. Introduction

It is well known that CdTe thin film solar cell offers one of the most promising photovoltaic devices for terrestrial applications due to the near-optimum bandgap and high absorption coefficient of CdTe. However, forming an ohmic contact to CdTe is very difficult because of the high electron affinity of CdTe and the self-compensation in CdTe. An approach to overcoming these problems is incorporation of p^+ region materials between CdTe and the metal electrode to provide the advantageous electrical properties. These materials should have long-term stability of the electrical contact to CdTe and should not cause chemical reactions at the interface. Conventionally, a Cu layer or a material doped with Cu is used to form back contacts with a low barrier height. Unfortunately, Cu will diffuse along the grain boundaries down to the main junction resulting in the degradation of device performance. New material such as antimony telluride possesses the expected characteristics mentioned above, which can provide stable ohmic back contacts to CdTe [1, 2].

Antimony telluride is a binary V–VI group compound semiconductor with the form of A_2B_3 , which is mentioned as the thermoelectric generators and coolers, and back contacts

for photovoltaic devices because of its high Seebeck coefficient, low thermal conductivity, low electrical resistivity, low bandgap, and long-term stability [1–3].

To obtain Sb_2Te_3 thin films, a number of techniques have been used in the literature, such as thermal evaporation [4, 5], atomic layer epitaxy (ALE) [6], sputtering [2, 7], electrochemical method [8], flash evaporation [9], and metalorganic chemical vapor deposition (MOCVD) [10]. Among all these techniques, coevaporation offers several advantages in the growth of Sb_2Te_3 thin films for CdTe solar cells, such as the desirable stoichiometry, simple evaporation equipment, and a relatively short fabrication processing time.

In this study, we describe the preparation, structure, morphology, and electrical properties of coevaporated Sb_2Te_3 thin films. These are helpful to fabricate stable CdTe solar cells with Sb_2Te_3 back contacts.

2. Experimental

Sb_2Te_3 thin films were grown by a coevaporation method at room temperature in a high-vacuum chamber with base pressure about 9×10^{-4} Pa. Sb foil (99.999% purity) and Te powder (99.999% purity) were evaporated on the glass substrates from two independent sources. The deposition

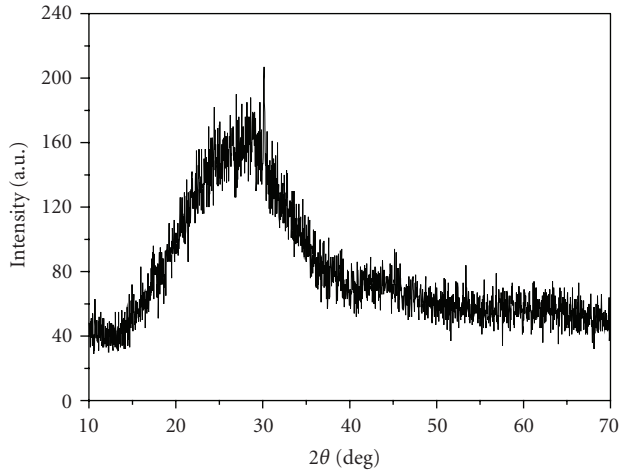


FIGURE 1: XRD pattern of Sb_2Te_3 thin films as-deposited.

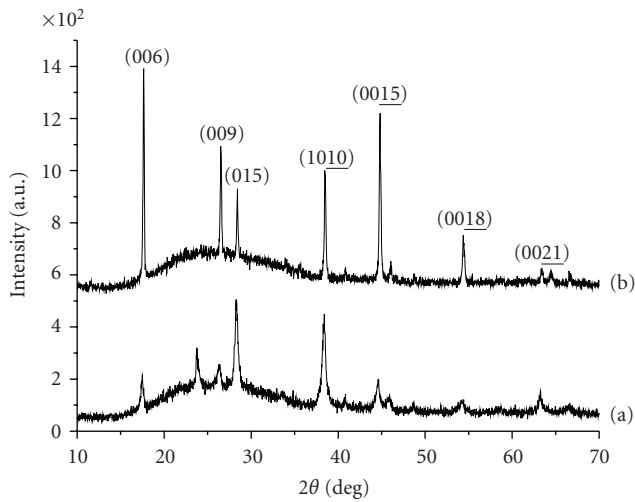


FIGURE 2: XRD patterns of Sb_2Te_3 thin films annealed at 473 K (a) and 613 K (b).

rates and the thickness of thin films were independently controlled by two LHC-2 thickness monitors. The substrates were cleaned prior to deposition, and a postdeposition treatment was performed in N_2 ambient.

XRD measurements were used to study the Sb_2Te_3 structure, and XRF was performed to determine chemical composition of the thin films. Surface analysis of Sb_2Te_3 thin films was carried out using XPS, and surface morphology of Sb_2Te_3 thin films was observed by AFM. Dark conductivity was measured with electron beam evaporation deposited Ni-strips using two-probe technology. The four-probe Van der Pauw method was used to carry out the Hall measurements to determine the Hall coefficient, mobility, and carrier concentration.

3. Results and Discussion

To determine the composition of the Sb-Te alloys, x-ray fluorescence spectra analysis of Sb-Te systems as-deposited

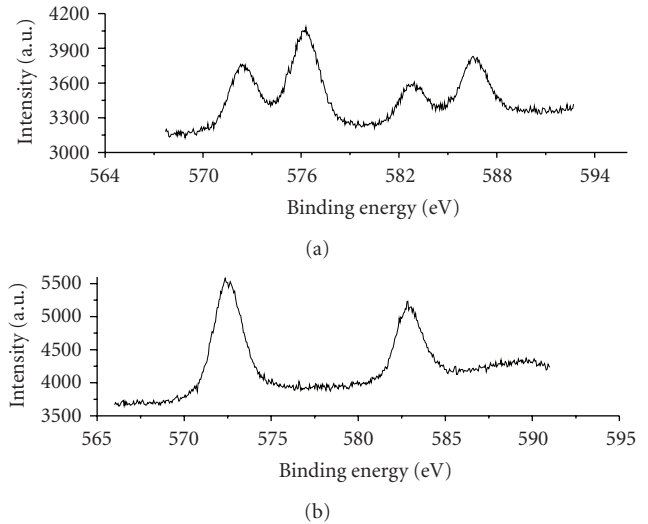


FIGURE 3: Te 3d spectra for Sb_2Te_3 thin films as-deposited (a) and annealed at 613 K (b).

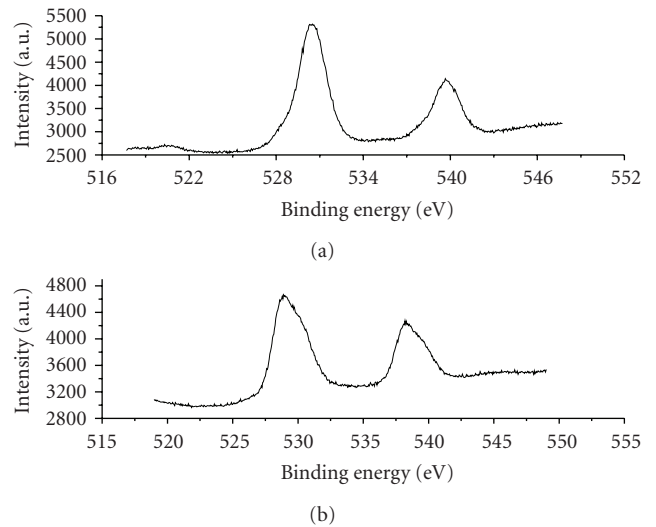


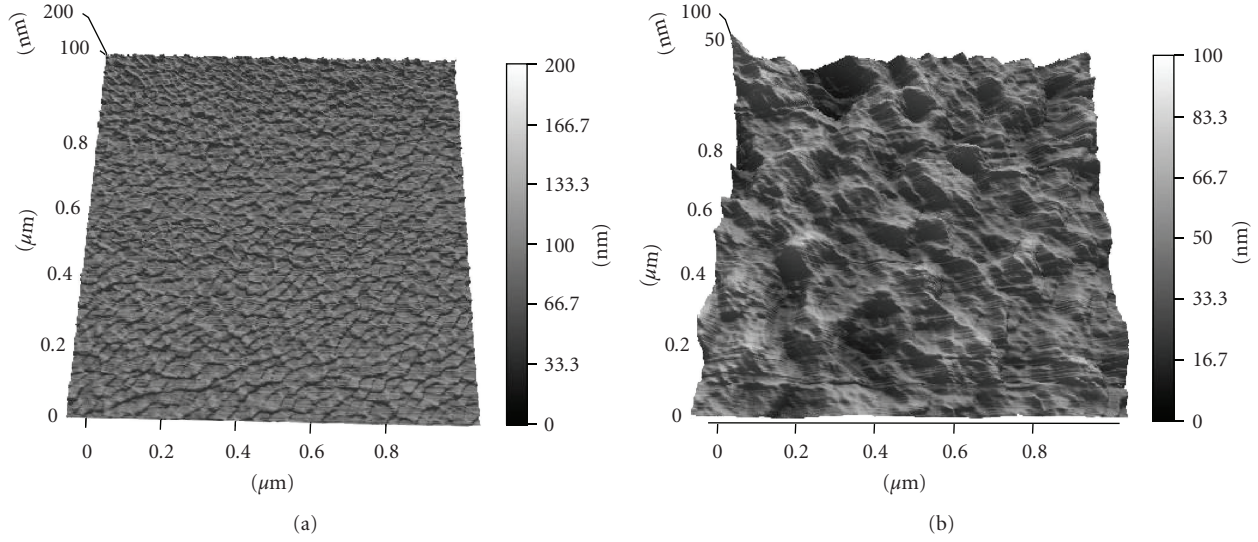
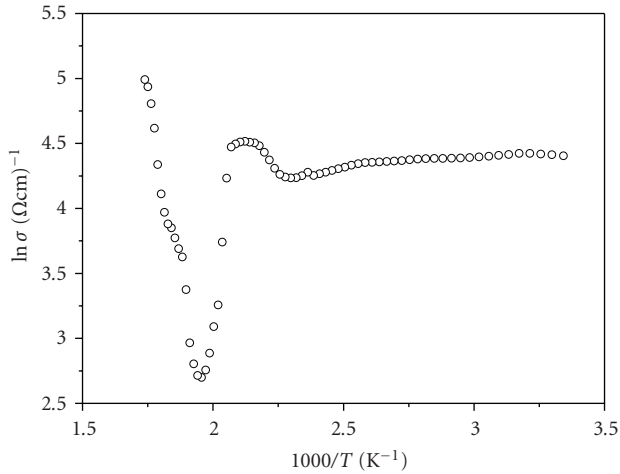
FIGURE 4: Sb 3d spectra for Sb_2Te_3 thin films as-deposited (a) and annealed at 613 K (b).

was carried out. The contents of two kinds of elements, Sb and Te, for as-grown thin films from XRF quantitative analysis are 0.0554 and 0.0941 mg/cm^2 , respectively. The stoichiometric ratio (Te:Sb) is 1.62:1 in the Sb_2Te_3 thin films, which is good agreement with the standard value, 1.5:1 (a relative error of 10% is assumed). After annealing, there are not significant changes of stoichiometry in the Sb_2Te_3 thin films.

Figure 1 shows x-ray diffraction pattern of Sb_2Te_3 thin films deposited by coevaporation at room temperature on the glass substrates. As-deposited Sb_2Te_3 films are an amorphous structure. Bätzner et al. [1], and Romeo et al. [2] have reported that Sb_2Te_3 thin films as the back contact materials were deposited on a substrate kept at a temperature of 573 K and, thus, CdTe solar cells with crystalline Sb_2Te_3

TABLE 1: Hall parameters for Sb_2Te_3 thin films.

Sample	Mobility ($\text{cm}^2 \text{V}^{-1} \text{S}^{-1}$)	Hall coefficient ($\text{cm}^3 \text{C}^{-1}$)	Carrier concentration (cm^{-3})
Sb_2Te_3 as-deposited	44.49	0.082	7.60×10^{19}
Sb_2Te_3 annealed at 613 K	169.86	0.11	5.87×10^{19}

FIGURE 5: AFM images of Sb_2Te_3 thin films as-deposited (a) and annealed at 613 K (b).FIGURE 6: Temperature dependence of dark conductivity for Sb_2Te_3 films.

thin films demonstrated the good device performance. In this work, however, the films were deposited at room temperature, so the postdeposition treatment was desirable for Sb_2Te_3 ohmic contact to CdTe. It was found that it had no effect on the Sb_2Te_3 amorphous phase after annealing at a low temperature (<473 K). Then these samples were annealed at a temperature of 473 K in N_2 ambient, whose XRD pattern shown in Figure 2(a) reveals their polycrystalline nature with the peaks corresponding to (006), (009), (015), (1010), (0015), (0018), and (0021) planes of Sb_2Te_3 . Besides the

diffraction peaks of rhombohedra Sb_2Te_3 , the pattern shows a weak diffraction peak is present at about 2θ of 23.76° , which could be assigned to the TeO_2 due to the oxidation of thin film surface as confirmed by XPS analysis. The thin films were annealed at 613 K shown in Figure 2(b). The strongest intense line indicates the (006) plane is at about 2θ of 17.45° , and the additional weak peaks are at about 2θ of 17.5° , 26.4° , 28.4° , 40.8° , 44.8° , 54.5° , and 64.2° corresponding to the (009), (015), (1010), (0015), (0018), and (0021) planes of Sb_2Te_3 , while the weak diffraction peak of TeO_2 disappears at about 2θ of 23.76° . From Figure 2, one can see that an effect of the annealing temperature on the structure of the thin films, annealing at a higher temperature, would readily promote the formation of single-phase Sb_2Te_3 with very strong (001) preferential orientation and effectively suppress a TeO_2 secondary phase.

Figures 3–4 show the XPS spectra of Sb_2Te_3 thin films. Te 3d5/2 (572.5 eV) and Te 3d3/2 (582.9 eV) peaks are observed (Figure 3), which well agrees with the results reported for Sb_2Te_3 in the literature [11]. Additional peaks (576.2 and 586.6 eV) for Te 3d shown in Figure 3(a), indicating a chemical environment different from Sb_2Te_3 , can be ascribed to Te-O. The Te-O bond does not exist on the film surface after crystallization at 613 K, which indicates that as-deposited thin film surface is much easy to be oxidized after exposure to the atmosphere. For the Sb 3d spectra as shown in Figure 4, the values of 539.6 eV (3d3/2) and 530.3 eV (3d5/2) are ascribed to Sb-O bonding, and 529–530 eV (3d5/2) and 538–539 eV (3d3/2) to Sb metallic bonding [11, 12]. The Sb 3d peaks at 530.5 and 539.7 eV in Figure 4(a) correspond to Sb-O, which shows that as-deposited film surface easily

forms antimony oxide. Sb-Te bonds are demonstrated in polycrystalline films (Figure 4(b)) at 528.9 and 538.2 eV. Therefore, a postdeposition treatment is an effective method to promote the formation of Sb-Te bond and prevent oxidation of thin film surface.

The particle size and morphology of the Sb_2Te_3 as a back contact material affect the electrical properties of solar cells. Therefore, it is possible to evaluate the quality of the films by AFM. Figure 5 shows AFM images of Sb_2Te_3 thin films as-deposited (a) and annealed at 613 K (b). The films annealed at a high temperature exhibit larger particles than that as-deposited films, and the root mean square (RMS) values are about 2.3 nm for as-deposited films and 7.6 nm for the annealed films. Obviously, the posttreatment process can promote the growth of the films, which is significant to reduce the grain boundary density.

As a good buffer layer between the absorber layer and metal electrode in the CdTe solar cells, the back contact material (e.g., Sb_2Te_3) is generally an intermediate degenerated semiconductor, which increases the conductivity and creates a tunneling barrier. So we studied the electronic properties of Sb_2Te_3 thin films from the Hall measurements. Table 1 shows the parameters for Sb_2Te_3 thin films such as mobility, Hall coefficient, and carrier concentration. The thin films as-deposited and annealed at 613 K are p-type semiconductor compounds and have high carrier concentrations, 7.60×10^{19} and $5.87 \times 10^{19} \text{ cm}^{-3}$, respectively. Although the carrier concentration decreases slightly, the mobility of the Sb_2Te_3 thin films increases after the heat treatment, which means that the polycrystalline Sb_2Te_3 thin films have higher conductivity than amorphous ones and the thin films without Cu doping are suitable to form a p^+ -region layer to reduce the barrier height.

Meanwhile, electrical conductivity measurements were made on as-deposited Sb_2Te_3 thin films in the temperature range 300–650 K. The plot of conductivity versus temperature is shown in Figure 6. The conductivity decreases slowly with increasing temperature in the lower temperature range and reaches the minimum values at 433 K, and then it increases. This kind of change may be attributed to the oxidation of Te or Sb on the surface of the thin films as evidenced by the XRD and XPS studies. Above 473 K, however, the conductivity decreases at a rapid rate and subsequently increases after passing the minimum at a temperature of 523 K. It indicates that the films undergo a phase transition, from amorphous to crystalline between 473 and 523 K. This is consistent with XRD spectra (see Figures 1 and 2). Similarly, this irreversible behavior has also been observed on Sb-Te and Se-Te alloy systems [13, 14].

4. Conclusions

Sb_2Te_3 thin films were prepared by the vacuum coevaporation technique, together with posttreatment. As-grown thin films, which are oxidized easily in air, are an amorphous phase. After annealing the polycrystalline Sb_2Te_3 , thin films having a rhombohedra structure were obtained. An abnormal temperature dependence of conductivity was observed

in the temperature range 300–650 K, which shows that an amorphous-crystalline phase transition occurs in the thin films. Annealed at a high temperature can prevent effectively the oxidation of the thin films and increase obviously the mobility of thin films.

Acknowledgment

This work was supported by the Science and Technology Program of Sichuan Province, China (Grant no. 2008GZ0027).

References

- [1] D. L. Bätzner, A. Romeo, M. Terheggen, M. Döbeli, H. Zogg, and A. N. Tiwari, "Stability aspects in CdTe/CdS solar cells," *Thin Solid Films*, vol. 451-452, pp. 536–543, 2004.
- [2] N. Romeo, A. Bosio, R. Tedeschi, A. Romeo, and V. Canevari, "Highly efficient and stable CdTe/CdS thin film solar cell," *Solar Energy Materials and Solar Cells*, vol. 58, no. 2, pp. 209–218, 1999.
- [3] D. M. Rowe, *CRC Handbook of Thermoelectrics*, CRC Press, 1995.
- [4] A. M. Farid, H. E. Atyia, and N. A. Hegab, "AC conductivity and dielectric properties of Sb_2Te_3 thin films," *Vacuum*, vol. 80, no. 4, pp. 284–294, 2005.
- [5] H. Zou, D. M. Rowe, and S. G. K. Williams, "Peltier effect in a co-evaporated Sb_2Te_3 (P)- Bi_2Te_3 (N) thin film thermocouple," *Thin Solid Films*, vol. 408, no. 1-2, pp. 270–274, 2002.
- [6] J. Y. Yang, W. Zhu, X. H. Gao, X. A. Fan, S. Q. Bao, and X. K. Duan, "Electrochemical aspects of depositing Sb_2Te_3 compound on Au substrate by ECALE," *Electrochimica Acta*, vol. 52, no. 9, pp. 3035–3039, 2007.
- [7] A. E. Abken and O. J. Bartelt, "Sputtered Mo/ Sb_2Te_3 and Ni/ Sb_2Te_3 layers as back contacts for CdTe/CdS solar cells," *Thin Solid Films*, vol. 403-404, pp. 216–222, 2002.
- [8] I. Y. Erdoğan and U. Demir, "Synthesis and characterization of Sb_2Te_3 nanofilms via electrochemical co-deposition method," *Journal of Electroanalytical Chemistry*, vol. 633, no. 1, pp. 253–258, 2009.
- [9] H. S. Soliman, S. Yaghmour, and H. G. Al-Solami, "Heat-treatment effect on the structural and optical properties of flash evaporated Sb_2Te_3 thin films," *European Physical Journal Applied Physics*, vol. 44, no. 1, pp. 59–64, 2008.
- [10] R. Venkatasubramanian, T. Colpitts, E. Watko, M. Lamvik, and N. El-Masry, "MOCVD of Bi_2Te_3 , Sb_2Te_3 and their superlattice structures for thin-film thermoelectric applications," *Journal of Crystal Growth*, vol. 170, no. 1–4, pp. 817–821, 1997.
- [11] M.-J. Shin, D.-J. Choi, M.-J. Kang et al., "Chemical bonding characteristics of $\text{Ge}_2\text{Sb}_2\text{Te}_5$ for thin films," *Journal of the Korean Physical Society*, vol. 44, no. 1, pp. 10–13, 2004.
- [12] S. S. Garje, D. J. Eisler, J. S. Ritch, M. Afzaal, P. O'Brien, and T. Chivers, "A new route to antimony telluride nanoplates from a single-source precursor," *Journal of the American Chemical Society*, vol. 128, no. 10, pp. 3120–3121, 2006.
- [13] Z. S. El Mandouh, "Structure and electrical properties of vacuum-deposited antimony telluride thin films on an amorphous substrate," *Journal of Materials Science*, vol. 30, no. 5, pp. 1273–1276, 1995.
- [14] V. Damodara Das and P. Jansi Lakshmi, "In situ electrical conductivity and amorphous-crystalline transition in vacuum-deposited amorphous thin films of a $\text{Se}_{50}\text{Te}_{50}$ alloy," *Journal of Applied Physics*, vol. 62, no. 6, pp. 2376–2380, 1987.

Research Article

ZnO-Nanorod Dye-Sensitized Solar Cells: New Structure without a Transparent Conducting Oxide Layer

Ming-Hong Lai,¹ Auttasit Tubtimtae,¹ Ming-Way Lee,¹ and Gou-Jen Wang²

¹Department of Physics, Institute of Nanoscience, National Chung Hsing University, Taichung 402, Taiwan

²Department of Mechanical Engineering, National Chung Hsing University, Taichung 402, Taiwan

Correspondence should be addressed to Ming-Way Lee, mwl@phys.nchu.edu.tw

Received 24 November 2009; Accepted 21 December 2009

Academic Editor: Gaetano Di Marco

Copyright © 2010 Ming-Hong Lai et al. This is an open access article distributed under the Creative Commons Attribution License, which permits unrestricted use, distribution, and reproduction in any medium, provided the original work is properly cited.

Conventional nanorod-based dye-sensitized solar cells (DSSCs) are fabricated by growing nanorods on top of a transparent conducting oxide (TCO, typically fluorine-doped tin oxide—FTO). The heterogeneous interface between the nanorod and TCO forms a source for carrier scattering. This work reports on a new DSSC architecture without a TCO layer. The TCO-less structure consists of ZnO nanorods grown on top of a ZnO film. The ZnO film replaced FTO as the TCO layer and the ZnO nanorods served as the photoanode. The ZnO nanorod/film structure was grown by two methods: (1) one-step chemical vapor deposition (CVD) (2) two-step chemical bath deposition (CBD). The thicknesses of the nanorods/film grown by CVD is more uniform than that by CBD. We demonstrate that the TCO-less DSSC structure can operate properly as solar cells. The new DSSCs yield the best short-current density of 3.96 mA/cm² and a power conversion efficiency of 0.73% under 85 mW/cm² of simulated solar illumination. The open-circuit voltage of 0.80 V is markedly higher than that from conventional ZnO DSSCs.

1. Introduction

Dye-sensitized solar cells (DSSC) are a promising low-cost, green energy source [1, 2]. A power conversion efficiency of 11.18% has been achieved in 2005 [3]. The high efficiency of DSSCs can be attributed to the structure of a photoelectrode which consists of a layer of nanoparticle TiO₂ sintered to a transparent-conducting oxide (TCO). The mesoporous TiO₂ nanoparticles increase the surface area for dye chemisorptions to a thousand folds over that of a flat electrode of the same size [4]. The progress in enhancing the performance of DSSCs has been slow over the last decade. One of the main problems is the limited diffusion length of the photogenerated electrons. The photogenerated carriers conduct via random hopping through a percolated path in a three-dimensional network of TiO₂ nanoparticles. Previous studies have shown that the photogenerated carriers must undergo 10³–10⁶ hoppings (trapping and detrapping) before they reach the collecting electrodes [5]. Carrier trapping, presumably by defect states at the surface of TiO₂ nanoparticles [6, 7], leads to a low electron diffusion

coefficient ($7 \times 10^{-6} \text{ cm}^2 \text{ V}^{-1} \text{ s}^{-1}$) [8], which is several orders of magnitude smaller than that of single-crystal TiO₂ [9].

To improve the electron transport, researchers have tried to design DSSCs without a nanoparticulate structure. One promising approach is to replace the TiO₂ nanoparticles with crystalline TiO₂ nanorods (or nanowires, nanotubes), thereby eliminating the grain boundaries between nanoparticles. TiO₂-nanorod DSSCs have yielded recombination time constants an order of magnitude longer and significantly higher charge-collection efficiencies than that of nanoparticulate DSSCs [10, 11].

Work on nanorod-based DSSCs has been based on the TiO₂ system [12, 13], although recently the ZnO system has also started to attract more attention [14, 15]. ZnO has an energy gap of 3.37 eV, nearly identical to that of TiO₂. Currently, ZnO nanorod arrays are grown on a TCO glass (fluorine-doped tin oxide—FTO). A disadvantage in this structure is that a heterogeneous interface exists between the FTO glass and the nanorods, which forms a source for electron scattering.

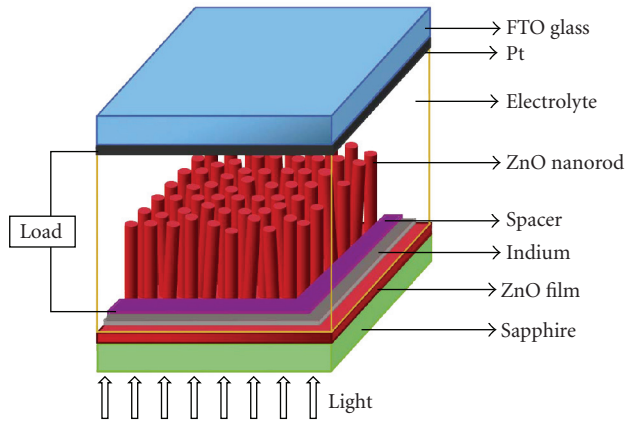


FIGURE 1: Schematic structure of the ZnO-nanorod dye-sensitized solar cell.

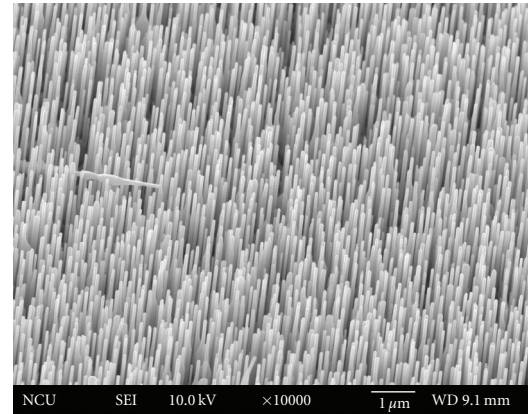
To increase the conversion efficiency of nanorod-based DSSCs, it would be desirable to eliminate the interface between FTO and the ZnO nanorods. Replacing the FTO layer with a ZnO film could eliminate the heterogeneous interface. Further more, since ZnO is transparent to the whole visible spectrum, it is a good TCO material. Chen et al. have recently carried out this concept by growing ZnO nanorods on a ZnO film using a two-step method [16]. In this work we grew ZnO nanorods on a ZnO film using two different techniques: one-step chemical vapor deposition (CVD) and two-step chemical bath deposition (CBD). The photovoltaic properties of the TCO-less DSSC samples were systematically investigated. The results were compared to those of a conventional ZnO-nanorod DSSC (i.e., ZnO nanorods grown on an FTO film). The electron transport characteristics were analyzed using the one-diode circuit model.

2. Experimental Procedure

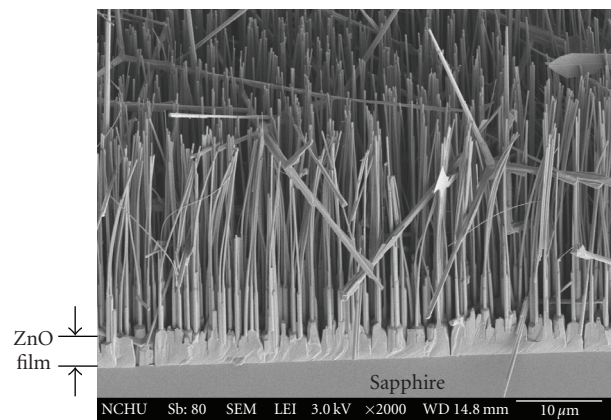
2.1. Sample Growth

2.1.1. CVD Growth. In the first experiment we grew ZnO nanorods on a ZnO film using the one-step CVD technique. High-purity Zn slugs (6N) were placed on an alumina boat inside a quartz one-inch diameter tube in a furnace. The c-plane (0001) sapphire single-crystalline substrates were placed 7 cm downstream from the Zn source. The growth conditions were: temperature 850–900°C and gas flow rates: 2 sccm (O_2) and 15 sccm (Ar), and growth time: 35 min. In the first stage of the growth process, a ZnO film grew on the sapphire substrate; in the second stage, ZnO nanorods started to grow on top of the ZnO film. The grown samples were examined by a scanning electron microscope (SEM). Photoluminescence (PL) spectra were measured using an HeCd laser of 325 nm wavelength.

2.1.2. CBD Growth. The second sample growth experiment employed a two-step CBD method. In the first step, a ZnO film was grown on a glass substrate; in the second step, ZnO



(a)



(b)

FIGURE 2: SEM images: (a) top view, (b) cross-sectional view, of ZnO nanorods on top of a ZnO film grown by the one-step CVD method.

nanorod arrays were synthesized on top of the ZnO film. The substrates were Corning 1737 glass. Aqueous solutions of 0.08 M of zinc nitrate hexahydrate $Zn(NO_3)_2 \cdot 6H_2O$ and 0.05 M of hexamethylenetetramine $C_6H_{12}N_4$ (HMT) were used as the precursors for the ZnO films. One M of hydrogen peroxide (H_2O_2) was added to the solution to make it more turbid (pH ~6.0–6.5), which is advantageous for obtaining more uniform thin films. A layer of ZnO film was deposited on the substrate after the reaction at 90°C for 1.3 h. For the growth of ZnO nanorods, the ZnO film-coated substrate was immersed vertically in a beaker containing a 0.01 M solution of the precursors used in the first step (zinc nitrate hexahydrate and HMT). The reaction was carried out at 95°C for 5 h. The process was repeated five-to-six times in order to obtain higher density and longer nanorods.

2.1.3. Growth of ZnO Nanorods for Conventional DSSCs. For comparison, a third reference sample was grown by the CBD method. The sample had the structure of conventional DSSCs—ZnO nanorods grown on an FTO glass substrate. Prior to the growth, a seed layer of ZnO nanoparticles was first deposited by immersing an FTO substrate into

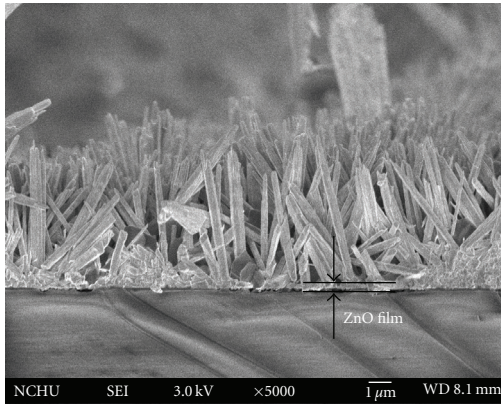


FIGURE 3: SEM image of ZnO nanorods on top of a ZnO film grown by the two-step CBD method.

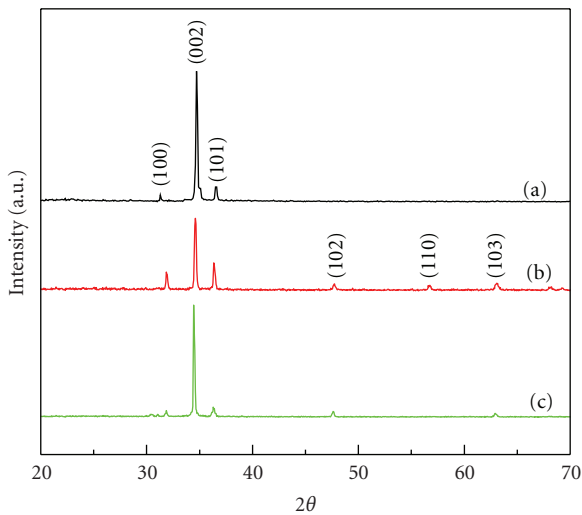


FIGURE 4: X-ray diffraction patterns of the ZnO nanorod/film samples. curve (a): CVD grown, curve (b): CBD grown, and curve (c): conventional.

a solution of 0.5 M zinc acetate $\text{Zn}(\text{CH}_3\text{COO})_2 \cdot 2\text{H}_2\text{O}$ and HMT for 30 min. ZnO nanorods were then grown on the substrate using the CBD method. The growth conditions were identical to those in Section 2.1.2.

2.2. Fabrication of Solar Cells. The TCO-less ZnO DSSCs were fabricated as follows. The ZnO film/nanorod sample was sensitized by immersion in a solution of 2×10^{-4} M N719 dye for 24 h at room temperature. An FTO glass with Pt foil $150 \mu\text{m}$ in thickness served as the counter electrode. The ZnO electrode and the counter electrode were assembled and sealed by a $25 \mu\text{m}$ thick parafilm spacer. The electrolyte was composed of 0.5 M LiI, 0.05 M I_2 , 0.5 M 4-tert-butylpyridine, and 0.6 M 1-butyl-methylimidazolium iodide in acetonitrile and valeronitrile. Figure 1 shows the schematic structure of a fabricated TCO-less DSSC on the grown ZnO film/nanorods.

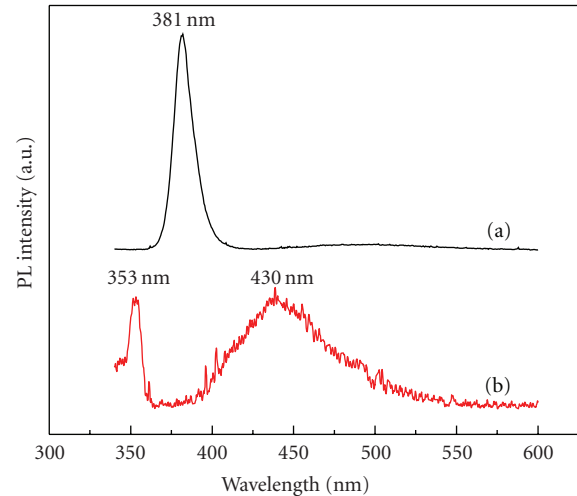


FIGURE 5: Room-temperature photoluminescence spectra of ZnO nanorods. Curve (a): CVD grown sample, curve (b): CBD grown sample.

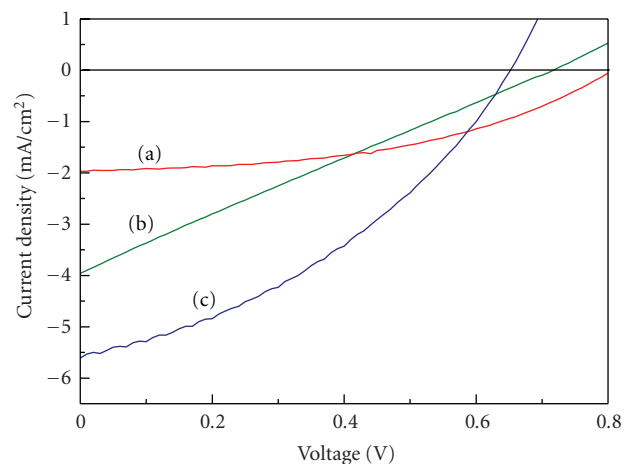


FIGURE 6: I - V characteristics of ZnO nanorod DSSCs. Curve (a): CVD-grown sample, curve (b): CBD-grown sample, and curve (c): conventional sample.

2.3. Photovoltaic Measurements. The current-voltage (I - V) characteristics measurements were performed using a 150 W Xe lamp (Oriel). A filter was placed in front of the sample to simulate the AM 1.5 spectrum. The active area of the cell was $0.3 \text{ cm} \times 0.3 \text{ cm}$. The photocurrent was recorded using a Keithley 2400 sourcemeter. The conversion efficiency is calculated as follows: $\eta = J_{sc} \cdot V_{oc} \cdot FF / I_{ph}$, where J_{sc} (mA/cm^2) is the short-circuit current density, V_{oc} is the open-circuit voltage, FF is the fill factor, and I_{ph} (mW/cm^2) is the intensity of the incident light.

3. Results and Discussion

3.1. Structure Characterization. Figure 2 shows (a) top view, (b) cross-sectional SEM images of ZnO nanorods on a ZnO film grown by the one-step CVD method. The nanorods

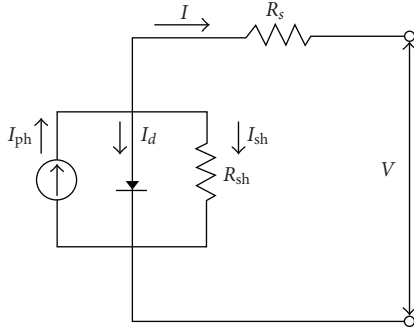


FIGURE 7: Equivalent circuit of the one-diode model.

TABLE 1: Photovoltaic characteristics of three ZnO-nanorod dye-sensitized solar cells grown by the one-step CVD, two-step CBD and conventional methods. The incident light intensity is 85 mW/cm^2 .

Sample	V_{oc} (V)	J_{sc} (mA/cm^2)	FF (%)	η (%)
CVD	0.80	1.97	39.4	0.73
CBD	0.72	3.96	20.0	0.66
conventional	0.65	5.51	38.2	1.37

have an average length of $\sim 20 \mu\text{m}$, diameter ranging from 100 to 200 nm and they are mostly vertically aligned with the substrate. A ZnO film of thickness $\sim 2 \mu\text{m}$ can be clearly seen. Figure 3 shows a SEM image of ZnO nanorods grown by the two-step CBD method. The nanorods have diameters ranging from 50 to 500 nm and length from 7 to $10 \mu\text{m}$. The ZnO film has a thickness ranging from 0.3 to $1 \mu\text{m}$. It can be seen that the CVD-grown nanorods have a more uniform distribution in thickness than that in the CBD sample. The thickness of the CVD-grown ZnO film is also more uniform.

Figure 4 shows the X-ray diffraction patterns of the ZnO film/nanorods grown by the three methods. The diffraction patterns correspond to the hexagonal wurtzite structure with lattice constants of $a = 3.176 \text{ \AA}$, $c = 5.187 \text{ \AA}$. In the CVD sample, the most pronounced peak is (002), indicating that the preferential growth is along the c axis of a nanorod. In contrast, the diffraction pattern of the conventional ZnO sample shows the main (002) peak along with many weak peaks, indicating no preferential orientation in the nanorod growth. The difference in nanorod orientation is an effect of the substrate. In the CVD growth, single-crystalline sapphire was used, resulting in oriented nanorods. In the conventional method, FTO glass without preferential orientations was used, resulting in randomly orientated nanorods.

Figure 5 shows the room-temperature PL spectra of ZnO nanorods grown by the CVD and CBD methods. The CVD sample shows a sharp blue peak at $\lambda = 380 \text{ nm}$, attributed to the free exciton emission of ZnO. In the CBD sample this blue peak is upshifted to 353 nm and a broad peak at 430 nm is observed. The latter peak can be attributed to singly ionized oxygen vacancies [17]. We observed that CVD processing in a lower oxygen partial pressure led to more oxygen vacancies and a larger 430 nm peak.

3.2. Photovoltaic Properties. Figure 6 shows the photocurrent-voltage (I - V) characteristics for three ZnO-nanorod DSSC samples grown by the CVD, CBD and conventional methods. The photovoltaic characteristics are listed in Table 1. The CVD-grown sample has an open circuit voltage V_{oc} of 0.80 V and an energy conversion efficiency $\eta = 0.73\%$. The CBD sample has a higher short-circuit current density of $J_{sc} = 3.96 \text{ mA/cm}^2$. The efficiency is very close to that of Chen et al. (0.77%) for a DSSC with the same TCO-less structure. The conventional DSSC has a conversion efficiency of $\eta = 1.37\%$. In general, the energy conversion efficiency of ZnO DSSCs is lower than that of TiO_2 DSSCs. Note that the efficiency of ZnO-nanorod-based DSSCs is typically 1%-2% [18].

A notable feature of the present result is that the open-circuit voltage V_{oc} of the TCO-less DSSCs is relatively high (0.80 V), about 20%–40% higher than that of conventional ZnO-nanorod DSSCs, typically $\sim 0.6 \text{ V}$ [19, 20]. According to the kinetic model, the open-circuit voltage is limited by $E_F - E_{redox}$, where E_F is the Fermi level of ZnO and E_{redox} is the redox potential of the electrolyte. The actual V_{oc} obtained in experiments is lower than the theoretical upper limit due to the dark current in the solar cell. The dark current is mainly caused by carrier recombination between the photoinjected electrons in the semiconductor and the positively charged dye molecules or electrolyte. Our present result suggests that carrier recombination in the TCO-less structure is reduced, resulting in a larger V_{oc} .

The conversion efficiencies of the TCO-less DSSCs are lower than those of the conventional DSSC. We attribute this to the large resistance in the ZnO film. We analyze the series resistance R_s and shunt resistance R_{sh} of the DSSC from I - V curve using the one-diode model. The equivalent circuit is shown in Figure 7. The equation of the circuit is

$$I = I_{ph} - I_d - I_{sh}$$

$$= I_{ph} - I_0 \left\{ \exp \left(q \frac{V + IR_s}{nkT} \right) - 1 \right\} - \frac{V + IR_s}{R_{sh}}, \quad (1)$$

where I_{ph} is the photo current, I_d is the diode current, I_{sh} is the shunt current, I_0 is the initial current, n is the diode factor, q the electric charge, and k is the Boltzmann constant. The I - V curve (a) in Figure 6 (the CVD sample) was taken for fitting. The best fit yields the parameters: $J_{ph} = 2.07 \text{ mA/cm}^2$, $J_0 = 0.37 \text{ nA/cm}^2$, $R_s = 1850 \Omega$, and $R_{sh} = 25 \text{ k}\Omega$. Considering recombination current in DSSCs, the diode factor n was set to 2 in the fitting. The series resistance R_s is relatively large for solar cells, which is because the ZnO film is undoped and, therefore, has a large resistance. Doping to the film with Ga or In should produce a lower-resistance film, which will increase the efficiency of the DSSCs.

The one-step growth method in the present work has several advantages over Chen's two-step MOCVD method. In Chen's method, a Ga-doped ZnO film was grown on the substrate in the first step; ZnO nanotips were grown on top of the ZnO film in the second step. The experimental conditions had to be varied during the two steps. In the present work, a one-step vapor-transport CVD method was used to grow the ZnO film/nanorod structure. The sample growth could be

completed in one run. The new method is simpler, reaction time is shorter, and the growth equipment is much cheaper than MOCVD.

4. Conclusion

In conclusion, we have demonstrated a new DSSC structure without a TCO layer. A ZnO film, grown by the one-step CVD or the two-step CBD method, is used to replace the TCO layer. The new structure eliminates the interface between the nanorod and the TCO film. The ZnO nanorods and ZnO films grown by the CVD method have more uniform thickness. The DSSC structure yields an open-circuit voltage markedly higher than that from DSSC on an FTO glass. Higher electrical conductance in the ZnO film is needed to improve the DSSC efficiency.

References

- [1] B. O'Regan and M. Grätzel, "A low-cost, high-efficiency solar cell based on dye-sensitized colloidal TiO₂ films," *Nature*, vol. 353, no. 6346, pp. 737–740, 1991.
- [2] M. Grätzel, "Perspectives for dye-sensitized nanocrystalline solar cells," *Progress in Photovoltaics*, vol. 8, no. 1, pp. 171–185, 2000.
- [3] M. K. Nazeeruddin, F. de Angelis, S. Fantacci, et al., "Combined experimental and DFT-TDDFT computational study of photoelectrochemical cell ruthenium sensitizers," *Journal of the American Chemical Society*, vol. 127, no. 48, pp. 16835–16847, 2005.
- [4] K. Kalyanasundaram, N. Vlachopoulos, V. Krishnan, A. Monnier, and M. Grätzel, "Sensitization of TiO₂ in the visible light region using zinc porphyrins," *Journal of Physical Chemistry*, vol. 91, no. 9, pp. 2342–2347, 1987.
- [5] K. D. Benkstein, N. Kopidakis, J. van de Lagemaat, and A. J. Frank, "Influence of the percolation network geometry on electron transport in dye-sensitized titanium dioxide solar cells," *Journal of Physical Chemistry B*, vol. 107, no. 31, pp. 7759–7767, 2003.
- [6] A. C. Fisher, L. M. Peter, E. A. Ponomarev, A. B. Walker, and K. G. U. Wijayantha, "Intensity dependence of the back reaction and transport of electrons in dye-sensitized nanocrystalline TiO₂ solar cells," *Journal of Physical Chemistry B*, vol. 104, no. 5, pp. 949–958, 2000.
- [7] J. van de Lagemaat and A. J. Frank, "Nonthermalized electron transport in dye-sensitized nanocrystalline TiO₂ films: transient photocurrent and random-walk modeling studies," *Journal of Physical Chemistry B*, vol. 105, no. 45, pp. 11194–11205, 2001.
- [8] Th. Dittrich, E. A. Lebedev, and J. Weidmann, "Electron drift mobility in porous TiO₂ (anatase)," *Physica Status Solidi A*, vol. 165, no. 2, pp. R5–R6, 1998.
- [9] L. Forro, O. Chauvet, D. Emin, L. Zuppiroli, H. Berger, and F. Lévy, "High mobility n-type charge carriers in large single crystals of anatase (TiO₂)," *Journal of Applied Physics*, vol. 75, no. 1, pp. 633–635, 1994.
- [10] G. K. Mor, K. Shankar, M. Paulose, O. K. Varghese, and C. A. Grimes, "Use of highly-ordered TiO₂ nanotube arrays in dye-sensitized solar cells," *Nano Letters*, vol. 6, no. 2, pp. 215–218, 2006.
- [11] K. Zhu, N. R. Neale, A. Miedaner, and A. J. Frank, "Enhanced charge-collection efficiencies and light scattering in dye-sensitized solar cells using oriented TiO₂ nanotubes arrays," *Nano Letters*, vol. 7, no. 1, pp. 69–74, 2007.
- [12] M. Adachi, Y. Murata, I. Okada, and S. Yoshikawa, "Formation of titania nanotubes and applications for dye-sensitized solar cells," *Journal of the Electrochemical Society*, vol. 150, no. 8, pp. G488–G493, 2003.
- [13] M. Dürr, A. Schmid, M. Obermaier, S. Rosselli, A. Yasuda, and G. Nelles, "Low-temperature fabrication of dye-sensitized solar cells by transfer of composite porous layers," *Nature Materials*, vol. 4, no. 8, pp. 607–611, 2005.
- [14] M. Guo, P. Diao, X. Wang, and S. Cai, "The effect of hydrothermal growth temperature on preparation and photoelectrochemical performance of ZnO nanorod array films," *Journal of Solid State Chemistry*, vol. 178, no. 10, pp. 3210–3215, 2005.
- [15] J. B. Baxter and E. S. Aydil, "Nanowire-based dye-sensitized solar cells," *Applied Physics Letters*, vol. 86, no. 5, Article ID 045004, pp. 1–3, 2005.
- [16] H. Chen, A. Du Pasquier, G. Saraf, J. Zhong, and Y. Lu, "Dye-sensitized solar cells using ZnO nanotips and Ga-doped ZnO films," *Semiconductor Science and Technology*, vol. 23, no. 4, Article ID 045004, 2008.
- [17] K. Vanheusden, W. L. Warren, C. H. Seager, D. R. Tallant, J. A. Voigt, and B. E. Gnade, "Mechanisms behind green photoluminescence in ZnO phosphor powders," *Journal of Applied Physics*, vol. 79, no. 10, pp. 7983–7990, 1996.
- [18] C. Y. Jiang, X. W. Sun, G. Q. Lo, D. L. Kwong, and J. X. Wang, "Improved dye-sensitized solar cells with a ZnO-nanoflower photoanode," *Applied Physics Letters*, vol. 90, no. 26, Article ID 263501, 2007.
- [19] J.-J. Wu, G.-R. Chen, H.-H. Yang, C.-H. Ku, and J.-Y. Lai, "Effects of dye adsorption on the electron transport properties in ZnO-nanowire dye-sensitized solar cells," *Applied Physics Letters*, vol. 90, no. 21, Article ID 213109, 2007.
- [20] I.-D. Kim, J.-M. Hong, B. H. Lee, et al., "Dye-sensitized solar cells using network structure of electrospun ZnO nanofiber mats," *Applied Physics Letters*, vol. 91, no. 16, Article ID 163109, 2007.

Research Article

Fabrication of Dye-Sensitized Solar Cells with a 3D Nanostructured Electrode

Guo-Yang Chen,¹ Ming-Way Lee,² and Gou-Jen Wang^{1,3}

¹ Department of Mechanical Engineering, National Chung-Hsing University, Taichung 402, Taiwan

² Department of Physics, National Chung-Hsing University, Taichung 402, Taiwan

³ Institute of Biomedical Engineering, National Chung-Hsing University, Taichung 402, Taiwan

Correspondence should be addressed to Gou-Jen Wang, gjwang@dragon.nchu.edu.tw

Received 25 November 2009; Accepted 18 February 2010

Academic Editor: Leonardo Palmisano

Copyright © 2010 Guo-Yang Chen et al. This is an open access article distributed under the Creative Commons Attribution License, which permits unrestricted use, distribution, and reproduction in any medium, provided the original work is properly cited.

A novel Dye-Sensitized Solar Cell (DSSC) scheme for better solar conversion efficiency is proposed. The distinctive characteristic of this novel scheme is that the conventional thin film electrode is replaced by a 3D nanostructured indium tin oxide (ITO) electrode, which was fabricated using RF magnetron sputtering with an anodic aluminum oxide (AAO) template. The template was prepared by immersing the barrier-layer side of an AAO film into a 30 wt% phosphoric acid solution to produce a contrasting surface. RF magnetron sputtering was then used to deposit a 3D nanostructured ITO thin film on the template. The crystallinity and conductivity of the 3D ITO films were further enhanced by annealing. Titanium dioxide nanoparticles were electrophoretically deposited on the 3D ITO film after which the proposed DSSC was formed by filling vacant spaces in the 3D nanostructured ITO electrode with dye. The measured solar conversion efficiency of the device was 0.125%. It presents a 5-fold improvement over that of conventional spin-coated TiO₂ film electrode DSSCs.

1. Introduction

Dye-sensitized solar cells (DSSCs) that belong to the group of thin film solar cells are currently the most efficient second-generation solar technology available. The advantages of these promising solar cells are numerous including low cost, requiring no expensive manufacturing steps, large-scale feasibility [1], capable of working in low-light conditions, and higher efficiencies at higher temperatures. The European Union Photovoltaic Roadmap forecasts that DSSCs will be a potential significant renewable power source by 2020.

The DSSC consists of a transparent and conductive anode made of fluorine-doped tin dioxide deposited on a glass substrate, a thin layer of titanium dioxide (TiO₂) on the back of the conductive plate, photosensitive ruthenium-polypyridine dyes covalently bonded to the surface of the TiO₂, a thin iodide electrolyte layer, and a conductive counter electrode (typically platinum). The photocurrent in the DSSC is attributed to the photoelectrons that are produced when photons of sunlight (with enough energy to be absorbed) strike the dye on the surface of the TiO₂. Photoelectrons

move directly from the LUMO (Lowest Unoccupied Molecular Orbital), that is the excited state of the dye, to the conduction band of the TiO₂, and from there they diffuse to the conducting electrode. The dye molecules that have lost an electron strip one from the iodide electrolyte, which is oxidized into triiodide. The triiodide then regains its lost electron by mechanically diffusing to the counter electrode, where the electrons, after flowing through the external circuit, are reintroduced. The key factors that determine the photoelectric efficiency are the structure of individual elements and the type of dye used in the cell. The former affects the separation of the electron-hole pairs, the migration of photoelectrons and holes, and the recombination of photoelectrons and holes. The latter controls the short-circuit current (J_{sc}) and the open-circuit voltage (V_{oc}) of the cell.

The original DSSC was invented by O'Regan and Grätzel [2] in 1991. The use of a porous nanocrystalline TiO₂ thin film as the electrode greatly enhanced the binding area for the dye, resulting in a tremendously enlarged photoreaction area. The absorption capability of the dye to visible light captures

46% of the illumination from the sun. The conversion efficiency of the original solar cell was 7.1%. Since then, intensive efforts have been devoted to the improvement of the solar conversion efficiency. Recent progress in nanotechnology, particularly in porous nanostructured TiO₂, has further increased the efficiency to 12%, close to that of traditional low-cost commercial silicon panels.

The main focus in the development of new TiO₂ nanostructures has been how to enhance the efficiency of the photoreaction and the electron migration processes. Chou et al. [3] used the sol-gel method to fabricate TiO₂ nanostructures followed by spreading them on a TiO₂ thin film. An et al. [4] utilized reactive electrodeposition to produce nano grains of TiO₂. Different TiO₂ nanotube arrays [5–8] were invented to enable the multidirectional transfer of the photoelectrons. The total amount of photon absorption could also be enhanced because a nanotube array is thicker than a thin film. The photocurrent could be increased by adding various metallic oxides to a TiO₂ thin film [9, 10].

Since the average traveling distance of a photoelectron is only about 10 nanometers, most do not have enough momentum to reach the transparent conducting thin film electrode, resulting in a relatively low efficiency compared to silicon based solar cells. Therefore, the conversion efficiency could also be improved by increasing the conductivity of the transparent conducting thin film. Takaki et al. [11] used DC magnetron sputtering to fabricate transparent indium tin oxide (ITO) whiskers on a glass substrate. However, the efficiency of electron migration in the DSSC electrode was degraded by the irregular structure of the ITO whiskers. Wan et al. [12] used the self-catalytic vapor-liquid-solid growth method to synthesize one-dimensional ITO nanowires and whiskers on an yttrium stabilized zirconia (YSZ) substrate; however, their synthesizing procedure was complex, leaving room for further improvement. Wang et al. [13] used a template assisted method to grow high aspect ratio ITO nanotube arrays. However, the irregular arrangement of the ITO nanotubes would likely retard the transfer of photoelectrons. A more conductive electrode element for better solar conversion efficiency is desired.

The purpose of this study is to develop a novel scheme for fabrication of DSSCs with better solar conversion efficiency. In this novel scheme, the conventional thin film electrode is replaced by a 3-dimensional nanostructured ITO electrode, fabricated using RF magnetron sputtering, with the barrier layer of an anodic aluminum oxide (AAO) membrane being the template. The crystallinity and conductivity of the 3D ITO film are further enhanced by annealing [14]. Titanium dioxide nanoparticles are electrophoretically deposited on 3D ITO film. The proposed DSSC is formed after filling up vacant spaces in the 3D nanostructured ITO electrode with dye.

2. 3D Nanostructured Electrode Fabrication

2.1. Electrode Fabrication. The distinguishing characteristic of the novel DSSC is the replacement of the conventional thin film electrode by a 3D nanostructured ITO electrode. This is followed by electrophoretic deposition of TiO₂ on the

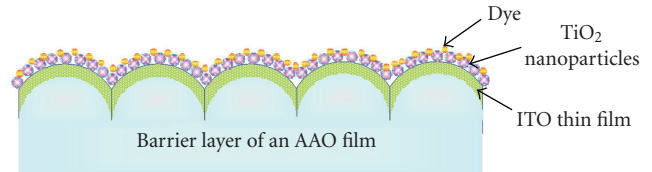


FIGURE 1: Schematic illustration of the proposed 3D nanostructured TiO₂/ITO/AAO electrode.

3D ITO film after which vacant spaces in the electrode are filled by the dye. Figure 1 shows a schematic illustration of the proposed 3D nanostructured electrode for DSSC.

The fabrication procedure includes preparation of the AAO membrane, modification of the barrier-layer surface modification, sputtering of the ITO thin film, deposition of the TiO₂ nanoparticles, and deposition of the dye. The process is itemized in detail below.

(1) *Preparation of the AAO Membrane* [15, 16]. The AAO films were prepared using a well-known anodizing process. Aluminum foils were cleansed and electropolished before anodization. AAO films, with a nanopore diameter of around 60 nm and a thickness of 50 μm were obtained by anodizing the polished aluminum foil in a 0.3 M phosphoric acid solution under an applied voltage of 90 V at 0°C for 2 hours.

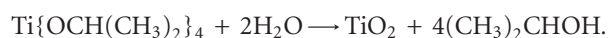
(2) *Modification of the Barrier-Layer Surface.* During the first stage, the remaining aluminum beneath the barrier layer was dissolved in an aqueous CuCl₂ · HCl solution that was prepared by dissolving 13.45 g of powdered CuCl₂ into 100 mL of a 35 wt% hydrochloric acid solution. The removal of the remaining aluminum reveals the honey-comb-like surface of the barrier-layer. The honey-combs have an average convex diameter of 80 nm. Then, the barrier-layer surface was immersed in a 30 wt% phosphoric acid at room temperature for 35 minutes to modify the surface structure.

(3) *Deposition of the ITO Thin Film.* The modified barrier-layer surface functioned as a template for deposition of the 3D nanostructured ITO thin film by radio frequency (RF) magnetron sputtering. The experimental conditions were as follows: pressure = 4.5×10^{-5} torr; temperature = 150°C; argon = 30 sccm; power = 50 W; processing time = 90 minutes. A 3D nanostructured ITO film with a thickness of about 30 nm was obtained after the sputtered film was cooled to room temperature.

(4) *Annealing.* The electrical properties and crystalline structure of RF magnetron sputtered thin films usually are not good enough [17–19]. An additional annealing process was utilized to further modify the surface structures of the 3D nanostructure of the ITO film and increase the conductance of the sample [20, 21]. The annealing procedures included: heating the sample to 150°C and 500°C, respectively at a rate of 9°C/sec where it remained for 10 minutes, then cooling the sample in air to room temperature.

(5) *Deposition of TiO₂ Nanoparticles.* The electrophoretic deposition method [22] was used to deposit TiO₂ nanoparticles uniformly on the ITO thin film. The deposition processes included the following.

(i) *Sol Preparation* [23]. In the sol preparation procedure, 30 mL Ti (IV) of isopropoxide [Ti(OCH(CH₃)₂)₄] (Alfa Aesar, Ward Hill, MA) were first added to 60 mL of glacial acetic acid (Fisher Scientific, Fair Lawn, NJ) after which the mixture was stirred for 5–10 minutes. Then 30 mL of DI-water were stirred into the mixture. White precipitates formed when the DI-water was added. The chemical reaction for this process is



After the formation of white precipitates, stirring continued until approximately 30 minutes after the solution became clear. Since the PH value of the final solution was about 2 and the isoelectric point (IEP) of TiO₂ is 6.2, the TiO₂ nanoparticles in the solution were positive charged. The final clear sol was stored at –20°C when not in use.

(ii) *Electrophoretic Deposition.* Electrophoretic deposition was conducted with a picoammeter (Sversa Stat II, Princeton Applied Research). The ITO thin film deposited sample was first placed at the working electrode (WE). The counter electrode was a Pt film; the reference electrode (RE) was Ag/AgCl. An electric potential of DC 1.4 V was applied during the electrophoretic deposition process. The deposition duration ranged from 180 seconds to 5400 seconds.

Titanium dioxide, which is found in natural minerals such as rutile, anatase, and brookite, acts as a photocatalyst under ultraviolet light (when in the form of anatase). A sintering process is usually applied to ensure that the TiO₂ nanoparticles are in the form of anatase. In this study, the sample was heated to the crystallization temperature of anatase (500°C) at a rate of 2°C/minute where it remained for 1 hour, then cooled in air to room temperature.

(iii) *Spin-Coating.* Since the TiO₂ nanoparticle film was not thick enough, an additional spin-coated TiO₂ layer was added. A 3 μm thick TiO₂ layer could be obtained using a first-stage rotating speed of 500 rpm followed by a second-stage rotating speed of 2000 rpm, both for 20 seconds.

(6) *Dye Deposition.* The device was then immersed in a solution of sensitized dye N3 (Dyesol) for 24 hours to allow the dye molecules to covalently bond to the surface of the TiO₂. Unbound particles were rinsed away in an ethanol solution. The absorption spectrum of N3 in the visible light scope ranges from 400 nm to 800 nm, having two peaks at 538 nm and 398 nm.

2.2. *DSSC Assembly.* A schematic illustration of the assembly of the DSSC is shown in Figure 2, including the fabrication of the counter electrode fabrication, preparation of the electrolyte, and assembly of the parts.

(1) *Counter Electrode Fabrication.* Platinum foil was chosen as the counter electrode material. The platinum foil was

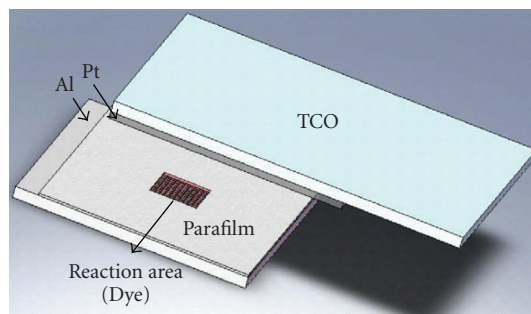
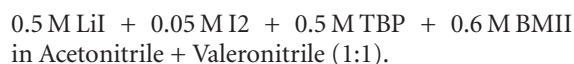


FIGURE 2: DSSC assembly.

electropolished before being attached to a transparent conductive oxide (TCO) thin film to ensure a better efficiency of light reflection into the cell body.

(2) *Electrolyte Preparation.* It is desirable that the electrolyte used in DSSCs has the following properties: high diffusion coefficient, fast oxidation-reduction reaction, and low intrinsic resistance. The recipe for the electrolyte employed in this study which satisfies these specifications is



(3) *Parts Assembly Procedure.* The parts assembly procedure: parafilm is cut into a rectangle. A 2 × 2 cm² square is punched into the center of the rectangular parafilm. A thin film of AB glue is applied to the bottom surface of the parafilm to attach it to the electrode. Fine clamped the electrode and the counter electrode. The electrolyte is injected into the cell body using a syringe. The photoreaction area can be well controlled by the square punched in the parafilm.

2.3. Fabrication Results and Discussion

(1) *Barrier-Layer Surface Modification Results.* Figure 3 shows SEM images of the original and the modified barrier-layer surface after being etched in a 30 wt% phosphoric acid for 35 minutes. Due to the stress concentration effect during anodization, the phosphoric acid etched out more alumina at the borders between the cells than from the cell surfaces, resulting in an orderly hemispheric barrier-layer surface.

(2) *ITO Resistance Measurement.* Since the ITO thin film on the AAO template was a 3D nanostructure, its electrical properties could not be represented in terms of the sheet resistance. Instead, the *I-V* curve of the ITO film was measured using a Keithley 2400 Digital Source Meter for a convenient estimation of its resistance. The resistance of the 3D ITO film was calculated by Ohm's law.

The resistances of annealed ITO films subjected to two annealing temperatures are illustrated in Figure 4. The curve indicated by AC denotes the resistances measured between locations A and C on the device as shown in Figure 5, while the BC curve indicates the resistances measured between

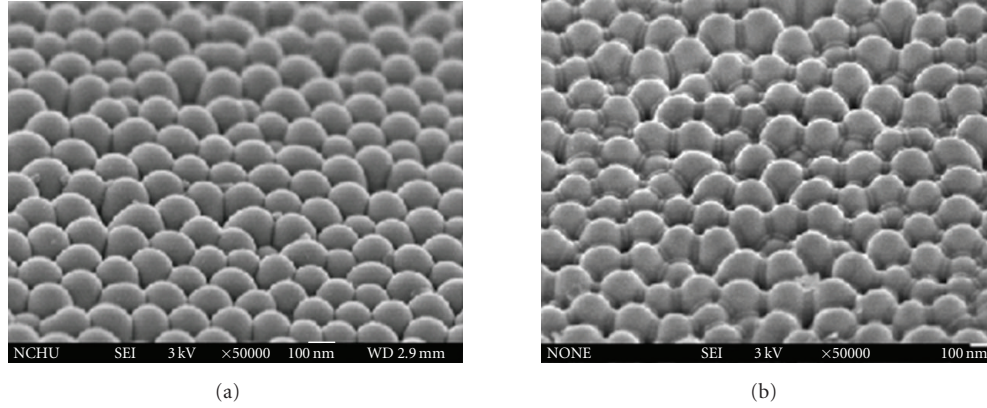


FIGURE 3: SEM images of the barrier-layer surfaces: (a) original, (b) after 35 minutes of etching.

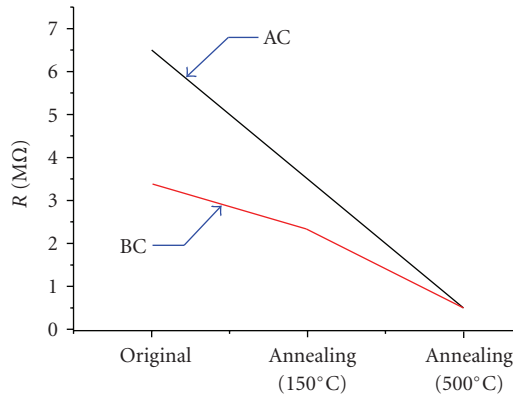


FIGURE 4: Resistances of ITO film annealed at different temperatures.

locations B and C. Location B is the middle point between location A and location C. It is observed that the resistance of the 3D ITO film was reduced from 6.5 M Ω to 0.5 M Ω . Therefore, an annealing temperature of 500°C was employed in this study.

(3) *TiO₂ Nanoparticles Deposition Results.* Figure 6 shows SEM images of nano-hemispheric TiO₂/ITO/AAO electrodes subjected to TiO₂ deposition for various durations. The morphology of the TiO₂ film varied with the deposition duration, starting from scattered nanoparticles to a complete thin film. It can be observed that after a 250-second deposition, the TiO₂ nanoparticles were uniformly deposited on the nano-hemispheric ITO array. The measured transparency of this device obtained using an optical power meter (model 1830C, Newport) was 70%.

The relative energy-dispersive X-ray spectroscopy (EDS) spectrum for the 3D TiO₂ film shown in Figure 6(b) is illustrated in Figure 7. It can also be seen that TiO₂ molecules were successfully deposited on the 3D ITO film.

In addition to heating to the crystallization temperature of anatase, 500°C, sintering was conducted at various temperatures. Figure 8 illustrates the X-ray diffraction (XRD) spectra deposited TiO₂ nanoparticles sintered at various

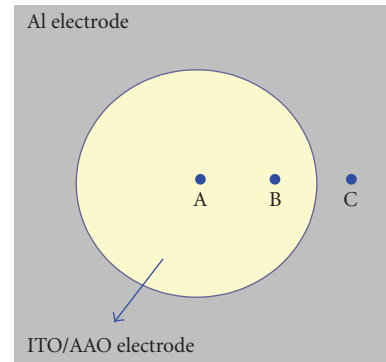


FIGURE 5: Schematic illustration of the reference locations for resistance measurement.

temperatures. The XRD spectra indicate that the TiO₂ nanoparticle sintered at temperatures higher than 500°C possesses better crystal lattices of anatase. However, the higher sintering temperature will induce a degradation in the ITO's conductivity so sintering at 500°C is suggested.

(4) *Dye Deposition Result.* Figure 9 shows an SEM image after N3 soaking of the device shown in Figure 6(b).

3. Solar Conversion Efficiency Measurement

3.1. *Apparatus Setup.* An Oriel Xe-lamp was used as the light source, and a Keithley 2400 picoammeter was employed to measure the dark-light and illuminated *I-V* curves of the DSSC during the efficiency measurement experiments. The position of the light source was adjusted such that AM 1.5 (100 mW/cm²) of power was delivered to the surface of the measured DSSC.

The solar conversion efficiency (η) of a DSSC can be estimated using the conversion efficiency formula

$$\eta = \frac{P_{\max}}{P_{\text{in}}}, \quad (1)$$

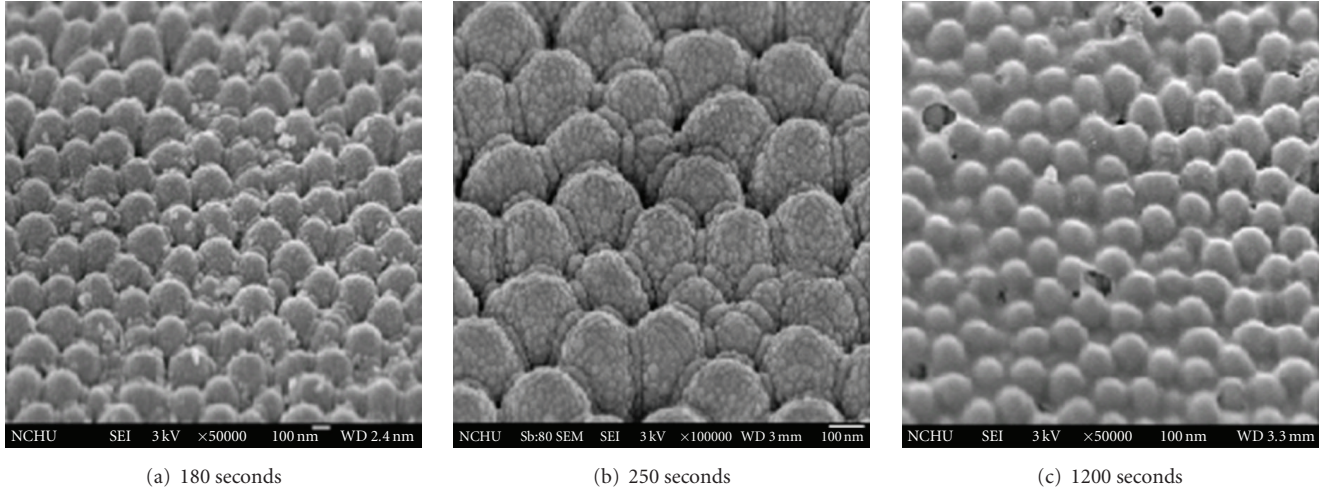


FIGURE 6: SEM images of nano-hemispheric $\text{TiO}_2/\text{ITO}/\text{AAO}$ electrodes after various deposition durations.

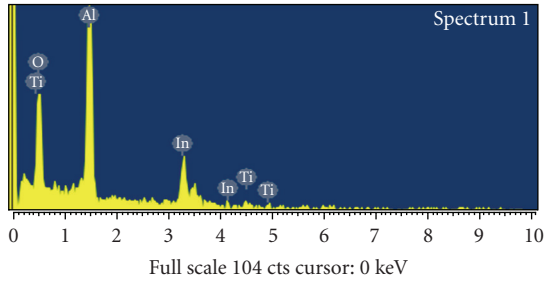


FIGURE 7: EDS spectrum for the TiO_2 film shown in Figure 6(b).

where P_{\max} , and P_{in} denote the maximum output power and the input power, respectively. Since a DSSC usually contains a series resistance and a shunt resistance, the fill factor (FF) is introduced to count both effects.

$$\text{FF} = \frac{P_{\max}}{J_{\text{sc}} \times V_{\text{oc}}}, \quad (2)$$

where V_{oc} is the open-circuit voltage and J_{sc} is the short-circuit current. The solar conversion efficiency of a DSSC can be calculated by

$$\eta = \frac{J_{\text{sc}} \times V_{\text{oc}} \times \text{FF}}{P_{\text{in}}}. \quad (3)$$

3.2. Measurement Results and Discussions. Efficiency measurements for three kinds of electrode were conducted.

(1) *Electrophoretically Deposited TiO_2 Nanoparticle Electrode.* The open-circuit voltage and the current density were measured to be 0.59 V and 0.0176 (mA/cm^2), respectively. The fill factor and the solar conversion efficiency were calculated to be 36.3% and 0.005% according to (2) and (3).

(2) *Spin-Coated TiO_2 Film Electrode.* The spin-coated TiO_2 film was 3 μm thick. Measurement results were as follows:

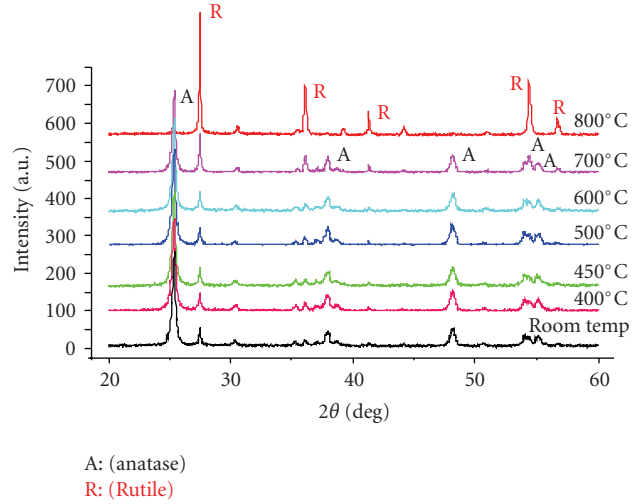


FIGURE 8: XRD spectra for the deposited TiO_2 nanoparticles sintered at various temperatures.

open-circuit voltage = 0.79 V; current density = 0.083 (mA/cm^2); fill factor = 33.3%; solar conversion efficiency = 0.0257%.

(3) *Deposited TiO_2 Nanoparticle and Spin-Coated TiO_2 Film Composite Electrode.* An additional spinning-coated TiO_2 layer with a thickness of 3 μm was added to the deposited TiO_2 nanoparticles. The measurement results are shown in Figure 10. The horizontal part of the dark current was about 0 μA , approaching the standard. The open-circuit voltage and the current density were measured to be 0.66 V and 0.436 (mA/cm^2), respectively. Accordingly, the fill factor and the solar conversion efficiency were calculated to be 37% and 0.125%.

Although the solar conversion efficiency of the proposed DSSC is only 0.125%, this is a 5-fold improvement over that of the conventional DSSC fabricated using a spin-coated

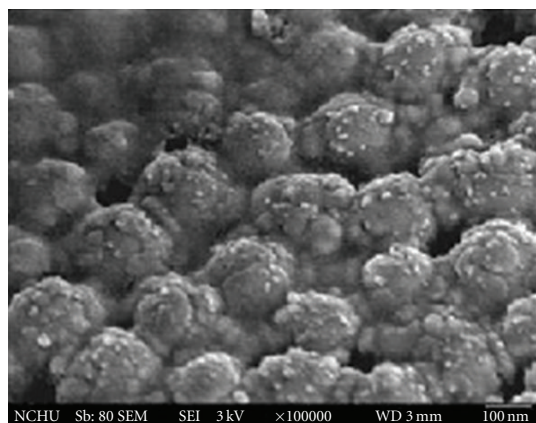


FIGURE 9: SEM image after N3 soaking.

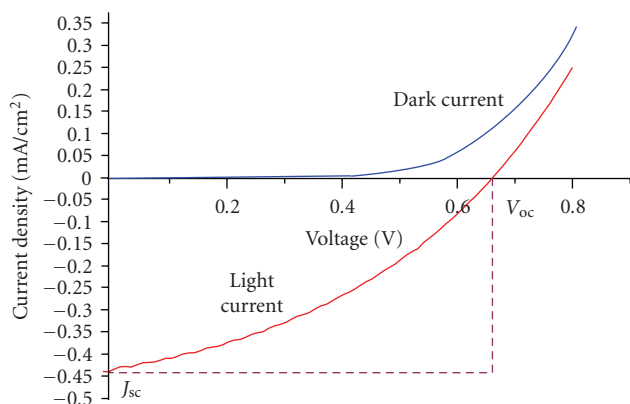


FIGURE 10: Conversion efficiency measurement of the proposed DSSC.

TiO₂ film electrode. The low conversion efficiency can be attributed to the following factors.

(1) *The Deposited TiO₂ Nanoparticle Layer Was Not Thick Enough.* The thickness of the deposited TiO₂ nanoparticle layer was about several tens of nm. Compared to the 10 μm thickness of the conventional TiO₂ thin film electrode, this did not seem thick enough. As a result, light only had a short retention period in the cell.

(2) *The ITO Film Was Not Conductive Enough.* The resistance measurement results shown in Figure 4 indicate that the resistance of the ITO film produced by annealing at 500°C was still on the scale of MΩ. It can be presumed that electrons could not be conveyed efficiently through the ITO electrode.

4. Conclusion

A novel DSSC scheme for better energy conversion efficiency is proposed. The characteristic feature is the replacement of the conventional thin film electrode by a sputtered 3D nanostructured ITO electrode fabricated using an AAO template.

The electrophoretic deposition of TiO₂ nanoparticles on the 3D ITO film was followed by soaking in N3 dye to fill vacant spaces in the electrode.

The measured open-circuit voltage and the current density of the proposed scheme were 0.66 V and 0.436 (mA/cm²), respectively. Accordingly, the fill factor and the solar conversion efficiency were calculated to be 37% and 0.125%. It improved 5-fold over that of the conventional spin-coated TiO₂ film electrode DSSC. We expect to improve the conversion efficiency in future works.

Acknowledgment

The authors would like to address their thanks to the National Science Council of Taiwan for their financial support of this work under grant NSC-98-ET-E-005-004-ET.

References

- [1] D. L. Morel, E. L. Stogryn, A. K. Ghosh, et al., "Organic photovoltaic cells. Correlations between cell performance and molecular structure," *Journal of Physical Chemistry*, vol. 88, no. 5, pp. 923–933, 1984.
- [2] B. O'Regan and M. Grätzel, "A low-cost, high-efficiency solar cell based on dye-sensitized colloidal TiO₂ films," *Nature*, vol. 353, no. 6346, pp. 737–740, 1991.
- [3] T. P. Chou, Q. Zhang, B. Russo, G. E. Fryxell, and G. Cao, "Titania particle size effect on the overall performance of dye-sensitized solar cells," *Journal of Physical Chemistry C*, vol. 111, no. 17, pp. 6296–6302, 2007.
- [4] H.-J. An, S.-R. Jang, R. Vittal, J. Lee, and K.-J. Kim, "Cationic surfactant promoted reductive electrodeposition of nanocrystalline anatase TiO₂ for application to dye-sensitized solar cells," *Electrochimica Acta*, vol. 50, no. 13, pp. 2713–2718, 2005.
- [5] J. H. Park, S. Kim, and A. J. Bard, "Novel carbon-doped TiO₂ nanotube arrays with high aspect ratios for efficient solar water splitting," *Nano Letters*, vol. 6, no. 1, pp. 24–28, 2006.
- [6] J. M. Macák, H. Tsuchiya, A. Ghicov, and P. Schmuki, "Dye-sensitized anodic TiO₂ nanotubes," *Electrochemistry Communications*, vol. 7, no. 11, pp. 1133–1137, 2005.
- [7] M. Paulose, K. Shankar, O. K. Varghese, G. K. Mor, B. Hardin, and C. A. Grimes, "Backside illuminated dye-sensitized solar cells based on titania nanotube array electrodes," *Nanotechnology*, vol. 17, no. 5, pp. 1446–1448, 2006.
- [8] P. Xiao, B. B. Garcia, Q. Guo, D. Liu, and G. Cao, "TiO₂ nanotube arrays fabricated by anodization in different electrolytes for biosensing," *Electrochemistry Communications*, vol. 9, no. 9, pp. 2441–2447, 2007.
- [9] S.-M. Paek, H. Jung, Y.-J. Lee, N.-G. Park, S.-J. Hwang, and J.-H. Choy, "Nanostructured TiO₂ films for dye-sensitized solar cells," *Journal of Physics and Chemistry of Solids*, vol. 67, no. 5-6, pp. 1308–1311, 2006.
- [10] Z.-S. Wang, C.-H. Huang, Y.-Y. Huang, et al., "A highly efficient solar cell made from a dye-modified ZnO-covered TiO₂ nanoporous electrode," *Chemistry of Materials*, vol. 13, no. 2, pp. 678–682, 2001.
- [11] S. Takaki, Y. Aoshima, and R. Satoh, "Fabrication of indium tin oxide whiskers by sputtering," *Japanese Journal of Applied Physics, Part 1*, vol. 45, no. 4, pp. 2714–2721, 2006.
- [12] Q. Wan, P. Feng, and T. H. Wang, "Vertically aligned tin-doped indium oxide nanowire arrays: epitaxial growth and electron field emission properties," *Applied Physics Letters*, vol. 89, no. 12, Article ID 123102, 3 pages, 2006.

- [13] H.-W. Wang, C.-F. Ting, M.-K. Hung, et al., "Three-dimensional electrodes for dye-sensitized solar cells: synthesis of indium-tin-oxide nanowire arrays and ITO/TiO₂ core-shell nanowire arrays by electrophoretic deposition," *Nanotechnology*, vol. 20, no. 5, Article ID 055601, 2009.
- [14] S. J. Limmer, S. V. Cruz, and G. Z. Cao, "Films and nanorods of transparent conducting oxide ITO by a citric acid sol route," *Applied Physics A*, vol. 79, no. 3, pp. 421–424, 2004.
- [15] Y. Fang, D. Agrawal, G. Skandan, and M. Jain, "Fabrication of translucent MgO ceramics using nanopowders," *Materials Letters*, vol. 58, no. 5, pp. 551–554, 2004.
- [16] X. Wang and G.-R. Han, "Fabrication and characterization of anodic aluminum oxide template," *Microelectronic Engineering*, vol. 66, no. 1–4, pp. 166–170, 2003.
- [17] S. Uthanna, P. S. Reddy, B. S. Naidu, and P. Jayarama Reddy, "Physical investigations of DC magnetron sputtered indium tin oxide films," *Vacuum*, vol. 47, no. 1, pp. 91–93, 1996.
- [18] T. Karasawa and Y. Miyata, "Electrical and optical properties of indium tin oxide thin films deposited on unheated substrates by d.c. reactive sputtering," *Thin Solid Films*, vol. 223, no. 1, pp. 135–139, 1993.
- [19] L.-J. Meng, A. Macarico, and R. Martins, "Study of annealed indium tin oxide films prepared by rf reactive magnetron sputtering," *Vacuum*, vol. 46, no. 7, pp. 673–680, 1995.
- [20] L.-J. Meng and F. Placido, "Annealing effect on ITO thin films prepared by microwave-enhanced dc reactive magnetron sputtering for telecommunication applications," *Surface and Coatings Technology*, vol. 166, no. 1, pp. 44–50, 2003.
- [21] S. Bhagwat and R. P. Howson, "Use of magnetron-sputtering technique for the control of the properties of indium tin oxide thin films," *Surface and Coatings Technology*, vol. 111, no. 2-3, pp. 163–171, 1999.
- [22] G. Cao, "Growth of oxide nanorod arrays through sol electrophoretic deposition," *Journal of Physical Chemistry B*, vol. 108, no. 52, pp. 19921–19931, 2004.
- [23] T. P. Chou, Q. Zhang, B. Russo, G. E. Fryxell, and G. Cao, "Titania particle size effect on the overall performance of dye-sensitized solar cells," *Journal of Physical Chemistry C*, vol. 111, no. 17, pp. 6296–6302, 2007.

Research Article

Efficiency Improved by H₂ Forming Gas Treatment for Si-Based Solar Cell Applications

Yuang-Tung Cheng,¹ Jyh-Jier Ho,¹ William Lee,² Song-Yeu Tsai,² Liang-Yi Chen,¹ Jia-Jhe Liou,¹ Shun-Hsyung Chang,³ Huajun Shen,⁴ and Kang L. Wang⁴

¹Department of Electrical Engineering, National Taiwan Ocean University, No. 2 Pei-Ning Road, Keelung 20224, Taiwan

²Photovoltaics Technology Center, Industrial Technology Research Institute, No. 195 Chung Hsing Road,

⁴Sec. Chu Tung, Hsin Chu 31061, Taiwan

³Department of Microelectronic Engineering, National Kaohsiung Marine University, No. 142 Haijhuang Road, Kaohsiung 81143, Taiwan

⁴Device Research Laboratory, Department of Electrical Engineering, University of California, Los Angeles, CA 90095, USA

Correspondence should be addressed to Jyh-Jier Ho, jackho@mail.ntou.edu.tw

Received 14 March 2010; Accepted 29 March 2010

Academic Editor: Leonardo Palmisano

Copyright © 2010 Yuang-Tung Cheng et al. This is an open access article distributed under the Creative Commons Attribution License, which permits unrestricted use, distribution, and reproduction in any medium, provided the original work is properly cited.

The photovoltaic (PV) effects have been investigated and improved using efficient treatments both on single-crystalline (sc) and on multicrystalline (mc) silicon (Si) solar cells. The major effect of forming gas (FG) treatment on solar cell performance is the fill-factor values, which increase 3.75% and 8.28%, respectively, on sc-Si and mc-Si solar cells. As for the optimal 15%-H₂ ratio and 40-minute FG treatment, the conversion efficiency (η) values drastically increase to 14.89% and 14.31%, respectively, for sc- and mc-Si solar cells. Moreover, we can measure the internal quantum efficiency (IQE) values increase with H₂-FG treatment under visible wavelength (400~900 nm) radiation. Thus based on the work in this research, we confirm that H₂ passivation has become crucial both in PV as well as in microelectronics fields. Moreover, the developed mc-Si solar cell by proper H₂ FG treatment is quite suitable for commercial applications.

1. Introduction

Due to high price of fossil energy source and huge pollution of environmental issue in recent years, the development of renewable energy regains our attention. The development of the solar energy industry is one of the most popular technologies in renewable energy. For the solar energy becoming a practical renewable energy, it is widely accepted that we must have efficient ways to convert radiation into electricity as called photovoltaic (PV) effect. Nowadays, however, the unit price of converting power by solar energy is much higher than that of the traditional energy source. Thus, how to enhance the overall efficiency and reduce the manufacturing cost is an important subject for developing the solar energy industry [1, 2].

The crystalline silicon-based (Si-based) solar cell is not only still heavily dependent on the materials base of

the semiconductor industry but also features an excellent stability, technology maturity, and an easy acquisition. It also fulfils these requirements for the rapidly expanding solar energy market [3, 4]. For a Si crystalline growth, if any grain boundary exists inside the crystal, the dangling bond will be formed by the breaking interface in a Si atom. In any *pn*-junction of the solar-cell process, meanwhile, the emitting electrons inside the crystalline Si are highly active and easily combined with other elements [5, 6]. For the dangling bond in the band gap, the excess of positively charged states in dangling bond gives rise to energy level deep, thus enhancing *n* types Si crystalline by irradiating the material, or by extrinsic doping.

It is well known that cost reductions of the developed solar cell can be achieved either by a reduction of manufacturing cost or by an increase in solar cell efficiency and defects in the bulk of Si to remove the band-gap

levels into the valence or conduction bands [5–8]. Among the types of Si-based crystalline, single crystalline (sc-Si), multicrystalline (mc-Si), and amorphous (a-Si), the mc-Si wafer owns the highest growth rate and the lowest fabrication cost [3, 4]. Unfortunately, the mc-Si contains a large number of defects and dislocation suffered from lattice mismatch, thus yielding to the least conversion efficiency on the PV applications [4].

For enhancing the conversion efficiency in the solar-cell application, the treatment with hydrogen (H_2) forming gas (FG) at appropriate temperature can interact with impurities. The passivation effect of H_2 gas can also be used for improving the grain boundary of the mc-Si to achieve a better efficiency [9, 10]. It is widely accepted that the FG treats with H_2 gas in the recent Si-based solar cells from the viewpoint of fabrication cost and performance.

Practically all PV devices incorporate a pn -junction in a semiconductor across which the photo voltage is developed. At first in this paper, we simulate the phosphorus (P) diffusion process on a p -type Si substrate and obtain the optimal parameters for developing the solar cell. Then, the H_2 FG treatments on sc- and mc-Si solar cells are used for improving their performance parameters. Solar-cell operation can be modeled by considering the ideal equivalent scheme [11], consisting of a current source and two diodes in parallel. The current source models include the light-generated (I_L) or short-circuit (I_{SC}) current density. The first solar-cell diode models the diffusion current from base and emitter regions and the second diode represents generation-recombination (GR) current in the junction space-charge region.

The illuminated current-voltage (I-V) characteristics in our developed solar cell are described by [11]

$$I = I_{sc} - I_0 \left\{ \exp \left[\frac{q(V + R_S I)}{nkT} \right] - 1 \right\} - \frac{V + IR_S}{R_{sh}}, \quad (1)$$

where I_0 represents the saturation current with a constant value, k is Boltzmann's constant and T is temperature in degrees Kelvin. In a real device, the dissipating power effects electrically to two parasitic resistances in series (R_s) and in parallel (R_{sh}) with our developed solar cell.

Two of the most figures of merit to evaluate the designed solar-cell performance are the conversion efficiency (η , in %) and the internal quantum efficiency (IQE), which can be expressed as [12]

$$\begin{aligned} \eta &\equiv \frac{P_{out}}{P_{in}} = [FF] \times \left(\frac{V_{OC} \times I_{SC}}{P_{in}} \right) \\ &= \left[\left(\frac{P_{max}}{V_{OC} \times I_{SC}} \right) \times 100\% \right] \times \left(\frac{V_{OC} \times I_{SC}}{P_{in}} \right), \end{aligned} \quad (2)$$

$$IQE = \frac{I_{electron}}{I_{photon}(1 - R)}, \quad (3)$$

where FF (in %) is the fill factor, V_{OC} is the open-circuit voltage, and I_{SC} is the short-circuit current, in the ideal equivalent scheme. $I_{electron}$ is the induced electron current of solar cell, I_{photon} is the incident photon current and R is reflection coefficient on the absorbed layer.

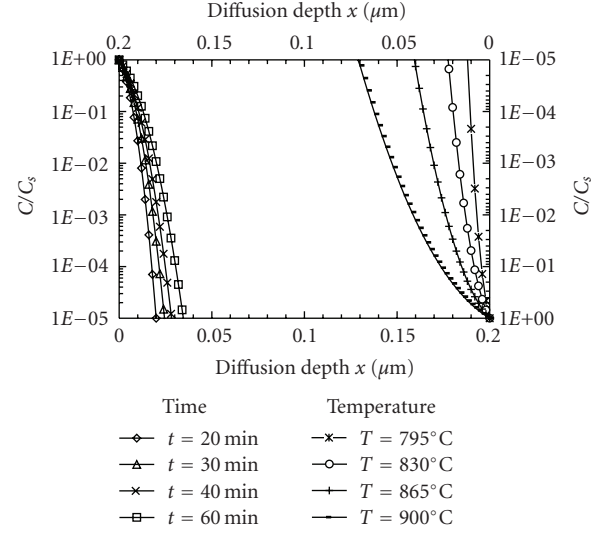


FIGURE 1: The profile curves of dopant concentration ratio (C/C_s) on the corresponding diffuse distance (x) with changing time (on bottom-left axis) and temperature (on top-right axis) respectively, for the phosphorus diffusion.

To measure the PV effect, the I-V curves are displayed on a curve tracer (Wacom, WXS-220S-L2). For simplification of terrestrial solar-cell characterization, the induced photocurrents (I) of the developed devices are measured under the air mass (AM 1.5 G) with a standard value of 1000 W/m^2 . The quality of the surface passivation was revealed by light beam-induced current measurements, which were obtained by Semilab WT-2000. We also measured the sample's IQE by PV Measurement (Model: QEX7).

2. Solar Cell Design and Fabrication

The main structure of a solar cell design is first to diffuse the P doped on a p -type Si substrate. Assume that the simple one-dimensional diffusion process in our developed solar-cell model, the dopant concentration ($C(x, t)$, in cm^{-3}), and the diffusion coefficient (D) solved by the Fick equation under constant surface concentration (C_s) at the diffusion length ($x = 0$) can be expressed by [11]

$$\begin{aligned} C(x, t) &= C_s \operatorname{erfc} \left(\frac{x}{2\sqrt{Dt}} \right), \\ D &= D_0 \exp \left(\frac{-E_a}{kT} \right), \end{aligned} \quad (4)$$

where erfc is the complementary error function, $\sqrt{Dt} \cdot E_a$ (in eV) is the activation energy of diffusion, and k is the Boltzmann constant.

The above critical diffusion parameters of temperatures (T) and time (t) were determined by a computer with a MATLAB program (version 6.X). For simulating the P and drive-in diffusion, Figure 1 shows the profile curves of dopant concentration ratio (C/C_s) on the corresponding diffuse distance (x) with changing time (on bottom-left axis) and temperature (on top-right axis), respectively. The

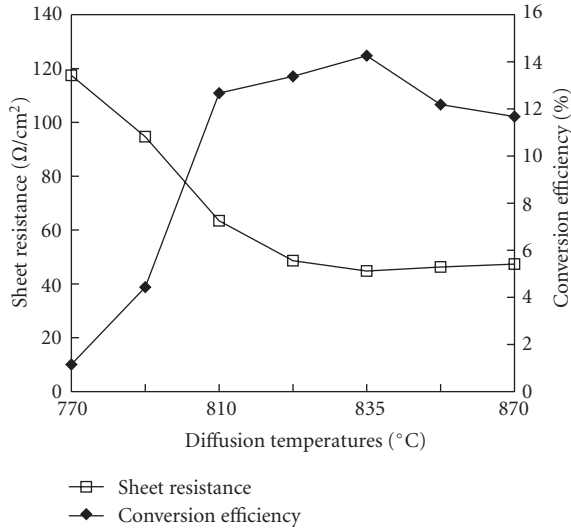


FIGURE 2: The sheet resistance (in Ω/cm^2) and conversion efficiency (in %) with respect to temperatures (from 770°C to 900°C) of the solar-cell prototypes with and without drive-in diffusion processes.

diffusion time and temperature are varied from 20 minutes to 60 minutes, and from 790°C to 900°C , respectively. In these curves of Figure 1, we can clearly observe that the diffusion profile of changing temperature influences more than those of changing diffusion time. For more precise investigation on a optimal condition, therefore, we select the 30-minute diffusion time to fabricate the solar-cell prototypes with fine trimming the diffusion temperatures.

During the P-doped process, we select the *p*-type sc-Si substrate with/without the drive-in diffusion to form the solar-cell prototype. Figure 2 illustrates the sheet resistance (in Ω/cm^2) and the conversion efficiency (in %), respectively, as a function of different temperatures (from 770°C to 900°C) of the solar-cell prototypes with and without drive-in diffusion processes. Among the diffusion processes described above, the maximum conversion efficiency value (14.26% calculated from (2)) of the prototype is at 835°C diffusion temperature, thus causing efficiency decreases as further increases in the diffusion temperature beyond 835°C . The sheet resistance decreases initially with increasing the diffusion temperatures and reaches a minimum value at 835°C -diffusion temperature. With this optimal diffusion parameters at 835°C for a solar-cell prototype, the sheet resistance is measured to be $44.7 \Omega/\text{cm}^2$, and its corresponding conversion efficiency is 14.26%.

In general diffusion process, the heavily doped ($\geq 10^{18} \text{cm}^{-3}$) region which contains a dead layer near the top surface usually decreased the PV characteristics of a solar cell [13, 14]. The creation of an emitter by diffusion of P from a POCl_3 (phosphorus oxy-chloride) ambient at high temperature (above 800°C) is a standard drive-in process in industry [15]. During the diffusion process, we first predeposit a diffusion layer on the surface and then perform the drive-in (redistribution) diffusion at the fixed total impurity mass.

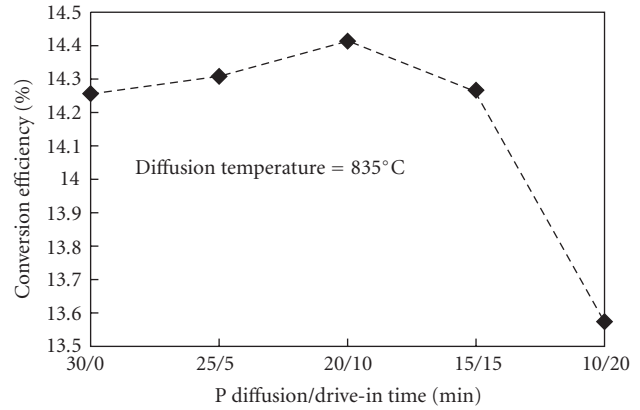


FIGURE 3: The conversion efficiency of the sc-Si prototype using same total 30-minute diffusion with the different drive-in times.

Under the total 30-minute time with predeposit and drive-in diffusion (at 835°C), Figure 3 shows the most improved 14.41% conversion efficiency for 20 minutes and 10 minutes, respectively, on predeposit and drive-in diffusion. As described previously, this improved PV phenomenon is attributed to the fact that drive-in process diffused by POCl_3 ambient can eliminate the dead layer and enhance the solar-cell performance.

In the future development of PV materials, most important is efficiency, and not to be neglected, lowest possible cost. Today the market is dominated by crystalline Si in its mc- and sc- form. Even though the mc-Si material is the least cost for manufacturing a solar cell [5], the developed mc-Si solar cell still owns less conversion efficiency than that of an sc-Si prototype ($\eta = 14.41\%$ at Figure 3). The low-efficiency reason is that the grain boundary effect may increase series resistance, reduce lifetime, and increase dark (leakage current) of a dependent photocurrent [11]. Among the treatment methods for enhancing the PV performance, the passivation effect of H_2 FG is commonly used to remove the band-gap levels into the valence or conduction bands [5–8].

3. Treatment Result and Discussion

Before any treatment of the mc-Si solar cell upon predeposit P and drive-in diffusion, a 100-nm Si_xN_y and SiO_2 antireflection coating was deposited on the front at 200°C by plasma enhanced chemical vapor deposition as described in our previously work [16–20]. When the metallization of both sides was finished, the samples were immediately fired in the belt furnace at 950°C . This was followed by the FG process. It was used by introducing H_2 FG (mixed gas, $\text{N}_2:\text{H}_2 = 85\%:15\%$) with 3600 sccm for 10 to 40 minutes at 400°C in atmosphere.

Both the I_{SC} (in Amp) and the V_{OC} (in Volt) of the developed solar cells all with respect to different H_2 FG time (in minutes) on the sc- and mc-Si substrates for comparison are illustrated in Figure 4. This figure illustrates axes with the different scale, in which the bottom and top axes annotate

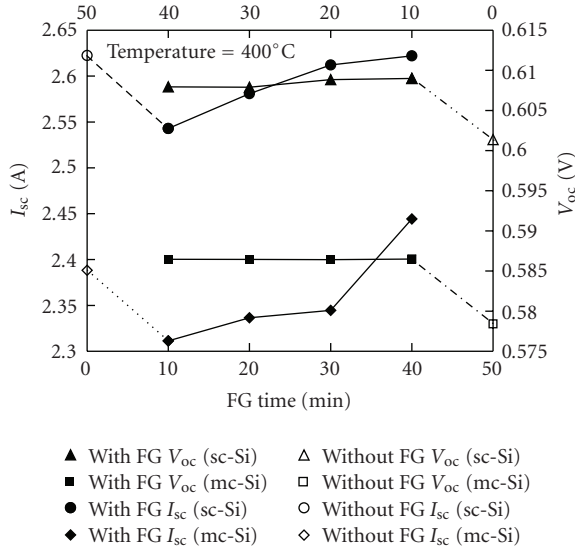


FIGURE 4: The open-circuit voltages (V_{OC}) and the short-circuit currents (I_{SC}) of sc- and mc-Si solar cells without ($t = 0$ min) and with different H_2 FG treatment time.

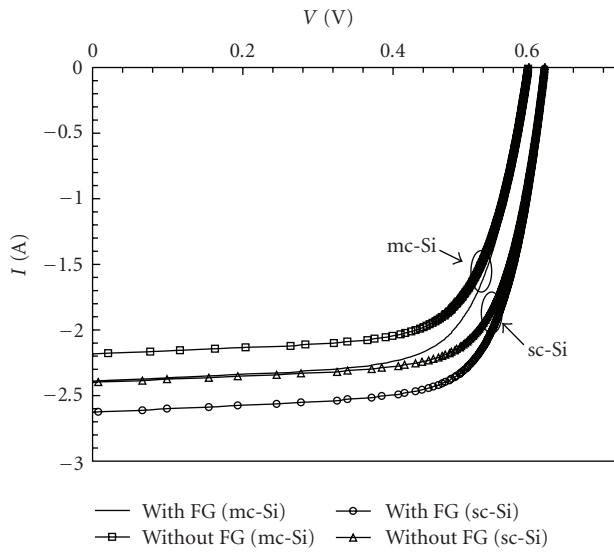


FIGURE 5: Improved Fill Factor of sc- and mc-Si Solar Cells at H_2 FG Treatment: 40 minutes (sc-Si: 69.92% \rightarrow 73.93%, mc-Si: 59.43% \rightarrow 72.63%).

FG time with opposite approaching direction, while the left and right axes denote I_{SC} and V_{OC} , separately. In both sc- and mc-Si solar cells without FG treatment (at $T = 0$ minute as reference value), I_{SC} values are 2.622 A and 2.388 A. Values of V_{OC} are 0.6013 V and 0.5784 V, respectively, for sc- and mc-Si solar cells. Among the H_2 FG times, the I_{SC} values decrease initially and then increase with respect to the bottom-left axis, while the V_{OC} values with respect to the top-right axis vary not much after 10-minute treatment. These values imply that there exist two competing effects during the H_2 treatment. One is degradation effect which decreases the shunt resistance and increases the leakage

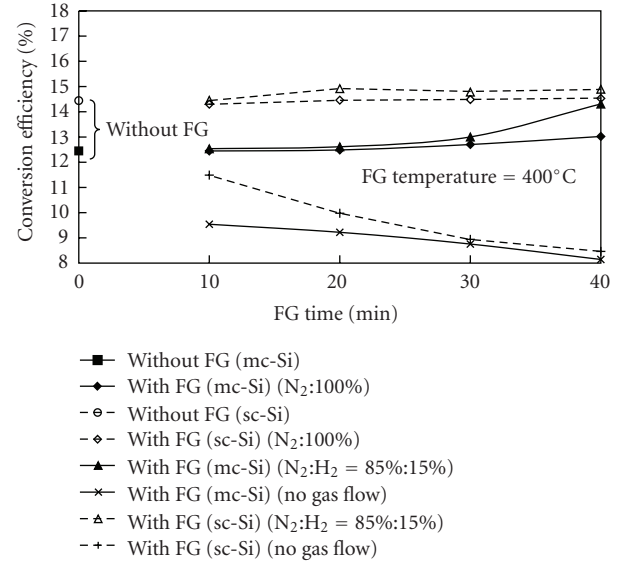


FIGURE 6: Improved energy conversion efficiency (η) of sc-Si and mc-Si solar cells with/without different H_2 FG (for mixed gas ratios) treatment time.

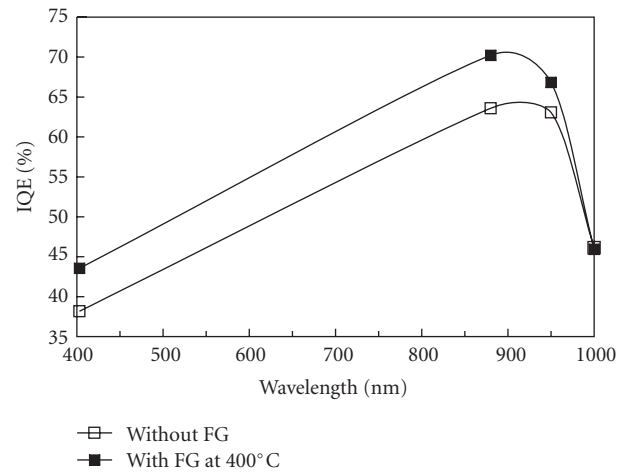


FIGURE 7: Improved internal quantum efficiency (IQE) of the mc-Si solar cells with/without by H_2 FG treatment.

current at the high temperature of 400°C . The other is H_2 FG effect which passivates the defects in the device [21]. The degradation effect dominates at the first 10 minutes and then the passivation effect takes control for longer treatment time. The decrement is still large for 30-minute H_2 treatment for mc-Si solar cell. This could be due to the grain boundaries of the mc-Si and takes longer time to passivate them [21]. The I-V curves shown in Figure 5 can evaluate the PV effect on the developed solar cells. The FF values after 40-minute H_2 FG treatment can be improved by 3.75% and 8.28%, respectively, for the developed sc- and mc-Si solar cells.

Figure 6 shows the η values (calculated by (2) from Figures 4 and 5) of the sc- and mc-Si solar cells with/without H_2 FG treatment time at different gas ratios. The η values without FG treatment on sc- and mc-Si solar cells are also

shown at zero FG treatment time. There are low conversion efficiencies without any gas flow both on sc- and mc-Si solar cells. Since the sc-Si material has few impurity and grain boundary as mentioned previously, there is very small space for improvement on FG treatment. This is the reason why these efficiency values on mc-Si solar cell show the increasing effect on a longer FG time (between 30 and 40 minutes) while there is no significant effect on the sc-Si solar cells.

This figure also illustrates the passivation effect on the different FG H₂-ratio of our developed sc- and mc-Si solar cells. For safety consideration the 15%-H₂ ratio is the maximum value to avoid the H₂ explosion. As for the optimal H₂ ratio of 15% on FG treatment, the η values drastically increase to 14.89% and 14.31% at 40 minutes, respectively, for sc- and mc-Si solar cells. Note that these two values at 40-minute H₂ FG have only 0.58% difference on the sc- and mc-Si solar cells. Thus, we prove that the conversion efficiency can be improved by H₂ FG treatment (with optimal 15%-H₂ at 40-minute treatment time) for the cheaper mc-Si solar cell.

Moreover, we can measure the IQE values increase with H₂-FG treatment under visible wavelength (400~900 nm) radiation (as shown in Figure 7). However, the measured IQE value under long wavelength (about 1000 nm) is basically the same for samples with and without H₂ FG treatment. This suggests that H₂ FG treatment provides better passivation in the area near the surface. For these deeper areas which H₂ atoms cannot reach, the passivation effect is not obvious. This is why the quantum efficiency under long wavelength remains the same (or even worse) after H₂ treatment. Because H₂ atoms cannot travel very deep in the developed device, the region deep in the device was not well passivated. Therefore, the developed solar cell was even degraded at long wavelength with H₂ FG treatment.

4. Conclusion

The effects on sc-Si and mc-Si solar cells are investigated. The η values are increased with the H₂ FG treatment. The increment is larger for the mc-Si solar cell than that of the sc-Si solar cell. Probably due to the existence of grain boundaries as well as high concentration of impurities, the FG treatment with the optimal 40-minute time and 15%-H₂ ratio has more impact on mc-Si compare to that on sc-Si. The V_{OC} is also increased for the both cases. The increment saturates for 10-minute FG time for the both cases, which suggests that it could be due to the quality improvement of the metallization. There are two effects during the H₂ treatment. The degradation effect dominates at the first 10 minutes and the passivation effect dominates for the longer treatment time, which results in the change of the decrement of the I_{SC}. The LBIC measurements show that the IQE values improved with FG treatment, especially in the visible radiation (wavelength range from 400 nm to 900 nm). Therefore, increasing the H₂ FG treatment time (40 minutes) is an applicable method to improve the developed sc-Si and mc-Si performance for solar cell applications. It should be recognized that the P diffusion deep into the bulk of a solar

cell is a prerequisite for efficient passivation and concomitant improvement in the solar-cell performance. Based on the work in this research, the developed mc-Si solar cell by proper H₂ FG treatment is quite suitable for commercial applications.

Acknowledgment

The authors acknowledge financial support from *The National Science Council of Taiwan* under contract nos. NSC 98-2221-E-019 -003 and NSC 98-2221-E-022 -018.

References

- [1] G. P. Willeke, "Thin crystalline silicon solar cells," *Solar Energy Materials and Solar Cells*, vol. 72, no. 1–4, pp. 191–200, 2002.
- [2] S. Steckemetz, A. Metz, and R. Hezel, "Thin Cz-silicon solar cells with rear silicon nitride passivation and screen printed contacts," in *Proceedings of the 17th European Photovoltaic Solar Energy Conferences*, pp. 1902–1905, Munich, Germany, October 2001.
- [3] A. Jäger-Waldau, "Status of PV Research, Solar Cell Production and Market Implementation in Japan, USA and the European Union," Joint Research Centre, European Commission, September 2002.
- [4] A. Goetzberger, C. Hebling, and H. W. Schock, "Photovoltaic materials, history, status and outlook," *Materials Science and Engineering R*, vol. 40, no. 1, pp. 1–46, 2003.
- [5] P. Sana, A. Rohatgi, J. P. Kalejs, and R. O. Bell, "Gettering and hydrogen passivation of edge-defined film-fed grown multicrystalline silicon solar cells by Al diffusion and forming gas anneal," *Applied Physics Letters*, vol. 64, no. 1, pp. 97–99, 1994.
- [6] B. L. Sopori, X. Deng, J. P. Benner, et al., "Hydrogen in silicon: a discussion of diffusion and passivation mechanisms," *Solar Energy Materials and Solar Cells*, vol. 41–42, pp. 159–169, 1996.
- [7] B. Sopori, M. I. Symko, R. Reedy, K. Jones, and R. Matson, "Mechanism(s) of hydrogen diffusion in silicon solar cells during forming gas anneal," in *Proceedings of the 26th IEEE Photovoltaic Specialists Conference (PVSC '97)*, pp. 25–30, September–October 1997.
- [8] A. G. Aberle, "Surface passivation of crystalline silicon solar cells: a review," *Progress in Photovoltaics: Research and Applications*, vol. 8, no. 5, pp. 473–487, 2000.
- [9] B. L. Sopori, X. Deng, J. P. Benner, et al., "Hydrogen in silicon: a discussion of diffusion and passivation mechanisms," *Solar Energy Materials and Solar Cells*, vol. 41–42, pp. 159–169, 1996.
- [10] A. Rohatgi, P. Doshi, J. Moschner, A. G. Lauinger, A. Aberle, and D. S. Ruby, "Comprehensive study of rapid, low-cost silicon surface passivation technologies," *IEEE Transactions on Electron Devices*, vol. 47, no. 5, pp. 987–993, 2000.
- [11] J. Nelson, *The Physics of Solar Cells*, chapters 1.1 & 8, Imperial College Press, London, UK, 2005.
- [12] S. M. Sze, *Semiconductor Devices: Physics and Technology*, chapters 9 & 13, John Wiley & Sons, New York, NY, USA, 2nd edition, 2002.
- [13] J. Lossen, L. Mittelstädt, S. Dauwe, K. Lauer, and C. Beneking, "Making use of silicon wafers with low lifetimes by adequate POCl₃ diffusion," in *Proceeding of the 20th European Photovoltaic Solar Energy Conference (EPSEC '05)*, Barcelona, Spain, June 2005.

- [14] P. Choulat and F. Duerinckx, "Minimizing the dead layer of industrial phosphorus emitter formed by POCl_3 diffusion," in *Proceeding of the 15th International Photovoltaic Science & Engineering Conference (PVSEC '05)*, Shanghai, China, 2005.
- [15] T. Saitoh, T. Warabisako, E. Kuroda, H. Itoh, S. Matsubara, and T. Tokuyama, "Impurity gettering of polycrystalline solar cells fabricated from refined metallurgical-grade silicon," *IEEE Transactions on Electron Devices*, vol. 27, no. 4, pp. 671–677, 1980.
- [16] J. J. Ho, C. Y. Chen, R. Y. Hsiao, and O. L. Ho, "The work function improvement on indium-tin-oxide epitaxial layers by doping treatment for organic light-emitting device applications," *Journal of Physical Chemistry C*, vol. 111, no. 23, pp. 8372–8376, 2007.
- [17] J. J. Ho, C. Y. Chen, C. M. Huang, W. J. Lee, W. R. Liou, and C. C. Chang, "Ion-assisted sputtering deposition of antireflection film coating for flexible liquid-crystal display applications," *Applied Optics*, vol. 44, no. 29, pp. 6176–6180, 2005.
- [18] J. J. Ho and C. Y. Chen, "Monolithic integration of poly-SiGe:H *pin* diode with WO_3 electrochromic film for opto-switching applications," *Electronics Letters*, vol. 41, no. 20, pp. 1140–1141, 2005.
- [19] C. Y. Chen and J. J. Ho, "Low-temperature poly-sige alloy growth of high gain/speed *pin* infrared photosensor with gold-induced lateral crystallization (Au-ILC)," *IEEE Transactions on Electron Devices*, vol. 50, no. 8, pp. 1807–1812, 2003.
- [20] Y.-T. Cheng, J. J. Ho, W. J. Lee, et al., "Investigation of low-cost surface processing techniques for large-size multicrystalline silicon solar cells," *International Journal of Photoenergy*, vol. 2010, Article ID 268035, 6 pages, 2010.
- [21] L. Carnel, H. Dekkers, I. Gordon, et al., "Study of the hydrogenation mechanism by rapid thermal anneal of SiN:H in thin-film polycrystalline-silicon solar cells," *IEEE Electron Device Letters*, vol. 27, no. 3, pp. 163–165, 2006.

Review Article

Debundling and Selective Enrichment of SWNTs for Applications in Dye-Sensitized Solar Cells

F. Bonaccorso

Engineering Department, University of Cambridge, Cambridge CB3 0FA, UK

Correspondence should be addressed to F. Bonaccorso, fb296@cam.ac.uk

Received 31 December 2009; Accepted 8 April 2010

Academic Editor: Gaetano Di Marco

Copyright © 2010 F. Bonaccorso. This is an open access article distributed under the Creative Commons Attribution License, which permits unrestricted use, distribution, and reproduction in any medium, provided the original work is properly cited.

We present an overview of the recent developments in de-bundling and sorting of Single-Wall Carbon Nanotubes (SWNTs), which are useful for hi-tech applications in dye sensitized solar cells (DSSCs). Applications of SWNTs as transparent and conductive films, catalyst, and scaffold in DSSCs are also reviewed.

1. Introduction

The direct utilization of solar radiation to produce electricity in photovoltaic (PV) devices is at the centre of an ongoing research effort to utilize the renewable energy. Silicon (Si) is by far the most widely used absorber and currently dominates the market of PV devices [1]. Despite significant development over the past decades, the high cost of Si-based solar cells is a bottleneck for the implementation of solar electricity on large scale. The development of new materials and concepts for the PV devices is thus fundamental to reduce the overall production cost of PV technology and to increase their efficiency. Recent trends suggest that the development and successful utilization of nanomaterials could potentially lead to the realization of high efficient and low-cost solar cells. In this context, Single Wall Carbon Nanotubes (SWNTs) have been proposed as a promising material in organic [2, 3] and dye sensitized solar cells (DSSCs) [4–13]. However, as-produced SWNTs usually form entangled networks of bundles or ropes [14–17], due to van der Waals attraction forces along their length [18–21]. When in a bundle, SWNTs are far from their optimum mechanical, thermal, and optical properties [22–27]. Thus in order to fully exploit the technological potential of nanotubes for DSSCs, it is crucial to develop simple debundling techniques. Individualization/debundling of SWNTs is also crucial for the separation of SWNTs by chirality or between metallic (m-SWNTs) and semiconducting nanotubes (s-SWNTs), overcoming the limitations related to polydispersivity. SWNTs

can be sorted by diameter [28–36], chirality [37–41], their metallic or semiconducting nature [32, 42–51], and length [36, 52, 53].

Here we focus on the possible strategies to use enriched SWNTs in DSSCs, where they can serve multiple purposes such as: (1) transparent and conductor (TC) window at the photoanode, (2) charge transport, and (3) catalyst.

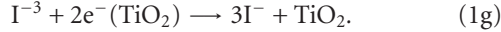
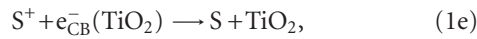
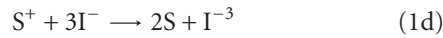
Indeed, enriched m-SWNTs can be used as TC films at the photoanode as well as catalyst at the counter electrode (cathode). For example, the conductivity of TC produced using highly enriched m-SWNTs can be enhanced by a factor of 6 in the visible spectrum with respect to unsorted material [54]. On the other hand, for the improvement of the DSSCs performance, m-SWNTs and/or chirality enriched s-SWNTs with a suitable energy gap would facilitate electron transport from mesoscopic TiO₂ particles to photoelectrode. Therefore, nanotubes enrichment is a vital step to improve the performances of nanotubes-based DSSCs. Here, we review the state of the art of the use of SWNTs in DSSCs.

2. Structure and Mechanism of DSSCs

DSSC is a new “type” of photoelectrochemical solar cell, used already by Becquerel for the discovery of the photovoltaic effect almost two century ago, which uses a liquid electrolyte as a charge transport medium [55]. The schematic representation of a DSSC is shown in Figure 1. A DSSC typically consists of a high porosity nanocrystalline photoanode made

of a wide band gap semiconductor (usually the n-type semiconductor TiO_2 with a bandgap of 3.2 eV) nanoparticles (15 to 20 nm diameter). The TiO_2 nanoparticles are deposited on a transparent conducting oxide (TCO) glass supported and sensitized with a self-assembled monolayer of dye molecules anchored to the TiO_2 surface [55]. The main difference, with respect to conventional cells, relies on the functional element responsible for light absorption (dye molecules), which is separated from the charge carrier transport itself [56]. The photoanode is immersed in an electrolyte solution containing a redox couple (iodide/iodine) and placed on a platinum counter electrode. Commonly, the platinum layer is deposited on transparent glass which is, in turn, coated by a conductive layer such as Indium Tin oxide (ITO) [1, 57].

The mechanism of a DSSC is listed schematically below [58]:



When illuminated, the dye molecules capture the incident photons ($h\nu$) generating electron/holes pairs (1a) [55]. The resultant electrons, at excited states S^* , which lie energetically above the conduction band (CB) edge of the TiO_2 , are quickly injected into the conduction band (CB) of the TiO_2 (1b) and transported to the electron-collecting counter electrode, the cathode [55]. In this condition, the electron injection to the semiconductor (1b) can occur successfully, competing with the deactivation reaction (1c). Regeneration of dye molecules is accomplished by capturing electrons from a liquid electrolyte (iodide/iodine solution), sandwiched on the cathode, that catalyses the reduction of tri-iodide [55]. For efficient operation of the cell, the rate of electron injection must be faster than the decay of the dye-excited state [55]. Also, the oxidation of iodide (1d) and the reduction of iodine (1f) must effectively compete with the charge-separated state recombination reactions (1e) and (1g) that decrease the current production.

The most important electrochemical parameters for a solar cell are the open circuit voltage (V_{OC}), the maximum voltage under open circuit conditions, and the short circuit current (I_{SC}), that is, the maximum current when the cell is short circuited. Another key parameter of the solar cell is the fill factor (FF), defined as

$$\text{FF} = \frac{(V_{\text{max}} \times I_{\text{max}})}{(V_{\text{OC}} \times I_{\text{SC}})}, \quad (2)$$

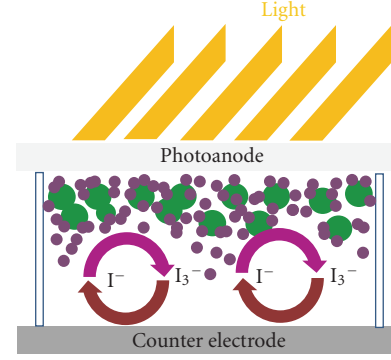


FIGURE 1: Schematic representation of the structure of a dye sensitized solar cell. The cell has 3 primary parts. On the top is a transparent photoanode made of Indium-doped tin oxide (ITO) deposited on the back of a transparent glass. On the back of the conductive plate is a layer of titanium dioxide (TiO_2), which forms into a highly porous structure with an extremely high surface area (green beads). A thin layer of a photosensitive ruthenium-polypyridinedye (purple beads) [55] is covalently bonded to the surface of the TiO_2 . A separate backing is made with a thin layer of the iodide electrolyte (I^-/I_3^-) spread over a conductive sheet, typically platinum metal (the counter electrode). The front and back parts are then joined and sealed together to prevent the electrolyte from leaking.

where V_{max} and I_{max} are the maximum voltage and current of the cell, respectively. The performance of a solar cell is determined by the energy conversion efficiency, η , defined as

$$\eta = \frac{P_{\text{max}}}{P_{\text{inc}}} \quad (3)$$

where $P_{\text{MAX}} = I_{\text{SC}} \times V_{\text{OC}} \times \text{FF}$ and P_{inc} is the power incident light on the cell. On the other hand, the fraction of absorbed photons that is converted to electrical current defines the internal photocurrent efficiency (IPCE).

3. Routes to Dispersion and Individualization of SWNTs

The methods for debundling of SWNTs can be roughly classified in two major categories: covalent and noncovalent functionalization [59]. Significant research effort has been conducted in this field over the last 10 years [60–66]. Functionalization generally involves the creation of defect sites on SWNTs, where different functional groups can be attached. The ends of as-produced SWNTs can either be open or contain highly curved unstable fullerene-like end caps [67, 68]. SWNT sidewalls also contain defects, generally in the form of pentagon and heptagon pairs, sp^3 hybridized defects and vacancies in the lattice [69, 70]. Strong oxidative treatments are used to remove the catalyst particles and to open additional defect sites on the SWNT sidewalls and end caps, resulting in carboxylic ($-\text{COOH}$) functional groups at these locations [62, 71–74]. Depending on the functional groups attached, stable SWNT dispersions in aqueous and organic solvents can be obtained [75]. However, this approach has certain disadvantages because of

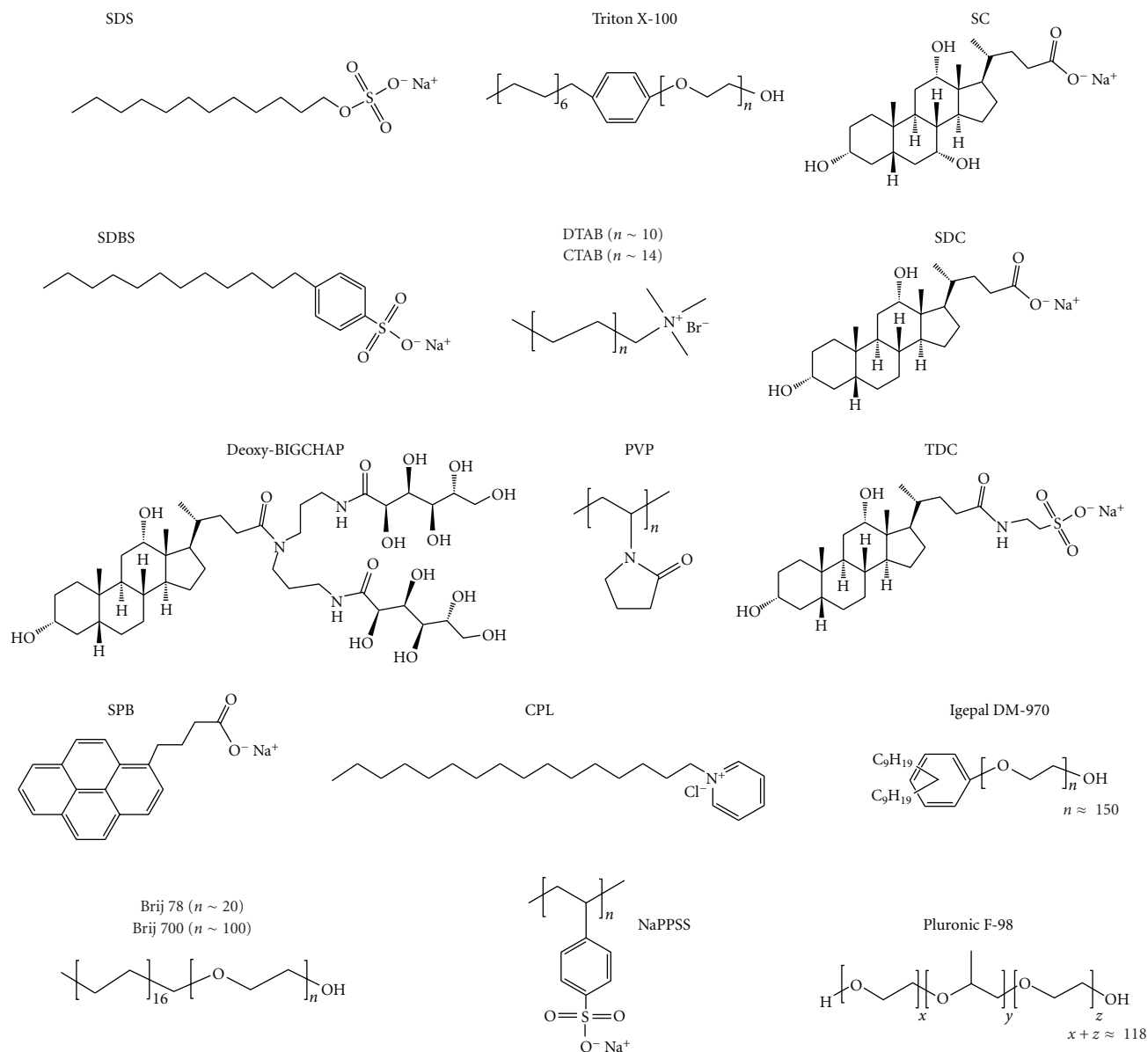


FIGURE 2: Chemical structures of some commonly used surfactants and polymers for SWNT dispersion in aqueous solutions. Abbreviations: SDS: sodium dodecyl sulfate; SDBS: sodium dodecylbenzenesulphonate; PVP: polyvinylpyrrolidone; Deoxy-BIGCHAP: N,N-bis(3-Gluconamidopropyl)deoxycholamide; SPB: Sodium Pyrenebutyrate; DTAB: dodecyltrimethylammonium bromide; CTAB: cetyltrimethylammonium bromide; CPL: Cetylpyridinium Chloride; NaPSS: sodium polystyrene sulphonate; SC: sodium cholate; SDC: sodium deoxycholate; TDC: sodium taurodeoxycholate.

the possible damage of SWNTs during the functionalization procedure, due to disruptions in their extended π -network, therefore preventing their use in many applications [76–80].

An alternative approach relies on the use of noncovalent interactions that relies on the physical adsorption of dispersant molecules on the SWNT sidewalls. This second method does not damage the nanotube surface and consists, in the addition of highly soluble dispersant agents [61–66, 81] into solution. Adsorption of dispersant molecules is a nondestructive method to individualize SWNTs in aqueous solutions, inducing only small shifts (<50 meV) in transition energies due to change in dielectric environment

[80]. Surfactants and deoxyribonucleic acid (DNA) are mostly used in aqueous SWNT dispersions while polymers, depending on their solubility, are used for both aqueous and organic solvent dispersions. Much effort has been devoted towards finding suitable molecules to interface the nonpolar sidewalls of SWNTs with water. To date, stable dispersions of pristine SWNTs in water/D₂O have been achieved with the aid of ionic and nonionic surfactants [61, 63, 65], DNA [66, 82, 83], water soluble polymers [63–65, 84], polypeptides [84–86] and cellulose derivatives [87]. The most common surfactants able to stably individualize SWNTs in water [61, 63, 65] include Triton-X, Pluronic, Igepal, and Brij series on

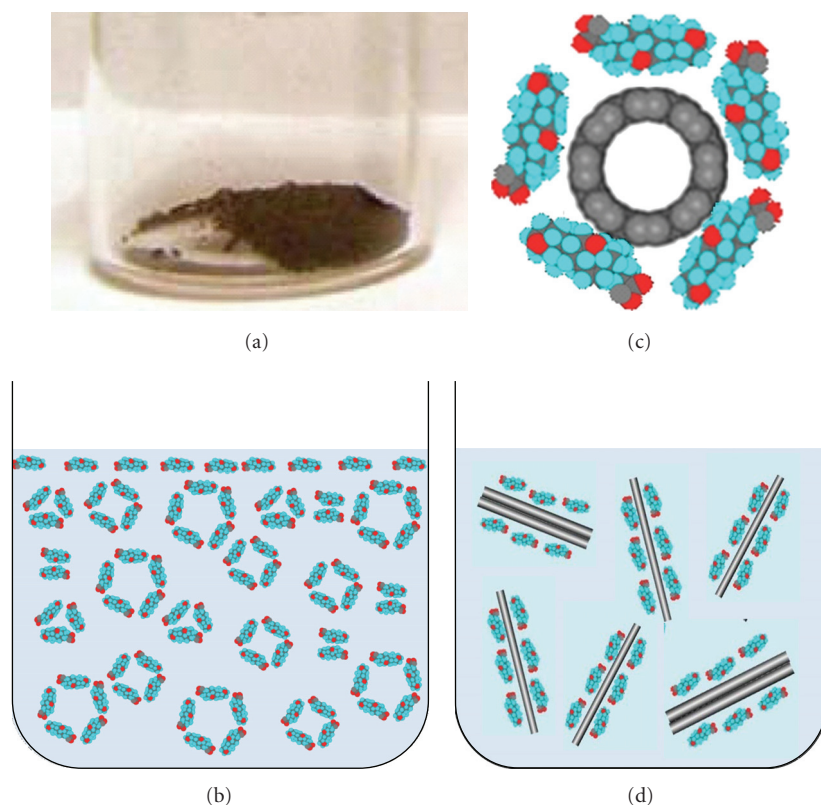


FIGURE 3: (Color) Schematics of SWNT dispersion mechanism in water by physical adsorption of dispersant molecules. (a) SWNTs powders. (b) Surfactant micelles formation in aqueous solution. The insertion of SWNTs in the surfactant aqueous solution and the ultrasonic treatment cause the wrapping of surfactants around SWNT sidewalls. The surfactants wrap with their nonpolar tail the SWNT sidewalls while extending their polar or ionic end in contact with aqueous solution. (c) Cross-sectional view of the possible arrangement of the SDC molecules around the SWNT sidewalls. (d) Final dispersion with individual and bundled SWNTs wrapped by surfactant molecules.

the nonionic side and sodium dodecyl sulfate (SDS), sodium dodecylbenzenesulphonate (SDBS), sodium cholate (SC), sodium deoxycholate (SDC), sodium taurodeoxycholate (TDC), dodecyltrimethylammonium bromide (DTAB), and cetyltrimethylammonium bromide (CTAB) on the ionic side (see Figure 2). When SWNTs are individualized by the shear forces from the formation and collapse of cavities generated by ultrasounds [88], surfactants wrap with their nonpolar tail the SWNT sidewalls while extending their polar or ionic end in contact with aqueous solution; see Figure 3. This process makes the SWNTs compatible with the aqueous medium and prevents their reaggregation [61, 63, 65]. Large SWNT bundles together with catalyst particles are removed via ultracentrifugation, leaving the supernatant enriched in small bundles and individually dispersed SWNTs [89]. Water-soluble polymers are reported to wrap around SWNTs [64, 90] facilitating their debundling. The wrapping of SWNTs by water-soluble polymers is thermodynamically favored by the removal of the hydrophobic interface between the SWNT sidewall and the aqueous medium [64, 90]. Cellulose derivatives were also employed as dispersants for SWNTs in water, resulting in high concentration of individual SWNTs. SWNTs can also be individualized in aqueous dispersions of Gum Arabic (GA), a highly branched arabinogalactan polysaccharide [90, 91]. DNA is an excellent

SWNT dispersant in water [66, 82, 83]. Reference [66] proposed that single-stranded DNA (ss-DNA) forms a helical wrap around SWNT sidewalls by π -stacking. The authors showed that the binding free-energy of ss-DNA to SWNTs is higher than the energy between two SWNTs, facilitating the dispersion process [66]. Other biomolecules, such as polypeptides, are also efficient in dispersing SWNTs in water [85, 86]. Reference [85] designed a peptide, called nano-1, which folds into an α -helix. Its hydrophobic side interacts with the SWNT sidewalls whereas the hydrophilic side interacts with the aqueous medium. Carboxymethyl cellulose [87, 92] and hydroxyethyl cellulose [87] have also been reported to individualize SWNTs with higher loading compared to surfactants and polymers.

4. Characterization of SWNT Dispersions

Optical techniques to probe SWNTs are very advantageous from the experimental point of view. The measurements are nondestructive and can usually be carried out at room temperature under ambient pressure. Optical Absorption (OAS), Photoluminescence Excitation (PLE), and Raman spectroscopy are usually used for the characterization of the SWNT dispersions. These methods are employed to assess the concentration and presence of individual SWNTs or their

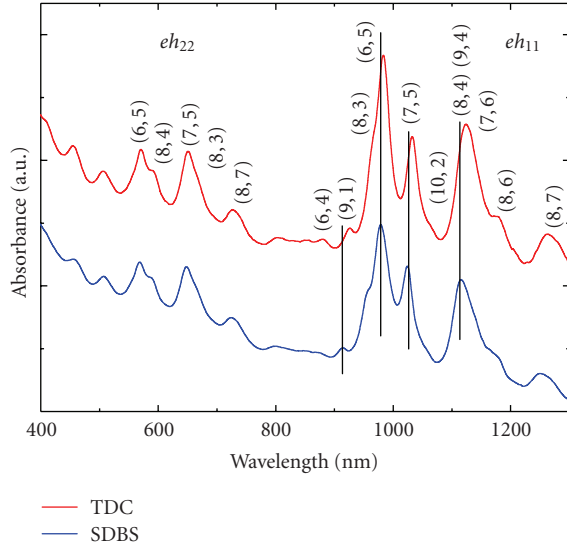


FIGURE 4: Optical absorption spectrum of CoMoCAT SWNTs dispersed in DI water using TDC (red line) and SDBS (blue line) as surfactant. The absorption peaks from different SWNT species are assigned according to [12, 33]. The shift in the peak positions and widths is due to different surfactants, which change the dielectric environment. The vertical lines are intended to guide the eyes.

bundles and may be used as independent or complementary characterization tools [93–99].

4.1. Optical Absorption Spectroscopy. OAS of nanotube dispersions detects various properties of nanotubes, such as excitonic transition energy, bundle status, and nanotube loading in the dispersions [100, 101]. In OAS, the broadening and red-shift of absorption peaks usually indicate the presence of SWNT bundles [61, 102]. The excitonic transitions of SWNTs are also strongly modulated by different dielectric environments [65, 103–105]. Absorption spectra of CoMoCAT SWNTs dispersed in aqueous dispersion with the aid of different surfactants are presented in Figure 4. The spectra illustrate the shift in absorption peaks due to different dielectric environments surrounding the SWNTs.

4.2. Photoluminescence Excitation Spectroscopy. Compared to absorption spectra, PLE maps (see, Figure 5) offer richer details of the SWNT optical properties and of their interaction with the surrounding dielectric environment [96, 106, 107]. Exciton-exciton resonances are the major features in PLE maps of SWNT dispersions. The (eh_{ii}, eh_{11}) resonances ($i = 1, 2, \dots$, etc.) from different species of SWNTs appear as sharp features $(\lambda_{ex}, \lambda_{em})$, where λ_{ex} and λ_{em} are the excitation and emission wavelengths, respectively. Other peaks detected in PLE maps are associated to excitonic phonon sidebands [108–110], excitonic energy transfer (EET) [106, 107, 111], or bright phonon sidebands (BSs) of dark K-momentum excitons [112]. EET occurs in bundles when the excitation of the eh_{ii} of large bandgap donor SWNTs (d-SWNT) induces emission from the eh_{11} of a smaller bandgap acceptor (a-SWNT) [106, 107]. EET can thus identify the presence of

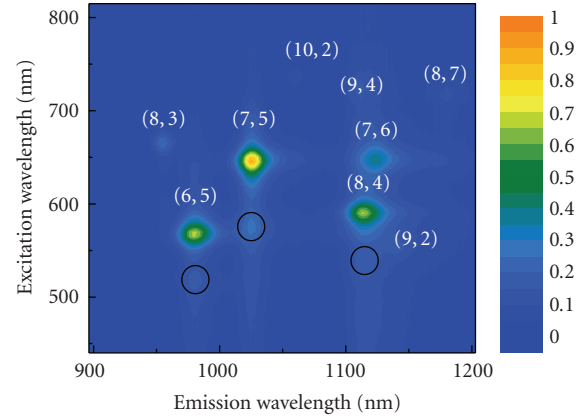


FIGURE 5: PLE map for SDBS-encapsulated CoMOCAT SWNT dispersion. Each (eh_{22}, eh_{11}) resonance is labeled with the chiral index of the corresponding SWNT. Open circles indicate the positions of phonon sidebands eh_{22}^{ph} of SWNTs. Broad and elongated spectral features are assigned to EET between s-SWNTs.

small bundles in dispersion [106, 107]. EET is also largely independent from perturbations induced by surrounding dielectric environments, since d- and a-SWNTs must be in the same bundle for EET to happen [106, 107, 113]. Indeed, the EET range is limited to a few nanometers and governed by the Förster resonance [106, 110, 113]. In general, the PL intensity does not directly reveal the relative abundance of SWNTs [114]. However, the relative PL intensity of different chiralities can be used to compare the effectiveness of their individualization.

4.3. Raman Spectroscopy. Raman spectroscopy is a fast, powerful, and nondestructive method for the characterization of carbon materials. A number of important informations, such as diameter, chirality, metallic or semiconducting nature, and orientation can be obtained from Raman characterization of SWNTs. The Raman spectra of SWNTs consist of a rich set of features.

The low-frequency features in the 120 to 350 cm^{-1} region for the usual SWNTs diameter range (~ 0.7 – 2 nm) are the so-called radial breathing modes (RBMs) [99]. The RBM modes are unique in SWNTs and used to determine the diameter and chirality of SWNT samples [115–119]. *RBM* position $Pos(RBM)$ is inversely related to SWNT diameter, d , [115, 116] by $Pos(RBM) = C_1/d + C_2$. The combination of $Pos(RBM)$ with the excitation wavelength and the “Kataura plot” [120], it is possible to derive the SWNT chirality [117–119]. A variety of C_1 and C_2 have been proposed for this relation [115–117, 119].

Raman spectroscopy can also probe any possible damage during ultrasonic dispersions, by monitoring the evolution of the D peak [121–123]. Indeed, the D peak appears in materials in the presence of structural disorder [121–123]. It originates by a breathing mode of hexagonal rings and it is observed in the frequency region between 1200 and 1400 cm^{-1} [121–123].

The Raman spectrum of SWNTs, in the range 1500–1600 cm^{-1} , is characterized by the presence of two distinct features so-called G^+ and G^- bands. The origin of these two bands arises by the splitting of the double degenerate, Raman-active E_{2g} mode of graphene [124–127]. In s-SWNTs, they originate from the longitudinal (LO) and tangential (TO) modes [125]. The positions of the G^+ and G^- peaks, $Pos(G^+)$, $Pos(G^-)$, are diameter dependent and the separation between them decreases with increasing diameter [125]. In m-SWNTs, the assignment of the G^+ and G^- bands is the opposite, and the full width at half maximum of the G^- peak, $FWHM(G^-)$, is larger while $Pos(G^-)$ is downshifted with respect to s-SWNTs [125]. Doping could also modify both the $FWHM$ s and peaks' positions [128–130]. In s-SWNTs, doping upshifts $Pos(G^+)$ but does not influence $FWHM(G^+)$ [128, 129]. In m-SWNTs, electron or hole doping causes $Pos(G^-)$ blueshift and $FWHM(G^-)$ decrease [128, 129]. Although a large number of excitation wavelengths are necessary for a complete characterization of SWNT samples [119, 131], useful information can be derived even with few excitations, in particular when Raman compares the same SWNTs dispersed in different solvents and/or surfactants or the final dispersion with the starting material.

5. State of the Art in SWNT Separation/Enrichment

Currently available SWNT synthesis methods yield nanotubes with uncontrolled diameter, chirality, and, consequently, optical properties. Postproduction enrichment is the more reliable route towards the separation/enrichment of SWNTs. Greater understanding of the dispersion mechanism, especially in aqueous environments, is crucial for the separation of SWNTs. This is because, well-established techniques for the separation of biological molecules, for example, conventional and density gradient ultracentrifugation [132], electrophoresis [133], and variations of chromatography [134] are the prime candidates for successful SWNT sorting.

Sorting of SWNTs in a liquid environment usually follows the strategy of “amplifying” their subtle differences in chemical reactivity by covalent and noncovalent functionalization [59, 60].

Methods based on electrophoresis and its variants were the first to be demonstrated for the sorting of SWNTs. In conventional methods of electrophoresis, nanotubes are sorted with respect to their relative mobility in gel [36, 49], capillary [30], or free-solution electrophoresis [46] in response to a direct (dc) or alternating current (ac) field [30, 36, 46, 49]. Ion exchange (IEC), column (CC), and size exclusion (SEC) chromatography may be used to sort SWNTs by length, electronic type, or diameter. Separation by diameter or m- versus s-SWNTs by chromatography is possible through wrapping with single-strand deoxyribonucleic acid (ss-DNA) [29, 37, 40]. Centrifugal force can be used to separate mixtures based on their density. In the case of SWNTs sorting, centrifugation can be performed in a constant, step, or linear density gradient medium. Conventional ultracentrifugation is carried out in a

constant density medium, sorting SWNTs according to their sedimentation coefficient, which strongly depends on their molecular weight and shape [135]. Like IEC, SWNT sorting by the conventional ultracentrifugation method suffers from convolution among their diameter and length [135]. On the other hand, nanotube sorting is achieved by exploiting the buoyant density difference of surfactant-encapsulated individual tubes [31–33, 35]. This results in a spatial separation inside an ultracentrifuge cell, overcoming the limitations of conventional ultracentrifugation in a constant density medium [35]. DGU allows also the separation of s- and m-SWNTs [32]. The m- versus s-SWNTs separation is achieved in a co-surfactants mixture, resulting in different buoyant densities between the two species. Recently, [136] demonstrated that nanotube individualization and uniform coverage by surfactant molecules are key parameters in the separation mechanism.

6. SWNTs as Transparent Conductive Electrodes

The different debundling and sorting strategies, discussed above, together with film fabrication methods have been employed in the investigation of SWNTs as a coating agent to form TCs, which are a crucial component both in solar cells [2] and many other optoelectronic devices, such as flat-panel displays [137, 138]. The current choice of material for such applications is crystalline ITO, a doped n-type semiconductor, with transmittance (T) higher than 80%, coupled with sheet resistance (R_s) as low as $10 \Omega/\square$ on glass [57, 139–141]. ITO is the most expensive components of a DSSC [13]. However, other than the cost, there are other problems related to the use of ITO. Indeed, ITO requires deposition at high temperature, hindering the deposition on some substrates (e.g., polymeric substrates). Another disadvantage is related to the reduced conductivity of large area electrodes ($\sim 10 \text{ cm}^2$). Moreover, the brittleness of ITO limits its use in applications where flexibility is required. Thus far, other metal oxides [142], thin metal films [143–145], metal grids [146] and carbonaceous materials such as graphene and carbon nanotube (CNT) have been investigated for ITO replacement. In particular, CNT networks and composites have several advantages with respect to commercially available TCs. Indeed, SWNTs have high T in the visible and infrared region coupled with high environmental stability and flexibility [147]. SWNTs are generally inert to bases, humidity, and high temperatures. Finally, SWNT films can be fabricated at low cost. Reference [147] reported a TC film of pure SWNTs. The SWNTs network, produced by vacuum filtration of a surfactant-assisted dispersion of SWNTs followed by a transfer printing process, showed R_s of $\sim 30 \Omega/\square$ coupled with T > 70% in the visible region and >90% in the near IR. In [148] an acid treatment was introduced in order to remove the surfactant from the flexible film produced by vacuum filtration and deposited on PET. Reference [149] presented an acid treatment of the filtered films in order to improve conductivity via stable postdeposition functionalization. Reference [150] demonstrated that transport in SWNT networks is dominated by resistance at network junctions. In the same work it is also demonstrated that acid

treatment reduces junction resistances whereas annealing significantly increases this resistance [150]. A different transfer technique, exploiting a polydimethylsiloxane (PDMS) stamp, was introduced in [151]. The method combines a PDMS-based transfer-printing technique with vacuum filtration, and allows controlled deposition and patterning of highly conducting SWNT films [151]. Reference [152] also demonstrated the application of such patternable films in electrochromic devices. Many aspects related to SWNT films for transparent and plastic electronics, such as properties and fabrication technologies are reviewed in [153]. Reference [154] investigated R_s as a function of nanotube network density showing 2D percolation behaviour. Spin coating and rod coating of the SWNT dispersions are used as alternatives to the vacuum filtration technique for the fabrication of TC films [155, 156]. A T of about 80% coupled with R_s of 85 Ω/\square was shown by a SWNT film spin coated on PET from an initial dispersion in dichloroethane (DCE) [155]. Recently, [156] reported the fabrication of SWNT films by draw-down rod coating of purified HiPco SWNTs dispersed in water at high concentration with the aid of surfactants [156]. The authors investigated the influence of surfactants on the rheological behaviour for coating and drying [156]. Doping by fuming sulfuric acid yielded the films with R_s as low as 80 and 140 Ω/\square coupled with T of 70% and 80%, respectively [156]. SWNT dispersions in aqueous solution or organic solvents were also investigated for the development of TC polymer-nanotube composites. The most promising route involves the use of conductive polymers as matrix [157–160]. Reference [157] via a vacuum filtration of an aqueous dispersions of poly(3,4-ethylenedioxythiophene):poly(styrene sulfonate) (PEDOT:PSS) and SDS/SWNTs produced composites with R_s of 80 Ω/\square and T of 75% (at 550 nm). Functionalized SWNTs, dispersed either in water [158] or in organic solvents [159], embedded in PEDOT:PSS matrix have also been investigated. Another conductive polymer investigated to date is P3HT. Composites produced by drop casting of a CNT-P3HT dispersion in chloroform are reported in [160]. However, in the case of P3HT, high conductivity is limited by the oxidation of polymer itself, which requires a reduction treatment in hydrazine. Non conductive polymer matrix has been also employed in SWNT-PE (polyethylene) composites, produced by nanotube infiltration (R_s of 50 $k\Omega/\square$ with optical transparency of 80%) [161]. Layer-by-layer assembly of Polyvinyl-Alcohol (PVA) and SWNT/PSS composite [162] shows lower conductivities (10^2 - 10^3 S/m at room temperature) compared to pure CNT films (10^4 - 10^6 S/m), but higher than most of other PVA-SWNT or polymer-SWNT composites [163, 164].

Figure 6 summarizes the best results reported thus far for SWNTs-based TCs. The performances of SWNTs-based TCs are compared with those of ITO and other materials. Although the performances of SWNTs-based TCs are slightly lower with respect to ITO or graphene produced by chemical vapour deposition (CVD) [165], they compare favourably with graphene films produced by liquid phase exfoliation [166]. However, the use of sorted m-SWNTs at the TCs in DSSCs can boost the efficiency of SWNTs-based DSSCs. Indeed, [54] demonstrated an increase in conductivity of TCs

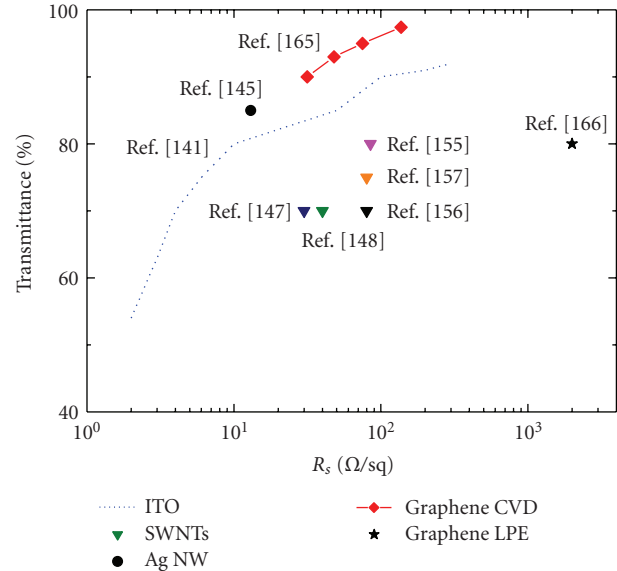


FIGURE 6: T versus R_s spectrum for different TCs. Legend: dotted line: ITO; red rhombuses: CVD graphene; black star: vacuum filtration of liquid phase-exfoliated (LPE) graphene; black dot: silver nanowires; triangles: SWNT films.

by using predominantly enriched m-SWNTs. The films were produced by vacuum filtration of sorted SWNT by DGU and showed R_s of 231 Ω/\square with 75% T in the visible, compared to R_s of 1340 Ω/\square for the unsorted material [54].

7. SWNTs as Counter-Electrodes in Dye Sensitized Solar Cells

The use of SWNTs at the counter electrode of DSSCs is attractive for several reasons. Regeneration of dye molecules is accomplished by capturing electrons from a liquid electrolyte (iodide/iodine solution), sandwiched on the counter electrode, which catalyses the reduction of tri-iodide [55]. Another important function of the counter electrode relies in the back transfer the electrons arriving from the external circuit to the redox system. The most important requirements for the counter electrode material are a high exchange current density and a low charge-transfer resistance [167].

Currently, DSSCs cathodes are made of Platinum (Pt) layers deposited on transparent glass which are, in turn, coated by a TC such as ITO [1]. Glass is brittle and has shape limitations while Pt is a rare and expensive material. Furthermore Pt tends to degrade over time when in contact with an iodide/iodine liquid electrolyte, reducing the overall efficiency of DSSCs [168]. During the last years strong efforts have been directed towards the replacement of such elements with low-cost and more versatile materials. Carbonaceous materials feature good catalytic properties, electronic conductivity, corrosion resistance towards iodine, high reactivity, abundance, and low cost [169]. In 1996 [170] demonstrated the importance of the high surface area introducing carbon black powder in graphite counter electrodes to enhance its catalytic activity. Since then,

other research groups have employed different carbonaceous materials such as: carbon black, activated carbon, graphite, CNTs, and recently graphene [4–9]. In particular, SWNTs combine advantages such as high electrical conductivity, chemical stability, and high surface area with good electrochemistry and catalytic properties making them suitable for applications in many energy conversion technologies such as counter electrode in DSSCs [171]. Moreover, SWNTs are efficient to catalyze the tri-iodide reduction and, thus, are good candidates to replace Platinum in DSSCs.

For example, SWNTs have a higher surface area with respect to multi wall CNTs (MWCNT) that have been investigated as counter electrode in DSSCs, achieving higher efficiency and longer stability with respect to Pt-sputtered counter electrode [168].

Reference [9] demonstrated that ozone-treated SWNTs films increases their catalytic activity due to the introduction of defects. In this view functionalized SWNTs could also be another option for application in counter electrodes. Metal sheets or foils are flexible substrates with excellent electrical and thermal conductivities [172]. Recently, [13] demonstrated the preparation of DSSC based on a novel stainless steel cathode coated with commercial low-cost nonpurified SWNTs. The authors achieved an overall solar energy conversion efficiency of 3.92%, which was higher than that obtained with Pt-transparent/FTO counter electrodes [13].

Enrichment of smaller diameter m-SWNTs may be useful for the improvement of the performance of the counter electrode in DSSCs. Indeed, considering that the chemical reactivity of a material is strongly related to the surface area-to-volume ratio, very small diameter SWNTs react faster than very large diameter SWNTs or MWNTs. Moreover, the use of high conductive m-SWNTs would improve the rate transfer of the electrons arriving from the external circuit to the redox system. A sorting strategy that involves a length separation followed by a diameter sorting of m-enriched SWNTs would produce long and small diameter m-SWNTs that are the ideal material for the fabrication of the counter electrode. Indeed, the use of long tubes should reduce the intertube connections increasing the conductivity of the film. The optimization of conductivity and catalytic activity of SWNTs films makes them ideal material to replace simultaneously both platinum and TC in DSSCs opening the way for inexpensive roll-to-roll processing.

8. Incorporation of SWNTs in TiO₂ Electrode

Electron transfer from the adsorbed dyes to the TiO₂ electrode, the suppression of charge recombination between the injected electrons and the oxidized dye, together with an efficient hole transport to the counter electrode are investigated strategies to enhance the performance of DSSCs. In this context, considerable efforts have been made to improve the cell performance by modifying TiO₂ electrodes using CNTs [12, 173, 174]. Reference [174] fabricated a DSSC using TiO₂-coated MWNTs, produced by Sol-Gel method, achieving an increase of 50% in conversion efficiency with respect to conventional DSSC, attributed to the increase in short circuit current density (J_{sc}). Recently, [12] reported

the use of an SWNT network as scaffolds of dye-sensitized TiO₂ particles to promote charge transport in mesoscopic semiconductor films. The authors demonstrated that the SWNT network in the film has no noticeable influence on the charge injection process from the excited Ru(II) tris-bipyridyl complex into TiO₂ particles [12]. However, SWNT network plays an important role in improving the charge separation, as the rate of back electron transfer between the oxidized sensitizer (Ru(III)) and the injected electrons becomes slower in the presence of the SWNTs scaffold [12]. DSSCs with SWNTs used as scaffold show an improvement in the photocurrent generation that is neutralized by a lower photovoltage [12]. Indeed, the apparent Fermi level of the TiO₂ and SWNT composite becomes more positive than that of pristine TiO₂ [12]. However, the efficiency of the DSSC employing the ITO/SWNT/TiO₂/Ru(II) electrode (0.13%) was smaller than that with the ITO/TiO₂/Ru(II) electrode (0.18%) [12]. This decrease was attributed to the reduction of the V_{oc} by about 60 mV [12]. Recently, [175] incorporated graphene into TiO₂ nanostructure photoanode to form graphene bridges in DSSCs, demonstrating that graphene can enhance the charge transport rate, preventing the charge recombination and increasing the light collection efficiency. Moreover, the efficiency is improved as well [175]. The authors also pointed out that SWNTs suffer some disadvantages with respect to graphene, essentially related to the one-dimensional structure that hinders a good contact with the TiO₂ nanoparticles [175]. Moreover, the work function of SWNTs was calculated and experimentally measured to be higher than MWNTs [176] and graphene [175]. This hinders the electron transport to the photoanode. However, it has been shown that the work function is diameter dependent, increasing with reduction of diameter [176]. In order to increase the performance of the DSSCs, it is highly desirable to use large diameter m-SWNTs or s-SWNTs with a suitable position of conduction band that would facilitate electron transport from mesoscopic TiO₂ particles to ITO electrode through the SWNTs.

9. Conclusions and Perspective

In this paper, we reviewed the state of the art concerning debundling and sorting of SWNTs, fundamental for many of nanotube-based applications. Further, some of the recent progresses on the application of SWNTs in DSSCs have been summarized. The use of enriched m-SWNTs generally improves the conductivity of transparent films compared with unsorted material. In the near future, the enrichment of metallic SWNTs with a defined diameter could permit the fabrication of transparent conductive coatings with tunable optical transmittance. The use of SWNTs as counter electrode opens up new industrial opportunities for large area, long-term stability, and low-cost DSSCs. In particular, a length separation followed by a diameter sorting of m-enriched SWNTs yields long and small diameter m-SWNTs. This is the ideal material for the fabrication of the counter electrode as long tubes should improve the conductivity of the cathode. At the same time small diameter tubes enhance the chemical reactivity. The excellent

electron transfer behaviour and the one-dimensional nature of SWNTs render them useful for the suppression of charge recombination between the injected electrons and the oxidized dye. Thus, nanotubes sorting is the ideal route to improve the performance of nanotube-based DSSCs.

Acknowledgments

The author acknowledges A. C. Ferrari, T. Hasan, G. Privitera, F. Torrisi, S. S. Awan, P. H. Tan, and G. Calogero for stimulating discussions and funding from the Newton International Fellowship.

References

- [1] C. G. Granqvist, "Transparent conductors as solar energy materials: a panoramic review," *Solar Energy Materials and Solar Cells*, vol. 91, no. 17, pp. 1529–1598, 2007.
- [2] J. van de Lagemaat, T. M. Barnes, G. Rumbles, et al., "Organic solar cells with carbon nanotubes replacing In_2O_3 : Sn as the transparent electrode," *Applied Physics Letters*, vol. 88, no. 23, Article ID 233503, 2006.
- [3] S. Bhattacharyya, E. Kymakis, and G. A. J. Amaratunga, "Photovoltaic properties of dye functionalized single-wall carbon nanotube/conjugated polymer devices," *Chemistry of Materials*, vol. 16, no. 23, pp. 4819–4823, 2004.
- [4] T. N. Murakami, S. Ito, Q. Wang, et al., "Highly efficient dye-sensitized solar cells based on carbon black counter electrodes," *Journal of the Electrochemical Society*, vol. 153, no. 12, pp. A2255–A2261, 2006.
- [5] K. Imoto, K. Takahashi, T. Yamaguchi, T. Komura, J.-I. Nakamura, and K. Murata, "High-performance carbon counter electrode for dye-sensitized solar cells," *Solar Energy Materials and Solar Cells*, vol. 79, no. 4, pp. 459–469, 2003.
- [6] Z. Huang, X. Liu, K. Li, et al., "Application of carbon materials as counter electrodes of dye-sensitized solar cells," *Electrochemistry Communications*, vol. 9, no. 4, pp. 596–598, 2007.
- [7] K. X. Li, Z. X. Yu, Y. H. Luo, D. M. Li, and Q. B. Meng, "Review of recent progress in solid-state dye-sensitized solar cells," *Journal of Materials Sciences and Technology*, vol. 23, pp. 577–573, 2007.
- [8] K. Suzuki, M. Yamaguchi, M. Kumagai, and S. Yanagida, "Application of carbon nanotubes to counter electrodes of dye-sensitized solar cells," *Chemistry Letters*, vol. 32, no. 1, pp. 28–29, 2003.
- [9] J. E. Trancik, S. C. Barton, and J. Hone, "Transparent and catalytic carbon nanotube films," *Nano Letters*, vol. 8, no. 4, pp. 982–987, 2008.
- [10] T. Hino, Y. Ogawa, and N. Kuramoto, "Preparation of functionalized and non-functionalized fullerene thin films on ITO glasses and the application to a counter electrode in a dye-sensitized solar cell," *Carbon*, vol. 44, no. 5, pp. 880–887, 2006.
- [11] A. Kongkanand, R. M. Dominguez, and P. V. Kamat, "Single wall carbon nanotube scaffolds for photoelectrochemical solar cells. Capture and transport of photogenerated electrons," *Nano Letters*, vol. 7, no. 3, pp. 676–680, 2007.
- [12] P. Brown, K. Takechi, and P. V. Kamat, "Single-walled carbon nanotube scaffolds for dye-sensitized solar cells," *Journal of Physical Chemistry C*, vol. 112, no. 12, pp. 4776–4782, 2008.
- [13] G. Calogero, F. Bonaccorso, O. M. Maragò, P. G. Gucciardi, and G. Di Marco, "Single wall carbon nanotubes deposited on stainless steel sheet substrates as novel counter electrodes for ruthenium polypyridine based dye sensitized solar cells," *Dalton Transaction*, vol. 39, pp. 2903–2909, 2010.
- [14] J. Tersoff and R. S. Ruoff, "Structural properties of a carbon-nanotube crystal," *Physical Review Letters*, vol. 73, no. 5, pp. 676–679, 1994.
- [15] A. Thess, R. Lee, P. Nikolaev, et al., "Crystalline ropes of metallic carbon nanotubes," *Science*, vol. 273, no. 5274, pp. 483–487, 1996.
- [16] C. Journet, W. K. Maser, P. Bernier, et al., "Large-scale production of single-walled carbon nanotubes by the electric-arc technique," *Nature*, vol. 388, no. 6644, pp. 756–758, 1997.
- [17] J. P. Lu, "Elastic properties of carbon nanotubes and nanoropes," *Physics Review Letters*, vol. 79, pp. 1297–1300, 1997.
- [18] T. Hertel, R. E. Walkup, and P. Avouris, "Deformation of carbon nanotubes by surface van der Waals forces," *Physical Review B*, vol. 58, no. 20, pp. 13870–13873, 1998.
- [19] J.-P. Salvetat, G. A. D. Briggs, J.-M. Bonard, et al., "Elastic and shear moduli of single-walled carbon nanotube ropes," *Physical Review Letters*, vol. 82, no. 5, pp. 944–947, 1999.
- [20] L. A. Girifalco, M. Hodak, and R. S. Lee, "Carbon nanotubes, buckyballs, ropes, and a universal graphitic potential," *Physical Review B*, vol. 62, no. 19, pp. 13104–13110, 2000.
- [21] M. J. López, A. Rubio, J. A. Alonso, L.-C. Qin, and S. Iijima, "Novel polygonized single-wall carbon nanotube bundles," *Physical Review Letters*, vol. 86, no. 14, pp. 3056–3059, 2001.
- [22] A. B. Dalton, S. Collins, E. Muñoz, et al., "Super-tough carbon-nanotube fibres," *Nature*, vol. 423, no. 6941, p. 703, 2003.
- [23] J. N. Coleman, U. Khan, and Y. K. Gun'ko, "Mechanical reinforcement of polymers using carbon nanotubes," *Advanced Materials*, vol. 18, no. 6, pp. 689–706, 2006.
- [24] S. Berber, Y.-K. Kwon, and D. Tománek, "Unusually high thermal conductivity of carbon nanotubes," *Physical Review Letters*, vol. 84, no. 20, pp. 4613–4616, 2000.
- [25] J.-C. Charlier, P. H. Lambin, and T. W. Ebbesen, "Electronic properties of carbon nanotubes with polygonized cross sections," *Physical Review B*, vol. 54, no. 12, pp. R8377–R8380, 1996.
- [26] Y.-K. Kwon, S. Saito, and D. Tománek, "Effect of intertube coupling on the electronic structure of carbon nanotube ropes," *Physical Review B*, vol. 58, no. 20, pp. R13314–R13317, 1998.
- [27] Y.-L. Li, I. A. Kinloch, and A. H. Windle, "Direct spinning of carbon nanotube fibers from chemical vapor deposition synthesis," *Science*, vol. 304, no. 5668, pp. 276–278, 2004.
- [28] M. Zheng, A. Jagota, M. S. Strano, et al., "Structure-based carbon nanotube sorting by sequence-dependent DNA assembly," *Science*, vol. 302, no. 5650, pp. 1545–1548, 2003.
- [29] M. S. Strano, M. Zheng, A. Jagota, et al., "Understanding the nature of the DNA-assisted separation of single-walled carbon nanotubes using fluorescence and raman spectroscopy," *Nano Letters*, vol. 4, no. 4, pp. 543–550, 2004.
- [30] S. K. Doorn, M. S. Strano, M. J. O'Connell, et al., "Capillary electrophoresis separations of bundled and individual carbon nanotubes," *Journal of Physical Chemistry B*, vol. 107, no. 25, pp. 6063–6069, 2003.
- [31] M. S. Arnold, S. I. Stupp, and M. C. Hersam, "Enrichment of single-walled carbon nanotubes by diameter in density gradients," *Nano Letters*, vol. 5, no. 4, pp. 713–718, 2005.
- [32] M. S. Arnold, A. A. Green, J. F. Hulvat, S. I. Stupp, and M. C. Hersam, "Sorting carbon nanotubes by electronic structure

- using density differentiation,” *Nature Nanotechnology*, vol. 1, no. 1, pp. 60–65, 2006.
- [33] J. Crochet, M. Clemens, and T. Hertel, “Quantum yield heterogeneities of aqueous single-wall carbon nanotube suspensions,” *Journal of the American Chemical Society*, vol. 129, no. 26, pp. 8058–8059, 2007.
- [34] F. Hennrich, K. Arnold, S. Lebedkin, A. Quintillá, W. Wenzel, and M. M. Kappes, “Diameter sorting of carbon nanotubes by gradient centrifugation: role of endohedral water,” *Physica Status Solidi B*, vol. 244, no. 11, pp. 3896–3900, 2007.
- [35] N. Nair, W.-J. Kim, R. D. Braatz, and M. S. Strano, “Dynamics of surfactant-suspended single-walled carbon nanotubes in a centrifugal field,” *Langmuir*, vol. 24, no. 5, pp. 1790–1795, 2008.
- [36] D. A. Heller, R. M. Mayrhofer, S. Baik, Y. V. Grinkova, M. L. Usrey, and M. S. Strano, “Concomitant length and diameter separation of single-walled carbon nanotubes,” *Journal of the American Chemical Society*, vol. 126, no. 44, pp. 14567–14573, 2004.
- [37] M. Zheng and E. D. Semke, “Enrichment of single chirality carbon nanotubes,” *Journal of the American Chemical Society*, vol. 129, no. 19, pp. 6084–6085, 2007.
- [38] S.-Y. Ju, J. Doll, I. Sharma, and F. Papadimitrakopoulos, “Selection of carbon nanotubes with specific chiralities using helical assemblies of flavin mononucleotide,” *Nature Nanotechnology*, vol. 3, no. 6, pp. 356–362, 2008.
- [39] S. N. Kim, Z. Kuang, J. G. Grote, B. L. Farmer, and R. R. Naik, “Enrichment of (6,5) single wall carbon nanotubes using genomic DNA,” *Nano Letters*, vol. 8, no. 12, pp. 4415–4420, 2008.
- [40] X. Tu, S. Manohar, A. Jagota, and M. Zheng, “DNA sequence motifs for structure-specific recognition and separation of carbon nanotubes,” *Nature*, vol. 460, pp. 250–253, 2009.
- [41] A. Nish, J.-Y. Hwang, J. Doig, and R. J. Nicholas, “Highly selective dispersion of single-walled carbon nanotubes using aromatic polymers,” *Nature Nanotechnology*, vol. 2, no. 10, pp. 640–646, 2007.
- [42] R. Krupke, F. Hennrich, H. V. Lohneysen, and M. M. Kappes, “Separation of metallic from semiconducting single-walled carbon nanotubes,” *Science*, vol. 301, no. 5631, pp. 344–347, 2003.
- [43] R. Krupke, F. Hennrich, H. B. Weber, M. M. Kappes, and H. V. Lohneysen, “Simultaneous deposition of metallic bundles of single-walled carbon nanotubes using ac-dielectrophoresis,” *Nano Letters*, vol. 3, no. 8, pp. 1019–1023, 2003.
- [44] R. Krupke, F. Hennrich, M. M. Kappes, and H. V. Lohneysen, “Surface conductance induced dielectrophoresis of semiconducting single-walled carbon nanotubes,” *Nano Letters*, vol. 4, no. 8, pp. 1395–1399, 2004.
- [45] R. Krupke, S. Linden, M. Rapp, and F. Hennrich, “Thin films of metallic carbon nanotubes prepared by dielectrophoresis,” *Advanced Materials*, vol. 18, no. 11, pp. 1468–1470, 2006.
- [46] W.-J. Kim, M. L. Usrey, and M. S. Strano, “Selective functionalization and free solution electrophoresis of single-walled carbon nanotubes: separate enrichment of metallic and semiconducting SWNT,” *Chemistry of Materials*, vol. 19, no. 7, pp. 1571–1576, 2007.
- [47] T. Tanaka, H. Jin, Y. Miyata, et al., “Simple and Scalable Gel-Based Separation of Metallic and Semiconducting Carbon Nanotubes,” *Nano Letters*, vol. 9, p. 1497, 2009.
- [48] K. Yanagi, Y. Miyata, and H. Kataura, “Optical and conductive characteristics of metallic single-wall carbon nanotubes with three basic colors; cyan, magenta, and yellow,” *Applied Physics Express*, vol. 1, no. 3, Article ID 034003, 2008.
- [49] T. Tanaka, H. Jin, Y. Miyata, and H. Kataura, “High-yield separation of metallic and semiconducting single-wall carbon nanotubes by agarose gel electrophoresis,” *Applied Physics Express*, vol. 1, no. 11, pp. 1140011–1140013, 2008.
- [50] K. Yanagi, T. Iitsuka, S. Fuj II, and H. Kataura, “Separations of metallic and semiconducting carbon nanotubes by using sucrose as a gradient medium,” *Journal of Physical Chemistry C*, vol. 112, no. 48, pp. 18889–18894, 2008.
- [51] K. Moshhammer, F. Hennrich, and M. M. Kappes, “Selective suspension in aqueous sodium dodecyl sulfate according to electronic structure type allows simple separation of metallic from semiconducting single-walled carbon nanotubes,” *Nano Research*, vol. 2, pp. 599–606, 2009.
- [52] G. S. Duesberg, J. Muster, V. Krstic, M. Burghard, and S. Roth, “Chromatographic size separation of single-wall carbon nanotubes,” *Applied Physics A*, vol. 67, no. 1, pp. 117–119, 1998.
- [53] K. Arnold, F. Hennrich, R. Krupke, S. Lebedkin, and M. M. Kappes, “Length separation studies of single walled carbon nanotube dispersions,” *Physica Status Solidi B*, vol. 243, no. 13, pp. 3073–3076, 2006.
- [54] A. A. Green and M. C. Hersam, “Colored semitransparent conductive coatings consisting of monodisperse metallic single-walled carbon nanotubes,” *Nano Letters*, vol. 8, no. 5, pp. 1417–1422, 2008.
- [55] B. O’Regan and M. Gratzel, “A low-cost, high-efficiency solar cell based on dye-sensitized colloidal TiO₂ films,” *Nature*, vol. 353, no. 6346, pp. 737–740, 1991.
- [56] A. Goetzberger, C. Hebling, and H.-W. Schock, “Photovoltaic materials, history, status and outlook,” *Materials Science and Engineering R*, vol. 40, no. 1, 2003.
- [57] T. Minami, “Transparent conducting oxide semiconductors for transparent electrodes,” *Semiconductor Science and Technology*, vol. 20, no. 4, pp. S35–S44, 2005.
- [58] G. Calogero and G. D. Marco, “Red Sicilian orange and purple eggplant fruits as natural sensitizers for dye-sensitized solar cells,” *Solar Energy Materials and Solar Cells*, vol. 92, no. 11, pp. 1341–1346, 2008.
- [59] S. Niyogi, M. A. Hamon, H. Hu, et al., “Chemistry of single-walled carbon nanotubes,” *Accounts of Chemical Research*, vol. 35, no. 12, pp. 1105–1113, 2002.
- [60] T. Hasan, Z. Sun, F. Wang, et al., “Nanotubes-Polymer Composites for Ultrafast Photonics,” *Advanced Materials*, vol. 21, p. 3874, 2005.
- [61] M. J. O’Connell, S. H. Bachilo, C. B. Huffman, et al., “Band gap fluorescence from individual single-walled carbon nanotubes,” *Science*, vol. 297, no. 5581, pp. 593–596, 2002.
- [62] J. Liu, A. G. Rinzler, H. Dai, et al., “Fullerene pipes,” *Science*, vol. 280, no. 5367, pp. 1253–1256, 1998.
- [63] M. F. Islam, E. Rojas, D. M. Bergey, A. T. Johnson, and A. G. Yodh, “High weight fraction surfactant solubilization of single-wall carbon nanotubes in water,” *Nano Letters*, vol. 3, no. 2, pp. 269–273, 2003.
- [64] M. J. O’Connell, P. Boul, L. M. Ericson, et al., “Reversible water-solubilization of single-walled carbon nanotubes by polymer wrapping,” *Chemical Physics Letters*, vol. 342, no. 3–4, pp. 265–271, 2001.
- [65] V. C. Moore, M. S. Strano, E. H. Haroz, et al., “Individually suspended single-walled carbon nanotubes in various surfactants,” *Nano Letters*, vol. 3, no. 10, pp. 1379–1382, 2003.

- [66] M. Zheng, A. Jagota, E. D. Semke, et al., "DNA-assisted dispersion and separation of carbon nanotubes," *Nature Materials*, vol. 2, no. 5, pp. 338–342, 2003.
- [67] M. A. Hamon, H. Hu, P. Bhowmik, et al., "End-group and defect analysis of soluble single-walled carbon nanotubes," *Chemical Physics Letters*, vol. 347, no. 1–3, pp. 8–12, 2001.
- [68] S. Niyogi, M. A. Hamon, H. Hu, et al., "Chemistry of single-walled carbon nanotubes," *Accounts of Chemical Research*, vol. 35, no. 12, pp. 1105–1113, 2002.
- [69] A. Hirsch, "Functionalization of single-walled carbon nanotubes," *Angewandte Chemie: International Edition*, vol. 41, no. 11, pp. 1853–1859, 2002.
- [70] S. Banerjee, T. Hemraj-Benny, and S. S. Wong, "Covalent surface chemistry of single-walled carbon nanotubes," *Advanced Materials*, vol. 17, no. 1, pp. 17–29, 2005.
- [71] J. Chen, A. M. Rao, S. Lyuksyutov, et al., "Dissolution of full-length single-walled carbon nanotubes," *Journal of Physical Chemistry B*, vol. 105, no. 13, pp. 2525–2528, 2001.
- [72] M. A. Hamon, J. Chen, H. Hu, et al., "Dissolution of single-walled carbon nanotubes," *Advanced Materials*, vol. 11, no. 10, pp. 834–840, 1999.
- [73] N. I. Kovtyukhova, T. E. Mallouk, L. Pan, and E. C. Dickey, "Individual single-walled nanotubes and hydrogels made by oxidative exfoliation of carbon nanotube ropes," *Journal of the American Chemical Society*, vol. 125, no. 32, pp. 9761–9769, 2003.
- [74] I. W. Chiang, B. E. Brinson, A. Y. Huang, et al., "Purification and characterization of single-wall carbon nanotubes (SWNTs) obtained from the gas-phase decomposition of CO (HiPco process)," *Journal of Physical Chemistry B*, vol. 105, no. 35, pp. 8297–8301, 2001.
- [75] B. Zhao, H. Hu, A. Yu, D. Perea, and R. C. Haddon, "Synthesis and characterization of water soluble single-walled carbon nanotube graft copolymers," *Journal of the American Chemical Society*, vol. 127, no. 22, pp. 8197–8203, 2005.
- [76] M. S. Strano, C. A. Dyke, M. L. Usrey, et al., "Electronic structure control of single-walled carbon nanotube functionalization," *Science*, vol. 301, no. 5639, pp. 1519–1522, 2003.
- [77] W. Zhu, N. Minami, S. Kazaoui, and Y. Kim, " π -chromophore-functionalized SWNTs by covalent bonding: substantial change in the optical spectra proving strong electronic interaction," *Journal of Materials Chemistry*, vol. 14, no. 13, pp. 1924–1926, 2004.
- [78] A. Calzolari, N. Marzari, I. Souza, and M. Buongiorno Nardelli, "Ab initio transport properties of nanostructures from maximally localized Wannier functions," *Physical Review B*, vol. 69, no. 3, Article ID 035108, 2004.
- [79] Y.-S. Lee, M. B. Nardelli, and N. Marzari, "Band structure and quantum conductance of nanostructures from maximally localized Wannier functions: the case of functionalized carbon nanotubes," *Physical Review Letters*, vol. 95, no. 7, Article ID 076804, 4 pages, 2005.
- [80] J. L. Bahr and J. M. Tour, "Covalent chemistry of single-wall carbon nanotubes," *Journal of Materials Chemistry*, vol. 12, no. 7, pp. 1952–1958, 2002.
- [81] Z. Sun, V. Nicolosi, D. Rickard, S. D. Bergin, D. Aherne, and J. N. Coleman, "Quantitative evaluation of surfactant-stabilized single-walled carbon nanotubes: dispersion quality and its correlation with zeta potential," *Journal of Physical Chemistry C*, vol. 112, no. 29, pp. 10692–10699, 2008.
- [82] H. Cathcart, S. Quinn, V. Nicolosi, J. M. Kelly, W. J. Blau, and J. N. Coleman, "Spontaneous debundling of single-walled carbon nanotubes in DNA-based dispersions," *Journal of Physical Chemistry C*, vol. 111, no. 1, pp. 66–74, 2007.
- [83] Y. Noguchi, T. Fujigaya, Y. Niidome, and N. Nakashima, "Single-walled carbon nanotubes/DNA hybrids in water are highly stable," *Chemical Physics Letters*, vol. 455, no. 4–6, pp. 249–251, 2008.
- [84] X. Zhang, T. Liu, T. V. Sreekumar, et al., "Poly(vinylalcohol)/SWNT Composite Film," *Nano Letters*, vol. 2003, no. 3, p. 1285, 2003.
- [85] G. R. Dieckmann, A. B. Dalton, P. A. Johnson, et al., "Controlled assembly of carbon nanotubes by designed amphiphilic peptide helices," *Journal of the American Chemical Society*, vol. 125, no. 7, pp. 1770–1777, 2003.
- [86] V. Zorbas, A. Ortiz-Acevedo, A. B. Dalton, et al., "Preparation and characterization of individual peptide-wrapped single-walled carbon nanotubes," *Journal of the American Chemical Society*, vol. 126, no. 23, pp. 7222–7227, 2004.
- [87] N. Minami, Y. Kim, K. Miyashita, S. Kazaoui, and B. Nalini, "Cellulose derivatives as excellent dispersants for single-wall carbon nanotubes as demonstrated by absorption and photoluminescence spectroscopy," *Applied Physics Letters*, vol. 88, no. 9, Article ID 093123, 2006.
- [88] P. R. Birkin, D. G. Offin, P. F. Joseph, and T. G. Leighton, "Cavitation, shock waves and the invasive nature of sono-electrochemistry," *Journal of Physical Chemistry B*, vol. 109, no. 35, pp. 16997–17005, 2005.
- [89] S. M. Bachilo, M. S. Strano, C. Kittrell, R. H. Hauge, R. E. Smalley, and R. B. Weisman, "Structure-assigned optical spectra of single-walled carbon nanotubes," *Science*, vol. 298, no. 5602, pp. 2361–2366, 2002.
- [90] R. Bandyopadhyaya, E. Nativ-Roth, O. Regev, and R. Yerushalmi-Rozen, "Stabilization of individual carbon nanotubes in aqueous solutions," *Nano Letters*, vol. 2, no. 1, pp. 25–28, 2002.
- [91] L. Picton, I. Bataille, and G. Muller, "Analysis of a complex polysaccharide (gum arabic) by multi-angle laser light scattering coupled on-line to size exclusion chromatography and flow field flow fractionation," *Carbohydrate Polymers*, vol. 42, no. 1, pp. 23–31, 2000.
- [92] T. Takahashi, K. Tsunoda, H. Yajima, and T. Ish II, "Dispersion and purification of single-wall carbon nanotubes using carboxymethylcellulose," *Japanese Journal of Applied Physics Part 1*, vol. 43, no. 6, pp. 3636–3639, 2004.
- [93] J. Lefebvre, J. M. Fraser, Y. Homma, and P. Finnie, "Photoluminescence from single-walled carbon nanotubes: a comparison between suspended and micelle-encapsulated nanotubes," *Applied Physics A*, vol. 78, no. 8, pp. 1107–1110, 2004.
- [94] A. Jorio, C. Fantini, M. A. Pimenta, et al., "Carbon nanotube population analysis from Raman and photoluminescence intensities," *Applied Physics Letters*, vol. 88, no. 2, Article ID 023109, 3 pages, 2006.
- [95] A. G. Rinzler, J. Liu, H. Dai, et al., "Large-scale purification of single-wall carbon nanotubes: process, product, and characterization," *Applied Physics A*, vol. 67, no. 1, pp. 29–37, 1998.
- [96] S. M. Bachilo, L. Balzano, J. E. Herrera, F. Pompeo, D. E. Resasco, and R. B. Weisman, "Narrow (n, m)-distribution of single-walled carbon nanotubes grown using a solid supported catalyst," *Journal of the American Chemical Society*, vol. 125, no. 37, pp. 11186–11187, 2003.

- [97] R. B. Weisman, S. M. Bachilo, and D. Tsyboulski, "Fluorescence spectroscopy of single-walled carbon nanotubes in aqueous suspension," *Applied Physics A*, vol. 78, no. 8, pp. 1111–1116, 2004.
- [98] O. Kiowski, S. Lebedkin, F. Hennrich, et al., "Photoluminescence microscopy of carbon nanotubes grown by chemical vapor deposition: influence of external dielectric screening on optical transition energies," *Physical Review B*, vol. 75, no. 7, Article ID 075422, 2007.
- [99] A. M. Rao, E. Richter, S. Bandow, et al., "Diameter-selective Raman scattering from vibrational modes in carbon nanotubes," *Science*, vol. 275, no. 5297, pp. 187–190, 1997.
- [100] T. Hasan, V. Scardaci, P. Tan, A. G. Rozhin, W. I. Milne, and A. C. Ferrari, "Stabilization and "debundling" of single-wall carbon nanotube dispersions in N-methyl-2-pyrrolidone (NMP) by polyvinylpyrrolidone (PVP)," *Journal of Physical Chemistry C*, vol. 111, no. 34, pp. 12594–12602, 2007.
- [101] T. Hasan, P. H. Tan, F. Bonaccorso, et al., "Polymer-assisted isolation of single wall carbon nanotubes in organic solvents for optical-quality nanotube—polymer composites," *Journal of Physical Chemistry C*, vol. 112, no. 51, pp. 20227–20232, 2008.
- [102] A. Hagen and T. Hertel, "Quantitative Analysis of Optical Spectra from Individual Single-Wall Carbon Nanotubes," *Nano Letters*, vol. 3, p. 383, 2003.
- [103] A. G. Walsh, A. N. Vamivakas, Y. Yin, et al., "Screening of excitons in single, suspended carbon nanotubes," *Nano Letters*, vol. 7, no. 6, pp. 1485–1488, 2007.
- [104] J. Kong, N. R. Franklin, C. Zhou, et al., "Nanotube molecular wires as chemical sensors," *Science*, vol. 287, no. 5453, pp. 622–625, 2000.
- [105] J. Maultzsch, H. Telg, S. Reich, and C. Thomsen, "Radial breathing mode of single-walled carbon nanotubes: optical transition energies and chiral-index assignment," *Physical Review B*, vol. 72, no. 20, 16 pages, 2005.
- [106] P. H. Tan, A. G. Rozhin, T. Hasan, et al., "Photoluminescence spectroscopy of carbon nanotube bundles: evidence for exciton energy transfer," *Physical Review Letters*, vol. 99, Article ID 137402, 4 pages, 2007.
- [107] P. H. Tan, T. Hasan, F. Bonaccorso, et al., "Optical properties of nanotube bundles by photoluminescence excitation and absorption spectroscopy," *Physica E*, vol. 40, no. 7, pp. 2352–2359, 2008.
- [108] V. Perebeinos, J. Tersoff, and P. Avouris, "Effect of exciton-phonon coupling in the calculated optical absorption of carbon nanotubes," *Physical Review Letters*, vol. 94, no. 2, Article ID 027402, 4 pages, 2005.
- [109] F. Plentz, H. B. Ribeiro, A. Jorio, M. S. Strano, and M. A. Pimenta, "Direct experimental evidence of exciton-phonon bound states in carbon nanotubes," *Physical Review Letters*, vol. 95, no. 24, Article ID 247401, 2005.
- [110] J. Lefebvre and P. Finnie, "Polarized photoluminescence excitation spectroscopy of single-walled carbon nanotubes," *Physical Review Letters*, vol. 98, Article ID 167406, 4 pages, 2007.
- [111] T. Kato and R. Hatakeyama, "Exciton energy transfer-assisted photoluminescence brightening from freestanding single-walled carbon nanotube bundles," *Journal of the American Chemical Society*, vol. 130, no. 25, pp. 8101–8107, 2008.
- [112] O. N. Torrents, M. Zheng, and J. M. Kikkawa, "Energy of K-momentum dark excitons in carbon nanotubes by optical spectroscopy," *Physical Review Letters*, vol. 101, no. 15, Article ID 157401, 2008.
- [113] H. Qian, C. Georgi, N. Anderson, et al., "Exciton energy transfer in pairs of single-walled carbon nanotubes," *Nano Letters*, vol. 8, no. 5, pp. 1363–1367, 2008.
- [114] S. Reich, C. Thomsen, and J. Robertson, "Exciton resonances quench the photoluminescence of zigzag carbon nanotubes," *Physical Review Letters*, vol. 95, no. 7, Article ID 077402, 4 pages, 2005.
- [115] H. Telg, J. Maultzsch, S. Reich, F. Hennrich, and C. Thomsen, "Erratum: chirality distribution and transition energies of carbon nanotubes," *Physical Review Letters*, vol. 93, no. 18, Article ID 177401, 2004.
- [116] J. C. Meyer, M. Paillet, T. Michel, et al., "Raman modes of index-identified freestanding single-walled carbon nanotubes," *Physical Review Letters*, vol. 95, no. 21, 4 pages, 2005.
- [117] A. Jorio, R. Saito, J. H. Hafner, et al., "Structural (n, m) determination of isolated single-wall carbon nanotubes by resonant Raman scattering," *Physical Review Letters*, vol. 86, no. 6, pp. 1118–1121, 2001.
- [118] M. Paillet, T. Michel, J. C. Meyer, et al., "Raman active phonons of identified semiconducting single-walled carbon nanotubes," *Physical Review Letters*, vol. 96, no. 25, Article ID 257401, 2006.
- [119] P. T. Araujo, S. K. Doorn, S. Kilina, et al., "Third and fourth optical transitions in semiconducting carbon nanotubes," *Physical Review Letters*, vol. 98, no. 6, Article ID 067401, 2007.
- [120] H. Kataura, Y. Kumazawa, Y. Maniwa, et al., "Optical properties of single-wall carbon nanotubes," *Synthetic Metals*, vol. 103, no. 1-3, pp. 2555–2558, 1999.
- [121] A. C. Ferrari and J. Robertson, "Interpretation of Raman spectra of disordered and amorphous carbon," *Physical Review B*, vol. 61, no. 20, pp. 14095–14107, 2000.
- [122] A. C. Ferrari and J. Robertson, "Resonant Raman spectroscopy of disordered, amorphous, and diamondlike carbon," *Physical Review B*, vol. 64, Article ID 075414, 13 pages, 2001.
- [123] A. C. Ferrari, "Raman spectroscopy of graphene and graphite: Disorder, electron-phonon coupling, doping and nonadiabatic effects," *Solid State Communications*, vol. 143, p. 47, 2007.
- [124] M. Lazzeri, S. Piscanec, F. Mauri, A. C. Ferrari, and J. Robertson, "Phonon linewidths and electron-phonon coupling in graphite and nanotubes," *Physical Review B*, vol. 73, no. 15, Article ID 155426, 2006.
- [125] S. Piscanec, M. Lazzeri, J. Robertson, A. C. Ferrari, and F. Mauri, "Optical phonons in carbon nanotubes: kohn anomalies, peierls distortions, and dynamic effects," *Physical Review B*, vol. 75, no. 3, Article ID 035427, 2007.
- [126] A. C. Ferrari, J. C. Meyer, V. Scardaci, et al., "Raman spectrum of graphene and graphene layers," *Physical Review Letters*, vol. 97, Article ID 187401, 4 pages, 2006.
- [127] T. M. G. Mohiuddin, A. Lombardo, R. R. Nair, et al., "Uniaxial strain in graphene by Raman spectroscopy: G peak splitting, Grüneisen parameters, and sample orientation," *Physical Review B*, vol. 79, Article ID 205433, 8 pages, 2009.
- [128] A. Das, A. K. Sood, A. Govindaraj, et al., "Doping in carbon nanotubes probed by Raman and transport measurements," *Physical Review Letters*, vol. 99, no. 13, Article ID 136803, 2007.
- [129] J. C. Tsang, M. Freitag, V. Perebeinos, J. Liu, and P. H. Avouris, "Doping and phonon renormalization in carbon nanotubes," *Nature Nanotechnology*, vol. 2, no. 11, pp. 725–730, 2007.

- [130] A. Das, S. Pisana, B. Chakraborty, et al., "Monitoring dopants by Raman scattering in an electrochemically top-gated graphene transistor," *Nature Nanotechnology*, vol. 3, no. 4, pp. 210–215, 2008.
- [131] C. Fantini, A. Jorio, M. Souza, M. S. Strano, M. S. Dresselhaus, and M. A. Pimenta, "Optical transition energies for carbon nanotubes from resonant raman spectroscopy: environment and temperature effects," *Physical Review Letters*, vol. 93, no. 14, Article ID 147406, 4 pages, 2004.
- [132] T. Svedberg and K. O. Pedersen, *The Ultracentrifuge*, 1940.
- [133] R. Westermeier, *Electrophoresis in Practice*, Wiley-VCH, Weinheim, Germany, 2005.
- [134] S. Ahuja, "Separation Science and Technology," in *Handbook of Bioseparations*, S. Ahuja, Ed., vol. 1, Academic Press, San Diego, Calif, USA, 2000.
- [135] M. C. Hersam, "Progress towards monodisperse single-walled carbon nanotubes," *Nature Nanotechnology*, vol. 3, no. 7, pp. 387–394, 2008.
- [136] F. Bonaccorso, T. Hasan, P. H. Tan, et al., submitted.
- [137] J. L. Kwo, M. Yokoyama, W. C. Wang, F. Y. Chuang, and I. N. Lin, "Characteristics of flat panel display using carbon nanotubes as electron emitters," *Diamond and Related Materials*, vol. 9, no. 3, pp. 1270–1274, 2000.
- [138] Q. H. Wang, M. Yan, and R. P. H. Chang, "Flat panel display prototype using gated carbon nanotube field emitters," *Applied Physics Letters*, vol. 78, no. 9, pp. 1294–1296, 2001.
- [139] I. Hamberg and C. G. Granqvist, "Evaporated Sn-doped In_2O_3 films: basic optical properties and applications to energy-efficient windows," *Journal of Applied Physics*, vol. 60, no. 11, pp. R123–R160, 1986.
- [140] K. Nomura, H. Ohta, K. Ueda, T. Kamiya, M. Hirano, and H. Hosono, "Thin-film transistor fabricated in single-crystalline transparent oxide semiconductor," *Science*, vol. 300, no. 5623, pp. 1269–1272, 2003.
- [141] J.-Y. Lee, S. T. Connor, Y. Cui, and P. Peumans, "Solution-processed metal nanowire mesh transparent electrodes," *Nano Letters*, vol. 8, no. 2, pp. 689–692, 2008.
- [142] F. Yang and S. R. Forrest, "Organic solar cells using transparent SnO_2 -F anodes," *Advanced Materials*, vol. 18, no. 15, pp. 2018–2022, 2006.
- [143] J. Meiss, M. K. Riede, and K. Leo, "Towards efficient tin-doped indium oxide (ITO)-free inverted organic solar cells using metal cathodes," *Applied Physics Letters*, vol. 94, no. 1, Article ID 013303, 3 pages, 2009.
- [144] B. O'Connor, C. Haughn, K.-H. An, K. P. Pipe, and M. Shtein, "Transparent and conductive electrodes based on unpatterned, thin metal films," *Applied Physics Letters*, vol. 93, Article ID 223304, p. 22, 2008.
- [145] S. De, T. M. Higgins, P. E. Lyons, et al., "Silver nanowire networks as flexible, transparent, conducting films: extremely high DC to optical conductivity ratios," *ACS Nano*, vol. 3, no. 7, pp. 1767–1774, 2009.
- [146] M. G. Kang, M.-S. Kim, J. Kim, and L. Jay Guo, "organic solar cells using nanoimprinted transparent metal electrodes," *Advanced Materials*, vol. 20, pp. 4408–4413, 2008.
- [147] Z. Wu, Z. Chen, X. Du, et al., "Transparent, conductive carbon nanotube films," *Science*, vol. 305, no. 5688, pp. 1273–1276, 2004.
- [148] H.-Z. Geng, K. K. Kim, K. P. So, Y. S. Lee, Y. Chang, and Y. H. Lee, "Effect of acid treatment on carbon nanotube-based flexible transparent conducting films," *Journal of the American Chemical Society*, vol. 129, no. 25, pp. 7758–7759, 2007.
- [149] B. B. Parekh, G. Fanchini, G. Eda, and M. Chhowalla, "Improved conductivity of transparent single-wall carbon nanotube thin films via stable postdeposition functionalization," *Applied Physics Letters*, vol. 90, no. 12, Article ID 121913, 2007.
- [150] P. N. Nirmalraj, P. E. Lyons, S. De, J. N. Coleman, and J. J. Boland, "Electrical connectivity in single-walled carbon nanotube networks," *Nano Letters*, vol. 9, no. 11, pp. 3890–3895, 2009.
- [151] Y. Zhou, L. Hu, and G. Grüner, "A method of printing carbon nanotube thin films," *Applied Physics Letters*, vol. 88, Article ID 123109, 2006.
- [152] L. Hu, et al., "patternable transparent carbon nanotube film for electrochromic devices," *Journal of Applied Physics*, vol. 101, Article ID 016102, 2007.
- [153] G. Grüner, "Carbon nanotube films for transparent and plastic electronics," *Journal of Materials Chemistry*, vol. 16, no. 35, pp. 3533–3539, 2006.
- [154] L. Hu, D. S. Hecht, and G. Grüner, "Percolation in transparent and conducting carbon nanotube networks," *Nano Letters*, vol. 4, no. 12, pp. 2513–2517, 2004.
- [155] J. H. Yim, Y. S. Kim, K. H. Koh, and S. Lee, "Fabrication of transparent single wall carbon nanotube films with low sheet resistance," *Journal of Vacuum Science and Technology B*, vol. 26, no. 2, pp. 851–855, 2008.
- [156] B. Dan, G. C. Irvin, and M. Pasquali, "Continuous and scalable fabrication of transparent conducting carbon nanotube films," *ACS Nano*, vol. 3, no. 4, pp. 835–843, 2009.
- [157] S. De, P. E. Lyons, S. Sorel, et al., "Transparent, flexible, and highly conductive thin films based on polymer-nanotube composites," *ACS Nano*, vol. 3, no. 3, pp. 714–720, 2009.
- [158] G. F. Wang, X. M. Tao, and R. X. Wang, "Flexible organic light-emitting diodes with a polymeric nanocomposite anode," *Nanotechnology*, vol. 19, Article ID 145201, 2008.
- [159] T. Mustonen, K. Kordás, S. Saukko, et al., "Inkjet printing of transparent and conductive patterns of single-walled carbon nanotubes and PEDOT-PSS composites," *Physica Status Solidi B*, vol. 244, no. 11, pp. 4336–4340, 2007.
- [160] H. Gu and T. M. Swager, "Fabrication of free-standing, conductive, and transparent carbon nanotube films," *Advanced Materials*, vol. 20, pp. 234433–4437, 2008.
- [161] I. O'Connor, S. De, J. N. Coleman, and Y. K. Gun'ko, "Development of transparent, conducting composites by surface infiltration of nanotubes into commercial polymer films," *Carbon*, vol. 47, no. 8, pp. 1983–1988, 2009.
- [162] B. S. Shim, Z. Tang, M. P. Morabito, A. Agarwal, H. Hong, and N. A. Kotov, "Integration of conductivity, transparency, and mechanical strength into highly homogeneous layer-by-layer composites of single-walled carbon nanotubes for optoelectronics," *Chemistry of Materials*, vol. 19, no. 23, pp. 5467–5474, 2007.
- [163] M. S. P. Shaffer and A. H. Windle, "Fabrication and characterization of carbon nanotube/poly(vinyl alcohol) composites," *Advanced Materials*, vol. 11, no. 11, pp. 937–941, 1999.
- [164] H. Guo, T. V. Sree Kumar, T. Liu, M. Minus, and S. Kumar, "Structure and properties of polyacrylonitrile/single wall carbon nanotube composite films," *Polymer*, vol. 46, no. 9, pp. 3001–3005, 2005.

- [165] S. Bae, H. K. Kim, Y. Lee, et al., 10.1038/NNANO.2010.132, (2010).
- [166] A. A. Green and M. C. Hersam, "Solution phase production of graphene with controlled thickness via density differentiation," *Nano Letters*, vol. 9, no. 12, pp. 4031–4036, 2009.
- [167] S. Anandan, "Recent improvements and arising challenges in dye-sensitized solar cells," *Solar Energy Materials and Solar Cells*, vol. 91, no. 9, pp. 843–846, 2007.
- [168] B.-K. Koo, D.-Y. Lee, H.-J. Kim, W.-J. Lee, J.-S. Song, and H.-J. Kim, "Seasoning effect of dye-sensitized solar cells with different counter electrodes," *Journal of Electroceramics*, vol. 17, no. 1, pp. 79–82, 2006.
- [169] H. S. Wroblowa and A. Saunders, "Flow-through electrodes. II. The I_3^-/I^- redox couple," *Journal of Electroanalytical Chemistry*, vol. 42, no. 3, pp. 329–346, 1973.
- [170] A. Kay and M. Grätzel, "Low cost photovoltaic modules based on dye sensitized nanocrystalline titanium dioxide and carbon powder," *Solar Energy Materials and Solar Cells*, vol. 44, no. 1, pp. 99–117, 1996.
- [171] W. J. Lee, E. Ramasamy, D. Y. Lee, and J. S. Song, "efficient dye-sensitized solar cells with catalytic multiwall carbon nanotube counter electrodes," *Applied Materials*, vol. 6, pp. 1145–1149, 2009.
- [172] X. Fang, T. Ma, M. Akiyama, G. Guan, S. Tsunematsu, and E. Abe, "Flexible counter electrodes based on metal sheet and polymer film for dye-sensitized solar cells," *Thin Solid Films*, vol. 472, no. 1-2, pp. 242–245, 2005.
- [173] S.-R. Jang, R. Vittal, and K.-J. Kim, "Incorporation of functionalized single-wall carbon nanotubes in dye-sensitized TiO_2 solar cells," *Langmuir*, vol. 20, no. 22, pp. 9807–9810, 2004.
- [174] T. Y. Lee, P. S. Alegaonkar, and J.-B. Yoo, "Fabrication of dye sensitized solar cell using TiO_2 coated carbon nanotubes," *Thin Solid Films*, vol. 515, no. 12, pp. 5131–5135, 2007.
- [175] N. Yang, J. Zhai, D. Wang, Y. Chen, and L. Jiang, "Two-dimensional graphene bridges enhanced photoinduced charge transport in dye-sensitized solar cells," *ACS Nano*, vol. 4, no. 2, pp. 887–894, 2010.
- [176] M. Shiraishi and M. Ata, "Work function of carbon nanotubes," *Carbon*, vol. 39, no. 12, pp. 1913–1917, 2001.

Research Article

Lateral Infrared Photovoltaic Effects in Ag-Doped ZnO Thin Films

Wenwei Liu,^{1,2} Songqing Zhao,² Kun Zhao,^{1,2,3} and Wei Sun²

¹ State Key Laboratory of Petroleum Resource and Prospecting, China University of Petroleum, Beijing 102249, China

² Laboratory of Optic Sensing and Detecting Technology, China University of Petroleum, Beijing 102249, China

³ International Center for Materials Physics, Chinese Academy of Sciences, Shenyang 110016, China

Correspondence should be addressed to Kun Zhao, zhk@cup.edu.cn

Received 18 November 2009; Revised 12 April 2010; Accepted 16 April 2010

Academic Editor: Mario Pagliaro

Copyright © 2010 Wenwei Liu et al. This is an open access article distributed under the Creative Commons Attribution License, which permits unrestricted use, distribution, and reproduction in any medium, provided the original work is properly cited.

A transient lateral photovoltaic effect has been observed in Ag-doped ZnO thin films. Under the nonuniform irradiation of a 1064 nm pulsed laser, the photovoltaic response shows high sensitivity to the spot position on the film surface. The highest photovoltaic responsivity of 27.1 mV mJ^{-1} was observed, with a decline time of $\sim 1.5 \text{ ns}$ and a full width at half-maximum (FWHM) of $\sim 4 \text{ ns}$. The photovoltaic position sensitivity can reach about $3.8 \text{ mV mJ}^{-1} \text{ mm}^{-1}$. This paper demonstrates the potential of Ag-doped ZnO films in the position-sensitive infrared detection

1. Introduction

ZnO is of technological importance and considerable scientific interest due to its unique properties such as direct wide band gap, large exciton, binding energy, strong emission, large saturation velocity ($3.2 \times 10^7 \text{ cm s}^{-1}$), high radiation resistance, and high breakdown voltage [1]. Therefore, ZnO is a promising candidate for high-power and high-frequency semiconductor devices such as ultraviolet (UV) detectors and laser devices [2–4]. Modification of ZnO properties by impurity incorporation is currently another important issue for possible applications in UV optoelectronics. Doping in ZnO with selective elements offers an effective method to adjust their electrical, optical, and magnetic properties, which is crucial for the practical applications. For example, Al doping in ZnO increased its conductivity without impairing the optical transmission, B doping decreased the resistivity [5], Mn-doped ZnO had ferromagnetism [6], and Ga_2O_3 in ZnO enhanced the near band edge UV emission [7], sulfur doping decreased dramatically the UV emission intensity [8]. The merits of wide band gap and large exciton binding energy of ZnO which lead to the research attentions, and Schottky contact, and p-n junction type of ZnO-based UV photodetectors have been realized and reported [9–11]. However, less attention has been paid to

the infrared characteristics in ZnO. Following up with our previous work, here, we show that Ag-doped ZnO thin film exhibits a lateral laser-induced photovoltage: the saturation values of this photovoltage vary with the the position of the laser spot under illumination with the 1064 nm-Nd:YAG-pulsed infrared laser. The lateral photovoltaic property is expected to make the ZnO a candidate for position-sensitive photodetectors, and the possible mechanisms are addressed.

2. Experimental

In our paper the silver-doped ZnO thin film was fabricated on fused quartz substrates ($10 \text{ mm} \times 10 \text{ mm}$) which was prepared from a ZnO mosaic target (1/4 area of the target was uniformly covered with high purity of silver slice in the shape of sector) on fused quartz substrates by pulsed laser deposition (PLD) [12] using a KrF excimer laser with the wavelength 248 nm, pulse duration 30 ms, energy density 1 J/cm^2 in O_2 atmosphere with the pressure $5 \times 10^{-4} \text{ Pa}$ and the substrate growth temperature is 450°C . The films thickness was controlled by the number of laser pulses at 450°C by pulsed-laser deposition. The SEM morphology of Ag-doped ZnO films deposited at substrate temperature of 450°C was reported in [13]. The film surfaces are very

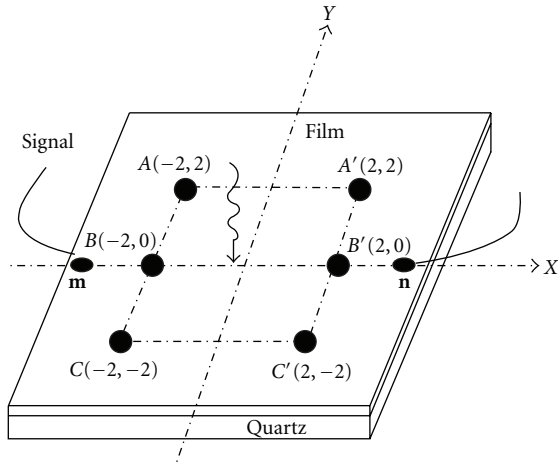


FIGURE 1: The schematic diagram displays the electrode settings, the laser spot, and the laser spot moving direction.

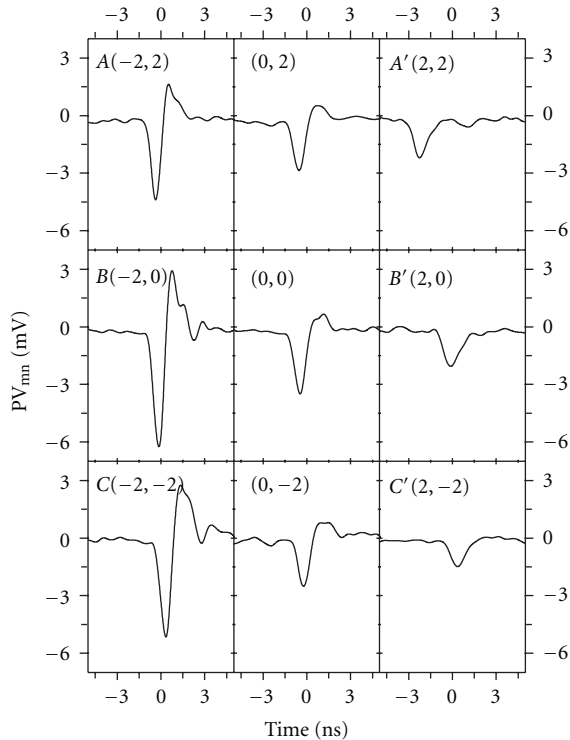


FIGURE 2: Photovoltaic signals PV_{mn} between **m** and **n** electrodes under the irradiation of 1064 nm pulse laser at selected positions of $(-2, 2)$, $(0, 2)$, $(2, 2)$, $(-2, -2)$, $(0, -2)$, and $(2, -2)$, respectively.

smooth, basically silver nanocluster uniformly distributed in the film.

For the measurement of optoelectric behaviors, the 1 mm diameter indium electrodes were made on the film surface. The 1064 nm infrared Nd:YAG laser (pulse duration of 25 ps, repetition rate of 10 Hz) was used as the light source at ambient temperature in air with a pulse energy of 0.23 mJ and a light spot of 2 mm in diameter locked by a diaphragm.

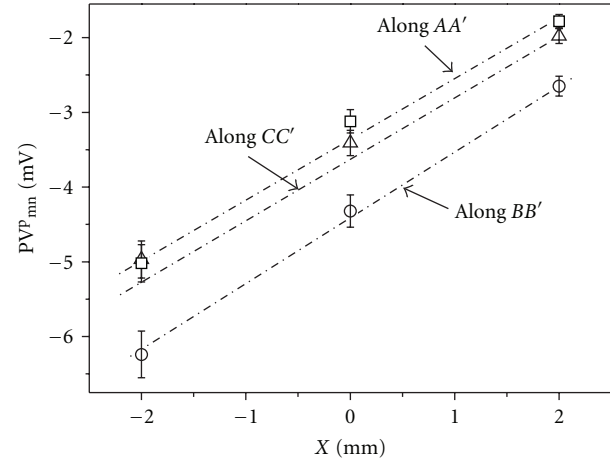


FIGURE 3: Dependence of the PV_{mn}^P on the position of the laser spot in the x direction when laser is irradiated on the ZnO surface.

As shown in Figure 1, the laser irradiated the sample along AA' , BB' , and CC' directions, and the photovoltaic signals from the anode (**m**) to cathode (**n**) were monitored with a sampling oscilloscope terminated into 50Ω . The square ($ACC'A'$) region as displayed in Figure 1 is chosen in order to avoid the effects from the light illumination on the edge and electrodes.

3. Result and Discussion

Initial photoconductive infrared (IR) detectors have been developed utilizing band-band transitions or dopant-to-band transitions. Here, we have the Ag as a dopant in ZnO, and we make it exposed to IR laser. Figure 2 showed the photovoltaic responses to the 1064 nm-pulsed laser irradiation varying with the laser spot along the AA' , BB' , and CC' directions. Two significant characteristics of the photovoltaic signals were found: (i) the maximum photovoltage is obtained when the laser spot is very close to the **m** electrode; (ii) moving the laser spot between the **m**, **n** electrodes leads to the photovoltage dropping. The highest photovoltaic responsivity of 27.1 mV mJ^{-1} was observed, with a decline time of $\sim 1.5 \text{ ns}$ and a full width at half-maximum (FWHM) of $\sim 4 \text{ ns}$, along the BB' direction close to the **m** electrode. The x direction-position sensitivity, which means the variation of the photovoltage in mV mJ^{-1} for a 1 mm displacement of the spot along x direction, is about $3.8 \text{ mV mJ}^{-1} \text{ mm}^{-1}$.

As displayed in Figure 3, the lateral photovoltage was obtained through two indium electrodes named **m** and **n** located in the middle of the two opposite film sides. The peak values of the laser induced photovoltages (PV_{mn}^P) were plotted as a function of the laser spot position x (along AA' , BB' , and CC' , the coordinate origin O was set at the centre between B and B') on the ZnO surface. In the region between the electrodes along the x -axis (shown in Figure 1), when the laser irradiated on the ZnO surface, the PV_{mn}^P varied very linearly with laser position x . It is clear that the absolute

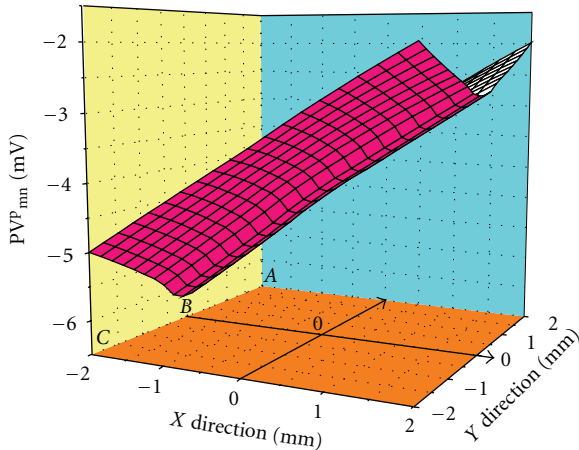


FIGURE 4: Three-dimensional plot for the PV_{mn}^P as a function of the laser spot position.

PV_{mn}^P value depends on the position of the spot on the x -axis and undergoes a sign drop while the laser spot travels from m to n . The biggest absolute signal value occur when the light spot is close to B .

Figure 4 summarizes the spatial distribution of the PV_{mn}^P . The schemae looks like an open book with the ridge toward X - Y plane. The photovoltaic signals are almost symmetrical. The dependence of the photovoltage of laser spot position shows a higher value for the laser spot close to the m electrode while a lower value close to the n electrode. The result indicated the potential in position-sensitive detection at room temperature.

Ag-doped ZnO thin film exhibits a sharp absorption edge at 370 nm [12] in agreement with its band gap of 3.37 eV and photocarrier can be easily generated under UV light illumination. However, the photon energy of 1064 nm laser is 1.165 eV, and it is impossible for the 1064 nm photons to excite the electron-hole pairs in either the Ag-doped ZnO thin film or the insulating quartz substrate. The above fact demonstrates the other aspects playing a crucial role in the photoresponse process in the present sample.

The lattice mismatch between the ZnO and quartz (major component is SiO_2 and high concentration traps exist resulting from impurities or defects) lead to the Ag doping on the fused quartz as surface plasmon at the interface which plays the role of capping buffer layer. So, many microdomains originated from the interface between the film and substrate and even run through the thickness of the whole film, resulting into nanorods, nanowires, and nanoclusters [13]. Thus, there are many metal-insulator (MI) contact structures in Ag-doped ZnO/quartz film. Based on MI contact theory [14], the Fermi level (E_f) of Ag immediately after contact is higher than that of SiO_2 , and electrons will be transferred from the Ag into SiO_2 to equalize the E_f . During the transmission, a portion of electrons are trapped by positively charged centres in the crystal and are accumulated in traps as discussed by Terner [14] and Liu et al. [15]. The contact potential difference in the equilibrium state is estimated as ~ 0.64 eV being determined by the metal

and insulator work functions, which is smaller than the 1064 nm photon energy of 1.165 eV. Under 1064 nm laser irradiation, a number of trapped electrons are freed into the conduction band of SiO_2 and removed by the built-in electric field. Eventually, the photovoltages were induced. Further experiments, such as polarization, doping concentration, interface, and tilting angle dependences, are in progress in order to clarify the underlying detection mechanism of the Ag-doped ZnO thin film.

4. Conclusions

In summary, we have observed the lateral photovoltaic effects in the Ag-doped ZnO thin film under the irradiation of the 1064 nm pulse laser. The largest photovoltaic responsivity is ~ 27.1 $mV mJ^{-1}$ with the decline time of ~ 1.5 ns and a FWHM of ~ 4 ns. The peak photovoltage shows a high sensitivity of laser spot position between the contacts on the film surface. In addition, avoiding cryogenic cooling not only reduces the cost and weight but also simplifies the infrared detector system, allowing widespread usage. ZnO is a feasible solution to the future of uncooled IR detection, and the promising initial results demonstrate the possibility of Ag-doping ZnO as a candidate of IR position detector.

Acknowledgment

This paper has been supported by NCET, NSFC, RFDP, and Beijing Natural Science Foundation.

References

- [1] C. E. Johnson, W. A. Weimer, and D. C. Harris, "Characterization of diamond films by thermogravimetric analysis and infrared spectroscopy," *Materials Research Bulletin*, vol. 24, no. 9, pp. 1127–1134, 1989.
- [2] K. W. Liu, J. G. Ma, J. Y. Zhang, et al., "Ultraviolet photoconductive detector with high visible rejection and fast photoresponse based on ZnO thin film," *Solid-State Electronics*, vol. 51, no. 5, pp. 757–761, 2007.
- [3] S. Chu, M. Olmedo, Z. Yang, J. Kong, and J. Liu, "Electrically pumped ultraviolet ZnO diode lasers on Si," *Applied Physics Letters*, vol. 93, no. 18, Article ID 181106, p. 3, 2008.
- [4] D.-K. Hwang, M.-S. Oh, J.-H. Lim, Y.-S. Choi, and S.-J. Park, "ZnO-based light-emitting metal-insulator-semiconductor diodes," *Applied Physics Letters*, vol. 91, no. 12, Article ID 121113, 3 pages, 2007.
- [5] B. J. Lokhande, P. S. Patil, and M. D. Uplane, "Studies on structural, optical and electrical properties of boron doped zinc oxide films prepared by spray pyrolysis technique," *Physica B*, vol. 302-303, pp. 59–63, 2001.
- [6] P. Sharma, A. Gupta, K. V. Rao, et al., "Ferromagnetism above room temperature in bulk and transparent thin films of Mn-doped ZnO," *Nature Materials*, vol. 2, no. 10, pp. 673–677, 2003.
- [7] R. Al Asmar, S. Juillaguet, M. Ramonda, et al., "Fabrication and characterization of high quality undoped and Ga_2O_3 -doped ZnO thin films by reactive electron beam co-evaporation technique," *Journal of Crystal Growth*, vol. 275, no. 3-4, pp. 512–520, 2005.

- [8] G. Shen, J. H. Cho, J. K. Yoo, G.-C. Yi, and C. J. Lee, "Synthesis and optical properties of S-doped ZnO nanostructures: nanonails and nanowires," *Journal of Physical Chemistry B*, vol. 109, no. 12, pp. 5491–5496, 2005.
- [9] S. Liang, H. Sheng, Y. Liu, Z. Huo, Y. Lu, and H. Shen, "ZnO Schottky ultraviolet photodetectors," *Journal of Crystal Growth*, vol. 225, no. 2–4, pp. 110–113, 2001.
- [10] T. K. Lin, S. J. Chang, Y. K. Su, B. R. Huang, M. Fujita, and Y. Horikoshi, "ZnO MSM photodetectors with Ru contact electrodes," *Journal of Crystal Growth*, vol. 281, no. 2-4, pp. 513–517, 2005.
- [11] J. L. Liu, F. X. Xiu, L. J. Mandalapu, and Z. Yang, "P-type ZnO by Sb doping for PN-junction photodetectors," in *Zinc Oxide Materials and Devices*, vol. 6122 of *Proceedings of the SPIE*, January 2006.
- [12] W. Liu, S. Zhao, K. Zhao, et al., "Ultraviolet photovoltaic characteristics of silver nanocluster doped ZnO thin films," *Physica B*, vol. 404, no. 8–11, pp. 1550–1552, 2009.
- [13] S. Zhao, Y. Zhou, K. Zhao, et al., "Violet luminescence emitted from Ag-nanocluster doped ZnO thin films grown on fused quartz substrates by pulsed laser deposition," *Physica B*, vol. 373, no. 1, pp. 154–156, 2006.
- [14] W. J. Turner, "Photoemission from silver into sodium chloride, thallium chloride, and thallium bromide," *Physical Review*, vol. 101, no. 6, pp. 1653–1660, 1956.
- [15] H. Liu, K. Zhao, S. Zhao, et al., "Ultrafast and spectrally broadband photovoltaic response in quartz single crystals," *Journal of Physics D*, vol. 42, no. 7, Article ID 075104, 2009.

Research Article

Characterizations of Chitosan-Based Polymer Electrolyte Photovoltaic Cells

M. H. Buraidah, L. P. Teo, S. R. Majid, R. Yahya, R. M. Taha, and A. K. Arof

Centre for Ionics University of Malaya, Physics Department, University of Malaya, 50603 Kuala Lumpur, Malaysia

Correspondence should be addressed to A. K. Arof, akarof@um.edu.my

Received 7 December 2009; Accepted 11 March 2010

Academic Editor: Gaetano Di Marco

Copyright © 2010 M. H. Buraidah et al. This is an open access article distributed under the Creative Commons Attribution License, which permits unrestricted use, distribution, and reproduction in any medium, provided the original work is properly cited.

The membranes 55 wt.% chitosan-45 wt.% NH₄I, 33 wt.% chitosan-27 wt.% NH₄I-40 wt.% EC, and 27.5 wt.% chitosan-22.5 wt.% NH₄I-50 wt.% buthyl-methyl-imidazolium-iodide (BMII) exhibit conductivity of 3.73×10^{-7} , 7.34×10^{-6} , and 3.43×10^{-5} S cm⁻¹, respectively, at room temperature. These membranes have been used in the fabrication of solid-state solar cells with configuration ITO/TiO₂/polymer electrolyte membrane/ITO. It is observed that the short-circuit current density increases with conductivity of the electrolyte. The use of anthocyanin pigment obtained by solvent extraction from black rice and betalain from the callus of *Celosia plumosa* also helps to increase the short-circuit current.

1. Introduction

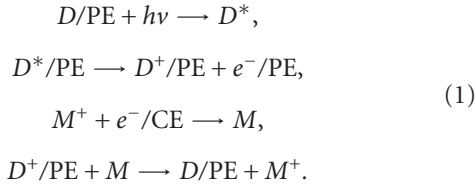
Solid polymer electrolytes are being utilized in the fabrication of solid-state photoelectrochemical (PEC) cells. The configuration of such cells in general is photoactive electrode/polymer electrolyte/counter electrode. The polymer electrolyte basically consists of polymer and salt together with a redox couple. Examples include polyethylene oxide (PEO)-KI-I₂ [1, 2], chitosan-PEO-NH₄I-I₂ [3], PEO-NH₄I-I₂ [4], and polyvinylchloride (PVC)-LiClO₄ [5]. In order to enhance performance of the PEC cell, plasticizers have been used either as an additive or as a solvent or cosolvent. Examples include PEO-poly(vinylidene fluoride) (PVDF)-LiI-I₂ [6] which were dissolved in propylene carbonate and dimethoxyethane, polyvinyl pyrrolidone (PVP)-polyethylene glycol (PEG)-KI-I₂ [7], PEO-ethylene carbonate (EC)-propylene carbonate (PC)-KI-I₂ [8], and poly(epichlorohydrin-co-ethylene oxide) (P(EPIEO))-poly(ethylene glycol) methyl ether (P(EGME))-NaI-I₂ [9].

The photoactive electrode is usually a semiconducting material, can be inorganic or organic, and serves to produce photoelectrons when illuminated. The most common inorganic semiconducting material used is TiO₂ [10–13]. Other inorganic semiconductor materials include CdSe [14], ZnTe

[3], and ZnSe [15]. Organic semiconductor materials include the polythiophenes. Examples are poly(3-methylthiophene) (P3MT) [2] and poly[3-(4-octylphenyl)thiophene] (POPT) [16]. Counter electrodes that have been used include graphite [5] and platinum (Pt) [17–20]. A large difference in the Fermi levels between the photoanode and counter electrode under illumination will exhibit a large potential difference and thus will enable a larger current to be delivered by the device.

Types of redox couples or mediators include I⁻/I₃⁻ [21–24], 5-mercapto-1-methyltetrazole cesium salt (CsT)/di-5-(1-methyltetrazole) (T₂) [14], Fe³⁺/Fe²⁺ [25], Co(II/III) [26], OH⁻/O₂⁻, and S/S²⁻ [27]. The performance of these PEC cells can be improved by soaking the photoactive electrode with a suitable dye material. When the PEC cell is illuminated, electrons in the dye are excited and injected into the conduction band of the semiconductor photoelectrode. The dye-sensitizer is thereby oxidized. The mediator (I⁻/I₃⁻ couple) in the electrolyte regenerates the oxidized dye producing photocurrent and photovoltage in the cell. Examples of dye materials are Ru(4,4'-dicarboxylic acid-2,2' bipyridine)₂(thiocyanate) [28] and (tri(cyanato)-2,2'-terpyridyl-4,4'-tricarboxylate) Ru(II) [29]. Natural dyes are also being used in dye-sensitized solar cells (DSSCs). These include anthocyanin [30], chlorophyll [31], and

carotenoid [32]. The photovoltaic performance of a solid-state DSSC may be explained as follows [33]:



Here D is the dye, PE is photoelectrode, CE is counter electrode, and M is redox couple or mediator. In this work, polymer electrolytes consisting of chitosan and NH_4I with ethylene carbonate (EC) as plasticizer and ionic liquid (IL) as ionic dopant were prepared and used in TiO_2/ITO cells. Anthocyanin, a natural pigment that was extracted from black rice, and betalain that was extracted from callus of *Celosia plumosa* (locally known as *balong ayam*) were used as the material to enhance electron injection into the conduction band of the photoelectrode.

2. Experimental

Details of electrolyte preparation can be found in previous works [34, 35]. Conductivity of the electrolytes was calculated using the equation

$$\sigma = \frac{d}{R_b A}, \tag{2}$$

where σ is conductivity, and A and d are area and thickness of the electrolyte film, respectively. R_b is the bulk resistance which is derived from the high-frequency intercept on the Cole-Cole plots. The impedance of the samples was measured using the HIOKI 3531-01 LCR Hi-Tester in the frequency range from 50 Hz to 1 MHz from room temperature to 343 K. For solar cell application, the electrolyte was added with some iodine crystals, I_2 (10% of salt amount) to provide the redox couple I^-/I_3^- .

The anthocyanin pigment was extracted from black rice grains and betalain from callus of *Celosia plumosa*. Black rice and callus were immersed in 95% ethanol and methanol solution, respectively. The pigment solutions were kept at room temperature in the dark for 24 hours. Filtration was done to remove the residues and the pH of the dye was adjusted accordingly by adding hydrochloric acid. Procedure for callus production can be found in [36].

An indium tin-oxide (ITO) glass ($2.5 \times 2.5 \text{ cm}^2$) with sheet resistance of $5 \Omega \text{ cm}^{-2}$ was cleaned with distilled water and acetone. A part of the ITO layer was covered and the active area of the ITO layer is about 0.16 cm^2 . TiO_2 paste (JGC Catalysts & Chemicals Ltd) was doctor-bladed on the ITO substrate to form the photoactive cathode. The TiO_2 layer was then heated at 773 K for 1 hour. The thickness of the film was controlled using adhesive tape of thickness $100 \mu\text{m}$. After cooling to 373 K, the TiO_2 electrode was immersed in an anthocyanin solution for 24 hours and the ITO sheet resistance of $11 \Omega \text{ cm}^{-2}$ was obtained. The photoelectrode was washed with water to remove impurities and then with ethanol to remove trapped water from the initial washing.

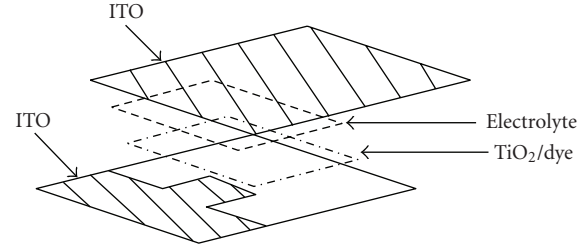


FIGURE 1: Diagram of PEC cell.

TABLE 1: Electrolytes composition and conductivity at ambient temperature.

Sample	Conductivity (S cm^{-1})
55 wt.% chitosan-45 wt.% NH_4I	3.73×10^{-7}
33 wt.% chitosan-27 wt.% NH_4I -40 wt.% EC	7.34×10^{-6}
27.5 wt.% chitosan-22.5 wt.% NH_4I -50 wt.% BMII	3.43×10^{-5}

BMII: Buthyl-methyl-imidazolium-iodide.

An equal area of polymer electrolyte was placed above the TiO_2 photoelectrode. Another ITO glass plate (counter electrode) was placed over the whole assembly and clamped with a paper clip. The J - V characteristics of the dye-sensitized solar cells were obtained under white light illumination (100 mW cm^{-2}) using a Keithley 2400 electrometer.

The assembly of the fabricated cell is shown in Figure 1.

3. Results and Discussion

Table 1 lists the composition of the polymer electrolytes and the respective room temperature conductivity.

Figure 2 shows the plot of log conductivity versus temperature for each of the electrolyte listed in Table 1. It is noticed in all plots that conductivity increases with temperature. The conductivity-temperature relationship is Arrhenian.

Tables 2 to 4 list the short-circuit current density J_{sc} , open circuit voltage (OCV), fill factor (ff), efficiency (η) of PEC cells and the type of polymer electrolyte, redox couple, and dye material used. The photoactive and counter electrodes of all the PEC cells listed are TiO_2 and ITO coated with platinum, respectively, except for PEC cells utilizing the chitosan containing electrolyte where the photoactive electrode is TiO_2 and the counter electrode is ITO glass without any catalytic material coating.

The conductivity of an electrolyte depends on the ability of the polymer host to solvate the salt. Polymers with higher dielectric constant will serve the purpose better. Apart from that, the lattice energy of the salt should be low since this would help to increase dissociation of the salt. Thus, it may be understood why the different electrolyte systems in Table 2 exhibit different room temperature conductivity. From the results in Table 2, it may be inferred that the dielectric constant of PBA [37] is slightly higher than that

TABLE 2: Characteristics of PEC cells using polymer-salt systems.

Sample	Dye	Intensity (mW cm ⁻²)	Redox couple	σ (S cm ⁻¹)	J_{sc} (mA cm ⁻²)	OCV (V)	ff	η (%)	Ref.
91 wt.% Poly(butyl acrylate) + 9 wt.% NaI	Ru(dcbpy) ₂ (NCS) ₂	100	I ⁻ /I ₃ ⁻	2.10×10^{-6}	2.20	0.61	0.37	0.51	[37]
87.5 wt.% PEO + 12.5 wt.% NaI	Ru(dcbpy) ₂ (NCS) ₂	100	I ⁻ /I ₃ ⁻	2.02×10^{-6}	1.51	0.83	0.61	0.76	[38]
92 wt.% PEO + 8 wt.% KI	Ru(dcbpy) ₂ (NCS) ₂	100	I ⁻ /I ₃ ⁻	6.33×10^{-5}	5.04	0.62	0.63	1.96	[1]
89 wt.% P(EPI-EO) + 11 wt.% NaI	Ru(dcbpy) ₂ (NCS) ₂	100	I ⁻ /I ₃ ⁻	1.9×10^{-5}	0.55	0.75	—	0.19	[9]
71 wt.% P(EPI-EO) + 29 wt.% NaI	Ru(dcbpy) ₂ (NCS) ₂	120	I ⁻ /I ₃ ⁻	1.0×10^{-5}	0.46	0.71	0.67	0.22	[39]
55 wt.% Chitosan + 45 wt.% NH ₄ I	None	56.4	I ⁻ /I ₃ ⁻	3.73×10^{-7}	0.005	0.15	0.22	—	[35]

TABLE 3: Characteristics of PEC cells using plasticized polymer-salt systems.

Polymer electrolyte Sample	Dye	Intensity (mW cm ⁻²)	Redox couple	σ (S cm ⁻¹)	J_{sc} (mA cm ⁻²)	OCV (V)	ff	η (%)	Ref.
27.2 wt.% PEO + 2.8 wt.% Pr ₄ N ⁺ I ⁻ + 70 wt.% EC	Ru(dcbpy) ₂ (NCS) ₂	100	I ⁻ /I ₃ ⁻	4.9×10^{-5}	0.051	0.44	0.48	0.01	[40]
PEO + LiI + EC + PC	Ru(dcbpy) ₂ (NCS) ₂	27	I ⁻ /I ₃ ⁻	1.2×10^{-3}	2.10	0.60	0.62	2.90	[41]
13.5 wt.% PAN + 7.3 wt.% Pr ₄ N ⁺ I ⁻ + 32.3 wt.% EC + 46.9 wt.% PC	Ru(dcbpy) ₂ (NCS) ₂	60	I ⁻ /I ₃ ⁻	3.0×10^{-3}	3.73	0.69	—	2.99	[42]
43.5 wt.% P(EPI-EO) + 13 wt.% NaI + 43.5 wt.% P(EGME)	Ru(dcbpy) ₂ (NCS) ₂	100	I ⁻ /I ₃ ⁻	1.7×10^{-4}	1.88	0.7	—	0.52	[9]
33 wt.% chitosan + 27 wt.% NH ₄ I + 40 wt.% EC	None	56.4	I ⁻ /I ₃ ⁻	7.3×10^{-6}	0.007	0.22	0.18	—	[35]

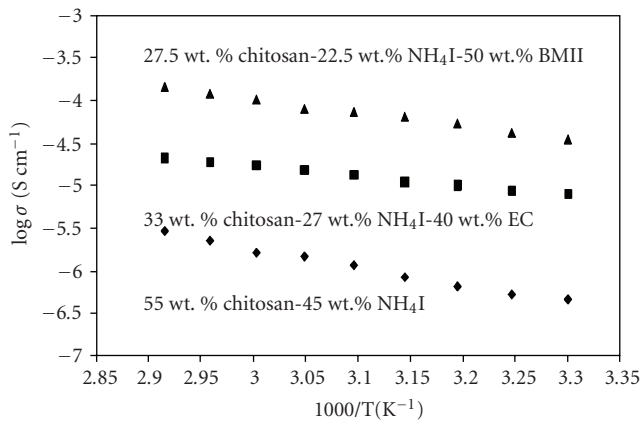


FIGURE 2: Temperature dependence of ionic conductivity.

of PEO [38] because for a higher salt content in the PEO-NaI electrolyte, the conductivity is almost similar to that of PBA-NaI electrolyte at room temperature (assumed 298 K). The composition of the P(EPI-EO)-NaI electrolyte [9] and that of PEO-NaI electrolyte [38] are almost similar. However, the P(EPI-EO)-NaI electrolyte exhibits a conductivity of almost one order of magnitude higher than that of PEO-NaI

electrolyte. This has been attributed to the presence of Cl in P(EPI-EO) that played a part in reducing the crystallinity of the polymer [45, 46], thus resulting in higher conductivity.

Again referring to Table 2, the composition of the PEO-KI electrolyte [1] is almost similar to the composition of PBA-NaI electrolyte [37], but the conductivity of the former is more than one order of magnitude higher. Although it has been inferred that the dielectric constant of PBA is slightly higher than PEO, the higher conductivity of the PEO-KI electrolyte may be attributed to the lower lattice energy of KI compared to that of NaI (according to calculations performed using the Kapunstinskii and Born-Haber equations). Hence, assuming temperature to be the same, the number density of mobile cations is higher in the PEO-KI electrolyte than that in the PBA-NaI electrolyte resulting in a higher conductivity. Another example from Table 2 showing the fact that lower lattice energy of salt results in higher conductivity can be observed from the conductivity of the PEO-KI and PEO-NaI electrolyte systems. At almost similar composition, higher conductivity was observed in the PEO-KI electrolyte compared to PEO-NaI electrolyte. The lattice energy of KI is 614.5 kJ mol⁻¹ and that of NaI is 674 kJ mol⁻¹. The lower conductivity of P(EPI-EO)-based electrolyte with 29 wt.% NaI compared to the same polymer-based electrolyte with 11 wt.% NaI has been attributed to ion pairs formation

TABLE 4: Characteristics of PEC cells using polymer-salt-ionic liquid systems.

Polymer electrolyte Sample	Dye	Intensity (mW cm ⁻²)	Redox couple	σ (S cm ⁻¹)	J_{sc} (mA cm ⁻²)	OCV (V)	ff	η (%)	Ref.
52.5 wt.% PEO + 17.5 wt.% KI + 30 wt.% EMImTFSI	Ru(dcbpy) ₂ (NCS) ₂	100	I ⁻ /I ₃ ⁻	8.82×10^{-5}	4.02	0.77	0.56	1.75	[43]
15 wt.% PEO + 5 wt.% KI + 80 wt.% EMISCN	Ru(dcbpy) ₂ (NCS) ₂	27	I ⁻ /I ₃ ⁻	2.25×10^{-5}	1.89	0.65	0.52	0.63	[44]
17.5 wt.% PEO + 2.5 wt.% NaI + 80 wt.% EMImTFO	Ru(dcbpy) ₂ (NCS) ₂	60	I ⁻ /I ₃ ⁻	4.72×10^{-5}	5.65	0.79	0.55	2.45	[38]
27.5 wt.% Chitosan + 22.5 wt.% NH ₄ I + 50 wt.% BMII	Anthocyanin from black rice	100	I ⁻ /I ₃ ⁻	3.43×10^{-5}	0.065	0.23	0.22	—	—
27.5 wt.% Chitosan + 22.5 wt.% NH ₄ I + 50 wt.% BMII	Betalain from callus of <i>Celosia plumosa</i>	100	I ⁻ /I ₃ ⁻	3.43×10^{-5}	0.029	0.14	0.22	—	—

and cross linking sites that hinder segmental motion of the polymer chains thereby decreasing ionic mobility and consequently conductivity [9].

The lower OCV and J_{sc} exhibited by the cell utilizing the chitosan-NH₄I electrolyte are probably due to the smaller number of photoelectrons injected into the conduction band of the TiO₂. In the absence of a catalyst coating such as Pt in the counter electrode leads to a slower rate of I₃⁻ reduction to I⁻. This delays the photocurrent and photovoltage generation that accounts for the low J_{sc} and OCV [35]. According to Yen et al. [47] the I₃⁻ + 2e⁻ → 3I⁻ reaction rate is extremely slow if the ITO counter electrode is not coated with catalytic materials.

From Table 3, conductivity for the electrolyte 43.5 wt.% P(EPI-EO) + 43.5 wt.% P(EGME) + 13 wt.% NaI [9] is nine times higher than that of the unplasticized electrolyte 89 wt.% P(EPI-EO) + 11 wt.% NaI; see Table 2. The employment of poly(ethylene glycol) methyl ether has resulted in more salt to dissociate resulting in a higher conductivity. The conductivity of the PAN + Pr₄NI + EC + PC electrolyte [42] is greater than the conductivity of PEO + Pr₄NI + EC [40] by almost 2 orders of magnitude. This could be attributed to the higher dielectric constant of PAN which is 6.27 [48] compared to that of PEO which is 5 [49] and to the presence of the PC plasticizer. With addition of plasticizer to the chitosan-NH₄I electrolyte, the conductivity has increased to more than one order of magnitude.

The incorporation of ionic liquid to the electrolytes (Table 4) also improved performance of the PEC cell as shown in the work of Singh et al. [38]. The incorporation of 1-ethyl-3-methylimidazolium trifluoromethanesulfonate (EMImTFO) in the PEO-NaI electrolyte has increased the conductivity from 2.02×10^{-6} S cm⁻¹ to 4.72×10^{-5} S cm⁻¹. An increase by a factor of ~4 in J_{sc} of DSSC was found. The PEC cell employing chitosan-based electrolyte also showed increment in conductivity and in J_{sc} . The anthocyanin pigment pH is also an important factor affecting J_{sc} . In this work, anthocyanin extracted from black rice produced a $65 \mu\text{A cm}^{-2} J_{sc}$ and the cell employing the betalain pigment extracted from callus of *Celosia plumosa*

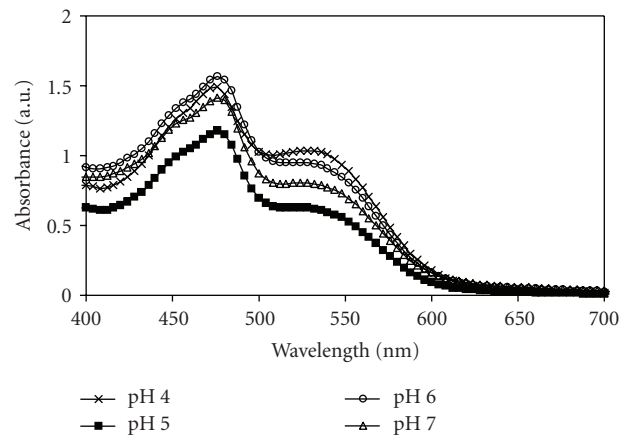


FIGURE 3: The absorption spectra of betalain at different pH.

[50, 51] produced $29 \mu\text{A cm}^{-2} J_{sc}$. The absorbance of the betalain pigment solution depends on its pH, as shown in Figure 3.

Rahman et al. [5] investigated the effect of electrolyte conductivity on OCV and J_{sc} of the ITO/TiO₂/PVC-LiClO₄/graphite solar cell. They have shown that both OCV and J_{sc} increase with electrolyte conductivity. From Table 2, the short-circuit current density J_{sc} for the PEC cell with PBA-NaI electrolyte is about 1.5 times larger than that of the solar cell employing PEO-NaI electrolyte. The PBA-NaI electrolyte also exhibits higher conductivity compared to PEO-NaI electrolyte. An almost similar situation can be observed in the work of Nogueira and coworkers [9, 39]. The solar cell utilizing the lower conducting electrolyte 71 wt.% P(EPI-EO)-29 wt.% NaI exhibits a short-circuit current density that is smaller than the solar cell utilizing the higher conducting electrolyte 89 wt.% P(EPI-EO)-11 wt.% NaI. This implies that higher conductivity of the electrolyte results in higher J_{sc} of the solar cell. However, the DSSCs employing PBA-NaI [37] and PEO-NaI [38] electrolytes with lower conductivity exhibit higher J_{sc} compared to the cells using P(EPI-EO)-NaI electrolytes [9, 39]. The DSSCs utilizing PBA-NaI and

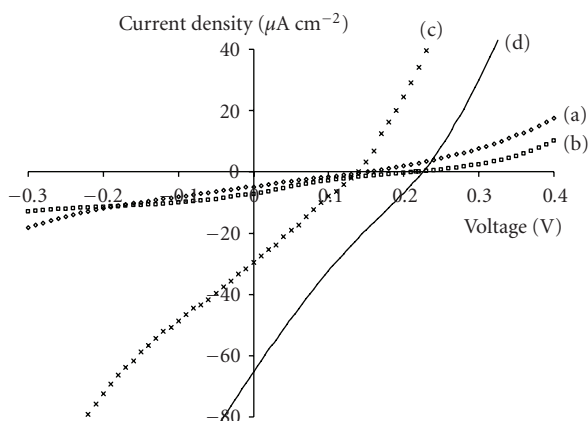


FIGURE 4: Current density versus voltage characteristics under illumination for (a) ITO/TiO₂/55 wt.% chitosan+45 wt.% NH₄I/ITO, (b) ITO/TiO₂/33 wt.% chitosan+27 wt.% NH₄I+40 wt.% EC/ITO, (c) ITO/TiO₂/betalain dye (callus of *Celosia plumosa*)/27.5 wt.% chitosan+22.5 wt.% NH₄I+50 wt.% BMII/ITO, and (d) ITO/TiO₂/anthocyanin dye (black rice)/27.5 wt.% chitosan+22.5 wt.% NH₄I+50 wt.% BMII/ITO.

PEO-NaI electrolyte have an extra layer coated on the ITO glass beneath the TiO₂ semiconducting photoelectrode layer. This underlayer consists of Ti(IV)bis(ethyl acetoacetato)-diisopropoxide coating. According to these authors, the Ti(IV)bis(ethyl acetoacetato)-diisopropoxide coating suppresses electron back recombination to the oxidized electrolyte. It is not clear from literature whether the DSSCs employing P(EPI-EO)-NaI electrolyte have this underlayer coating. If this is the case, it may be understood why the J_{sc} exhibited by these DSSCs is lower when the conductivity of the electrolyte is about one order of magnitude higher than the PBA-NaI and PEO-NaI electrolyte. The recombination is more evident in the absence of the underlayer leading to a depletion of the number of free electrons flowing through the external circuit resulting in a low J_{sc} . The low OCV exhibited by the cells using the chitosan electrolyte is probably due to the small difference in Fermi level of the TiO₂ and Fermi level of the redox couple. Figure 4 shows the plot of current density versus voltage characteristics for DSSC employing electrolytes of 55 wt.% chitosan+45 wt.% NH₄I, 33 wt.% chitosan+27 wt.% NH₄I+40 wt.% EC, and 27.5 wt.% chitosan+22.5 wt.% NH₄I+50 wt.% BMII.

4. Conclusions

Ethylene carbonate and ionic liquid enhance the conductivity of the electrolyte with chitosan as polymer host and NH₄I as doping salt. Log σ versus T dependence follows the Arrhenius rule. Betalain pigment from calli of *Celosia plumosa* and anthocyanin pigment from black rice can serve as dye in solid-state solar cell applications. It was found that the dielectric constant of polymer and lattice energy of salt influence the conductivity. The conductivity in turn affects the short-circuit current density of the solar cells.

Acknowledgments

The authors thank the University of Malaya and M. H. Buraidah thanks the SLAB scheme for financial support.

References

- [1] G. P. Kalaigan, M.-S. Kang, and Y. S. kang, "Effects of compositions on properties of PEO-KI-I₂ salts polymer electrolytes for DSSC," *Solid State Ionics*, vol. 177, no. 11-12, pp. 1091–1097, 2006.
- [2] T. Yohannes, T. Solomon, and O. Inganäs, "Polymer-electrolyte-based photoelectrochemical solar energy conversion with poly(3-methylthiophene) photoactive electrode," *Synthetic Metals*, vol. 82, no. 3, pp. 215–220, 1996.
- [3] S. A. Mohamad, R. Yahya, Z. A. Ibrahim, and A. K. Arof, "Photovoltaic activity in a ZnTe/PEO-chitosan blend electrolyte junction," *Solar Energy Materials and Solar Cells*, vol. 91, no. 13, pp. 1194–1198, 2007.
- [4] B. Bhattacharya, H. M. Upadhyaya, and S. Chandra, "Photoelectrochemical studies of an ion conducting polymer (PEO)/semiconductor (Si) junction," *Solid State Communications*, vol. 98, no. 7, pp. 633–638, 1996.
- [5] M. Y. A. Rahman, M. M. Salleh, I. A. Talib, and M. Yahaya, "Effect of ionic conductivity of a PVC-LiClO₄ based solid polymeric electrolyte on the performance of solar cells of ITO/TiO₂/PVC-LiClO₄/graphite," *Journal of Power Sources*, vol. 133, no. 2, pp. 293–297, 2004.
- [6] Y. Yang, C. Zhou, S. Xu, et al., "Improved stability of quasi-solid-state dye-sensitized solar cell based on poly (ethylene oxide)-poly (vinylidene fluoride) polymer-blend electrolytes," *Journal of Power Sources*, vol. 185, no. 2, pp. 1492–1498, 2008.
- [7] J. Wu, P. Li, S. Hao, H. Yang, and Z. Lan, "A polyblend electrolyte (PVP/PEG+KI+I₂) for dye-sensitized nanocrystalline TiO₂ solar cells," *Electrochimica Acta*, vol. 52, no. 17, pp. 5334–5338, 2007.
- [8] O. A. Ileperuma, M. A. K. L. Dissanayake, S. Somasundaram, and L. R. A. K. Bandara, "Photoelectrochemical solar cells with polyacrylonitrile-based and polyethylene oxide-based polymer electrolytes," *Solar Energy Materials and Solar Cells*, vol. 84, no. 1–4, pp. 117–124, 2004.
- [9] V. C. Nogueira, C. Longo, A. F. Nogueira, M. A. Soto-Oviedo, and M.-A. De Paoli, "Solid-state dye-sensitized solar cell: improved performance and stability using a plasticized polymer electrolyte," *Journal of Photochemistry and Photobiology A*, vol. 181, no. 2-3, pp. 226–232, 2006.
- [10] M. Matsumoto, H. Miyazaki, K. Matsuhira, Y. Kumashiro, and Y. Takaoka, "A dye sensitized TiO₂ photoelectrochemical cell constructed with polymer solid electrolyte," *Solid State Ionics*, vol. 89, no. 3-4, pp. 263–267, 1996.
- [11] Z. Lan, J. Wu, D. Wang, S. Hao, J. Lin, and Y. Huang, "Quasi-solid state dye-sensitized solar cells based on gel polymer electrolyte with poly(acrylonitrile-co-styrene)/NaI + I₂," *Solar Energy*, vol. 80, no. 11, pp. 1483–1488, 2006.
- [12] O. A. Ileperuma, M. A. K. L. Dissanayake, and S. Somasundaram, "Dye-sensitized photoelectrochemical solar cells with polyacrylonitrile based solid polymer electrolytes," *Electrochimica Acta*, vol. 47, no. 17, pp. 2801–2807, 2002.
- [13] P. K. Singh, K.-W. Kim, N.-G. Park, and H.-W. Rhee, "Mesoporous nanocrystalline TiO₂ electrode with ionic liquid-based solid polymer electrolyte for dye-sensitized solar cell application," *Synthetic Metals*, vol. 158, no. 14, pp. 590–593, 2008.

- [14] J.-M. Philiat and B. Marsan, "All-solid-state photoelectrochemical cell based on a polymer electrolyte containing a new transparent and highly electropositive redox couple," *Electrochimica Acta*, vol. 44, no. 17, pp. 2915–2926, 1999.
- [15] S. A. Mohamad, M. H. Ali, R. Yahya, Z. A. Ibrahim, and A. K. Arof, "Photovoltaic activity in a ZnSe/PEO-chitosan blend electrolyte junction," *Ionics*, vol. 13, no. 4, pp. 235–240, 2007.
- [16] T. Yohannes and O. Inganaäs, "Photoelectrochemical studies of the junction between poly[3-(4-octylphenyl)thiophene] and a redox polymer electrolyte," *Solar Energy Materials and Solar Cells*, vol. 51, no. 2, pp. 193–202, 1998.
- [17] A. Kambili, A. B. Walker, F. L. Qiu, A. C. Fisher, A. D. Savin, and L. M. Peter, "Electron transport in the dye sensitized nanocrystalline cell," *Physica E*, vol. 14, no. 1-2, pp. 203–209, 2002.
- [18] A. Fukui, R. Komiya, R. Yamanaka, A. Islam, and L. Han, "Effect of a redox electrolyte in mixed solvents on the photovoltaic performance of a dye-sensitized solar cell," *Solar Energy Materials and Solar Cells*, vol. 90, no. 5, pp. 649–658, 2006.
- [19] Z. Lan, J. Wu, D. Wang, S. Hao, J. Lin, and Y. Huang, "Quasi-solid-state dye-sensitized solar cells based on a sol-gel organic-inorganic composite electrolyte containing an organic iodide salt," *Solar Energy*, vol. 81, no. 1, pp. 117–122, 2007.
- [20] S. Yanagida, G. K. R. Senadeera, K. Nakamura, T. Kitamura, and Y. Wada, "Polythiophene-sensitized TiO₂ solar cells," *Journal of Photochemistry and Photobiology A*, vol. 166, no. 1–3, pp. 75–80, 2004.
- [21] H. Santa-Nokki, S. Busi, J. Kallioinen, M. Lahtinen, and J. Korppi-Tommola, "Quaternary ammonium polyiodides as ionic liquid/soft solid electrolytes in dye-sensitized solar cells," *Journal of Photochemistry and Photobiology A*, vol. 186, no. 1, pp. 29–33, 2007.
- [22] A. Sergawie, T. Yohannes, and T. Solomon, "A comparative study on liquid-state photoelectrochemical cells based on poly(3-hexylthiophene) and a composite film of poly(3-hexylthiophene) and nanocrystalline titanium dioxide," *Synthetic Metals*, vol. 157, no. 2-3, pp. 75–79, 2007.
- [23] Z. Lan, J. Wu, J. Lin, M. Huang, P. Li, and Q. Li, "Influence of ionic additives NaI/I₂ on the properties of polymer gel electrolyte and performance of quasi-solid-state dye-sensitized solar cells," *Electrochimica Acta*, vol. 53, no. 5, pp. 2296–2301, 2008.
- [24] M. G. Kang, K. S. Ryu, S. H. Chang, and N.-G. Park, "A new ionic liquid for a redox electrolyte of dye-sensitized solar cells," *ETRI Journal*, vol. 26, no. 6, pp. 647–652, 2004.
- [25] M. A. Butler and D. S. Ginley, "Principles of photoelectrochemical, solar energy conversion," *Journal of Materials Science*, vol. 15, no. 1, pp. 1–19, 1980.
- [26] S. A. Sapp, C. M. Elliott, C. Contado, S. Caramori, and C. A. Bignozzi, "Substituted polypyridine complexes of cobalt(II/III) as efficient electron-transfer mediators in dye-sensitized solar cells," *Journal of the American Chemical Society*, vol. 124, no. 37, pp. 11215–11222, 2002.
- [27] S. K. Deb, "Dye-sensitized TiO₂ thin-film solar cell research at the national renewable energy laboratory (NREL)," *Solar Energy Materials and Solar Cells*, vol. 88, no. 1, pp. 1–10, 2005.
- [28] Q. Dai, D. B. Menzies, D. R. MacFarlane, et al., "Dye-sensitized nanocrystalline solar cells incorporating ethylmethylimidazolium-based ionic liquid electrolytes," *Comptes Rendus Chimie*, vol. 9, no. 5-6, pp. 617–621, 2006.
- [29] M. Grätzel, "Dye-sensitized solar cells," *Journal of Photochemistry and Photobiology C*, vol. 4, no. 2, pp. 145–153, 2003.
- [30] Q. Dai and J. Rabani, "Photosensitization of nanocrystalline TiO₂ films by anthocyanin dyes," *Journal of Photochemistry and Photobiology A*, vol. 148, no. 1–3, pp. 17–24, 2002.
- [31] S. Hao, J. Wu, Y. Huang, and J. Lin, "Natural dyes as photosensitizers for dye-sensitized solar cell," *Solar Energy*, vol. 80, no. 2, pp. 209–214, 2006.
- [32] E. Yamazaki, M. Murayama, N. Nishikawa, N. Hashimoto, M. Shoyama, and O. Kurita, "Utilization of natural carotenoids as photosensitizers for dye-sensitized solar cells," *Solar Energy*, vol. 81, no. 4, pp. 512–516, 2007.
- [33] M. Gorlov and L. Kloo, "Ionic liquid electrolytes for dye-sensitized solar cells," *Dalton Transactions*, no. 20, pp. 2655–2666, 2008.
- [34] M. H. Buraidah, L. P. Teo, S. R. Majid, and A. K. Arof, "Ionic conductivity by correlated barrier hopping in NH₄I doped chitosan solid electrolyte," *Physica B*, vol. 404, no. 8–11, pp. 1373–1379, 2009.
- [35] M. H. Buraidah, L. P. Teo, S. R. Majid, and A. K. Arof, "Characteristics of TiO₂/solid electrolyte junction solar cells with I⁻/I₃⁻ redox couple," *Optical Materials*, vol. 32, no. 6, pp. 723–728, 2009.
- [36] R. M. Taha, "Tissue culture studies of *Citrus hystrix* D.C and *Severinia buxifolia* (Poir) Tenore," *Asia-Pacific Journal of Molecular Biology and Biotechnology*, vol. 1, no. 1, pp. 36–42, 1993.
- [37] J. H. Kim, M.-S. Kang, Y. J. Kim, J. Won, and Y. S. Kang, "Poly(butyl acrylate)/NaI/I₂ electrolytes for dye-sensitized nanocrystalline TiO₂ solar cells," *Solid State Ionics*, vol. 176, no. 5-6, pp. 579–584, 2005.
- [38] P. K. Singh, K.-W. Kim, and H.-W. Rhee, "Development and characterization of ionic liquid doped solid polymer electrolyte membranes for better efficiency," *Synthetic Metals*, vol. 159, no. 15-16, pp. 1538–1541, 2009.
- [39] A. F. Nogueira and M. De Paoli, "Dye sensitized TiO₂ photovoltaic cell constructed with an elastomeric electrolyte," *Solar Energy Materials and Solar Cells*, vol. 61, no. 2, pp. 135–141, 2000.
- [40] T. M. W. J. Bandara, M. A. K. L. Dissanayake, O. A. Ileperuma, K. Varaprathan, K. Vignarooban, and B.-E. Melander, "Polyethyleneoxide (PEO)-based, anion conducting solid polymer electrolyte for PEC solar cells," *Journal of Solid State Electrochemistry*, vol. 12, no. 7-8, pp. 913–917, 2008.
- [41] Y. Ren, Z. Zhang, S. Fang, M. Yang, and S. Cai, "Application of PEO based gel network polymer electrolytes in dye-sensitized photoelectrochemical cells," *Solar Energy Materials and Solar Cells*, vol. 71, no. 2, pp. 253–259, 2002.
- [42] M. A. K. L. Dissanayake, L. R. A. K. Bandara, R. S. P. Bokalawala, P. A. R. D. Jayatilaka, O. A. Ileperuma, and S. Somasundaram, "A novel gel polymer electrolyte based on polyacrylonitrile (PAN) and its application in a solar cell," *Materials Research Bulletin*, vol. 37, no. 5, pp. 867–874, 2002.
- [43] P. K. Singh, K.-W. Kim, and H.-W. Rhee, "Electrical, optical and photoelectrochemical studies on a solid PEO-polymer electrolyte doped with low viscosity ionic liquid," *Electrochemistry Communications*, vol. 10, no. 11, pp. 1769–1772, 2008.
- [44] B. Bhattacharya, S. K. Tomar, and J. K. Park, "A nanoporous TiO₂ electrode and new ionic liquid doped solid polymer electrolyte for dye sensitized solar cell application," *Nanotechnology*, vol. 18, pp. 485711–485714, 2007.
- [45] M. A. Silva, M.-A. De Paoli, and M. I. Felisberti, "Phase behavior of poly(ethylene oxide)/poly(epichlorohydrin) blends," in *Proceedings of 4th Simposio Latinoamericano de Polimeros*, pp. 440–442, Gramado, Brazil, 1994.

- [46] G. Goulart Silva, N. H. T. Lemes, C. N. Polo da Fonseca, and M.-A. De Paoli, "Solid state polymeric electrolytes based on poly(epychlorhydrin)," *Solid State Ionics*, vol. 93, pp. 105–116, 1996.
- [47] M.-Y. Yen, C.-Y. Yen, S.-H. Liao, et al., "A novel carbon-based nanocomposite plate as a counter electrode for dye-sensitized solar cells," *Composites Science and Technology*, vol. 69, no. 13, pp. 2193–2197, 2009.
- [48] W. Lu, J.-B. Peng, K.-X. Yang, L.-F. Lan, Q.-L. Niu, and Y. Cao, "Polymer thin-film transistor based on a high dielectric constant gate insulator," *Chinese Physics*, vol. 16, no. 4, pp. 1145–1149, 2007.
- [49] M. Kumar and S. S Sekhon, "Role of plasticizer's dielectric constant on conductivity modification of PEO-NH₄F polymer electrolytes," *European Polymer Journal*, vol. 38, no. 7, pp. 1297–1304, 2002.
- [50] W. Schliemann, Y. Cai, T. Degenkolb, J. Schmidt, and H. Corke, "Betalains of *Celosia argentea*," *Phytochemistry*, vol. 58, no. 1, pp. 159–165, 2001.
- [51] D. Strack, T. Vogt, and W. Schliemann, "Recent advances in betalain research," *Phytochemistry*, vol. 62, no. 3, pp. 247–269, 2003.

Research Article

Preparation of a Counter Electrode with *P*-Type NiO and Its Applications in Dye-Sensitized Solar Cell

Chuen-Shii Chou,^{1,2} Chin-Min Hsiung,^{1,2} Chun-Po Wang,²
Ru-Yuan Yang,^{1,3} and Ming-Geng Guo²

¹Research Center of Solar Photo-Electricity Applications, National Pingtung University of Science and Technology, Pingtung 912, Taiwan

²Powder Technology R&D Laboratory, Department of Mechanical Engineering, National Pingtung University of Science and Technology, Pingtung 912, Taiwan

³Department of Materials Engineering, National Pingtung University of Science and Technology, Pingtung 912, Taiwan

Correspondence should be addressed to Chuen-Shii Chou, cschou@mail.npust.edu.tw

Received 30 November 2009; Revised 20 March 2010; Accepted 10 May 2010

Academic Editor: Stephen M. Goodnick

Copyright © 2010 Chuen-Shii Chou et al. This is an open access article distributed under the Creative Commons Attribution License, which permits unrestricted use, distribution, and reproduction in any medium, provided the original work is properly cited.

This study investigates the applicability of a counter electrode with a *P*-type semiconductor oxide (such as NiO) on a dye-sensitized solar cell (DSSC). The counter electrode is fabricated by depositing an NiO film on top of a Pt film, which has been deposited on a Fluorine-doped tin oxide (FTO) glass using an ion-sputtering coater (or E-beam evaporator), using a simple spin coating method. This study also examines the effect of the average thickness of TiO₂ film deposited on a working electrode upon the power conversion efficiency of a DSSC. This study shows that the power conversion efficiency of a DSSC with a Pt(E)/NiO counter electrode (4.28%) substantially exceeds that of a conventional DSSC with a Pt(E) counter electrode (3.16%) on which a Pt film was deposited using an E-beam evaporator. This result is attributed to the fact that the NiO film coated on the Pt(E) counter electrode improves the electrocatalytic activity of the counter electrode.

1. Introduction

Solar power is the most notable among renewable energy resources because of its low environmental impact and global availability. Among alternative forms of solar cells, dye-sensitized solar cells (DSSCs), as proposed by O'Regan and Grätzel [1], have attracted considerable interest since 1991 because of its properties, such as low production cost and low environmental impact during fabrication [2, 3].

In the past few years (2006–2009), several methods have been utilized in modifying the structure of a working electrode (TiO₂ electrode) to improve the performance of DSSCs [4–22]. Novel sensitizers were synthesized and applied in DSSCs to promote the absorption of the visible spectrum [3, 23–29]. Novel electrolytes were proposed to prevent leakage of the electrolyte or to increase the lifetime (or performance) of DSSCs [30–35]. Moreover, a quasisolid DSSC with straight ion paths based on an anodically oxidized

Al₂O₃ film, which was full of nanopores from one side of the film to the other, was presented [36].

The counter electrode is an equally important component of the DSSC. The role of the counter electrode is to transfer electrons from an external circuit to the tri-iodide and iodine in the redox electrolyte. Currently, a layer of platinum (Pt) coated on a transparent conducting oxide (TCO) substrate is widely used as a counter electrode in DSSCs. Besides platinum (Pt), carbon materials (such as graphite powder and carbon black [37, 38], hard carbon spherule [39], single-walled carbon nanotubes [40], multiwalled carbon nanotubes [41], and nanosized carbon powder [42, 43]) have been used to prepare platinum-free counter electrodes.

Aside from the carbon materials, counter electrodes with metal oxide biphasic materials (such as Pt/NiO [44, 45] and Pt/TiO₂ [45]) have been prepared using an RF magnetron cosputtering system. However, these highly efficient Pt/NiO (or Pt/TiO₂) bi-phase counter electrodes are

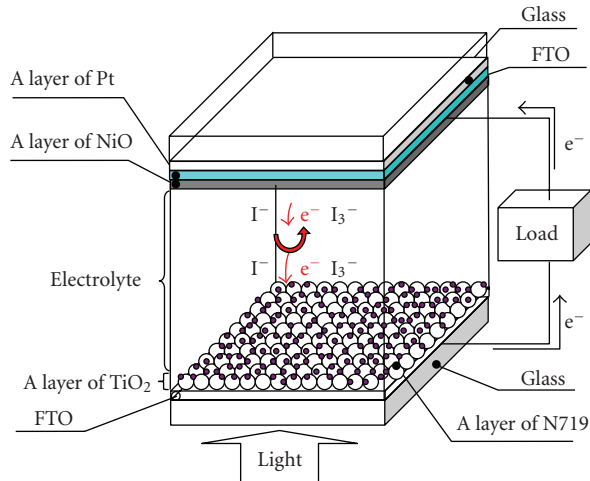


FIGURE 1: Schematic of the dye-sensitized solar cell with a Pt/NiO counter electrode.

obtained using an expensive vacuum technology which requires a sophisticated process control. Aside from this observation, Kay and Grätzel reported that a small amount of platinum might be dissolved in the electrolyte by oxidation and complex formation with iodide/tri-iodide (such as PtI_4 or H_2PtI_6) [37]. This may degrade the performance of counter electrodes after a certain period of exposure to light. Accordingly, decreasing the oxidation of Pt film in contact with the electrolyte is one of the most important factors in increasing the power conversion efficiency of DSSC; this is worthy of further study.

Therefore, in this study, a simple method (i.e., spin coating) was used to deposit a NiO film on top of a Pt film (Figure 1), which had been deposited on a FTO-glass (Fluorine-doped tin oxide, $\text{SnO}_2:\text{F}$) substrate using an E-beam evaporator (or ion-sputter coater) to protect the Pt film from oxidation and corrosion. The effect of *P*-type NiO on the electrocatalytic activity of the counter electrode and the power conversion efficiency of DSSC was investigated. A comparison of a DSSC with the proposed counter electrode with the conventional DSSC was also made in this study.

2. Experimental Details

The experiments involved (1) preparing the colloid of TiO_2 particles (P-25); (2) preparing the working electrode and measuring its properties; (3) preparing the colloid of *P*-type NiO; (4) preparing the counter electrode and measuring its properties; (5) assembling the DSSC by fitting the working electrode, the counter electrode, the electrolyte, and the copper conductive tape; (6) making J-V measurements of the DSSC.

2.1. Preparing and Measuring the Working Electrode. Fabricating a DSSC working electrode with a film of TiO_2 particles (Figure 1) followed these steps: (1) a colloid of TiO_2 particles (P-25) was prepared and homogenized; (2) using spin coating, the colloid of TiO_2 particles was deposited on top

of a FTO-glass substrate, and it was then sintered at 500°C for 1 h in a high-temperature furnace (Thermolyne, 46100); (3) the FTO-glass substrate with the film of TiO_2 particles was immersed into a (3×10^{-4} M) solution of N-719 dye (Ruthenium, $\text{RuL}_2(\text{NCS})_2$) and ethyl alcohol ($\text{CH}_3\text{CH}_2\text{OH}$, 95%) at 70°C for 6 h. The area of TiO_2 electrode of DSSC was 0.25 cm^2 in this study.

An α -step (Dekeak 6M) surface profiler was utilized to obtain the average thickness of the film on the FTO-glass substrate of the working electrode. In order to show the crystal structure of the TiO_2 powder, which was obtained by heating the solution of TiCl_4 , its X-ray diffraction (XRD) patterns were measured using a powder X-ray diffractometer (Shimadzu, XRD-6000).

2.2. Preparing and Measuring the Counter Electrode. The procedure for fabricating a counter electrode of DSSC with a film of Pt sandwiched between a NiO film and a FTO-glass substrate (Figure 1) is as follows. (1) The *P*-type NiO was obtained by annealing the Ni powder in a high-temperature furnace at 500°C ; (2) the NiO colloid was prepared by mixing 1 g of NiO with solvents (20 ml of DI water, 1 ml of ethanol, 0.1 ml of acetylacetone, and 0.1 ml of Triton X-100) and then homogenized in an ultrasonic homogenizer for 30 min; (3) using spin coating, 2-3 ml of the NiO colloid was deposited on top of a Pt film, which had been deposited on the FTO-glass substrate using an E-beam evaporator (or ion-sputter coater); (4) this substrate was then sintered at 500°C for 1 h in a high-temperature furnace.

In this study, in order to show the effect of the vacuum level on the performance of a DSSC, an E-beam evaporator (Kaoduen Tech. Corp.) with a vacuum level of 4×10^{-7} Torr and an ion-sputter coater (Hitachi E-1010) with a vacuum level of 10^{-2} Torr were used to deposit a Pt film on the FTO-glass substrate of the counter electrode. The area of a Pt film of counter electrode was 4.0 cm^2 in this study. Aside from this, the two-stage spin coating was used in this study: (1) in the first stage, the rotation speed of 1000 rpm and the duration of 5 s were used to remove the extra NiO colloid from the substrate; (2) in the second stage, the rotation speed of 1500 rpm and the duration of 15 s were used to homogenize the NiO film on the substrate.

The image and the micrograph of the counter electrode with a Pt film were obtained using a digital camera (Panasonic DMC-LZ2) and a scanning electron microscope (HITACHI S-4700), respectively. The reflectance and the cyclic voltammogram (CV) of the counter electrode were obtained using a UV-VIS-NIR spectrophotometer (Jasco V-600) and an electrochemical workstation (CH Instruments CHI-660C), respectively. Further, the surface roughness and the 3D micrograph of the counter electrode were obtained using an atomic force microscope (Digital Instrument NanoMan-NS4+D3100).

2.3. Assembling and Testing the DSSC. The working electrode, the counter electrode, and the copper conductive tape (Ted Pella) were fitted together, with the space between two electrodes adjusted to approximately $25\ \mu\text{m}$ for the liquid

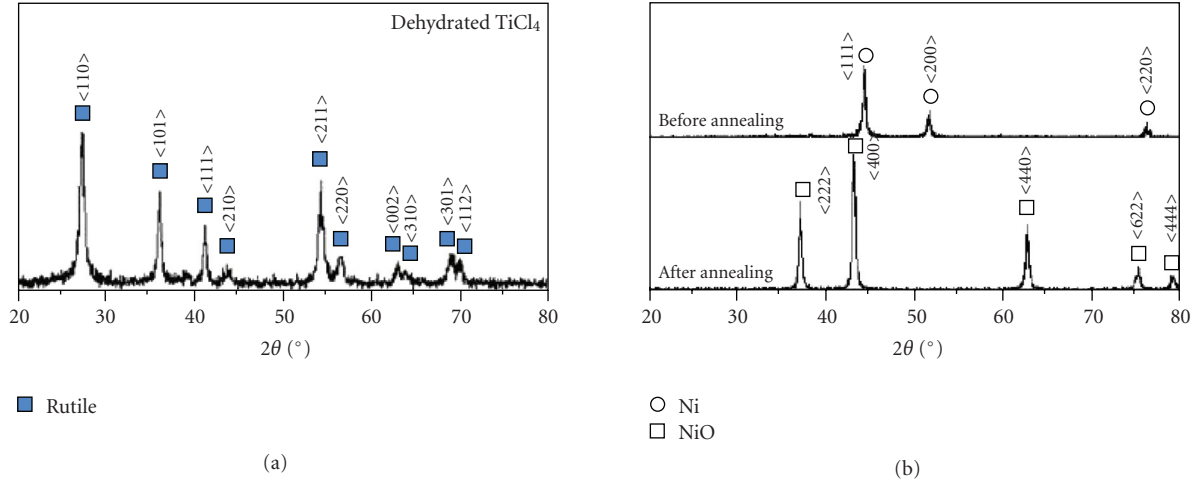


FIGURE 2: XRD patterns of Ni, NiO, and dehydrated TiCl₄.

electrolyte. After sealing, the liquid electrolyte was injected into the cell through a prepared hole in the cell. The detailed preparation of the photoanode and the DSSC assembly were presented in [22].

A digital source meter (Keithley 2000) measured the open-circuit photovoltage and the short-circuit photocurrent of the DSSC, and a solar simulator (Science Tech. SS150) illuminated the DSSC. The power conversion efficiency η of the DSSC is determined by

$$\eta(\%) = \frac{V_{oc} J_{sc} FF}{P_{in}} \times 100, \quad (1)$$

where V_{oc} , J_{sc} , and P_{in} represent the open-circuit photovoltage, the short-circuit photocurrent per unit area, and the incident light power (100 mW/cm²), respectively. Aside from this, fill factor (FF) is given by

$$FF = \frac{V_{max} J_{max}}{V_{oc} J_{sc}}, \quad (2)$$

where V_{max} and J_{max} represent the voltage and the current per unit area at the maximum output power point, respectively.

3. Results and Discussion

3.1. Characteristics of TiCl₄ and NiO. Figure 2 shows the X-ray diffraction (XRD) patterns of dehydrated TiCl₄, as well as powders of Ni and NiO. The solid square, circle, and square in Figure 3 represent rutile, Ni, and NiO, respectively. From JCPDS 89-4920 (rutile), the XRD patterns of the dehydrated TiCl₄ show that three major peaks of rutile at $2\theta = 27.47^\circ$, $2\theta = 36.14^\circ$, and $2\theta = 54.31^\circ$ correspond to the diffraction from the $\langle 110 \rangle$, $\langle 101 \rangle$, and $\langle 211 \rangle$ planes, respectively. The purpose of immersing a FTO-glass substrate in the TiCl₄ solution before depositing the TiO₂ (P-25) colloid is to prevent the FTO-glass substrate from dye (or electrolyte) contamination, which might penetrate through the cavities of the TiO₂ (P-25) film. Ito et al. observed that TiCl₄ treatment induced improvements in the adhesion and mechanical strength of a nanocrystalline TiO₂ layer [22].

From JCPDS 89-5881 (nickel oxide), the XRD patterns of the NiO powder, obtained by annealing the Ni powder, show that three major peaks of NiO at $2\theta = 37.3^\circ$, $2\theta = 43.3^\circ$, and $2\theta = 62.9^\circ$ correspond to the diffraction from the $\langle 222 \rangle$, $\langle 400 \rangle$, and $\langle 440 \rangle$ planes, respectively. Instead of depositing and annealing Ni to form a NiO deposit on platinum, we have preferred to spin coat a previously formed NiO before sintering. This is because, compared with the Ni powder, NiO powder can be more easily dispersed in the solvent.

3.2. Characteristics of the Counter Electrode. This study used four kinds of counter electrode: (1) a counter electrode with a Pt film deposited on the FTO-glass substrate using an E-beam evaporator (called Pt(E)), (2) a counter electrode with a Pt film deposited on the FTO-glass substrate using an ion-sputter coater (called Pt(S)), (3) a counter electrode prepared by depositing a NiO film on top of Pt(E) (called Pt(E)/NiO), and (4) a counter electrode prepared by depositing a NiO film on top of Pt(S) (called Pt(S)/NiO).

Figure 3 shows the images and the SEM micrographs (20 kx) of the counter electrodes of Pt(E) and Pt(S). Figure 4 shows the variations in reflectance with light wavelength of the Pt(E), Pt(S), Pt(E)/NiO, and Pt(S)/NiO counter electrodes. For the counter electrodes used in this study, the reflectance increases with an increase in wavelength. For example, for the Pt(E) counter electrode, as the wavelength increases to 800 nm, its reflectance goes up to 50.4% (Figure 4). The light-reflecting character of the Pt film is desirable because it increases the light harvesting efficiency of the sensitizing dye [45, 46]. Aside from this, at a fixed wavelength, the reflectance of the Pt(E) counter electrode substantially exceeds that of the Pt(S) counter electrode. For example, at a fixed wavelength of 800 nm, the reflectance of the counter electrodes of Pt(E) and Pt(S) are 50.4% and 13.4%, respectively. This result is attributed to the fact that the vacuum level of the ion-sputter coater used in this study (10^{-2} Torr) is not higher than that of the E-beam evaporator (4×10^{-7} Torr), so the target (such as Pt) and the residual

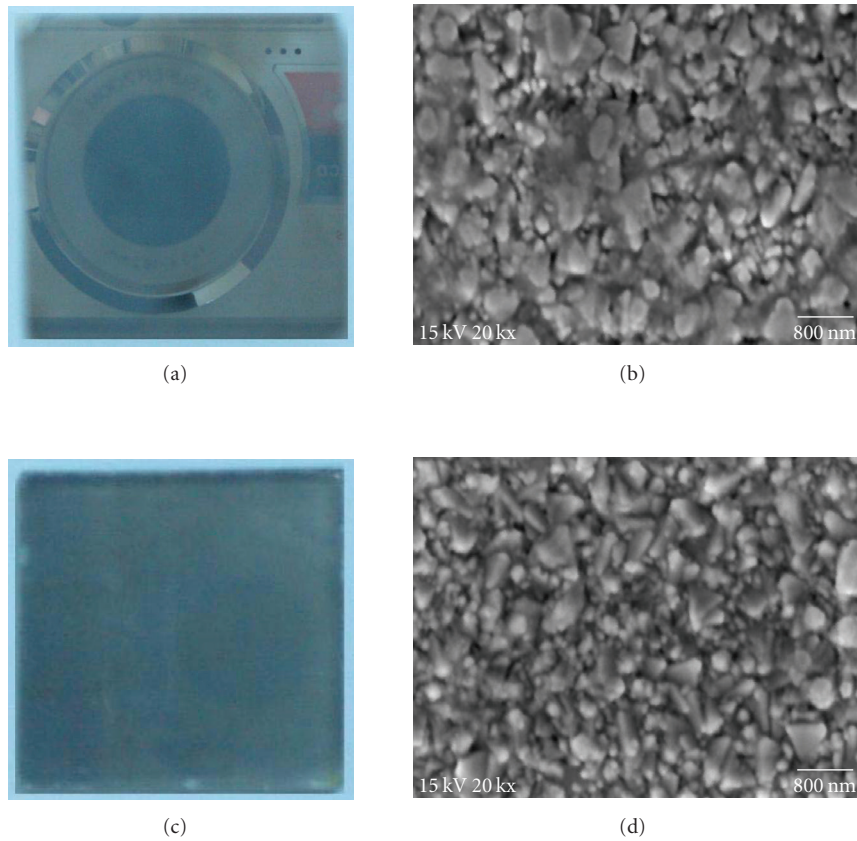


FIGURE 3: Image of the Pt(E) counter electrode (a), SEM micrograph (20 kx) of the Pt(E) counter electrode (b), image of the Pt(S) counter electrode (c), and SEM micrograph (20 kx) of the Pt(S) counter electrode (d).

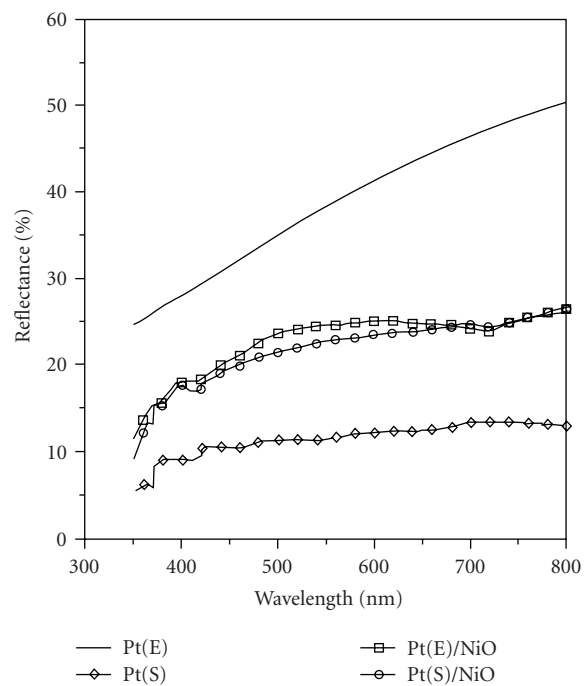


FIGURE 4: Variations in reflectance with the wavelength of the light for counter electrodes of Pt(E), Pt(S), Pt(E)/NiO, and Pt(S)/NiO.

TABLE 1: Test conditions and power conversion efficiencies of DSSCs.

Counter Electrode		Working Elect rode		J_{sc} (mA/cm ²)	V_{oc}	FF(%)	η (%)	
	RMS(nm)	Ra(nm)	Average film thickness (μ m)					
D1	Pt(E)	18.570	14.213	12.0	9.15	0.65	50.42	3.00
D2				19.0	9.27	0.65	52.49	3.16
D3	Pt(S)	16.734	12.894	11.0	6.11	0.65	58.64	2.33
D4				15.0	8.28	0.65	44.98	2.34
D5	Pt(E)/NiO	123.30	97.321	12.4	9.05	0.65	59.77	3.51
D6				16.0	10.44	0.65	63.15	4.28
D7	Pt(S)/NiO	112.46	92.859	13.1	7.70	0.65	56.40	2.82
D8				14.8	8.45	0.65	50.06	2.92

Note: “(E)”, “(S)”, RMS, and Ra represent E-beam evaporator, sputtering, root mean square, and roughness average.

substance in the chamber are probably deposited on the substrate during sputtering. Therefore, unlike the Pt(E) counter electrode, the Pt(S) counter electrode is not able to mirror the digital camera, which was used to take images of the counter electrodes (Figure 3). At 800 nm wavelength, the reflectance of the Pt(E)/NiO counter electrode (26.6%) is close to that of the Pt(S)/NiO counter electrode (26.2%). Further, the sheet resistance of the Pt(S) counter electrode (9.73 Ω /sq) also substantially exceeds that of the Pt(E) counter electrode (5.57 Ω /sq).

Figure 5 shows the 3-D microstructures of the Pt(E), Pt(S), Pt(E)/NiO, and Pt(S)/NiO counter electrodes. The surface roughness average (Ra) of the Pt(E) counter electrode (14.213 nm) exceeds that of the Pt(S) counter electrode (12.894 nm), as shown in Figure 5. This is attributed to the fact that compared with evaporation, it is easier to maintain a stable deposition rate during sputtering, and it is also much easier to deposit a uniform film on a large area substrate [47]. Song and Lin observed that the hillock formation in a Pt/Ti film was obtained using UHV electron beam evaporation, but a rosette-type microstructure in the Pt/Ti film was obtained using DC-sputtering [48]. Aside from this, Zhou et al. indicated that the increased roughness improved the light scattering of the counter electrode [49].

Figure 6 shows the CVs of the Pt(E), Pt(S), Pt(E)/NiO, and Pt(S)/NiO counter electrodes. The oxidation and reduction peaks of I^-/I_3^- on these counter electrodes are similar. For example, their oxidation potential ranges from 0.4 V to 0.9 V, and the reduction potential ranges from 0.0 V to 0.5 V (Figure 6). The presence of a NiO film enhances the current density during the redox process. For example, in the oxidation process, the highest current density of Pt(E)/NiO (7.2 mA/cm²) exceeds that of Pt(E) (6.1 mA/cm²). In the reduction process, the lowest current density of Pt(E)/NiO (-5.2 mA/cm²) also exceeds that of Pt(E) (-3.9 mA/cm²). This result is attributed to the fact that a larger active surface area due to a deposited NiO film corresponds to a more energetic electrocatalytic activity. A similar tendency was also observed by Kim et al. [45] and Yoon et al. [46].

3.3. Photoelectrochemical Behaviour. The J-V characteristics of DSSC in all tests are shown in Figure 7, and Table 1 presents the open-circuit photovoltage (V_{oc}), the short-circuit photocurrent per unit area (J_{sc}), the fill factor (FF),

and the power conversion efficiency (η) of the DSSC in tests D1 to D8. In this study, the V_{oc} of the DSSC is kept at 0.65 V. The power conversion efficiency of DSSC with Pt(E) (or Pt(E)/NiO) exceeds 3%.

At a fixed counter electrode, as the average thickness of TiO₂ film increases, the power conversion efficiency increases. For example, for the Pt(E) counter electrode, the power conversion efficiency increases from 3.00% to 3.16% as the average thickness of the TiO₂ film increases from 12.0 μ m (in test D1) to 19.0 μ m (in test D2). The J-V curve of DSSC with a thicker TiO₂ film is above that of DSSC with a thinner TiO₂ film (Figure 7). This result is due to the following: (1) a TiO₂ film with a larger average thickness contains more TiO₂ (P-25) particles, which may absorb more ultraviolet light; (2) the working electrode with a thicker TiO₂ film corresponds to a higher adsorptive capability of the dye because more tiny cavities are created in this film on a FTO-glass substrate so that the larger number of electrons may be excited as the DSSC is exposed to the light.

Although the average thickness of the TiO₂ film in test D1 (12.0 μ m) is very close to that in test D3 (11.0 μ m), the power conversion efficiency of DSSC with a Pt(E) counter electrode in test D1 (3.00%) substantially exceeds that of DSSC with a Pt(S) counter electrode in test D3 (2.33%). This result may be due to the following: (1) the Pt(S) counter electrode sheet resistance (9.73 Ω /sq) significantly exceeds the Pt(E) counter electrode sheet resistance (5.57 Ω /sq); (2) at a fixed wavelength, the Pt(E) counter electrode reflectance remarkably exceeds the Pt(S) counter electrode reflectance. Fang et al. showed that in order for a DSSC to have better power conversion efficiency, a counter electrode should have the following characteristics: (1) good conductivity for transferring electrons, (2) excellent catalytic activity for I^-/I_3^- redox, and (3) light-reflecting ability to improve light-harvesting efficiency [50].

Most interestingly, the presence of a NiO film remarkably promotes the power conversion efficiency of DSSC. For example, the power conversion efficiencies of DSSC in tests D2 (with a Pt(E) counter electrode) and D6 (with a Pt(E)/NiO counter electrode) are 3.16% and 4.28%, respectively. Furthermore, the power conversion efficiencies of DSSC in tests D4 (with a Pt(S) counter electrode) and D8 (with a Pt(S)/NiO counter electrode) are 2.34% and 2.92%, respectively. These results are due to the following: (1) the

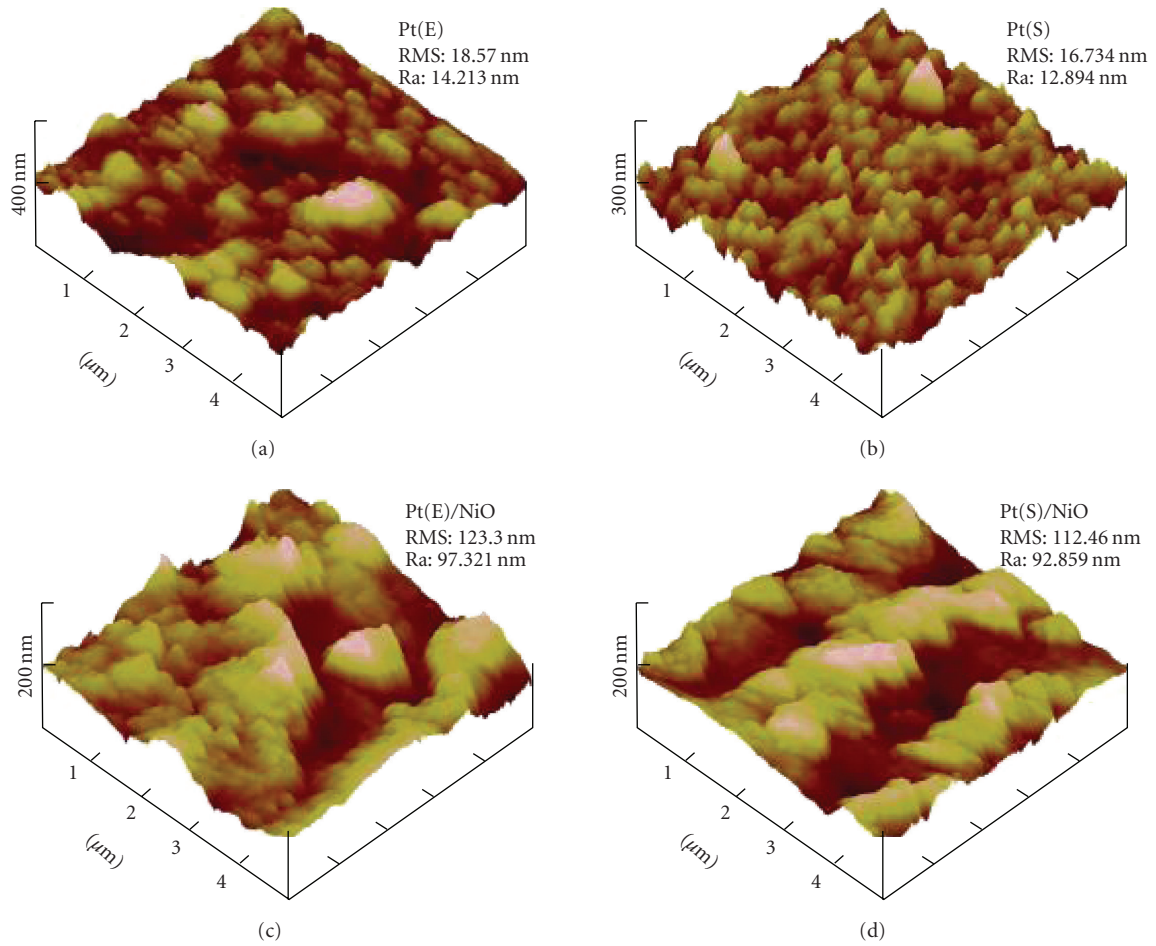


FIGURE 5: The 3-D micro-structure of counter electrodes. (a) Pt(E), (b) Pt(S), (c) Pt(E)/NiO, and (d) Pt(S)/NiO.

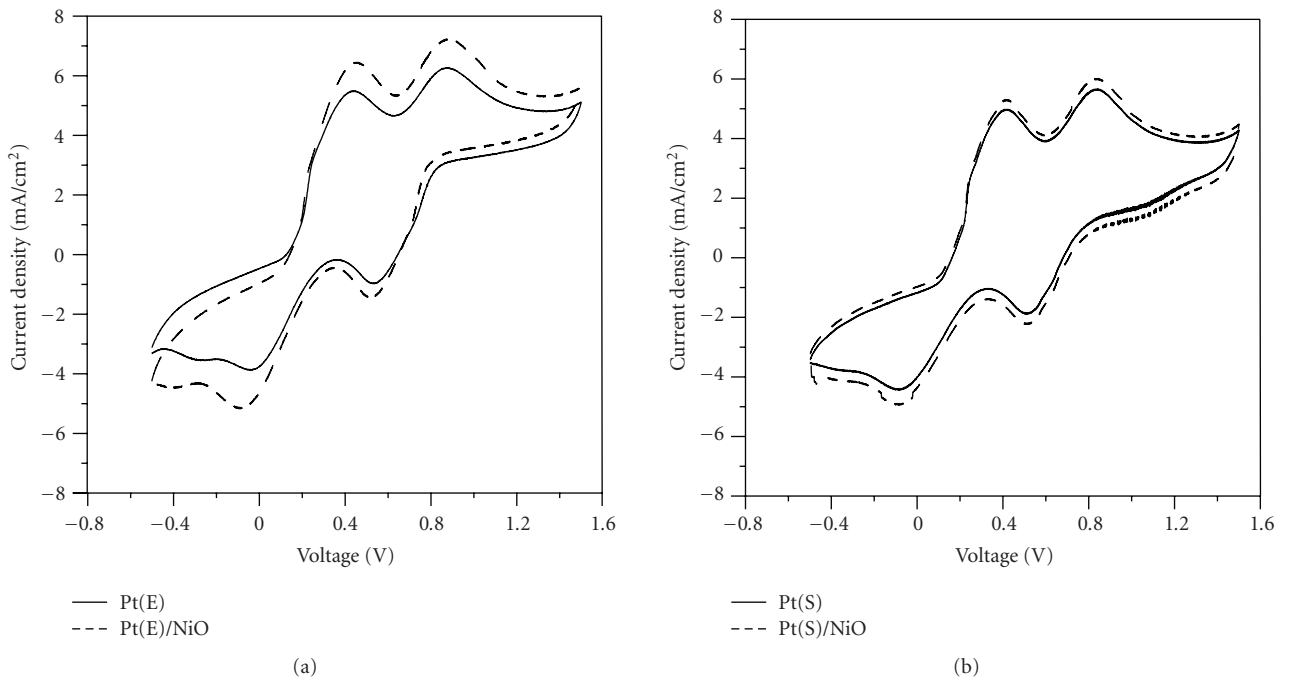


FIGURE 6: Cyclic voltammograms (CVs) of counter electrodes of Pt(E), Pt(S), Pt(E)/NiO, and Pt(S)/NiO.

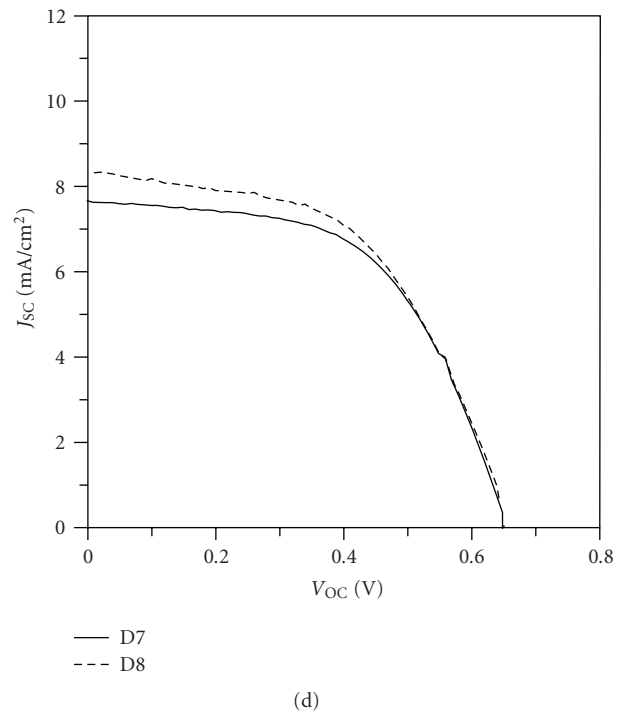
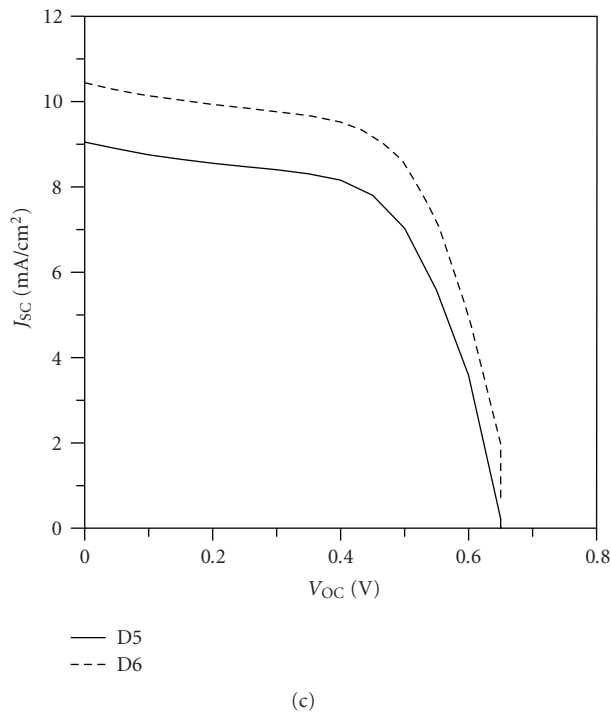
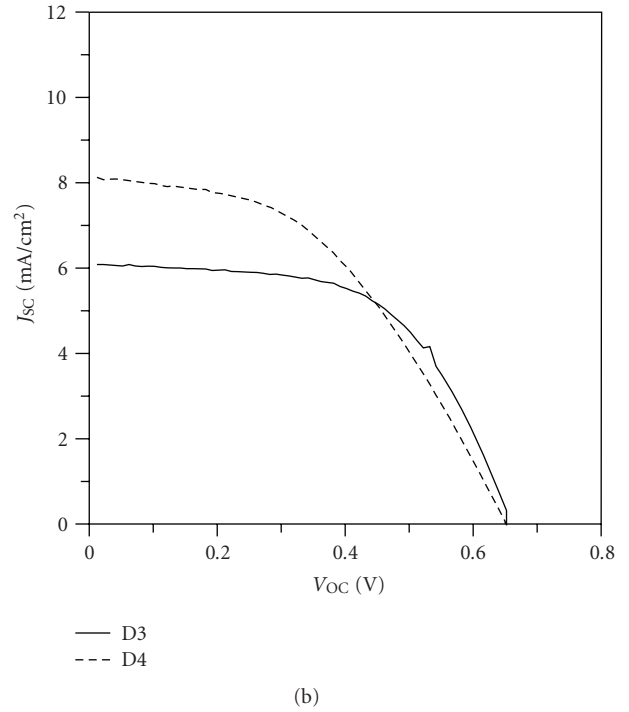
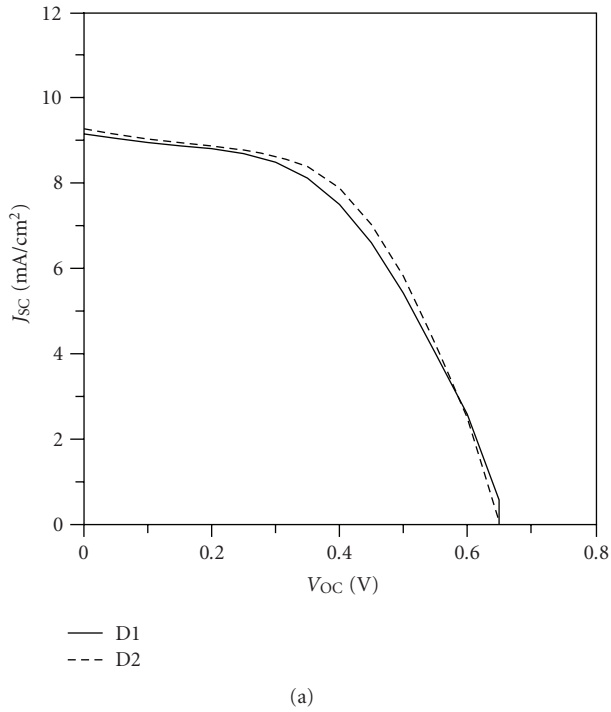


FIGURE 7: J - V characteristics in tests D1 to D8.

NiO film deposited on top of Pt(E) (or Pt(S)) substantially enhances the surface roughness average (Ra) of the counter electrode (Table 1); (2) the increased roughness improves the light scattering as well as the electroactive area of a counter electrode. Kim et al. [45] showed that the overall conversion efficiency of DSSC increased to 3.62% and 4.21% through the use of Pt/NiO and Pt/TiO₂ bi-phase counter electrodes, respectively.

4. Conclusion

The effect of different kinds of counter electrodes on the power conversion efficiency of a DSSC was investigated. The power conversion efficiency of the DSSC with a Pt(E) counter electrode exceeds that of the DSSC with a Pt(S) counter electrode because the Pt(E) counter electrode has better reflectance. Furthermore, the power conversion efficiency of

the DSSC with a Pt(E)/NiO counter electrode exceeds that of the DSSC with a Pt(E) counter electrode because the Pt(E)/NiO counter electrode has better electrocatalytic activity. Most importantly, this study supports the application of a NiO film deposited on the Pt-FTO substrate using a simple spin coating method to improve the performance of a DSSC. However, the optimal process for fabricating a DSSC with a NiO film on the counter electrode, which can promote the electrocatalytic activity of the counter electrode, must be implemented to yield a DSSC with a satisfactory power conversion efficiency.

Concerning the possible application of this nontransparent cathode that the NiO is deposited on top of the Pt film, it may decline the transparency of photovoltaic windows. However, besides photovoltaic windows, the other real applications of DSSC, such as DSSC lampshade, flower-shaped DSSC, and leaf-shaped DSSC, whose transparency may not be seriously considered, have received substantial attention, too. We believe that this counter electrode may facilitate the performance of aforementioned devices of DSSC.

Acknowledgments

The authors would like to thank the National Science Council, Taiwan for financially supporting this research under Contract nos. NSC 97-2221-E-020-035 and NSC 97-2918-I-020-001. The authors would also like to thank the National Pingtung University of Science and Technology, Taiwan for their financial support to establish the Research Center of Solar Photo-Electricity Applications.

References

- [1] B. O'Regan and M. Grätzel, "A low-cost, high-efficiency solar cell based on dye-sensitized colloidal TiO₂ films," *Nature*, vol. 353, no. 6346, pp. 737–740, 1991.
- [2] N. S. Lewis, "Toward cost-effective solar energy use," *Science*, vol. 315, no. 5813, pp. 798–801, 2007.
- [3] S. Kim, D. Kim, H. Choi et al., "Enhanced photovoltaic performance and long-term stability of quasi-solid-state dye-sensitized solar cells via molecular engineering," *Chemical Communications*, no. 40, pp. 4951–4953, 2008.
- [4] M. Wei, Y. Konishi, H. Zhou, H. Sugihara, and H. Arakawa, "Utilization of titanate nanotubes as an electrode material in dye-sensitized solar cells," *Journal of the Electrochemical Society*, vol. 153, no. 6, pp. A1232–A1236, 2006.
- [5] G.-S. Kim, H.-K. Seo, V. P. Godble, Y.-S. Kim, O.-B. Yang, and H.-S. Shin, "Electrophoretic deposition of titanate nanotubes from commercial titania nanoparticles: application to dye-sensitized solar cells," *Electrochemistry Communications*, vol. 8, no. 6, pp. 961–966, 2006.
- [6] S.-J. Roh, R. S. Mane, S.-K. Min, W.-J. Lee, C. D. Lokhande, and S.-H. Han, "Achievement of 4.51% conversion efficiency using ZnO recombination barrier layer in TiO₂ based dye-sensitized solar cells," *Applied Physics Letters*, vol. 89, no. 25, Article ID 253512, 2006.
- [7] Y. H. Su, W. H. Lai, L. G. Teoh, M. H. Hon, and J. L. Huang, "Layer-by-layer Au nanoparticles as a Schottky barrier in a water-based dye-sensitized solar cell," *Applied Physics A*, vol. 88, no. 1, pp. 173–178, 2007.
- [8] J. Bandara and J. P. Yasomane, "P-type oxide semiconductors as hole collectors in dye-sensitized solid-state solar cells," *Semiconductor Science and Technology*, vol. 22, no. 2, pp. 20–24, 2007.
- [9] S. Ito, T. N. Murakami, P. Comte et al., "Fabrication of thin film dye sensitized solar cells with solar to electric power conversion efficiency over 10%," *Thin Solid Films*, vol. 516, no. 14, pp. 4613–4619, 2008.
- [10] S. Sumikura, S. Mori, S. Shimizu, H. Usami, and E. Suzuki, "Syntheses of NiO nanoporous films using nonionic triblock co-polymer templates and their application to photo-cathodes of p-type dye-sensitized solar cells," *Journal of Photochemistry and Photobiology A*, vol. 199, no. 1, pp. 1–7, 2008.
- [11] S. Sumikura, S. Mori, S. Shimizu, H. Usami, and E. Suzuki, "Photoelectrochemical characteristics of cells with dyed and undyed nanoporous p-type semiconductor CuO electrodes," *Journal of Photochemistry and Photobiology A*, vol. 194, no. 2-3, pp. 143–147, 2008.
- [12] C.-S. Chou, R.-Y. Yang, M.-H. Weng, and C.-H. Yeh, "Study of the applicability of TiO₂/dye composite particles for a dye-sensitized solar cell," *Advanced Powder Technology*, vol. 19, no. 6, pp. 541–558, 2008.
- [13] C.-S. Chou, R.-Y. Yang, M.-H. Weng, and C.-H. Yeh, "Preparation of TiO₂/dye composite particles and their applications in dye-sensitized solar cell," *Powder Technology*, vol. 187, no. 2, pp. 181–189, 2008.
- [14] K.-M. Lee, C.-W. Hu, H.-W. Chen, and K.-C. Ho, "Incorporating carbon nanotube in a low-temperature fabrication process for dye-sensitized TiO₂ solar cells," *Solar Energy Materials and Solar Cells*, vol. 92, no. 12, pp. 1628–1633, 2008.
- [15] B. Yoo, K. Kim, S. H. Lee, W. M. Kim, and N.-G. Park, "ITO/ATO/TiO₂ triple-layered transparent conducting substrates for dye-sensitized solar cells," *Solar Energy Materials and Solar Cells*, vol. 92, no. 8, pp. 873–877, 2008.
- [16] B. N. Pawar, G. Cai, D. Ham et al., "Preparation of transparent and conducting boron-doped ZnO electrode for its application in dye-sensitized solar cells," *Solar Energy Materials and Solar Cells*, vol. 93, no. 4, pp. 524–527, 2009.
- [17] K.-M. Lee, V. Suryanarayanan, and K.-C. Ho, "Influences of different TiO₂ morphologies and solvents on the photovoltaic performance of dye-sensitized solar cells," *Journal of Power Sources*, vol. 188, no. 2, pp. 635–641, 2009.
- [18] W. J. Lee, E. Ramasamy, and D. Y. Lee, "Effect of electrode geometry on the photovoltaic performance of dye-sensitized solar cells," *Solar Energy Materials and Solar Cells*, vol. 93, no. 8, pp. 1448–1451, 2009.
- [19] U. O. Krašovec, M. Berginc, M. Hočevar, and M. Topič, "Unique TiO₂ paste for high efficiency dye-sensitized solar cells," *Solar Energy Materials and Solar Cells*, vol. 93, no. 3, pp. 379–381, 2009.
- [20] T. Sawatsuk, A. Chindaduang, C. Sae-kung, S. Pratontep, and G. Tumcharern, "Dye-sensitized solar cells based on TiO₂-MWCNTs composite electrodes: performance improvement and their mechanisms," *Diamond and Related Materials*, vol. 18, no. 2-3, pp. 524–527, 2009.
- [21] H. Wang, Y. Liu, H. Xu et al., "An investigation on the novel structure of dye-sensitized solar cell with integrated photoanode," *Renewable Energy*, vol. 34, no. 6, pp. 1635–1638, 2009.
- [22] C.-S. Chou, R.-Y. Yang, C.-K. Yeh, and Y.-J. Lin, "Preparation of TiO₂/Nano-metal composite particles and their applications in dye-sensitized solar cells," *Powder Technology*, vol. 194, no. 1-2, pp. 95–105, 2009.

- [23] S. Hwang, J. H. Lee, C. Park et al., "A highly efficient organic sensitizer for dye-sensitized solar cells," *Chemical Communications*, no. 46, pp. 4887–4889, 2007.
- [24] J.-G. Chen, C.-Y. Chen, S.-J. Wu, J.-Y. Li, C.-G. Wu, and K.-C. Ho, "On the photophysical and electrochemical studies of dye-sensitized solar cells with the new dye CYC-B1," *Solar Energy Materials and Solar Cells*, vol. 92, no. 12, pp. 1723–1727, 2008.
- [25] S. Ito, H. Miura, S. Uchida et al., "High-conversion-efficiency organic dye-sensitized solar cells with a novel indoline dye," *Chemical Communications*, no. 41, pp. 5194–5196, 2008.
- [26] M. Xu, R. Li, N. Pootrakulchote et al., "Energy-level and molecular engineering of organic D- π -A sensitizers in dye-sensitized solar cells," *Journal of Physical Chemistry C*, vol. 112, no. 49, pp. 19770–19776, 2008.
- [27] C.-H. Yang, H.-L. Chen, Y.-Y. Chuang et al., "Characteristics of triphenylamine-based dyes with multiple acceptors in application of dye-sensitized solar cells," *Journal of Power Sources*, vol. 188, no. 2, pp. 627–634, 2009.
- [28] J. Pei, S. Peng, J. Shi et al., "Triphenylamine-based organic dye containing the diphenylvinyl and rhodanine-3-acetic acid moieties for efficient dye-sensitized solar cells," *Journal of Power Sources*, vol. 187, no. 2, pp. 620–626, 2009.
- [29] V. Kandavelu, H.-S. Huang, J.-L. Jian, T. C.-K. Yang, K.-L. Wang, and S.-T. Huang, "Novel iminocoumarin dyes as photosensitizers for dye-sensitized solar cell," *Solar Energy*, vol. 83, no. 4, pp. 574–581, 2009.
- [30] T. Kato, T. Kado, S. Tanaka, A. Okazaki, and S. Hayase, "Quasi-solid dye-sensitized solar cells containing nanoparticles modified with ionic liquid-type molecules," *Journal of the Electrochemical Society*, vol. 153, no. 3, pp. A626–A630, 2006.
- [31] T. C. Wei, C. C. Wan, and Y. Y. Wang, "Preparation and characterization of a micro-porous polymer electrolyte with cross-linking network structure for dye-sensitized solar cell," *Solar Energy Materials and Solar Cells*, vol. 91, no. 20, pp. 1892–1897, 2007.
- [32] S. Ganesan, B. Muthuraaman, V. Mathew, J. Madhavan, P. Maruthamuthu, and S. Austin Suthanthiraraj, "Performance of a new polymer electrolyte incorporated with diphenylamine in nanocrystalline dye-sensitized solar cell," *Solar Energy Materials and Solar Cells*, vol. 92, no. 12, pp. 1718–1722, 2008.
- [33] Y. Wang, Y. Sun, B. Song, and J. Xi, "Ionic liquid electrolytes based on 1-vinyl-3-alkylimidazolium iodides for dye-sensitized solar cells," *Solar Energy Materials and Solar Cells*, vol. 92, no. 6, pp. 660–666, 2008.
- [34] D. Shi, N. Pootrakulchote, R. Li et al., "New efficiency records for stable dye-sensitized solar cells with low-volatility and ionic liquid electrolytes," *Journal of Physical Chemistry C*, vol. 112, no. 44, pp. 17046–17050, 2008.
- [35] K.-M. Lee, P.-Y. Chen, C.-P. Lee, and K.-C. Ho, "Binary room-temperature ionic liquids based electrolytes solidified with SiO₂ nanoparticles for dye-sensitized solar cells," *Journal of Power Sources*, vol. 190, no. 2, pp. 573–577, 2009.
- [36] T. Kato and S. Hayase, "Quasi-solid dye sensitized solar cell with straight ion paths. Proposal of hybrid electrolytes for ionic liquid-type electrolytes," *Journal of the Electrochemical Society*, vol. 154, no. 1, pp. B117–B121, 2007.
- [37] A. Kay and M. Grätzel, "Low cost photovoltaic modules based on dye sensitized nanocrystalline titanium dioxide and carbon powder," *Solar Energy Materials and Solar Cells*, vol. 44, no. 1, pp. 99–117, 1996.
- [38] T. N. Murakami, S. Ito, Q. Wang et al., "Highly efficient dye-sensitized solar cells based on carbon black counter electrodes," *Journal of the Electrochemical Society*, vol. 153, no. 12, pp. A2255–A2261, 2006.
- [39] Z. Huang, X. Liu, K. Li et al., "Application of carbon materials as counter electrodes of dye-sensitized solar cells," *Electrochemistry Communications*, vol. 9, no. 4, pp. 596–598, 2007.
- [40] C.-S. Chou, R.-Y. Yang, M.-H. Weng, and C.-I. Huang, "The applicability of SWCNT on the counter electrode for the dye-sensitized solar cell," *Advanced Powder Technology*, vol. 20, no. 4, pp. 310–317, 2009.
- [41] E. Ramasamy, W. J. Lee, D. Y. Lee, and J. S. Song, "Spray coated multi-wall carbon nanotube counter electrode for tri-iodide (I₃⁻) reduction in dye-sensitized solar cells," *Electrochemistry Communications*, vol. 10, no. 7, pp. 1087–1089, 2008.
- [42] E. Ramasamy, W. J. Lee, D. Y. Lee, and J. S. Song, "Nanocarbon counterelectrode for dye sensitized solar cells," *Applied Physics Letters*, vol. 90, no. 17, Article ID 173103, 2007.
- [43] W. J. Lee, E. Ramasamy, D. Y. Lee, and J. S. Song, "Grid type dye-sensitized solar cell module with carbon counter electrode," *Journal of Photochemistry and Photobiology A*, vol. 194, no. 1, pp. 27–30, 2008.
- [44] S.-S. Kim, K.-W. Park, J.-H. Yum, and Y.-E. Sung, "Pt-NiO nanophase electrodes for dye-sensitized solar cells," *Solar Energy Materials and Solar Cells*, vol. 90, no. 3, pp. 283–290, 2006.
- [45] S.-S. Kim, K.-W. Park, J.-H. Yum, and Y.-E. Sung, "Dye-sensitized solar cells with Pt-NiO and Pt-TiO₂ biphasic counter electrodes," *Journal of Photochemistry and Photobiology A*, vol. 189, no. 2-3, pp. 301–306, 2007.
- [46] C. H. Yoon, R. Vittal, J. Lee, W.-S. Chae, and K.-J. Kim, "Enhanced performance of a dye-sensitized solar cell with an electrodeposited-platinum counter electrode," *Electrochimica Acta*, vol. 53, no. 6, pp. 2890–2896, 2008.
- [47] H. Fornander, J. Birch, P. Sandström, and J.-E. Sundgren, "Structure evolution of epitaxial Pd grown on MgO(001): a comparison between sputtering and electron-beam evaporation," *Thin Solid Films*, vol. 349, no. 1, pp. 4–9, 1999.
- [48] Z. Song and C. Lin, "Microstructure and electrical properties of PbZr_{0.48}Ti_{0.52}O₃ ferroelectric films on different Pt bottom electrodes," *Applied Surface Science*, vol. 158, no. 1, pp. 21–27, 2000.
- [49] K. Imoto, K. Takahashi, T. Yamaguchi, T. Komura, J.-I. Nakamura, and K. Murata, "High-performance carbon counter electrode for dye-sensitized solar cells," *Solar Energy Materials and Solar Cells*, vol. 79, no. 4, pp. 459–469, 2003.
- [50] X. Fang, T. Ma, G. Guan, M. Akiyama, T. Kida, and E. Abe, "Effect of the thickness of the Pt film coated on a counter electrode on the performance of a dye-sensitized solar cell," *Journal of Electroanalytical Chemistry*, vol. 570, no. 2, pp. 257–263, 2004.